Durham E-Theses

Surfactant Adsorption at Liquid−Solid Interfaces

DUDGEON, ALEXANDER,PAUL

How to cite:

DUDGEON, ALEXANDER,PAUL (2017) *Surfactant Adsorption at Liquid−Solid Interfaces*, Durham theses, Durham University. Available at Durham E-Theses Online: http://etheses.dur.ac.uk/12237/

Use policy

Surfactant Adsorption at Liquid–Solid Interfaces

A thesis submitted in partial fulfilment of the requirements for the degree of
Doctor of Philosophy at the University of Durham by:

Alexander Paul Dudgeon

Department of Chemistry

University of Durham

Collingwood College

April 2017

Abstract

Alexander Paul Dudgeon

Surfactant Adsorption at Liquid–Solid Interfaces

Surfactant adsorption to the liquid-solid interface is of great importance to many industrial and consumer processes; from detergency to crop spraying and drilling for oil, the understanding of how these molecules behave is crucial to their design and further efficiency improvement.

This thesis describes how a Raman spectrometer for use in total-internal reflection (TIR)-Raman spectroscopy was built and commissioned to provide a new, open bench system. The prime aim was to improve on the time resolution of our existing commercial spectrometer (to $<1\,$s) and allow for easy modification.

TIR-Raman spectroscopy allows us to be surface-selective by only measuring the Raman spectrum from very close to the interface, where the evanescent field excites molecules attached to, or very close to the surface. As this field decays exponentially with distance, only a small region at the interface is probed ($\approx100\,$nm).

Using an in-line mixer we were able to record adsorption and desorption isotherms on the surfaces. This technique utilised a continuously stirred tank to vary continually the concentration of solution entering the cell, hence a whole continuous range of concentrations (limited only by the time resolution) could be studied. The validity of our in-line mixer is tested with solutions of the Raman-active molecules acetonitrile, methanol, and sucrose.

The adsorption to silica of various anionic surfactants (sodium dodecyl sulphate (SDS) and sodium dodecylbenzenesulfonate (C_{12}LAS)), nonionic surfactants (polyethylene oxide alkyl ethers (C_nE_ms)) and cationic surfactants (single and double chained tertiary ammonium bromides (C_nTABs) and DHDAB) were investigated. Varying mixtures of nonionic and anionic surfactant adsorption on hydrophobic silica are covered briefly.

With the individual surfactants, the investigation started with a plain (acid-washed) silica hemisphere, then moved to various coatings applied to silica, using the same TIR-Raman technique. The additional model substrates studied were hydrophobic silica (treated with hexamethyldisilazane), zeolite, kaolinite, polyester and (although largely unsuccessful) haematite.

Acknowledgements

Preface

Please note, tables of nomenclature and abbreviations are available from page xi.

Declaration

The work in this thesis is based on research carried out at in Prof. Colin Bain's Resarch Group, the Department of Chemistry, University of Durham, England. No part of this thesis has been submitted elsewhere for any other degree or qualification and it is all my own work unless referenced to the contrary in the text.

Copyright Notice

Contents

List of Figures

List of Tables

Nomenclature and Abbreviations

Other than where defined elsewhere, the following symbols are used frequently:

Table 1: List of commonly used nomenclature

Symbol	Description
$\underline{E}$	Electric field
F	Force
γ_{sv}, γ_{lv} or γ_{sl}	Surface tension of solid-vapour, liquid-vapour or solid-liquid
γ_{X}	Activity coefficient of surfactant X in the micelle
Γ	Surface excess
G	Free energy
θ	Contact angle
K_B	Boltzmann constant [2] $((1.380\,648\,8 \pm 0.000\,001\,3) \times 10^{-23}\,\mathrm{J\,K^{-1}})$
λ	Wavelength
μ	Chemical potential
M	Molar concentration $(\mathrm{mol\,dm^{-3}})$
ν	Frequency
N	Aggregation number
n	Refractive index
p	Pressure
R	Molar gas constant [2] $((8.314\,462\,1 \pm 0.000\,007\,5)\,\mathrm{J\,K^{-1}\,mol^{-1}})$
r	Radius
σ	Charge
V	Volume
v	Velocity
x_{x}	Mole fraction of surfactant X in the micelle
y_{x}	Mole fraction of surfactant X in the monomer

Table 2: List of commonly used abbreviations

Abbreviation	Description
% vol.	Percent by volume
% wt.	Percent by weight
AFA	Abstract factor analysis
AFM	Atomic force microscopy
ATR-IR	Attenuated total reflection infra-red
CCD	Charge coupled device
CMC	Critical micelle concentration
CTAB	Cetyl trimethylammonium bromide
C_nE_m	Polyethylene oxide alkyl ethers
CVC	Critical vesicle concentration
DHDAB	Dihexyl dimethylammonium bromide
HPLC	High performance liquid chromatography
ESI	Electrospray ionisation
LED	Light emitting diode
LFA	Loading factor analysis
ND	Neutral density
NMR	Nuclear magnetic resonance
PET	Polyethylene terephthalate
PTFE	Polytetrafluoroethylene
RMM	Relative molecular mass
rpm	Revolutions per minute
SDS	Sodium dodecyl sulphate
SEM	Scanning electron microscopy
TFA	Target factor analysis
TIR	Total-internal reflection
UHP	Ultra-high purity

Chapter 1

Introduction

1.1 Project Aims

This project aims to investigate the kinetics and thermodynamics of surfactant adsorption
to various solid–liquid interfaces by total-internal reflection–Raman spectroscopy (TIR-
Raman). To study what occurs at the interface we require a surface selective technique;
TIR-Raman creates a thin evanescent wave, close to the interface which can be used to
probe the spectra of molecules only in this region. As different Raman-active molecules
have different spectra we can distinguish between them at the interface. The spectra
obtained are also polarisation-sensitive and this can provide additional information, such
as chain orientation. Various solid substrates are investigated, including hydrophilic and
hydrophobic silica, and silica coated with materials such as zeolite, kaolinite, haematite
and polyester.

The rate of adsorption (or desorption) is measured by repeatedly acquiring a Raman
spectrum of, typically, the $C-H$ stretching region—where the peaks of surfactant molecules
sticking to the hemisphere surface can be seen increasing (or decreasing) with time, as
surfactant solutions are pumped through the cell. We also combine the technique of
repeated acquisitions with a mixer which allows us to continuously vary the concentration
to record an isotherm.

The project also aims to improve on our existing TIR-Raman spectrometer, as our
existing apparatus has limited time resolution because it has a readout time of around
$1\,\mathrm{s}$. Additionally, with the apparatus being a commercial spectrometer adapted for TIR-
Raman use, it is not very flexible and cannot be modified easily or without great expense.
Constructing a spectrometer on the open bench allows for greater flexibility in every
component.

1.2 Background

Surfactant adsorption to interfaces has many applications, including printing, dyestuffs,
food additives, crop spraying, painting, adhesives, detergents, crude oil extraction, fracking,
paper or plastic recycling, and cosmetics. Biological surfactants are created by nature and
are often critical for the existence of life, while artificial surfactants have been artificially
created to aid or assist in a wide number of processes. While they have been studied

extensively, better understanding the kinetics of adsorption of surfactants is essential in many of their applications, for example the wetting of and subsequent dirt removal from fabrics, at varying temperatures, while still providing consistent cleaning results.

By studying the rate of surfactant adsorption to various substrates we can improve our understanding of the processes involved. This should allow tailoring of the system to achieve the desired results (for example, achieving greater detergency on a particular fabric by pre-treating it or adjusting the surfactants used).

1.2.1 Surfactants

A surfactant (<u>surf</u>ace <u>act</u>ive <u>age</u>nt) is an amphiphilic molecule which possesses a polar or ionic water "loving" part (hydrophilic) called the head, and a hydrocarbon water "hating" part (hydrophobic) called the tail, see figure 1.1 below. They are compounds which may adsorb to the polar-apolar interfaces of the liquid to which they are added, notably the liquid–solid and liquid–vapour interfaces. If two immiscible liquids are present they may also adsorb to this liquid–liquid interface, for example a mixture of oil and water. Their adsorption to the interfaces alters (lowers) the surface tension of the interfaces and modifies the behaviour of that interface. For example, in a foaming agent, a surfactant may adsorb to the liquid–vapour surface and allow for the stable formation of bubbles and/or foams.

Figure 1.1: A surfactant molecule (C_{14}TAB)

The tail portion of the molecule interacts very weakly with water molecules whereas the head-group can interact strongly via dipole–dipole or ion–dipole interactions and is solvated. The balance between interactions with the head and tail parts of a surfactant give them their surface-active properties. Surfactants are also sometimes referred to as association colloids or tensides.[3] While many detergents (cleaning agents) are surfactants, not all surfactants are detergents. The tails of some surfactant molecules can contain fluorocarbons, which can also make them oleophobic (oil "hating").

Surfactants adsorb to interfaces because hydrogen bonds in the water are broken at the liquid–vapour interface; with the surfactant at the interface there are fewer unfavourable hydrocarbon–water interactions and hence the free energy, compared to the surfactant in the bulk, is lower. This is known as the hydrophobic effect.[4]

Surfactants are classified by the charge the head-group possesses: those with a positive charge (and corresponding free counterion) are classified as cationic, negative are anionic and those without any overall charge are nonionic. Some surfactants have positive and negative charges on the same molecule and these are called zwitterionic. Anionic surfactants are often found, or can be formed from, natural sources, for example the hydrolysis of triglycerides (an ester consisting of glycerol and three fatty acids chains, from animal or plant fat) to form carboxylic acid salts commonly known as soaps. Cationic surfactants are usually synthetic and often possess antibacterial properties, as they can

destroy the cell wall of bacterial cells. Nonionic surfactants include natural triglycerides (main component of natural oils), and long-chain alcohols. Zwitterionic surfactants are also found in nature, as phospholipids which can be found in the phospholipid bilayer membranes of animal, plant and bacterial cells.

If the surface (substrate) possesses a charge then the adsorbed amount of a charged or polar surfactant will be affected by that charge on the surface, since like charges repel and opposite charges attract (entropic effect). Surfaces may also be hydrophobic or hydrophilic, for example surfaces with lots of exposed fluoride groups such as PTFE can be very hydrophobic and clean glass is hydrophilic.

The degree of roughness of the substrate (as very few real surfaces are perfectly flat), whether on the macro or molecular scale, can also affect wetting.[5] This nano-structuring is partly how a lotus leaf enhances the repulsion of water to keep clean.[6] If the contact angle is less than 90°, the liquid will fill up the gaps or pores in the "rough" surface, but for a contact angle greater than 90°, the liquid will not penetrate the gaps and can, therefore, be regarded as resting on a plane surface of part substrate and part air; since there is virtually no adhesion of the liquid to the entrapped air, the contact angle will increase. This is a possible cause of contact angle hysteresis, where the advancing and receding contact angles of a moving drop differ.[7]

Surfactant molecules, when added to water, initially are dissolved as free monomers. However, above a certain concentration, specific to the individual surfactant species, the molecules aggregate to form micelles (see figure 1.2). The concentration at which these micelles form is called the critical micelle concentration (CMC). When forming micelles, the free energy of the system is reduced because the hydrophobic parts of the surfactant molecules are removed from unfavourable interactions with water, even though there is an entropic penalty in restricting the translation and orientation of the surfactant molecules. At the CMC, monomers and micelles are in equilibrium and the change in free energy (ΔG) is zero.

Salts or other species dissolved or mixed into the solution (including pH) can affect the behaviour, and the CMC of ionic and zwitterionic surfactants. This is an important factor to consider when designing detergents, as hard water contains many dissolved ions which can lower the cleaning effectiveness.
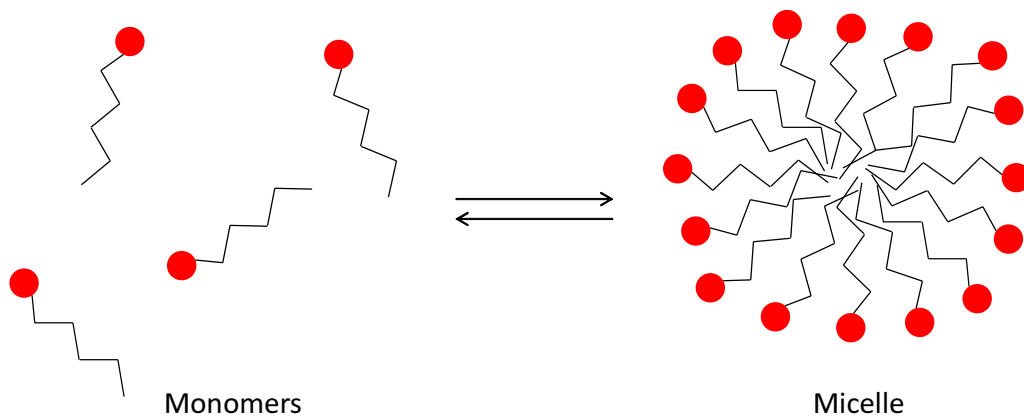
Figure 1.2: Monomers forming micelles, above the CMC

A hydrocarbon surfactant can lower the surface tension of water (for pure water $72.8\,\mathrm{mN\,m^{-1}}$ at $290\,\mathrm{K}$) to *ca.* $30\,\mathrm{mN\,m^{-1}}$ and fluorocarbon surfactants can lower this further to *ca.* $17\,\mathrm{mN\,m^{-1}}$.[3]

The surface or interfacial tension can be measured in various ways: directly measuring the force on the surface with a force gauge or microbalance connected to a Wilhelmy plate (or less commonly the Du Noüy ring), where the force on the Wilhelmy plate (F) relates to the surface tension γ and contact angle θ in equation 1.1; measuring the size or shape of a spinning or pendant drop; or measuring the maximum pressure of a bubble.

$$\gamma = \frac{F}{l\cos\theta} \tag{1.1}$$

where l is the wetted perimeter.

Ignoring electrical effects (using nonionic surfactants), the formation of n monomers of surfactant S to form a micelle M can be represented by the equilibrium:

$$nS \rightleftharpoons M \tag{R1.1}$$

We can then write the equilibrium constant K as:

$$K = \frac{[M]}{[S]^n} \tag{1.2}$$

If we then express the concentration of surfactant in monomeric units, where monomer concentration is C_s and the micelle concentration is C_m we obtain:[3]

$$K = \frac{C_m}{nC_s^n} \tag{1.3}$$

and the total surfactant concentration is $C = C_s + C_m$. We can then write that the free energy of micellisation at temperature T, and using the molar gas constant R, as:

$$\begin{aligned} -\Delta G^\circ &= RT\ln K \\ &= RT\ln\frac{C_m}{C^\circ} - nRT\ln\frac{C_s}{C^\circ} \end{aligned} \tag{1.4}$$

or, for one monomer:

$$-\Delta G^\circ = -\frac{RT}{n}\ln\frac{C_m}{C^\circ} - RT\ln\frac{C_s}{C^\circ} \tag{1.5}$$

where C° is the standard state concentration (1 Molal).

If we assume n is large (above the CMC):

$$-\Delta G^\circ = RT\ln\frac{C_s}{C^\circ} \tag{1.6}$$

If we also assume all new surfactant added goes into micelles above the CMC:

$$-\Delta G^\circ = RT\ln\frac{\mathrm{CMC}}{C^\circ} \tag{1.7}$$

Using a more complicated argument Phillips showed that for ionic surfactants: [3,8]

$$-\Delta G^\circ = RT \left(2 - \frac{p}{n} \right) \ln \frac{\text{CMC}}{C^\circ} \tag{1.8}$$

where p is the effective charge on the micelle with p counter-ions.

When aggregates (monomers, micelles and/or vesicles) are formed, the chemical potential (μ_n) for all the molecules in all aggregates, including monomers, must be equal (for a monomer $n = 1$). The chemical potential is defined as:

$$\mu_n = \mu_n^0 + \frac{RT}{n} \log X_n \tag{1.9}$$

where X_n is the mole fraction of micelles, or, if we reference to the monomer state, using mole fractions for simplicity:

$$X_n = \left[X_1 \exp \left(\frac{\mu_1^0 - \mu_n^0}{RT} \right) \right]^n \tag{1.10}$$

where μ_n^0 is the standard chemical potential of a monomer in an aggregate, containing n monomers. Stable aggregates will not form at values of n if the chemical potential of aggregates is equal to that of a monomer. Therefore to form aggregates there is minimum value of μ_n^0. Phase separation occurs when the aggregate size is infinite.

Temperature also affects the aggregation in an anomalous way; below a certain, sharp temperature (the Krafft point) the surfactant will instead "crash out" of solution as the limit of solubility is reached before aggregates are formed.

While a pure surfactant will form a certain size aggregate over others (in addition to monomers ($n = 1$)), there is polydispersity in the size of these aggregates, with a width $\approx \sqrt{N}$, for spherical micelles, where N is the mean aggregation number. Commercial surfactants are often not supplied pure as this would often make them more expensive and provide little advantage over the mixture (mixtures can even be beneficial). Therefore, as supplied, they often contain homologues with varying chain lengths and other impurities.

A useful scale for determining the packing of a surfactant is related to the curvature of aggregates formed, the surfactant packing parameter, P:

$$P = \frac{v}{l_c a_0} \tag{1.11}$$

where v is the tail-group volume, l_c is the length of the surfactant tail region and a_0 is the surface area per surfactant head-group. If $P < 1/3$ the surfactant head-groups are spread out from each other and the volume of the tail-group is small resulting in positive curvature and the formation of spherical micelles. For $1/3 \leq P \leq 1/2$ rod-like micelles form due to a reduction in curvature. $1/2 \leq P \leq 1$ (small a_0, large v) still results in positive curvature but the curvature is not large enough to form a rod. $P > 1$ results in negative curvature and the formation of a bilayer. Bilayers can also interdigitate to reduce curvature.

Thermodynamics of Surface Adsorption

Various models for the adsorption of surfactants onto hydrophilic surfaces have been suggested which describe systems between two limiting cases. [9] At one extreme, the

surfactant head-groups interact only weakly with the surface and the standard free energy of binding is too weak to compensate for the loss in translational entropy after adsorption, leading to low surface coverage until near the CMC. The sudden increase in concentration is known as the critical surface aggregation concentration (CSAC) and above this concentration aggregates (called admicelles) then adsorb to the surface. As the concentration increases, adsorption increases rapidly until around the CMC is reached. A monolayer does not form.[9] For hydrophobic surfaces, adsorption occurs at much lower concentrations, typically two orders of magnitude less than the CMC.[9,10] Should a monolayer form, the hydrophobic surface would attract a second layer of surfactant, in the opposite orientation, to eliminate unfavourable hydrophobic interactions with water at the interface. An example of this limit is the adsorption of polyethyleneglycol alkyl ethers with short head-groups.

The other extreme is the formation of a self-assembled monolayer where highly-favourable interaction between the head-group and the surface, combined with van der Waals interactions between adjacent tail-group chains, are strong and able to drive monolayer formation well below the CMC. Bilayers do not form at low concentrations because the loss of translational entropy upon adsorption is not compensated by the removal of unfavourable interactions between water and hydrophobic tail-groups.

Interactions between other substrates and surfactants behave within these limits and the behaviour depends on relative strengths of interaction between surfactant/substrate (which can be hydrophilic or hydrophobic) and interactions between tail-groups. Somasundaran and co-workers proposed a "four-region" model,[11] where surfactants first adsorb at isolated sites which grow as the concentration increases through inter-chain interactions to form hemi-micelles. Further increase in concentration leads to a bilayer or similar close-packed structure at the CMC. Gao *et al.* proposed an alternative model for adsorption to hydrophobic surfaces where adsorption occurs below the concentration for formation of hemi-micelles and the sparse monolayer develops into an admicelle.[12] Tyrode *et al.* developed a method for measuring both the adsorbed amount, and whether the adsorbed molecules are in the form of a bilayer or monolayer, using both sum-frequency and Raman spectroscopy.[9] They found that hemi-micelles or partial monolayers do not form in the first plateau of the isotherm and suggest that there is a continuous spectrum of adsorbate behaviour between the self-assembled monolayer and weak adsorption limit.[9]

A solid surface can be wetted by solutions when one fluid displaces another (for example an aqueous fluid replacing air). Wetting agents (a surfactant) can improve the wetting by lowering the interfacial tension.

Shaw categorises three types of wetting: spreading, adhesion, and immersion.[7] Spreading wetting occurs when a liquid on the surface spreads out to increase the solid–liquid contact area and decrease the solid–vapour area. Adhesion wetting occurs when a liquid makes contact with a surface and remains adhered to it, decreasing the liquid–vapour interface area. In immersion wetting the solid is immersed completely in the liquid, leaving the area of the liquid–gas interface the same.

For spreading wetting, the spreading coefficient is defined as:

$$S = \gamma_{sv} - (\gamma_{sl} + \gamma_{lv}) \tag{1.12}$$

Spreading occurs when $S \geq 0$. If spreading does not occur, at equilibrium, we can form Young's equation for the contact angle (θ):

$$\gamma_{\text{sl}} + \gamma_{\text{lv}} \cos \theta - \gamma_{\text{sv}} = 0 \tag{1.13}$$

For adhesion wetting the free energy (W_a) is given by the Young-Dupré equation:[7]

$$\begin{aligned} W_a &= (\gamma_{\text{sv}} - \gamma_{\text{sl}}) - \gamma_{\text{lv}} \\ &= \gamma_{\text{lv}} (\cos \theta + 1) \end{aligned} \tag{1.14}$$

from this, we can see that for a contact angle of 0°, $W_a = 2\gamma_{\text{lv}}$ and the attractive forces are greater than or equal to those between liquid-liquid, and the liquid adheres to the solid less than itself and complete wetting occurs.

For immersion wetting, the free energy change is:[7]

$$\begin{aligned} -\Delta G_i &= \gamma_{\text{sv}} - \gamma_{\text{sl}} \\ &= \gamma_{\text{lv}} \cos \theta \end{aligned} \tag{1.15}$$

so work must be done if $\gamma_{\text{sv}} < \gamma_{\text{sl}}$, otherwise wetting is spontaneous.

One might design a surfactant to be a wetting agent, but also not to cause complete wetting, for example in crop spraying where increasing surface coverage needs to be balanced against drainage from the surface of the leaves. Conversely, it might be advantageous to design a system which repels water, for example a fabric, where the surface needs to prevent capillary action from wicking water through the fabric whilst still allowing air to pass through ("breathable" fabric). Surfactants are also important for ore flotation, for example various constituents of crushed ore differ in their affinity to float on the surface, which can be modified by adding surfactants.[7] This technique can be used to extract minerals by floating solid metal ore particles or impurities: by introducing a foaming agent and bubbling air through the solution, followed by scraping the surface of the foam containing the ore particles, the ore can be extracted from solutions or sols.[7]

Surface coverage is the amount of surface covered in surfactant. In general this coverage depends on the bulk concentration in an isotherm (amount of adsorbate as a function of concentration, at constant temperature) and the relationship between them is the equation for the adsorption isotherm.

Detergency is the removal of dirt from a surface and while traditionally soaps (salts of fatty acids) were used, they do not work at high pH or in the presence of "hard" (Ca^{2+} and Mg^{2+}) ions, as they precipitate. Modern "soapless" detergents, such as sulphates, sulphonates and polyethelene oxides have been created. Some of these, however, have been found to be non-biodegradable, so their use has been phased out and replaced with more environmentally-friendly surfactants.[7]

To be a good detergent, the surfactant needs to be good at wetting the surface to be cleaned, to be able to remove the dirt into the bulk and keep this dirt in suspension so that it does not redeposit back onto the surface being cleaned. The type of dirt to be removed may be polar or apolar and vary in size, for example soil (mud) or perspiration. If we consider the energy change of solid dirt removal from a surface, we need to reduce

the dirt–water and water–surface interfacial tension in order to reduce the surface–dirt interfacial area. For liquid dirt such as oil, consideration of the contact angle (where the higher the angle, the easier removal becomes) allows us to determine if it will be removed from the surface. Solubilisation of the oil, such as forming micelles containing the oil, often promoted by adding polymers, is required to prevent redeposition. However, forming micelles may compete with the detergent action, as only the monomers contribute to it.[7,13] It is worth noting that fats and waxes can be solid at low temperatures, so increasing the temperature of the solution (to $\approx 45\,°C$) can aid removal, but this requires more energy to heat the water.

An adsorption isotherm, the amount of solute adsorbed to a surface of unit area plotted against equilibrium concentration, at constant temperature, is often used to express adsorption data. The amount of adsorbed material can be measured in a number of ways, including chemical and radiochemical techniques, colourimetry and various spectroscopic techniques.[3] Determining the depletion of solute removed by a substrate from solution is one common method, but requires sensitive techniques.[7] The adsorbed amount can also be determined from surface tension isotherms.

Physical adsorption to a surface is the most common means of adsorption, but chemisorption is possible for some reactive surfaces/solutes.

The Langmuir equation is the simplest monolayer adsorption isotherm:[7]

$$\frac{\Gamma}{\Gamma_\infty} = \frac{k_c}{1 + k_c} \tag{1.16}$$

where Γ is the surface excess (typically in $mol\,m^{-2}$), c is the concentration, and k is the rate coefficient. The Langmuir isotherm can be used to estimate the area per molecule if the area of the surface is known. For competitive adsorption, the equation becomes:

$$\frac{\Gamma_i}{\Gamma_{i,\infty}} = \frac{k_i c_i}{1 + \sum k_i c_i} \tag{1.17}$$

The electrical nature of the surface (net positive or negative) can govern adsorption to the surface, and the distribution of charge on the surface may depend on pH, or the relative solubility of any ions the surface may release. The net charge of the surface (σ_0) must be balanced by the solution close to the interface, and form the *electrical double layer*.[3,14] Solutes may be "specifically" adsorbed (non-electrical, partially or fully unsolvated) and the centre of the adsorbed ions are known as the *inner Helmholtz plane* (IHP), with a charge density (σ_β). Other solutes, which are fully solvated, are further from the surface and are known as the *outer Helmholtz plane* (OHP) or *Stern plane*. Further from this, the double layer is diffuse and is a mixture of positive and negative charges, with a charge density, σ_d. As electrical neutrality is required. $\sigma_0 + \sigma_\beta + \sigma_d = 0$. The *isoelectric* point (when the zeta potential, (ζ) = 0) is achieved when $\sigma_d = 0$ ($|\sigma_0| = |\sigma_\beta|$) and the mean potential of the Stern plane (ψ_d) is the potential in the interfacial double layer. ζ is the hydrodynamic slip plane.

The mechanisms of surfactant adsorption can also (in addition to the hydrophobic effect) occur via ion exchange, ion pairing, acid-base interaction, polarisation of π-electrons, and/or dispersive forces.[14]

Ion exchange involves replacement of adsorbed counter ions by charged ion surfactants.

Ion pairing involves charged surfactant molecules pairing with charged substrate sites. Acid-base interaction occurs when hydrogen bonds form or there are Lewis acid–Lewis base reactions. π-electrons on the substrate can interact and become polarised with electropositive surfactants, to adsorb them to the surface. Dispersive forces, via van der Waals interactions, can work on their own, but often combine with other mechanisms to strengthen them.[14]

To determine the adsorption mechanism one needs to observe the rate of adsorption in a kinetic experiment and the shape during an isotherm experiment. Looking at the isotherm it is useful to see if there are any plateaus, the extent of solvent adsorption, if the adsorption is monomolecular, the orientation of adsorbed molecules, the effect of temperature, and the nature of the interaction between substrate and adsorbent.[15]

Giles *et al.* classified and then later developed a theory for the classification[16,17] of isotherm shapes for adsorption small molecules on substrates in liquids. The different shapes classified are seen in figure 1.3. Four classes were identified, based on their initial shapes and then further subgrouped by their high-concentration behaviour. The L (Langmuir) class is the most common; L2 and L4 both have plateaus and are common for surfactants. The fifth subgroup are found where solutes associate in solution (for example, form micelles) and also contain highly surface-active impurities, since a maximum is not thermodynamically possible in a pure system.[15] For the S class, the initial shape is the reverse of L, giving an "S"-shape. H (high-affinity) class adsorb very strongly at low concentrations. C (constant partition) class have a linear portion showing constant partition between solution and substrate and occurs with microporous substrates.

If the interaction between adsorbent molecules is negligible, activation energy is independent of coverage, leading to an L or H isotherm. S isotherms occur when there is a greater interaction between solute and the substrate than solute and adsorbent, where cooperative adsorption occurs. H isotherms are seen for chemisorption or other strong interactions.[15]

Nonionic Surfactants

Nonionic surfactants (highly surface-active on hydrophobic surfaces) generally adsorb as L class and are reversible with little hysteresis.[15] However, they can form a stepped adsorption profile (L4), but this is often hard to detect without very sensitive techniques, given their low CMC.[15] Within a homologous series, increasing the length of the tail generally increases the maximum adsorption ($\Gamma_{\max}$) at the last plateau, whereas, increasing the head-group size (adding ethylene oxide groups to a polyoxyethlenated (POE) surfactant) decreases $\Gamma_{\max}$ because the area on the interface occupied by the POE group increases.[14,15]

Nonionics are physiosorbed, but differ from other surfactants in that fairly small changes in concentration, temperature or structure of the surfactant can result in a large change in adsorption. This is due to surfactant–surfactant interactions and surfactant–solvent interactions. Some nonionic surfactants, such as ethylene oxide head groups, may be slightly positively charged, but the primary attraction is via van der Waals interactions.

At low concentrations the surfactant molecules often lie flat on a hydrophobic surface because there is also some attraction to the hydrophobic group. As surface coverage increases the relative affinity of the surface for either the head or tail group my result in

9
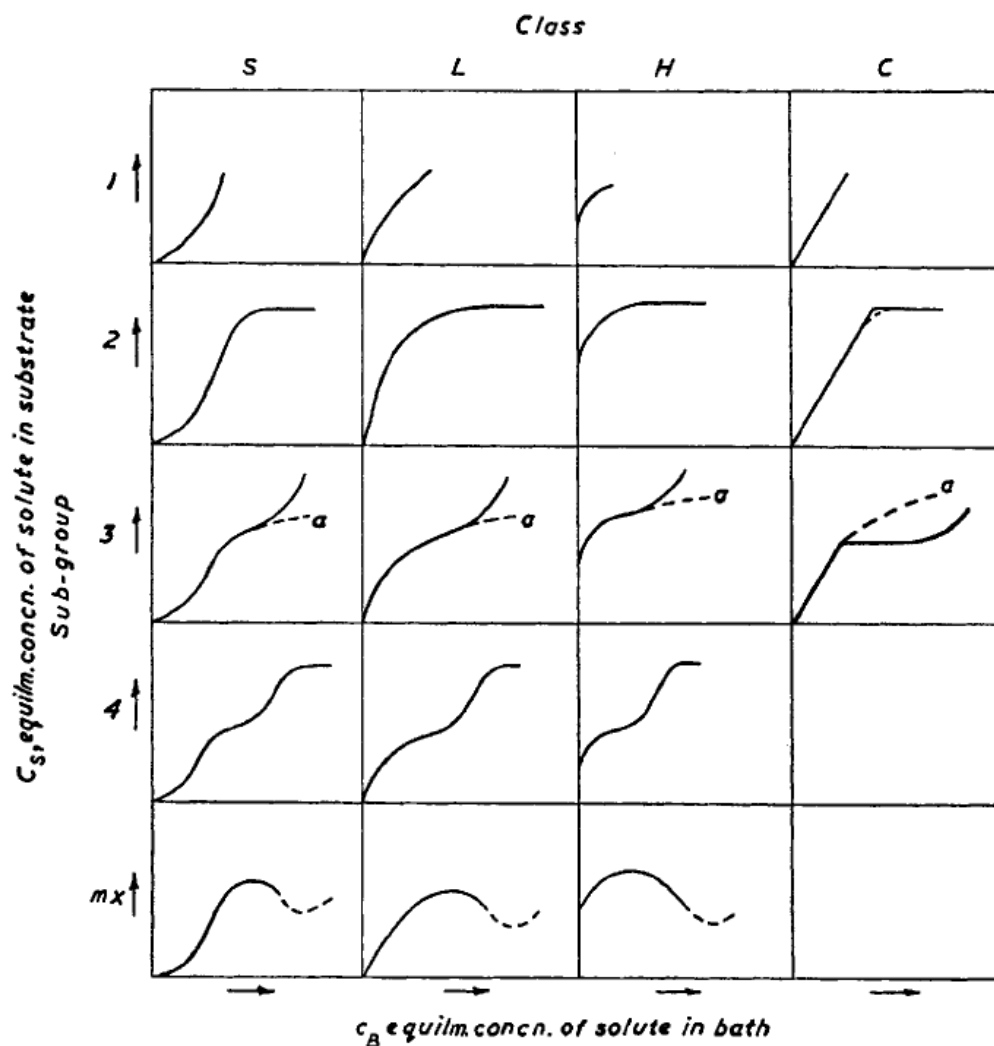
Figure 1.3: Classification of isotherm shapes, a designation used to describe some abnormalities. Reproduced with permission from reference 16. Copyright 1960 RSC

one or the other being slightly displaced from the surface.[15]

The orientation of the molecule, either head or tail orientated towards the solvent depends on the interactions between the surfactant and the surface. On a completely apolar surface in water the heads will be orientated towards the solution. On many polar substrates, there may be an affinity for the head-group through hydrogen bonding, hence the chains orientate with their tail into the solvent and the hydrophobic effect promotes the further adsorption of a second layer in reverse orientation with the polar groups again towards the water.[15]

As the concentration is increased the hydrophobic group is displaced from a hydrophobic surface and interaction between adjacent molecules may result in the formation of hemi-micelles (micelle segments attached to the surface, see figure 1.4).[14] On hydrophobic surfaces, admicelles (adsorbed micelles) may form.
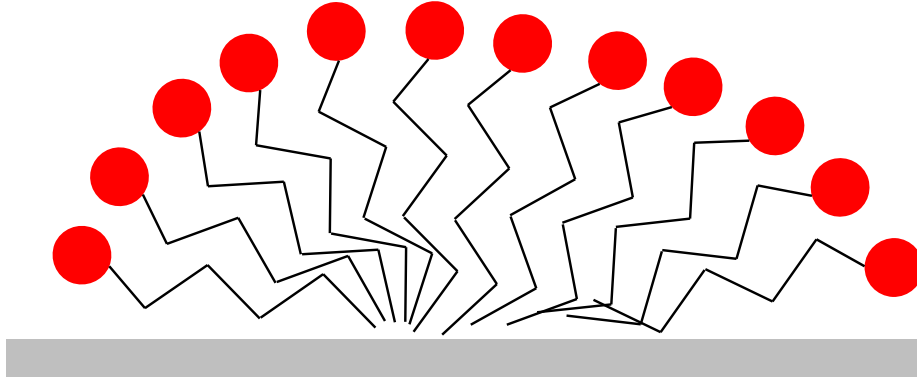
Figure 1.4: A hemi-micelle on a hydrophobic surface

Ionic Surfactants

The electrical interactions within the electrical double layer play a major role in the adsorption of charged species to a surface. For charged surfactants, adsorption can be treated as a special version of the standard ion adsorption model. The head-group, by definition, is located in the IHP and it is sometimes useful to consider the IHP and OHP coinciding at low surface coverage.[15]

The enthalpy of adsorption combines both the electrical interaction (ΔG_{elec}) and the specific interactions (ΔG_{spec}). If the net surface charge is a counterion to the surfactant ion, the electrical interaction promotes adsorption. However, this will only exist at very low surface coverage ($|\sigma_\beta| < |\sigma_0|$, where they are of opposite sign), or in the absence of other adsorbed ions ($\sigma_\beta = 0$). If the surface charge is the same as the surfactant, then electrical interactions will inhibit adsorption. At low surface coverage, ΔG_{elec} is likely to be the dominant term.

The remaining interactions (ΔG_{spec}) can be broken down into separate types, either by interaction type, or by which species are involved. For example, if we group them by

$$\Delta G_{spec} = \Delta G_{cc} + \Delta G_{cs} + \Delta G_{hs} \tag{1.18}$$

where ΔG_{cc} is from the chain–chain interactions, ΔG_{cs} and ΔG_{hs} account for the chain–substrate and head-group–substrate interactions, respectively.[15]

Hydrophobic interactions will be included in ΔG_{cc} and ΔG_{cs} and depend on the nature of the surface and any water associated with it.

ΔG_{cc} interactions can encourage the formation of structures such as admicelles (figure 1.5), particularly on hydrated mineral surfaces.[15] Interactions between the chain and the substrate (ΔG_{cs}) occur and are significant on weakly polar surfaces, such as polymers.[15] Other interactions exist between the head-group and substrate (ΔG_{hs}) which are not included in electronic interactions, such as hydrogen bonding.

At low surface coverage, the Langmuir isotherm can be used to calculate the mean adsorption free energy ($\overline{\Delta G_{ads}}$):[15]

$$\frac{\theta}{1-\theta} = \frac{C_1}{55.51} \exp\left(-\frac{\overline{\Delta G_{ads}}}{kT}\right) \tag{1.19}$$

where the fractional surface coverage, θ is given by Γ_1/N_s (N_s is the total number of
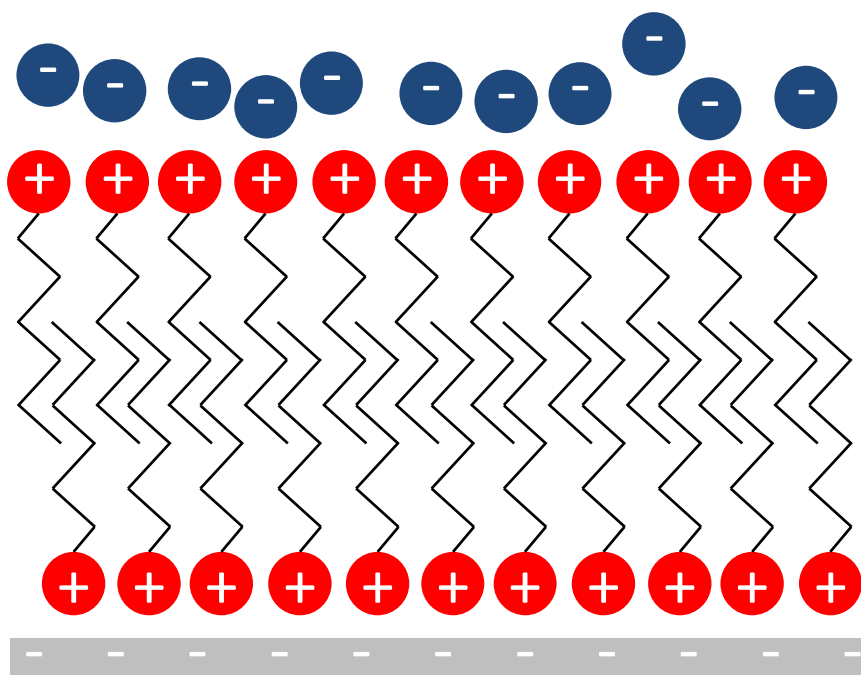
Figure 1.5: An admicelle of a cationic surfactant on a charged surface

adsorption sites per unit area), C_1 is the concentration in $\mathrm{mol\,dm^{-3}}$.

As bulk concentration increases surface coverage should also increase. Above the CMC any additional surfactant added will tend to increase the micelle concentration. If the surface is not heterogeneous then this may generate a plateau in the isotherm. Additionally, if the surfactant is not pure (for example, if there are different chain lengths) then micellar or bulk composition may differ from surface composition and cause an adsorption maximum. The adsorption "plateau" at the CMC is often assumed to be close-packed monolayer coverage of the surface, but knowledge of the molecular orientation is important, particularly when calculating molecular area.[15]

For ionic surfactants, care is needed as the electrical double layer may lead to depletion (or enhancement below the zero point of charge) of the bulk within a few Debye lengths (κ^{-1}) of the surface. Therefore data should only be used for concentrations if the penetration depth is much greater than the Debye length ($d \gg \kappa^{-1}$).[9]

On hydrophilic surfaces, surfactants adsorb to minimize exposure of hydrophobic groups to the water. This causes different structures to form, and can form bilayers at high surface coverages. The bilayered structures that are formed are somewhat influenced by the substrate. For cationic surfactants on a highly negatively charged surface such as mica, which is crystalline, the surface acts as a template, strongly influencing the arrangement of the aggregates.[18] Silica, which is amorphous and has a moderately charged surface, has a weak templating effect.[9,19] On silica, the type of aggregates found are similar to those found in solution at high concentrations. They form surface structures of spheres, rods, and bilayers which are similar to the spheres, rods, and vesicles that form in the bulk.[19] The surface can act as a counterion for the surfactant.[19] Single-chain cationic

surfactants form typical spherical micelles in the bulk at several times the CMC, but on addition of low concentrations of salicylate (o-hydroxybenzoate) they form wormlike micelles (wlm's) in the bulk, hence similar aggregate structures might be expected at the silica-solution interface.[19]

For highly polar surfaces such as silica and alumina, there may be little adsorption if the electrical interactions between charged surfactant and surface are unfavourable. There may be a minimum opposite charge threshold after which a monolayer may then form. For favourable surfactant-surface charge interactions, adsorption is high.[15] As substrate polarity decreases interactions will become more dependent on non-electrical interactions. Previous work in our own group by Tyrode *et al.*, using both TIR-Raman and sum-frequency spectroscopy, observed an L4 type isotherm for $C_{16}TAB$ on silica.[9]

Adsorption onto clays and silicates is more complicated to study theoretically, as the surface is often not homogeneous. The adsorption of $C_{16}TAB$ onto kaolinite was studied by Pearson and Wade and they noted an inflection in the isotherm at $\approx 50\,mM$ which they attributed to either adsorption to the positively charged crystal edges or (more likely) formation of a bilayer.[15] Other studies with SDS on kaolinite showed some time dependent behaviour, as well as strong pH dependence.[20]

Atkin *et al.* undertook an extensive review of cationics on solid–liquid interfaces.[21] They concluded that the isotherm needed to be divided into concentration spans (figure 1.6), each with a different adsorption process. They state that different adsorption mechanisms occur simultaneously, at different rates, and hence during one span multiple factors affect the kinetics. The spans are the electrostatic, electrostatic and hydrophobic, and hydrophobic concentration spans. The hydrophobic concentration span can be further sub-divided into regions above and below the CMC.

In the first span, the attraction is primarily electrostatic and the positively charged head-group makes nearby hydroxyl groups more acidic, thus inducing more charged sites near the initial charged site.[21]

In the second span, the hydrophobic tail-groups interact with hydrophobic parts on the substrate. The tails then act as nucleation sites for further adsorption of surfactant. This span ends when the ionisation of the substrate is at a maximum and the overall surface charge is neutral.[21]

Additional adsorption in the final span is only driven by hydrophobic interactions, and must overcome electrostatic repulsion. Head groups orientate away from the surface and counterions adsorb to the surface.[21] Above the CMC, micelles directly adsorb to the surface.[21] If the surface and surfactant are of the same charge, or on very hydrophobic surfaces, there will be no electrostatic concentration span.[21]

Figure 1.7 shows a typical log–log plot of an adsorption isotherm of surfactants at the solid–liquid interface.[22] In region I adsorption obeys Henry's law, that is, adsorption increases linearly with concentration. Region II shows a sudden increase in adsorption, while Region III shows a slower rate of increase in adsorption than region II. Region IV is the plateau region above the CMC. However this region may show a maximum if there are surface–active impurities, or under certain conditions of the solid surface, solid–liquid ratio, etc. this Region IV may show a maximum.[22]

In a homologous series, a longer hydrocarbon chain makes the surfactant "more hydrophobic" because hydrogen-bonded water molecules are required to solubilise longer

Cationic Surfactant Adsorption Mechanism on Oxide Surfaces

The Electrostatic Concentration Span

The Electrostatic and Hydrophobic Concentration Span

The Hydrophobic Concentration Span (below the cmc)

Note: when present, the SAR occurs between the onset of the isotherm plateau and the cmc.

The Hydrophobic Concentration Span (above the cmc)
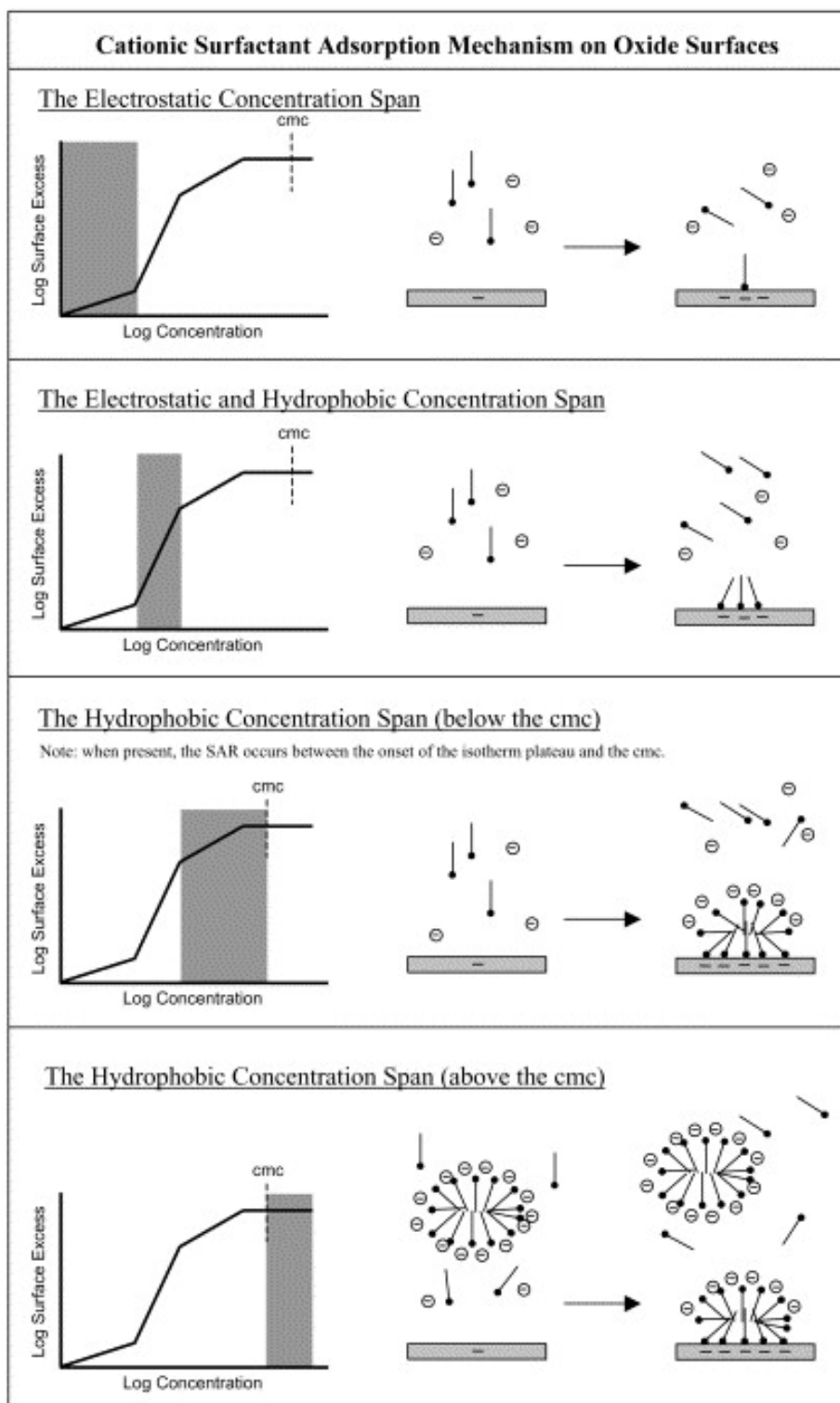
Figure 1.6: The different adsorption processes in each of the proposed concentration spans. Reproduced with permission from reference 21. Copyright 2003 Elsevier

tail-groups, lowering the system entropy.[21] This results in aggregates being the more favourable state and lowers the CMC. Chain length also affects adsorption behaviour, resulting in a lowering of the concentration at which each isotherm feature appears.[21]

14
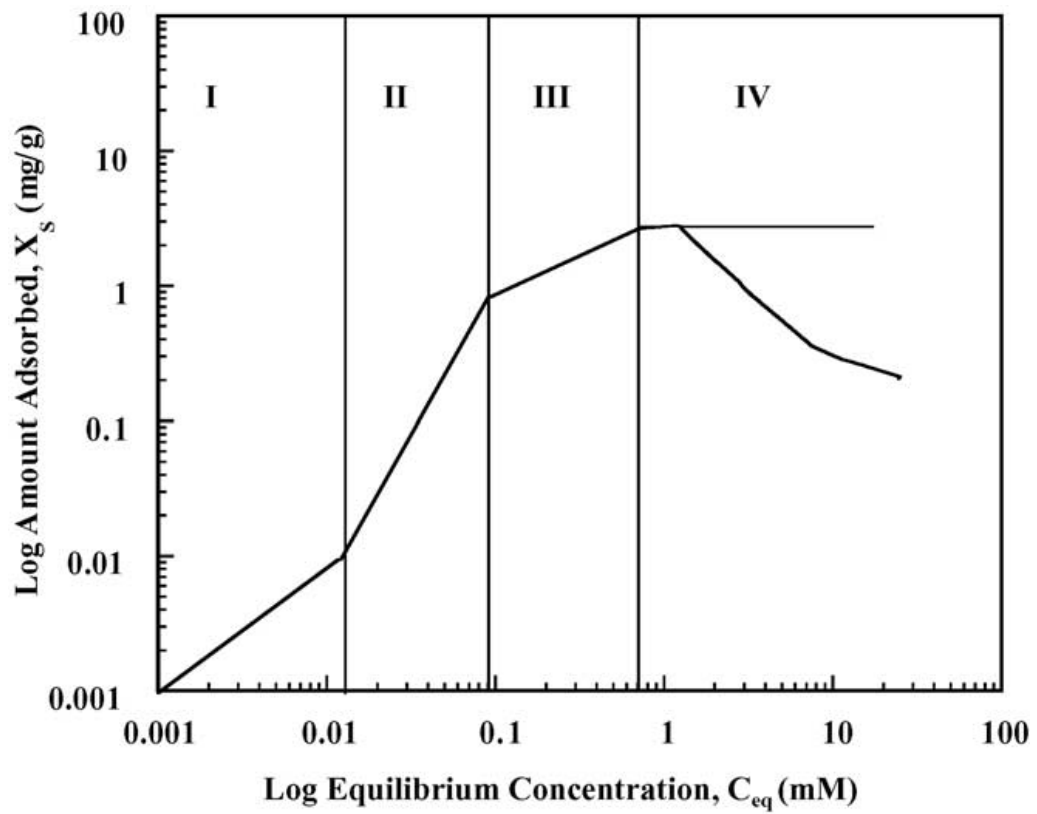
Figure 1.7: Typical adsorption isotherm of surfactants on the solid-liquid interface. Reproduced with permission from reference 22. Copyright 2005 Elsevier

Kinetics of Micellisation

The half-life of micelle formation and breakdown has been shown, using techniques such as pressure jump[23] and stopped-flow,[24] to be *ca.* 10^{-3} s to 1 s. The rate of interchange of monomer and micellar surfactant molecules has been shown by ultrasonic relaxation to be faster, and have a lifetime of *ca.* 10^{-7} s.[25]

Micelles, at low concentrations, are dispersed in solution however, at higher concentrations micelles can aggregate to form organised complex structures, such as sheets.[21]

Aniansson and Wall developed[26] and then refined[27] a model for micelle formation and breakdown. They suggested that ionic monomers change one monomer at a time and that counterions diffuse faster than the monomers and therefore do not affect the rate. For every aggregation number they stated that the kinetics follow the equilibrium:[26,28]

$$X_1 + X_N \underset{k_N^d}{\overset{k_N^a}{\rightleftharpoons}} X_{N+1} \tag{R1.2}$$

for every aggregation number.

The system as a whole is described by partial differential equations:[1]

$$\frac{d[X_1]}{dt} = \sum_{N=1} k_d^N [X_{N+1}] - k_a^N [X_1][X_N] \tag{1.20a}$$

$$\begin{aligned}\frac{d[X_N]}{dt} =& k_{N-1}^a [X_{N-1}][X_1] + k_N^d [X_{N+1}] \\ & - k_N^a [X_N][X_1] - k_{N-1}^d [X_N], \text{ for } N \geq 2\end{aligned} \tag{1.20b}$$

These are known as the Becker-Döring equations. These equations result in the size distribution of the system responding in two steps when a small perturbation is applied. For example, if the solution is diluted rapidly there is a rapid decrease in the average micelle size (loss of monomers) and a slower progress to equilibrium.[1] The slower process involves micellar breakdown. However, the result from this calculation can sometimes yield unrealistic time-scales (years), showing that the model does not describe the process fully.[1]

The concentration and composition of micelles, as well as size and shape, may differ greatly in the mixture when compared to the pure surfactant. Additionally, the composition of the micelle may differ to the equilibrium in the bulk and this may have important applications depending on the intended use, as generally only monomers, rather than micelles or other aggregates are assumed to adsorb to interfaces.[29]

Kinetics of Surface Adsorption

The dynamic nature of micelles, means that, above the CMC, the rate of adsorption of surfactants to an interface is highly dependent on micellar processes. It was initially assumed that only free monomer surfactant molecules could adsorb when they diffuse to the surface; however, previous work in our group by Colegate and Bain using a liquid jet to study rapidly expanding surfaces has shown that direct adsorption of micelles of nonionic surfactants to the air–water interface can occur at a diffusion-controlled rate.[30] They said that previous models assumed a zero rate for micellar adsorption as a

no-flux boundary condition, hence the micelles must break down into monomers before adsorption to the surface. While this could be assumed to be case for ionic surfactants in the absence of added electrolytes, they showed that micelles of $C_{14}E_8$ did directly adsorb, by ellipsometry on a gravity-driven jet, where the surface expansion rate is very high (up to $10^3\,s^{-1}$).[30] This adsorption could be switched off by addition of a cationic surfactant and switched on again by addition of an electrolyte. The adsorption process is driven by kinetics and the adsorption process destroys the micelle as a result of the Marangoni forces generated by the increased local surface tension.[30]

Paria and Khilar undertook a review of experimental studies of surfactant adsorption at hydrophilic solid–water interfaces.[31] They concluded that kinetics largely depend on the nature of the substrate and the surfactant type—if oppositely charged, the rate of adsorption and equilibration time are very fast; if nonionic, the kinetics depend on the diffusion coefficient of the monomer and the thickness of the stagnation layer. Isotherms, again, depend on the substrate and surfactant type, with ionic surfactants adsorbing to oppositely charged substrates in a four-region isotherm. They also found that hemi-micellar aggregation numbers at region II and III of the isotherms decreases with the decreasing surfactant chain length and that steric hindrance from the surfactant's functional group decreases the hemi-micellar aggregation number. Above the CMC they found that isotherms plateau. However, sometimes, for mixed surfactant systems, region IV shows a maximum, with the lower CMC surfactant in the mixture having a greater tendency for the surface. Above the CMC, the monomer concentration of the lower CMC surfactant decreases as they form mixed micelles. As expected, surfactant adsorption to similarly charged substrates is enhanced by electrolytes. An increase in temperature was found to decrease the maximum adsorbed amount for ionic and nonionic surfactants. Finally they found for mixed surfactant systems, anionic surfactant adsorption onto negatively charged surfaces is enhanced in the presence of a cationic surfactant, particularly if the surface is pre-treated with the cationic surfactant (mixing in the bulk can cause precipitation). For mixtures of anionic and nonionic surfactants, the isotherm does not change on increase in nonionic surfactant chain length, if the nonionic chain length is equal to or greater than the anionic surfactant chain. However, if the nonionic chain is shorter than the anionic, the isotherm will change due to less shielding of the anionic surfactant.[31]

1.2.2 Ionic Strength

Addition of an electrolyte such as a salt (for example NaCl) to the solution causes a decrease in adsorption of ionic surfactants onto oppositely charged substrates, and an increase when they have the same charge.[14] These effects are presumed to be due to the salt decreasing the electrostatic forces between charges by shielding (screening); decreasing the attraction between oppositely charged species and the repulsion between like charged species. Increasing the ionic strength of the aqueous phase increases this effect. In addition, adding polyvalent ions further increases this effect. It is possible that some of the electrolyte may first adsorb to the substrate forming sites which can then attract or

repel surfactant molecules. The ionic strength, I, is defined as:

$$I = \frac{1}{2} \sum_{i=1}^{n} \frac{c_i}{c^\circ} z_i^2 \qquad (1.21)$$

summed over all ions in the solution, where c_i is the ion concentration of ion, i, c° is the standard concentration and z_i is the charge on that ion.

1.2.3 Temperature

An increase in temperature generally decreases the adsorption of ionic surfactants because of an increase in the kinetic energy and a subsequent increase in the entropy which leads to a decrease in aggregate organisation at the surface, for SDS.[32] An increase in temperature however, can cause an increase in the adsorption of nonionic POE surfactants because of a decrease in solute–solvent interactions.[14] Later work on POE surfactants by Penfold *et al.* with neutron reflectometry has shown that there is little difference in adsorbed amount from 20 °C to 50 °C, but they did observe changes in structure.[33]

1.2.4 Streaming Potential

A streaming potential is an electrokinetic effect which causes voltage potential to form when an electrolyte solution is driven by a pressure gradient through a channel or a porous plug with charged walls and was first observed by Quincke, where he found that the difference of potential at the ends of a glass capillary tube containing a electrolyte was proportional to the difference in pressure between the two ends.[34,35] The phenomenon can be explained by the presence of a fixed double layer at a solid–liquid interface.[35] Streaming potentials are difficult to measure reproducibly, but are commonly measured with electrodes placed either side of a porous plug or capillary which liquid is forced through.[36] The measurement allows characterisation and determination of the ζ-potential of macroscopic surfaces.[36] The generation of a potential can cause problems if the flow rates are high and the liquid has a very low conductivity, for example fast flowing jet fuel can generate sparks.[36]

1.2.5 Bilayers

While some surfactants form micelles and monolayers, surfactants (or lipids) with two alkyl chains can form bilayers. The cylindrical shape of the two chains increases the hydrophobicity of the tail and reduces their solubility. The bilayers can arrange to form vesicles or lamellar phases. Marques *et al.* reviewed the effects of counterions and geometry on the self-organisation of double-chained surfactants.[37] Phospholipid bilayers are critical for life as they form the basis of cell membranes and also help encapsulate other intracellular structures. Research on bilayers can help model drugs, whether to improve adsorption through the membrane and target the contents, or disrupt it in the case of antibiotics targeting bacterial cells.

Above the critical aggregation concentration (CAC) the surfactant chains organise so that their hydrophobic tails touch both their adjacent neighbours in their layer and the layer underneath. These layers are known as 'leaflets'.

The low solubility and stronger hydrophobicity of double-chained surfactants leads to slower kinetics of adsorption and diffusion from their aggregate forms and system equilibrium can take a long time to achieve. This means that equilibration time and treatment during the creation of the bilayer are important.[37]

Work with a former project student, Harris, determined that dihexadecyl dimethyl-ammonium bromide (DHDAB) was the best option for carrying out investigations into how bilayers behaved and formed on silica using our TIR-Raman system.[38] During this study we trialled a selection of quaternary ammonium bromide surfactants with chain lengths varying from C_{12} to C_{18}. DHDAB was chosen because it was found to form good repeatable bilayers, which showed higher resistance to water rinses, compared to shorter-chained analogues. This is of great importance as the bilayer needs to stay intact during the experiment, and it takes a while to form stable bilayers. The self-assembly of these di-alkyl chain surfactants has been studied previously and they are known to form bilayers and vesicles.[33,39]

1.2.6 Mixed Binary Systems

Mixtures of surfactants are used in many daily applications such as washing detergents, flotation, oil recovery, surface wetting modification, foaming control, emulsification, catalysis, controlled release and separation processes.[29] Surfactant mixtures can also be used to clean up environmental water samples contaminated with other surfactants or oils.[40] Commercial surfactants are often mixtures, as manufacture of monoisomerically pure compounds is expensive, and often of no benefit, or even inferior in behaviour.[29] Many interesting phenomena may occur when mixing surfactants; these are described well in a book edited by Scamehorn and many references are taken from this book.[29]

Surfactants can work synergistically or provide different properties in the same mixture, for example cleaning and fabric softening or shampoo and conditioning. They may also be combined to help improve stability of the mixtures.[41] For example mixed surfactants have been used to create micelles to prevent drug degradation.[42] Some surfactant mixtures may cooperatively increase one of the component's solubilities by forming mixed micelles.

Ionic surfactants do not generally adsorb onto surfaces with like charge and, to overcome this limitation, mixtures of surfactants can be used.[43] For example, a positively charged surfactant does not readily adsorb to a positively charged surface, but if a nonionic surfactant is used first then the anionic surfactant may incorporate the cationic one. Somasundaran and co-workers[44,45] have studied systems where one surfactant of a binary mixture does not normally adsorb to the solid surface, but does in the presence of another surfactant which does.

Adsorption of binary surfactant mixtures to interfaces is classified as cooperative or competitive.[45] Cooperative adsorption is where one surfactant assists another to adsorb, so the adsorption from the mixture is increased compared to the pure components. For example, Woods found that mixtures of nonionic and ionic surfactants increased adsorption of the ionic to a silica interface because the nonionic surfactant molecules adsorbed between the cationic surfactants and reduced the electrostatic repulsions.[1,46] In competitive adsorption both surfactants compete for active surface sites.

As mentioned earlier, mixed surfactant systems are also often encountered even when

using single surfactants, as often the surfactant will not be 100 % pure: chain length may vary, different isomers and/or other impurities may be present. This causes problems if one is trying to study the pure system at interfaces as often these impurities accumulate at this surface if they are more surface active. Multiple recrystallizations to purify the target component are often necessary.

Other components in the solution, such as salt, can affect behaviour. Portet-Koltalo *et al.* found that the addition of salt to a mixture of SDS and $C_{12}E_9$ adsorbing to silica increases the SDS adsorption by $\approx 65\%$ due to the screening effect of the addition of a salt. [43] The adsorption of the nonionic surfactant also increases, but only in the presence of SDS. They, and others, assumed that this was due to the screening effect of NaCl introducing a more hydrophobic environment for the nonionic surfactant. However, at sufficiently high concentration they also found that both surfactants desorb because the formation of adsorbed aggregates is less favourable than free mixed micelles. [43]

Behaviour of ideal mixed micelle systems in solution are often approximated using the pseudo-phase separation model, developed by Shinoda in the book by Kurzendörfer, [47] where the monomers and micelles are considered to be separate thermodynamic phases. The system then becomes similar to vapour–liquid equilibrium and can be treated as dilute phases, one with minimal intermolecular interaction and a concentrated one where interactions are important. [29] An example of this analogy can be given between these two systems: the total monomer concentration of two similar surfactants lies between the CMCs of the individual surfactants; the vapour pressure of two mixed ideal liquids lies between the vapour pressures of the two liquids. If ideal solution theory holds, for a binary mixture of surfactants A and B, at equilibrium: [29]

$$C_m = \frac{CMC_A CMC_B}{n_A CMC_B + n_B CMC_A} \tag{1.22}$$

$$x_A = \frac{n_A C_m}{CMC_A}$$

where C_m is the total monomer concentration, CMC_x are the CMC values for A and B, n_x is the monomer mole fraction, and x_x are the micellar mole fractions, on a surfactant only basis, *i.e.* n_A is the number of moles of A in the micelle divided by the total number of moles of surfactant monomer ($n_A + n_B = 1$ and $x_A + x_B = 1$).

Surfactant mixtures containing a mixture of two or more nonionic, cationic, anionic and zwitterionic surfactants will have a CMC which is often less than predicted by equation 1.22. If the interactions between the surfactant components in the micelles can be described by regular solution theory then: [29]

$$n_B x_A CMC_A = n_A x_B CMC_B \exp\left[\frac{W(x_A^2 - x_B^2)}{RT}\right] \tag{1.23}$$

$$C_m = \frac{x_B CMC_B}{n_B} \exp\left[\frac{(W x_A^2)}{RT}\right]$$

where W is the interaction parameter.

The similar surfactants mix ideally because the environments are similar in the mixed micelle and the pure micelle. In the case of dissimilar surfactants, for example a nonionic and an ionic surfactant, separation of the charged head-groups reduces electrostatic

repulsion in the Stern layer and therefore reduces the barrier to form mixed micelles, lowering the CMC.[48] Additionally, studies using NMR have found that there may be a small contribution from the formation of oxonium ions (proton from water) with the head-group of a nonionic surfactant to generate a net positive charge which can stabilise or destabilise anionic and cationic systems respectively.[49] For binary systems involving changes in the hydrophilic tail, for example hydrocarbon/fluorocarbon surfactant mixtures, the CMC increases because the chains do not interact favourably. Nguyen *et al.* studied the thermodynamics of mixed micelle formation.[50] They developed a new method for calculating their composition by applying the Gibbs-Duhem equation 1.24[51] (which relates changes in chemical potential for components in a system) by treating the mixed micelle as a pseudophase resulting in equation 1.25. Their method only works for binary surfactant mixtures with similar CMC values, at constant temperature and pressure.

$$S \, \mathrm{d}T - V \, \mathrm{d}p + \sum_{i=1}^{c} n_i \mathrm{d}\mu_i = 0 \tag{1.24}$$

$$\frac{\mathrm{d}\ln CMC_M}{\mathrm{d}y_a} = \frac{y_a - x_a}{y_a y_b} \tag{1.25}$$

where $\mathrm{d}\mu$ is the change in chemical potential, S is entropy and p is pressure. x is the mole fraction in the micelle and y is the mole fraction of the individual monomers in the micelle.

When mixtures of surfactants adsorb to surfaces at low concentrations the interaction between molecules is minimal. However, above the CAC, aggregates form on the surface, known as admicelles (see figure 1.8). Again, similarly structured surfactants approximately obey ideal solution theory[52] and below the CMC, the total adsorption is in-between the adsorption of the two pure surfactants. For ionic/nonionic surfactant mixtures below the CMC, the amount adsorbed is increased.[53] Above the CMC, the relative ratio of admicelle to micelle formation depends on the nature of the surface and the surfactant. To minimise the adsorption to a surface, the other surfactant should promote micelle formation.

1.2.7 Hofmeister Effect

The Hofmeister Effect[55] is the effect by which different ions "salt out" or "salt in" proteins. "Salting out" is the equivalent of precipitation which occurs on the addition of salt to the solution. Salts are arranged in a series by their decreasing ability to "salt out". The mechanism is thought to be a result of changes in the interactions between water molecules and the proteins. Anions are commonly listed:[56]

$$SO_4^{2-} < HPO_4^{2-} < OH^- < F^- < HCOO^- < CH3COO^- < Cl^- < Br^- < NO_3^-$$
$$< I^- < SCN^- < ClO_4^-$$
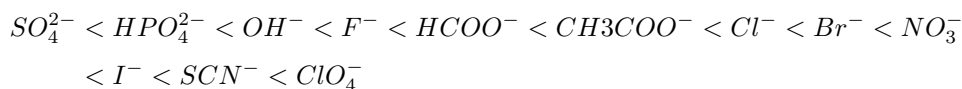
Electrolytes have an effect on charge and may cause sols (solid suspension in liquid) or other dissolved species to undergo flocculation (precipitation) at a certain concentration, and there is a marked increase when going from monovalent to divalent ions. This is due in part to the decreasing double-layer thickness and partly due increasing adsorption of
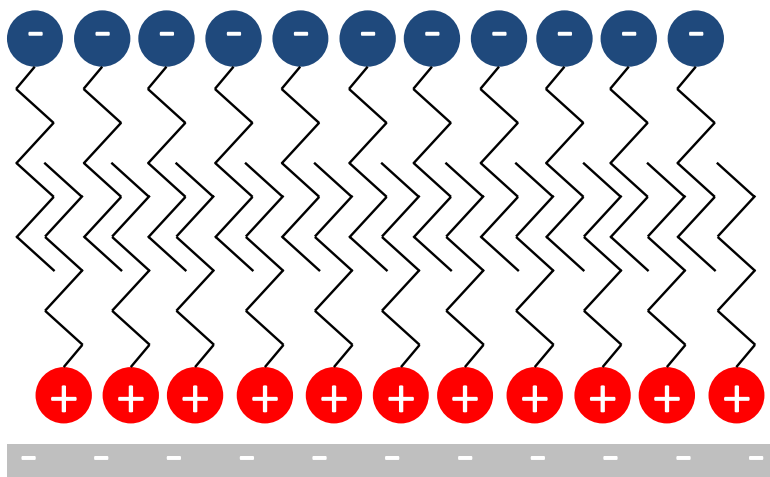
Figure 1.8: An admicelle of a cationic and anionic surfactant on a negatively charged surface. Adapted from reference 54

ions into the Stern layer. [36]

1.2.8 Spectroscopy

In this section we cover the theory behind Raman spectroscopy and Raman spectrometers before moving onto total-internal reflection (TIR) Raman spectroscopy.

Raman Principles

TIR-Raman spectroscopy is used in this thesis to study the adsorption of surfactants at the liquid–solid interface. Raman spectroscopy relies on inelastic scattering of monochromatic light. Most light scattered by a sample will be the same frequency as the excitation light; this is termed Rayleigh scattering. Incident light is also weakly inelastically scattered, where the final energy level of the species is in either a higher or lower vibrational (or rotational) energy level than the initial energy level. When the species ends up in a higher energy level, the frequency of scattered light will be lower and this is termed Stokes scattering. The opposite case, when the frequency of the scattered light is higher, is termed anti-Stokes scattering. The Stokes and anti-Stokes spectra appear symmetrically either side of the Rayleigh line. The energy level transitions for these scattering types are shown in figure 1.9. For this work, only Stokes scattering is of interest because higher-energy states are not very populated at room temperature and hence the anti-Stokes spectrum is very weak. Additionally, the optical long-pass edge filters we are using block the anti-Stokes light.

A molecule when exposed to an electric field will have its electron cloud polarised. This polarisation produces an induced dipole moment which can be represented by equation 1.26: [57]

$$\underline{P} = \alpha \underline{E} \tag{1.26}$$
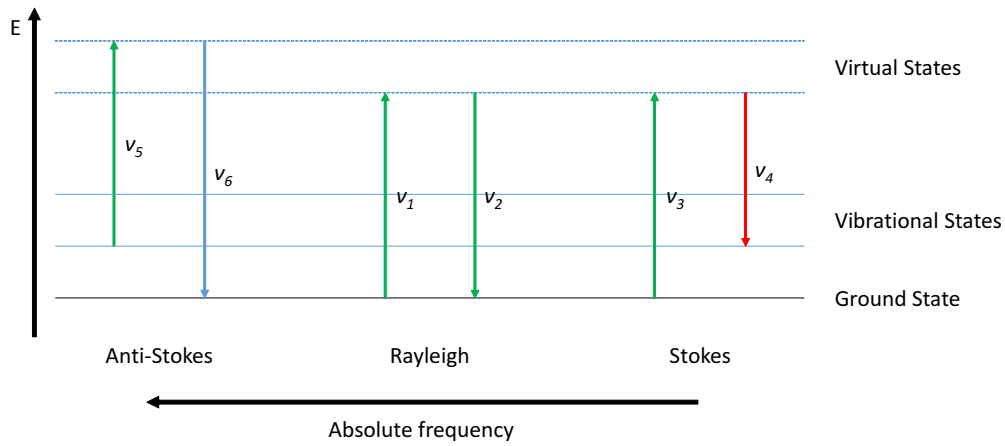
Figure 1.9: Types of scattering, where v represents the transition between the energy levels. Rayleigh scattering (v_2) and types of Raman scattering: Stokes (v_4) and Anti-Stokes (v_5). (v_1, v_3 and v_5) are the transitions to the virtual energy state.

where $\underline{P}$ is the induced electric moment, $\underline{E}$ is the electric field and α is the polarisability. Since $\underline{P}$ and $\underline{E}$ are vectors, α is a 2-tensor and therefore has 9 components. If the electric field is oscillating, as is the case of the electric field in an electromagnetic wave, with frequency ν is then:

$$\underline{E} = \underline{E}_0 \cos 2\pi\nu t \qquad (1.27)$$

where t is time. Hence the polarisability will fluctuate as:

$$\underline{P} = \alpha \underline{E}_0 \cos 2\pi\nu t \qquad (1.28)$$

If the molecule is undergoing a vibration with frequency ν_2, then the polarisability, α, is also a function of time. The vibration results in a change in polarisability:

$$\alpha = \alpha_0 + \left(\frac{d\alpha}{dq}\right)_0 \cos 2\pi\nu_2 t \qquad (1.29)$$

where q is the vibrational coordinate, at $q = 0$. Substituting this expression in equation 1.28 and expanding the product of cosines gives:

$$\underline{P} = \underline{E}_0 \alpha_0 \cos 2\pi\nu t + \frac{E_0}{2}\left(\frac{d\alpha}{dq}\right)_0 \{\cos\left[2\pi\left(\nu - \nu_2\right)t\right] + \cos\left[2\pi(\nu + \nu_2)t\right]\} \qquad (1.30)$$

The first term represents an oscillating induced dipole at the incident frequency that can radiate with frequency ν (Rayleigh scattering). The second and third terms give rise to emission at lower (Stokes) and higher (anti-Stokes) frequencies.

The Raman spectrum depends on the polarisation of both the incident light and the scattered light, because both the induced dipole and the electric field are vectors. In ordered systems, the polarisation dependence of the spectra gives information on the orientation of the molecules with respect to the electric field direction. The Raman tensor is symmetric and so only has six independent components. For a surface that is isotropic in the plane of the surface (which is the case in all the spectra presented here)

the number of independent components is reduced to four: $\alpha_{xx} = \alpha_{yy}$, $\alpha_{xz} = \alpha_{yz}$, α_{xy}, and α_{zz}. The last of these components has an induced dipole perpendicular to the surface (z-direction) and therefore predominantly scatters light along the surface, which is not efficiently collected with the current TIR set up. Consequently we can only measure three of the four independent components of α.

Total Internal Reflection

TIR occurs when a beam passes from an optically dense medium into a less dense medium above the critical angle. All light is reflected back into the dense medium and none of the energy passes into the second medium. The critical angle for transmitting (t) and incident (i) mediums of refractive indices, n, can be calculated as:[58]

$$\theta_c = \arcsin n_{ti} \tag{1.31}$$

$$\text{where } n_{ti} = \frac{n_t}{n_i}$$

Although there is no flux of energy across the interface, there is an electromagnetic field which propagates along the surface and decays exponentially with increasing distance normal to the interface:[58]

$$\frac{\underline{E}}{\underline{E}_0} = \exp\left(-\beta z\right) \tag{1.32}$$

$$\text{where } \beta = \frac{2\pi}{\lambda}\left(\frac{\sin^2\theta_i}{n_{ti}^2} - 1\right)^{\frac{1}{2}}$$

where β is the electric field amplitude decay coefficient of light of wavelength in the incident medium, λ, incident at angle, θ_i. $\underline{E}_0$ is the electric field at zero distance. The penetration depth of the electric field is $dp = 1/\beta$; for most cases dp is less than λ and $\underline{E}$ becomes negligible beyond a few wavelengths. This field is called the *evanescent field*. Raman scattering is proportional to the intensity of the light, and hence $|\underline{E}|^2$, therefore the Raman signal drops off rapidly with distance from the surface.[58] Most of the Raman signal comes from close to the interface[58] and hence the technique can be used to study the adsorption of species to the surface of the totally-internally reflecting medium as the electric field will interact with any adsorbed molecules, but with few bulk molecules.

The Raman Spectrometer

Raman spectrometers consist of a monochromatic excitation source (normally a laser, see paragraph below) and a filter after the sample to block this source from reaching the detector. After this filter, the spectrometer is similar to a conventional optical spectrometer in that the remaining light (Stokes or anti-Stokes) is separated into its component wavelengths by a diffraction grating (explained later). The separated light then falls on a detector, which converts the intensity of the light at that wavelength into an electrical signal.

Lasers

Lasers have transformed many areas of physics and chemistry, but also revolutionised many everyday tasks such as listening to music or watching films (CD and DVD media). Their use with fibre-optics has allowed the telecommunications industry to explode and they have been the main mechanism for enabling super high-speed internet connections across the globe. Lasers have even been used to interconnect orbiting satellites. [59]

Laser is an acronym for light amplification by stimulated emission of radiation. This stimulated emission occurs when an excited state is stimulated to emit a photon by radiation of the same frequency. Laser action requires positive feedback, where the more photons present of a particular frequency, the more photons of that frequency will be stimulated to be emitted. [60]

For laser action to occur, the system needs to have a metastable excited state; a state the system is in for long enough for stimulated emission to occur. The number of species in this excited state also needs to be greater than the lower state at which the transition ends. This is known as a population inversion because it is the opposite of the population at thermal equilibrium.

Population inversion requires a pump (often a bright source of light such as a flash lamp, LED or other laser) to provide the energy to reach an excited state, above the level at which the species lases. Non-radiative losses result in the species changing to the lasing state where it can lase and return to a lower state. If this lower state is also the ground state then this system is known as a three-level laser (figure 1.10). However, with this type of laser it is difficult to achieve population inversion because many ground state species must be promoted. To overcome this difficulty a four-level laser system (figure 1.11) can be used, where the lasing transition ends above the ground state. Achieving the inversion is then easier, as the ending transition is initially unpopulated. Provided the transition to the ground state is fast, the inversion can be maintained.
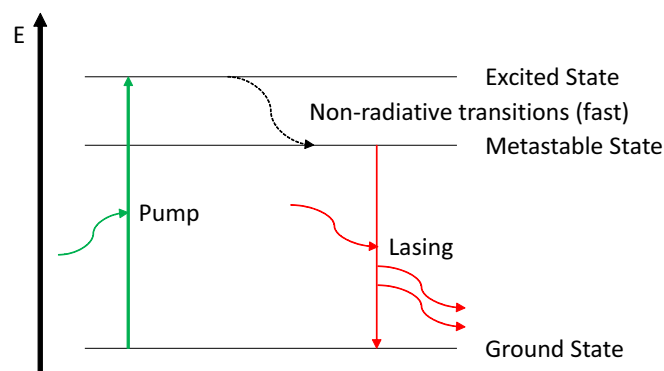
Figure 1.10: A three-level laser

Confining the laser to an optical cavity, enclosed by two mirrors (one semi-reflective to allow the laser light out), restricts the emission to one frequency, polarisation, and direction. Only one wavelength can be amplified by the laser medium and all other wavelengths interfere destructively. Light emitted from the cavity is also coherent.

Solid state lasers, such as ruby; neodymium-doped (Nd:) yttrium orthovanadate or yttrium aluminium garnet (Nd:YO$_4$ or Nd:YAG) use a solid crystal or a glass as the
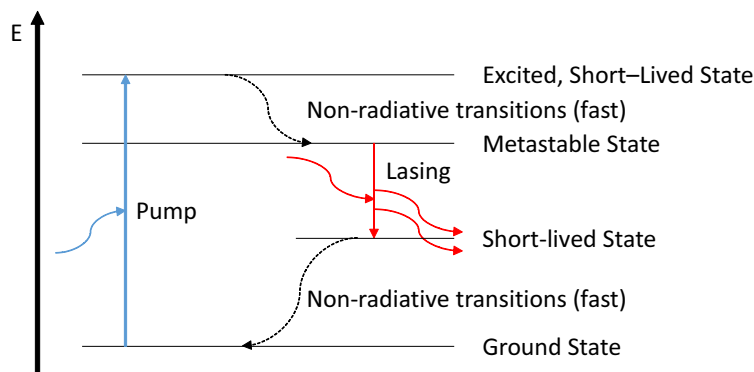
Figure 1.11: A four-level laser

active medium. Other types of lasers exist such as gas, dye, diode and chemical lasers. Lasers are often combined with materials which undergo nonlinear optical behaviour. This behaviour is where the laser beam changes the optical properties of the material, due to the intense electric field generated by the beam. This effect can be used to frequency double (or triple) the incident laser. Frequency doubling of an Nd:YO$_4$ laser (1064 nm) used in this study, produces green light at 532 nm.

Detectors

The detector allows the radiation to be recorded, normally to a computer. The conversion to a detectable voltage or current can be done by one or more elements in the detector, and these can be arranged in an array to provide spatial information (a spectrum or a picture).

A photomultiplier tube (PMT) converts, via the photoelectric effect on a photocathode, then amplifies, via dynodes held at a high voltage, a photon hitting the detector to an electrical current. Very sensitive detectors can produce up to 10^8 electrons per photon.[60]

Photodiodes can be used instead of a PMT. These conduct electricity when hit by photons. They are less sensitive than PMTs but easy to manufacture. Sensitivity can be improved using avalanche photodiodes which use a high voltage to amplify the photo-generated electrons. Selecting a material with an appropriate work function (the minimum energy required to remove an electron to infinite distance from the surface of a solid) allows for detection of a wide range of wavelengths.

A charge-coupled device (CCD) is formed of an array of photodiodes. This detector can either be used as an imaging array directly, or, more commonly for spectroscopy, as a wavelength detector when combined with a polychromator such as a diffraction grating. This is advantageous as all the wavelengths are collected simultaneously across a row of pixels.

Diffraction Gratings

In order to build and control our spectrometer, we need to understand how diffraction gratings work and what affects their efficiency.

Background on Gratings

A diffraction grating is a collection of reflecting (or transmitting) elements spread by a distance comparable to the wavelength of light.[61] These elements change the spacial modulation of of the light (or other electromagnetic wave). When diffracted, the incident wave will undergo a predictable change in electric field amplitude and/or phase. Gratings can either be reflective (reflection grating) or transmissive (transmission grating). Diffraction occurs on reflective gratings due to the interfering reflected light and in transmissive gratings due to the periodic variation in refractive index in the grating. These gratings are often made from a master which is then stamped or cast to form a replica. Master gratings can be made by mechanical ruling or holographically. Ruled gratings are created by drawing a diamond cutting tool across a surface, with the mechanism adjustable to create gratings with different groove spacings. Holographic gratings (correctly called interference gratings) are recorded photographically. The gratings used in this work are replica gratings created from ruled grating masters. Ruled gratings have the advantage that they can be more easily blazed during the engraving process, to enhance efficiency at particular wavelengths. Holographic gratings can be blazed by ion-beam etching or using standing waves.

The Grating Equation

When monochromatic light is incident at an angle (α) on a grating, it is diffracted, as shown in figure 1.12. Each groove can be thought of as a slit shaped source of diffracted light.[61] The diffracted light from each groove, of spacing d, interferes and constructive interference occurs at a set of angles, $\{\beta_m\}$ to the normal.

The relationship between the wavelength (λ) and the angle of incidence (α) is given as:[61]

$$m\lambda = d\left(\sin\alpha + \sin\beta\right) \tag{1.33}$$

where m is the diffraction order and d is the groove spacing. By convention, angles of incidence are measured from the grating normal to the beam and are defined as being negative past the grating normal from the incident beam (shown with the signs either side of the normal in the diagram). Other sign conventions do exist. In most spectrographs the wavelength is changed by rotating the grating about its central ruling and the light
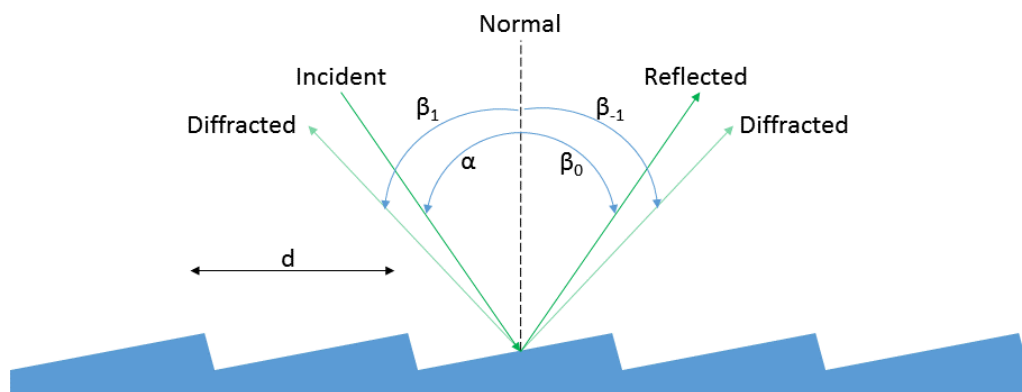
Figure 1.12: Diffraction at a plane grating

paths remain constant (constant-deviation). The scan angle, ϕ, varies with λ:

$$2K = \alpha - \beta = \text{constant} \tag{1.34}$$

$$m\lambda = 2d \cos K \sin \phi \tag{1.35}$$

where K is the half deviation angle. For constant-deviation spectrographs or monochromators the angles can be expressed as:

$$\alpha(\lambda) = \phi(\lambda) + K \tag{1.36a}$$

and

$$\beta(\lambda) = \phi(\lambda) - K \tag{1.36b}$$

where it can be seen that α, β and ϕ depend on λ. Hence we can use the scan angle to determine the wavelength diffracted at a particular angle.

Diffraction Order

The grating equation may hold true for several integer values of m and hence there may be multiple diffraction angles (β) at any given angle of incidence, and a large number will be created if $\lambda/d \ll 1$. Again, the sign convention is that positive values of integer m are to the left of the $m = 0$ ray.

As multiple diffraction rays are created, successive spectra overlap and any light of wavelength λ will overlap with light of wavelengths $\lambda/2, \lambda/3$ *etc.*, hence when trying to detect red (600 nm) light, ultraviolet light (300 nm) will also be detected, unless filtering (order sorting) is used.

Grating Efficiency and Blaze Angle

The energy of light after diffraction on a grating depends on many variables: power, polarisation, angle, diffraction order, grating material, and groove spacing. Complete understanding requires the use of Maxwell's equations, which is complicated. The simplest treatment for reflection gratings is the blaze condition:[61]

$$m\lambda = 2d \sin \theta_B \tag{1.37}$$

where θ_B is the grating's blaze angle which is the angle between the face of the groove and the plane of the grating. This is similar to treating each groove as a tiny "mirror" (although this is an oversimplification as ray optics cannot be assumed). This model serves as a rough guide to show that grating efficiency is enhanced when the following condition is also true:

$$2K = \alpha - \beta = 0 \tag{1.38}$$

This is the Littrow blaze condition and when not true, grating efficiency decreases as the angle moves further away from this condition. At the Littrow blaze condition, the most efficient wavelength for first-order diffraction is:

$$\lambda_B = 2d \sin \theta_B \tag{1.39}$$

Typically gratings are practically measured relative to the efficiency of aluminium, an example of which can be seen in figure 1.13. This figure shows that the gratings are very polarisation sensitive (when used at sub-optimum wavelengths) and have a fairly narrow region where they can be used at their greatest efficiency. Choosing a different master or blaze angle does significantly alter the behaviour. Therefore the choice of grating is very important for our work.
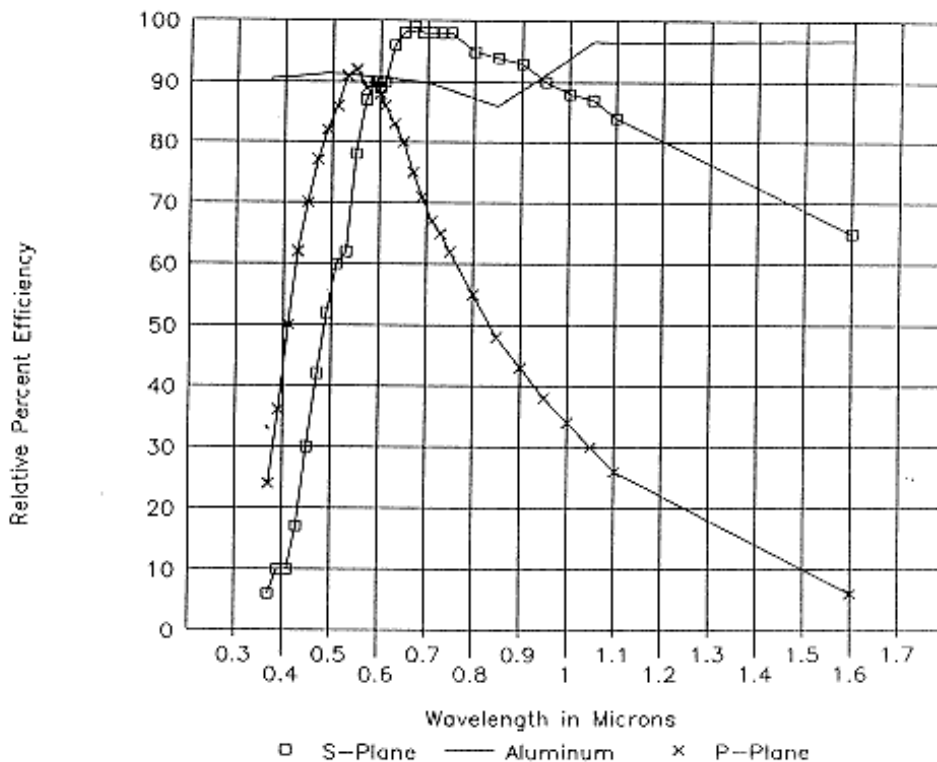
Figure 1.13: Grating efficiency curve of s and p polarised light for $1200 \, \text{mm}^{-1}$ plane ruled reflection grating with nominal blaze angle of 20° for 600 nm (1570 master, model 53-009BK01-340R, Richardson Gratings, Newport Corp., USA). Reproduced with permission from reference 62. Copyright 2015 Richardson Gratings

Figure 1.13 shows the efficiency curve for the grating we purchased. For s-polarised light, we can see that $2900 \, \text{cm}^{-1}$ stokes-shifted Raman scattering (which occurs at at 630 nm for 532 nm excitation, and at 815 nm for 660 nm excitation) would diffract at $\approx 95\%$ efficiency on the grating. For p-polarised light, this drops to $\approx 80\%$ and $\approx 50\%$ for 532 nm and 660 nm excitation, respectively. This is much less and hence the correct grating orientation is critical.

Total-Internal Reflection Spectroscopy

An extensive review of all forms of total-internal reflection spectroscopy techniques for studying soft matter was carried out by Woods and Bain.[63] They categorised them into emission spectroscopy, where the light given off by the sample is collected (TIR-Raman and TIR–fluorescence), and absorption spectroscopy, where the amount of light absorbed by the sample is measured, for example in ATR-[IR and visible] spectroscopy (where ATR is attenuated total reflectance and IR is infra-red), and cavity-enhanced

techniques. Other techniques, such as those using x-rays or non-liner spectroscopy, for example sum-frequency or second harmonic generation, have also been utilised to study soft matter. TIR–fluorescence was used initially to look at chlorophyll on water[64] but normally requires fluorescent labels.[63] By labelling only certain molecules, it is possible to view molecular processes. Typically this labelling technique is used for the study of biological cells.

Absorption spectroscopy techniques measure how much of the light at a particular wavelength is attenuated. This generally requires the more difficult task of measuring the small change against a large background. Multi-bounce prisms have improved signal levels (by increasing the amount of adsorption). Consistent removal of background (H_2O and CO_2) is difficult and often each spectrum requires its own background subtraction.

Literature Review of TIR-Raman Spectroscopy

Total-internal reflection Raman spectroscopy was first presented by Ikeshoji *et al.* in 1973 on carbon disulphide (CS_2) behind glass by adapting the ATR method for use with Raman.[65] Later work was primarily focused on dyes at air–liquid and solid–liquid interfaces, as the dye enhanced the Raman signal through resonance of the pump beam with an electronic transition.[66,67] The signal obtained was weak, even with the resonance, partly due to the signal being obscured by Raman scattering of the substrates. Iwamoto *et al.* used the technique, at the critical angle (where the penetration depth is greater) to look at polystyrene and they were the first to study a biological sample, bovine serum coated prisms.[68,69] This was the first demonstration of the use of this technique to look at films, and did not use any resonant enhancement. They were able to obtain much clearer spectra by using substrates which scattered light less and had a low fluorescence. They found that sapphire was the best substrate for characterising thin surface layers and that they could selectively take a spectrum of one of the two layers of polystyrene on a base layer of polyethylene by changing the angle of incidence.[70] They showed that the method was better than ATR-IR, as it could be used to study much thinner layers than previously possible.[68]

Schröter and colleagues used the technique to study the degree of polymerisation of thin films, including styrene/polystyrene mixtures.[71,72]

The technique was later used by Nickolov *et al.* to study the structure of water near Langmuir-Blodgett (LB) films of amphiphilic molecules by first using D_2O,[73] and then H_2O.[74] They showed that the orientation of the molecules can be determined from the scattering direction and polarisation.

To observe electric field induced changes in liquid crystals, Morikawa *et al.* used TIR-Raman with a pulsed laser to resolve the changes over time.[75]

Stimulated Raman scattering (SRS) was combined with TIR-Raman by Yui *et al.* (in contrast to the conventional (spontaneous) Raman spectroscopy) which uses a non-linear optical technique to utilise Stokes photons (either by trapping them or injecting them with the excitation (pump) photons) to amplify the Stokes signal. They used the technique to investigate the structure of water at the liquid–vapour interface.[76]

Watarai and Funaki developed a TIR system which also utilised resonance Raman spectroscopy and used it for investigating the liquid–liquid interface of toluene and

water.[77] The group used this system to study the behaviour of fluorescent dyes[77] and adsorption of metal complexes[78,79] at this interface. The group then used the same technique to look at self-assembled dye molecules.[80]

Bousquet *et al.* looked at the liquid–solid interface with polarised TIR-Raman.[81] They found that surfaces coated with silver caused structural changes in the liquid near the interface because of the excitation of the silver plasmons.

The first group to characterise the adsorption of a surfactant to a mineral (sphalerite, a zinc ore) using TIR-Raman were Beattie *et al.*. Their work was important in industry as the surfactants they studied are used to extract the mineral during processing by flotation.[82]

The technique was combined with a solid immersion lens by Michaels to study transparent organic conductors which could be used for displays.[83,84] He found this lens, combined with TIR-Raman, to be more surface selective than using a conventional confocal Raman microscope and he was able to produce high-resolution images from inside the conductor. Later Tran *et al.* used the solid immersion lens technique with attenuated TIR-Raman spectroscopy to look at thin polymer films.[85]

A scanning angle, TIR-Raman spectrometer was developed by McKee and Smith. This is technique that would allow a wide variety of substrates and penetration depths to be investigated.[86] They used their spectrometer to investigate monolayers on a gold film.[87] This spectrometer was later improved to have a larger scanning angle by Lesoine *et al.*, working in the same group.[88] They also used their technique to determine the location of polymer interfaces in bilayer films.[89] Later the group further developed the TIR-Raman technique to utilise plasmon waveguides.[87] These waveguides reduce the full width half-maximum of the reflectivity curves to increase the precision over traditional resonance techniques. They add a thin dielectric layer between the bulk substrate and the sample layer, which enhances the resonance, since there are multiple reflections within this layer. This technique allows for a greater area to be probed.

The TIR-Raman and ATR-IR spectroscopy techniques were combined by Kivioja *et al.* and used to measure the thickness of thin polystyrene films on polypropylene.[90] They used the band ratios of the two polymers to calculate the thickness. Their group later investigated ink films on coated paper surfaces, used in offset printing.[91] They wanted a non-destructive rapid technique to determine ink penetration, spreading and ink colour separation and found that TIR-Raman provided very good depth resolution.

Grenoble and Baldelli, similar to our own work, looked at cationic surfactant adsorption to hydrophilic and hydrophobic silica using TIR-Raman.[92] They found that the coverage of their surfactant (benzyldimethylhexadecylammonium (BDMHA$^+$) chloride) decreased by 50 % at the hydrophobic surface relative to bare hydrophilic silica. They attributed their findings to the surfactant adsorbing as hemispherical aggregates with their alkyl chains in close proximity to the hydrophobic surface.

Jubb *et al.* studied haematite using TIR-Raman.[93] They looked at the Raman-active sulphate ($SO_4{}^{2-}$) ion adsorption to, and removal from, a 100 nm haematite layer prepared using the same method adopted by us (see section 6.6), also developed by their group. They found that that sulphate adsorption increases with a decrease in pH as they expected.

Previous work within our own group has used TIR-Raman to look at other surfactant adsorption to silica,[46,94] supported lipid bilayers,[95,96] and lubricants under pressure in

a tribometer.[97–99] Another surface investigated successfully was cellulose.[100] Greene and Bain looked at the wax layer of barley leaves *in vivo*.[101] They found the limited penetration depth of TIR-Raman to be advantageous as it avoided deeper-lying florescent pigments.

Other Techniques for Studying Soft Matter

Various other techniques have been used to study surfactants at interfaces. While we will not go into detail, some of the techniques used include cyclic voltammetry,[102] neutron reflectometry,[103–107] ellipsometry,[103,106,108–111] maximum bubble pressure,[3,112] external reflection Fourier transform infra-red spectroscopy,[111] capillary electrophoresis,[113] and laser Doppler velocimetry.[108]

1.2.9 Flow Cell

The glass wall-jet flow cell, which we discuss further in chapter 4, is used as it has well-defined hydrodynamics.[1] The cell is symmetric along the direction of fluid flow and capped with a hemisphere. When the fluid exits this tube it is under Poiseuille flow so the flow, at velocity v, is steady and laminar, and along the z-axis ($v_r = v_0 = 0$), where v_r and v_0 are the radial and axial velocities respectively (see figure 1.14). The flow profile is parabolic with respect to r and the flow is fully developed within the tube. A no-slip boundary condition is applied under the hemisphere: $v(z = 0) = 0$. We also assume the concentration at any point in the tube is equal. This results in simpler mass transport equations reducing to a one-dimensional form along the tube axis.
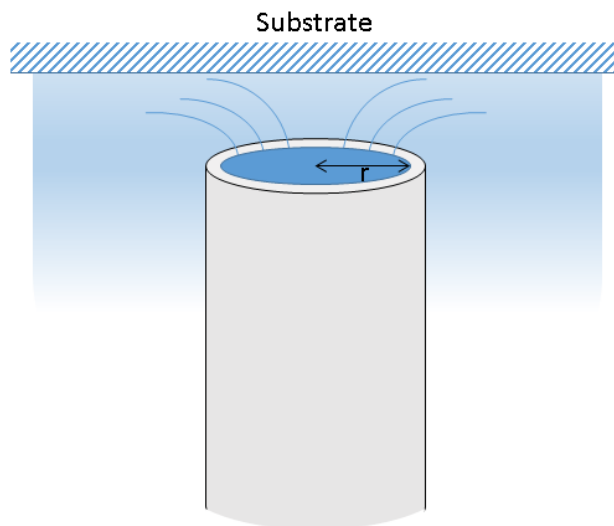
Figure 1.14: Flow cell

Compared with the dual-inlet channel flow cell, used previously in our group,[114,115] the wall-jet flow cell is advantageous as, at the interface, the solution is stationary and transport is by diffusion alone (no-slip boundary condition). Directly above the centre of the delivery tube there is a stagnation point where there is no radial convection.[1] At this

point the flux (J) is limited by:[1]

$$J = 0.77646 D^{2/3} \alpha^{1/3} c_0 \tag{1.40}$$

where D is the surfactant diffusion coefficient, c_0 the bulk concentration and α is a constant that can be calculated from hydrodynamic modelling.[1] Woods then showed that this equation is an incomplete description for adsorption as adsorption occurs before the flux limit is reached.[1] The disadvantage of the wall-jet flow cell is the uncertainty of the concentration profile of the injected solution, but he showed that the errors from this are small.[1]

A channel flow cell uses a shallow, wide channel, but this results in the flux varying with distance from the interface and the adsorption kinetics for surfactants can be affected by adsorption upstream. The variation in flux can be overcome by increasing the flow rate, but this requires large volumes of solution.[1] For the wall-jet cell, the concentration at time $t = 0$ is less well defined than for a dual-inlet channel flow cell.

1.2.10   In-line Mixer

A mechanically-driven in-line mixer was developed and used by Woods to increase the number of data points taken for a given concentration range and to speed up data acquisition.[1] The concentration can be continuously varied and hence the number of different concentrations is only limited by the acquisition time of the spectrometer. This method also makes data acquisition easier, as fewer multiple concentrations need to be made up. This method improves efficiency as the solutions do not need to be changed every 5–10 minutes. The in-line mixer is designed to be used to record isotherms not kinetics because the concentration is constantly changing. The tank is rapidly stirred using a magnetic stirrer bar to ensure thorough mixing.

For a pure surfactant, the mixer is first filled with pure water and the inlet is attached to a solution with a concentration $[A]_{\text{in}}$. The volume of the mixer is V and the flow rate is R. The concentration in the mixer follows the differential equation:

$$\frac{\mathrm{d}[A]}{\mathrm{d}t} = \frac{R}{V} \left([A]_{\text{in}} - [A]\right) \tag{1.41}$$

subject to the boundary condition that $[A]_{t=0} = 0$. The solution is:

$$[A] = [A]_{\text{in}} \left[1 - \exp\left(\frac{-Rt}{V}\right)\right] \tag{1.42}$$

A short time later, the concentration at the outlet from the mixer appears at the end of the tube just beneath the hemisphere. The concentration at the sample surface therefore increases continuously from zero, asymptotically approaching the final concentration $[A]_{\text{in}}$. The experiment can then be repeated with the mixer initially filled with surfactant solution and then diluted with pure water, in which case the concentration is a simple exponential decay with time constant V/R. If the time constant is long compared to the time taken for the surface to equilibrate, then the resulting surface will be at equilibrium with the solution, even though the solution composition is continuously changing.

Due to the exponential change in concentration, the concentration will never reach the

target concentration and hence the experiments need to be performed in both directions to obtain the desired concentration range. "In" measurements are where the mixer and cell are both filled with UHP water and the surfactant is pumped in, and "out" measurements are where the mixer and cell are filled with the pure surfactant solution and UHP water is pumped in.

Mixed surfactant isotherms can similarly be acquired if the mixer is first filled with surfactant B which is then replaced by surfactant A. The concentration profile with time is then:

$$[A] = [A]_0 \left[1 - \exp\left(\frac{-Rt}{V} \right) \right] \tag{1.43a}$$

$$[B] = [B]_0 \left[\exp\left(\frac{-Rt}{V} \right) \right] \tag{1.43b}$$

1.2.11 Substrates

The thermodynamics of adsorption to different surfaces, such as minerals like alumina,[116,117] haematite, zeolite, and polymers like cellulose[1,100] and polyester have been studied. This project is concerned with the adsorption to zeolite, kaolinite, polyester and haematite (iron (III) oxide) substrates. Hydrophobic silica surfaces are also of interest.

Silica

Silica in the form of silicates make up most of the Earth's crust and hence the chemistry of the silica surface has been widely studied. It is also commonly used as a model hydrophilic surface. Bulk silica consists of siloxane units in a tetrahedral lattice. Different surface preparation techniques and the nature of the solution can change which functional groups are at the surface. Figure 1.15 shows common silica functional groups.[21] Like other mineral oxides, the charge on silica depends on the relative H^+ and OH^- concentrations, as shown by equilibrium R1.3 and equilibrium R1.4.[21]

$$SiOH + H^+ \underset{k_1}{\rightleftharpoons} SiOH_2{}^+ \tag{R1.3}$$

$$SiOH + OH^- \underset{k_2}{\rightleftharpoons} SiO^- + H_2O \tag{R1.4}$$
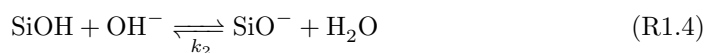
The relative magnitude of equilibrium constants k_1 and k_2 determine the charge at the interface and the isoelectric point occurs around pH 2. The surface possesses a net positive charge below around pH 6.[21] Silicon dioxide layers are often prepared by baking silicon wafers in an oven in an oxygen atmosphere (pyrogenic silica) and can be converted to hydroxylated silica by soaking in water or a basic solution.[21] Hydroxylated silica has a high density of hydroxyl groups ($\approx 4.5\,OH\,nm^{-2}$).[21] This allows hydrogen bonding between the hydrogen of one hydroxyl group and the oxygen of the neighbouring group (shown in figure 1.15B). This bond results in a low surface charge at normal pH levels.[21]

Chorro *et al.* investigated different silica preparation techniques and found that pretreatment with acid could reduce the maximum surface excess on adsorption by nearly 50 % and so it is essential that surfaces are prepared identically.[118]
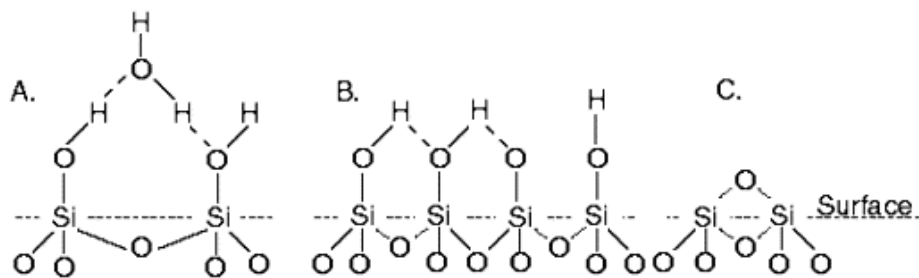
Figure 1.15: Schematic representation of the types of functional groups that occur on the silica surface. (A) Hydrated and (B) anhydrous silanol groups are associated with the hydroxylated surface whereas (C) siloxane-dehydrated groups occur mainly on the pyrogenic surface. Reproduced with permission from reference 21. Copyright 2003 Elsevier

Zeolite

Zeolites are a group of microporous, aluminosilicate minerals with pores around a few Å in size. Zeolites are composed of an aluminosilicate framework of Si and AlO_4 tetrahedra, where each oxygen is shared between two tetrahedra.[119] There are around 50 different types, some naturally occurring and some artificially created.[120] Zeolites are commonly used as fillers for plastics and in catalytic processes.[121,122] The zeolite A structure can be seen in figure 1.16. The negative charge on the framework is balanced by cations in the pores. The cations can be displaced, hence they are often used as a molecular sieves and as an adsorbent for cations, such as Na^+, K^+, Ca^{2+}, Mg^{2+}, or toxic and/or radioactive ions. Channels are formed by linked rings of tetrahedra and different zeolites have different sized channels. The larger the channel, the larger the cation that can enter. Water molecules are also found within the channels formed in the framework. Both the water and the cations can be exchanged without disrupting the framework.[119] Some zeolites have pores large enough ($\approx 9\,\text{Å}$) to accommodate small organic molecules.[119]

Lee *et al.* used zeolite microcrystals as model system because they can be produced in fairly uniform sizes and shapes, and monolayers of microcrystals can be applied as, for example, precursors for molecular sieve membranes,[124] low-dielectric materials,[125] and nonlinear optical films.[126]

Zeolites have refractive indices between 1.47 and 1.54 when dry[128] and they are often slightly birefringent ($\Delta n < 0.0015$);[119] their cation exchange capacity is $\approx 1200\,\mu\text{eq.\,g}^{-1}$.[129]

The name comes from the Greek *to boil*, and *stone* as they often swell (intumescence) when wetted.[130] When heated they remain structurally intact, in contrast to other hydrated compounds.[130] After dehydration the channels can be filled again with water or used to adsorb ammonia, mercury vapour or other substances (often toxic). Upon rinsing with a concentrated NaCl brine solution, the zeolite releases the previously adsorbed species,[130] hence the process can be reversible. The name prefix, for example, Na-zeolite A denotes the cation present in the pores, which can be exchanged with another to form, for example, Ca-zeoilte A.

Surfactant adsorption to zeolites is of interest as zeolites, when modified by cationic surfactants, can be used to remove anionic surfactants such as SDS from wastewater.[131]
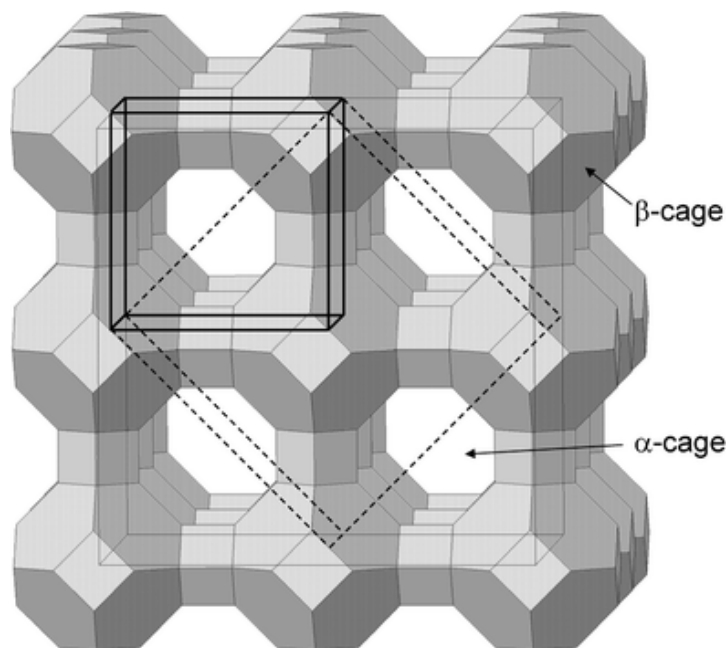
Figure 1.16: Zeolite A structure. Reproduced with permission from reference 127. Copyright 2006 RSC

Zeolites are also added to detergents to control water hardness by exchanging Ca-zeolite with the "hard" sodium ions in hard water thereby improving the detergents' effectiveness.[132]

Surfactants are sometimes used to modify the pore size of zeolites[121,122] for example zeolite A was modified by Frida *et al.* by heating with $C_{16}TAB$ to improve its use as a filler in polypropylene.[121] They found this method reduced the pore size from $74\,\mu m$ to $1\,\mu m$, and by using this modified zeolite in polypropylene forming they were able to increase the decomposition temperature. The nonionic surfactant $C_{12}E_6$ has been found to reduce the growth of synthesised zeolite A particles.[133] $C_{16}TAB$-modified zeolite Y was investigated and found to have antibacterial activity by Salim *et al.*.[134]

The adsorption of cationic surfactants onto natural zeolites (negative surface charge) was studied by Xu and Boyd who found that at low concentrations of surfactant, surfactant cations are exchanged with exchangeable cations from the zeolite until a monolayer is formed.[135] At higher concentrations hemi-micelles, micelles, bilayers (or more (admicelles)) are attached to the external surface, with additional layers of surfactant bound by hydrophobic interactions.[131,135] The adsorption of surfactant can change the external surface charge of the zeolite and the substrate can provide anion exchange capacity,[131,136] useful for adsorbing contaminants such as chromate and other inorganic anions.[136]

Kaolinite

Kaolinite is an insoluble[130] clay silicate from the kandite group[128] with the formula $Al_2Si_2O_5(OH)_4$. It is composed of an extended sheet with two components, a layer of $(Si_4O_{10})^{4-}$ is linked to a layer of $(OH)_6-Al_4-(OH)_2O_4$ (dioctahedral) by SiO_4 tetrahedra.[119,128] The structure of kaolinite is shown in figure 1.17. It is often used in the manufacture of bricks and china clay, and as a filler for paints, inks, paper and

plastics.[119,137] It is a mineral found widely in nature hence, contributes to the properties of soils.[137] It is also used as a cheap adsorbent of heavy metals in wastewater treatment.[138] As it is very common, it has been widely studied.[137,139] It is well known that it has a heterogeneous surface charge due to the isomorphous substitution of Si^{4+} by Al^{3+}.[139] The charge on the edges can vary upon pH, due to the protonation/deprotonation of surface hydroxyl groups.[139] It has a low cation exchange capacity ($10\,\mu eq.\,g^{-1}$ to $100\,\mu eq.\,g^{-1}$) but a comparably high (to other clays) anion exchange capacity, through exchange of OH^{-} ions.[119]
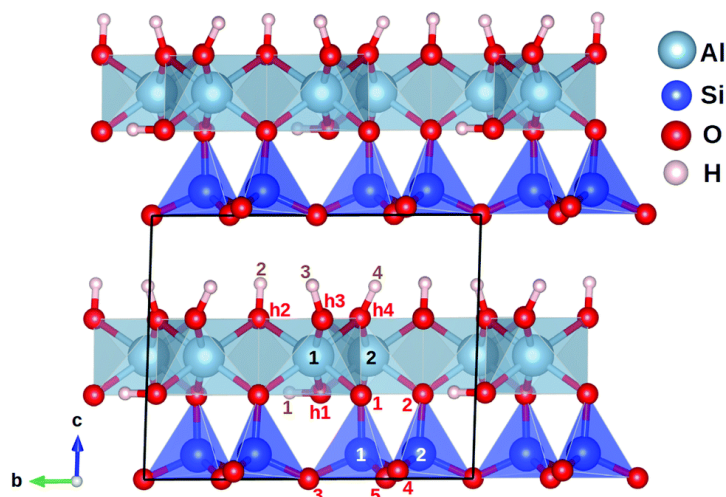
Figure 1.17: Kaolinite structure. Reproduced with permission from reference 140. Copyright 2015 RSC

Polyester

Polyester is a polymer that contains the ester ($-RCO_2R'-$) functional group as the linker, where R and R' are the carboxylic acid and the alcohol, respectively (see figure 1.18). They are formed by a condensation reaction (loss of water). A common form, polyethylene terephthalate (PET), made from ethylene glycol and terephthalic acid, is often woven into threads to make fabrics for clothing or upholstery, under the commercial names of Terylene or Dacron.[141] Polyester fibres can be hydrophobic and absorb less water than nylon, but can undergo hydrolysis at prolonged exposure to temperatures above $50\,°C$.[142] Polyesters are also commonly used to make plastic bottles, capacitors, liquid-crystal displays and other commercial products. The adsorption of surfactants to polyester is interesting as surfactants are used as detergents and during dyeing.[143] Polyester (and nylon or acetate) dyeing is often performed at high temperatures and with solvents so alternatives are being sought to lower the cost, environmental impact and reduce the damage by hydrolysis.[143] As PET is hydrophobic, it readily adsorbs and holds oils, so detergents needed to be developed to clean these fabrics.[144] These are often POE nonionic surfactants.[14,145] Anti-redeposition agents (often polymers) have been developed to prevent soils from redepositing onto the fabric.[144] Other coatings have been developed to improve the feel and finish of the fabric.[14]
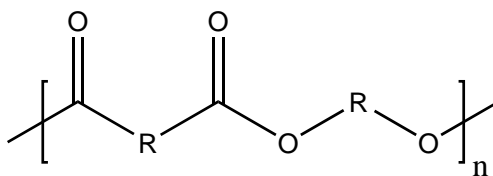
Figure 1.18: Polyester structure

Haematite

Haematite (Fe_2O_3), structure shown in figure 1.19, consists of layers of oxygen ions and layers of iron ions perpendicular to the triad axis. The oxygen ions are arranged in a distorted hexagonal packing.[119] Cation layers contain the ions in six-fold coordination which differs to that of spinel (a magnesium aluminium mineral), where they are in four-fold coordination.
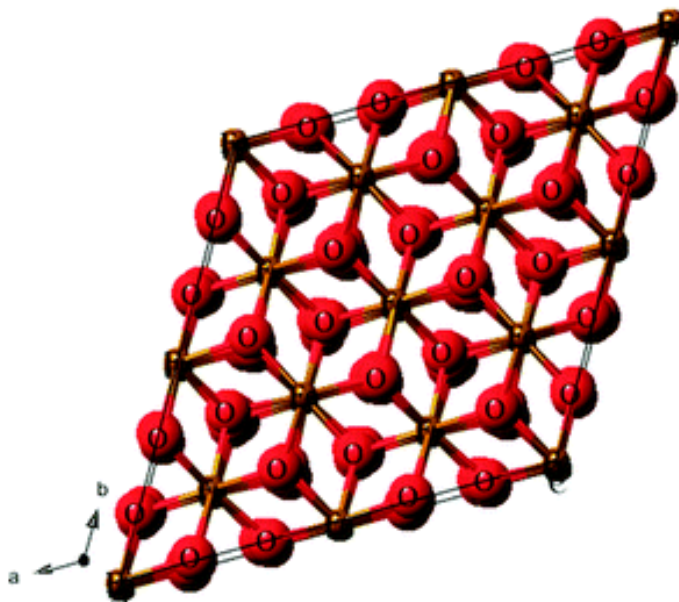
Figure 1.19: Haematite structure. Adapted with permission from reference 146. Copyright 2015 RSC

Haematite and the other main iron oxides (maghemite and magnetite) are of great interest as they have a range of applications that include opto-electronics, medicine, environmental remediation (contamination removal), pigments, corrosion protection, and gas sensing.[147]

1.2.12 Factor Analysis

Introduction

To process our data, we use a technique called principal component analysis (PCA). This technique allows us to determine how much of a particular molecule or component is present in our spectra.

Background

PCA was devised around the 1930s by behavioural scientists, but was not applied to chemical problems until 1970.[148] Target factor analysis (TFA) uses PCA with an additional step which represents the results in a more physically realistic way as opposed to the abstract components. When computers were introduced, the use of factor analysis increased as a chemometric technique due its ability to extensively analyse large data sets without too many simplifying assumptions, which were commonplace before computers existed.[148] A global definition of factor analysis is given by Malinowski as:[148]

> *Factor analysis is a multivariate technique for reducing matrices of data to their lowest dimensionality by use of orthogonal factor space and transformations that yield predictions and/or recognisable factors.*

Factor analysis of a data matrix involves analysing the data to produce an abstract reproduction where both the "principal" factor solution and the number of factors are obtained. This process is called *eigenanalysis*[148] and produces eigenvalues and eigenvectors where each of the eigenvectors represent an abstract factor. The eigenvalue measures the relative importance of the eigenvector (largest being most important). For experiments with no experimental error or random noise the number of eigenvectors would equal the number of controlling factors, however experimental error introduces additional eigenvectors (s) of which, only the largest (the controlling factors) have physical meaning. In factor analysis the data matrix ($\mathbf{D}$) is decomposed into the product of an abstract row ($\mathbf{R}$) matrix and an abstract column ($\mathbf{C}$) matrix. The complete principal factor solution is then computed as:[148]

$$\mathbf{D}_{r \times c} = \mathbf{R}_{r \times s} \mathbf{C}_{s \times c} \qquad (1.44)$$

As there are an additional s factors, there are additional columns and rows in the row and column matrices respectively (s is equal to the smallest of r or c) and there are more eigenvectors than necessary. The eigenanalysis technique used in this thesis is singular value decomposition (SVD), since it is known to be stable, fast, and algorithms already exist in various programming languages (MATLAB is used here). The SVD program produces three matrices:

$$\mathbf{D}_{r \times c} = \mathbf{U}_{r \times s} \mathbf{S}_{s \times s} \mathbf{V}'_{r \times s} \qquad (1.45)$$

where $\mathbf{S}$ is a diagonal matrix and its elements are the square roots of the eigenvalues. PCA separates the data into two sets of eigenvectors, $\mathbf{U}$ and $\mathbf{V}$; one spanning the rows and the other the columns, respectively, and which are orthonormal to each other. $\mathbf{U} = \mathbf{R}\mathbf{S}^{-1}$ and $\mathbf{V}' = \mathbf{C}$, if all eigenvalues are non-zero. The elements in each row of $\mathbf{U}$ represent the coordinate positions of the row on the factor axes and the same is true for each row of $\mathbf{V}$ on the columns of the factor axes. Eigenvectors are arranged in decreasing order of importance.

To determine how many of the s factors are physically important, the abstract factors are split into a primary set (n) and a null set ($s - n$). The primary set account for all the real features of the data and the null set, for experimental error and are eliminated from the initial solution. When eliminated, the factor model is "compressed" to include only the physically significant factors and $\mathbf{R}$ and $\mathbf{C}$ become $\overline{\mathbf{R}}$ and $\overline{\mathbf{C}}$. These compressed

factors can usefully be multiplied to generate $\overline{\mathbf{D}}$, the original data with the noise removed. If the error in the data is known then the selection of the number of factors can be done (in our systems of pure surfactant in water on silica $n = 2$, the silica+water component and the surfactant component), if the error is not known further numerical methods would be required.

Next the transformation of the principal factors into recognisable parameters is required. The transformation matrix $\mathbf{T}$ is used:

$$\begin{aligned}
\overline{\mathbf{D}} &= \overline{\mathbf{R}}\,\overline{\mathbf{C}} \\
&= \left\{\overline{\mathbf{R}}\mathbf{T}\right\}\left\{\mathbf{T}^{-1}\overline{\mathbf{C}}\right\} \\
&= \widehat{\mathbf{X}}\widehat{\mathbf{Y}}
\end{aligned} \tag{1.46}$$

$\widehat{\mathbf{X}}$ and $\widehat{\mathbf{Y}}$ are the transformed row and column matrices and represent the contribution of each spectra. In TFA the target to be tested is provided (normally the spectrum of the component on its own). In this study, target factors are obtained from manual subtraction of water (first mean of 15 spectra of empty cell) and a mean of the last 15 spectra of the highest concentration solution. Figure 1.20 shows the targets for an example experiment. Taking a mean reduces the noise in the targets. Figure 1.21 shows a selection of the raw spectral data for $C_{16}TAB$ on silica.

Testing of the targets allows development of physically significant models and each potential factor can be tested individually, applied to either rows or columns. The target testing is summarised by:

$$\overline{\mathbf{R}}\mathbf{t} = \widehat{\mathbf{x}} \overset{?}{=} \mathbf{x} \tag{1.47}$$

$\mathbf{t}$ is the target transformation vector and results from a least-squares operation of the individual target, $\mathbf{x}$. If $\mathbf{x}$ is a real factor, the predicted vector $\widehat{\mathbf{x}}$ will be similar and the test can be accepted. Statistical methods can then be applied to evaluate acceptance of the test by calculating the %SL (percentage significance level). A %SL greater than 5% is taken as a valid test factor.

Loading factor analysis (LFA) is then used to calculate factor loadings and the errors in the loadings, *i.e.* how much of each target (component weight) is present in each spectra. The component weights produced for the first two results from the TFA are shown in figure 1.22 and the LFA-generated improved (refined) spectra are shown in figure 1.23. The component weight of the surfactant spectrum is divided by the component weight of the water spectrum at that point in time to account for any drift in laser power or focus. The improved spectra look like the target spectra so separation has been successful.

If the surface is not completely clean, the target factors may be offset which results in a cleaner spectrum having a negative surface excess. Other systematic errors may result from a drift in the baseline during an experiment, which may show up in the surfactant factor. This may sometimes be removed by subtracting the baseline so that the base of each spectrum lies at zero counts.
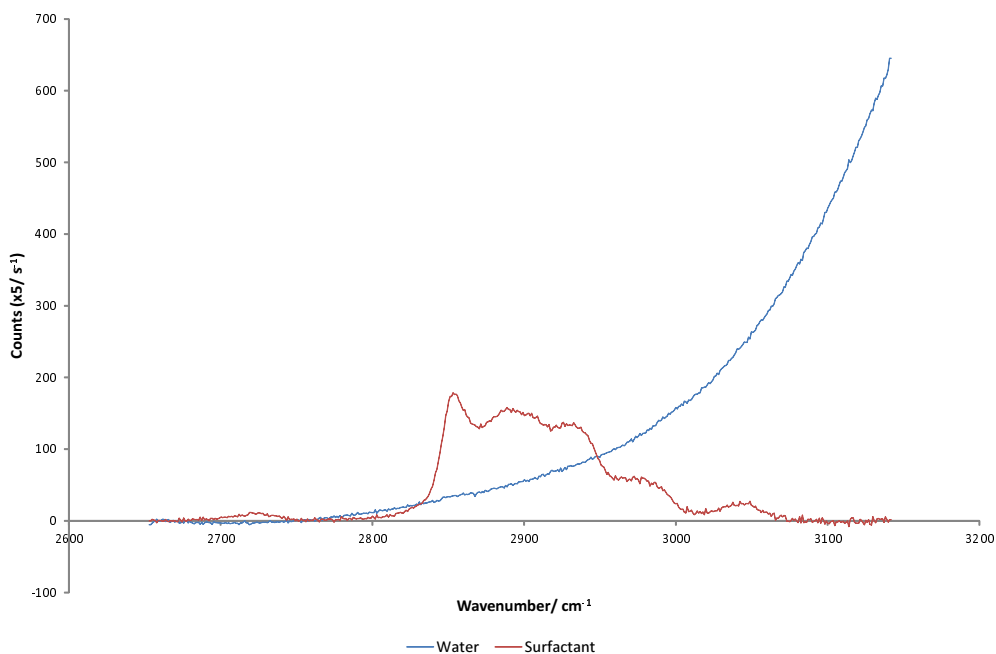
Figure 1.20: Target factors for analysing spectra in figure 1.21
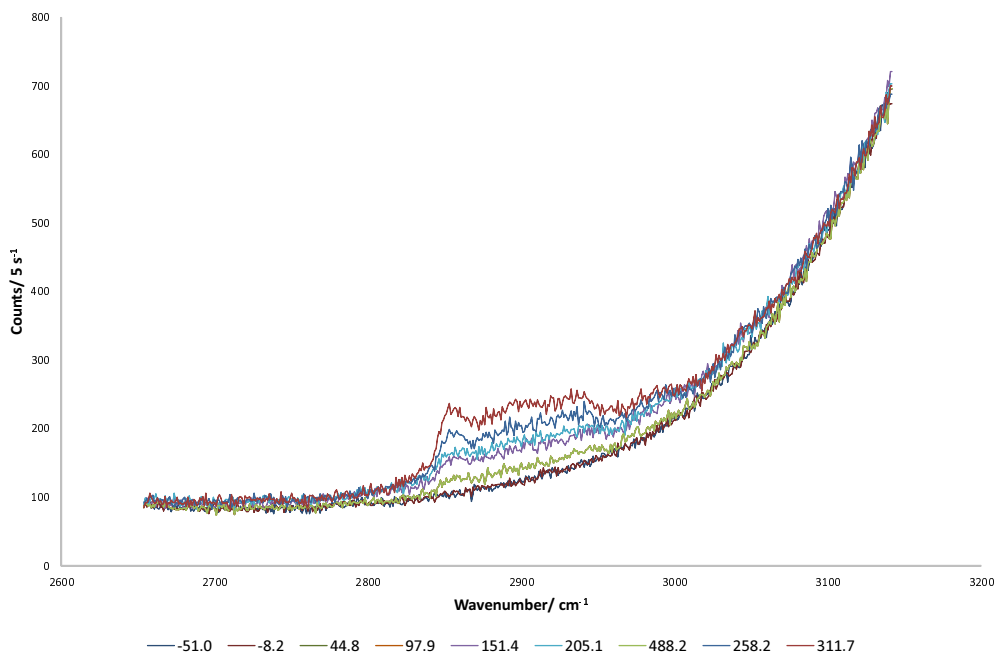
Figure 1.21: Selected raw spectral data for $10\,\mathrm{mM}$ C_{14}TAB adsorption on silica, legend shows elapsed time in seconds, every 50 measurements. The time is offset from the time the surfactant reaches the surface, hence there are negative times, before the surfactant arrives

41
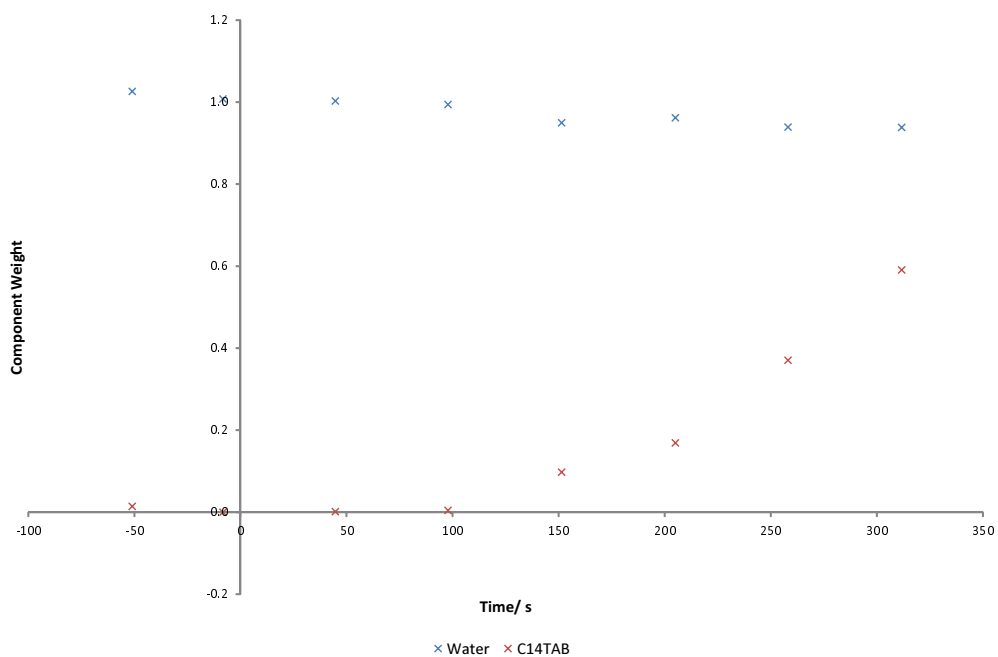
Figure 1.22: Selected component weights against offset time for C_{14}TAB
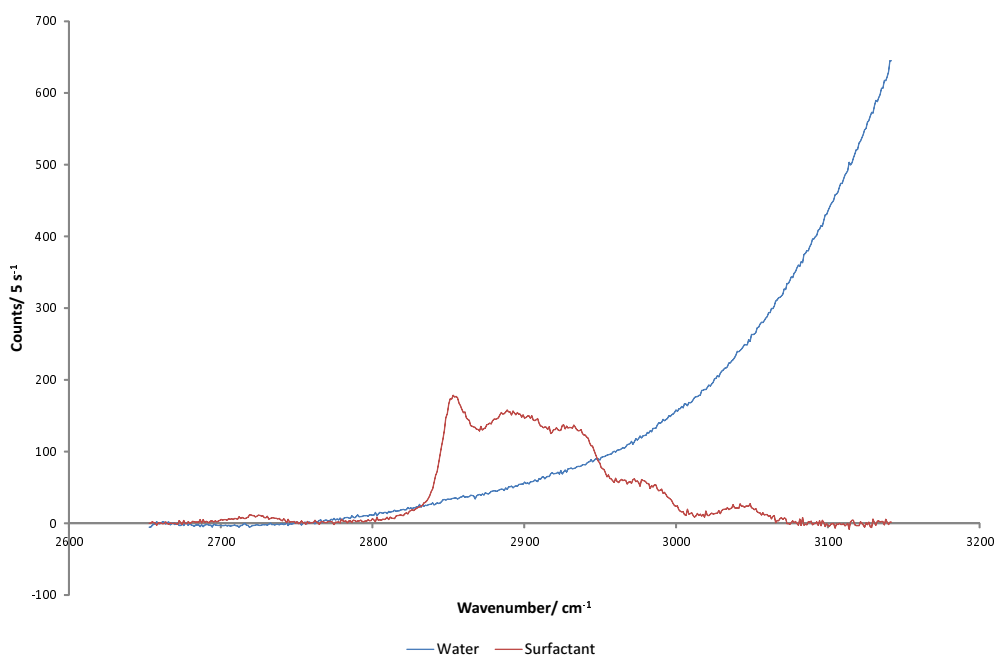
Figure 1.23: Refined spectra for C_{14}TAB after TFA

Chapter 2

Spectrometer

This chapter, after introducing the existing instrument used at the beginning of my PhD, focuses on the reasoning and methods for the development and construction of a new Raman spectrometer for TIR-Raman. This new spectrometer was used for the majority of experiments in this project. The new design has a faster readout time and by rotating the cell so that the surface is vertical, aims to reduce the problems due to adherence of bubbles to the interface.

2.1 Renishaw Spectrometer

A Renishaw Raman spectrometer microscope, (Ramascope 1000, Renishaw, Wootton-under-edge, UK) was used at the start of this project before the new spectrometer was constructed. The Renishaw spectrometer system is similar to our new design (and was used as a design base). Figure 2.1 shows a schematic of the spectrometer's optical components. The external optics were designed and assembled by Eric Tyrode. [9] A continuous-wave, frequency doubled 532 nm, diode pumped solid state (DPSS) laser (Opus 532, Laser Quantum, UK) beam of up to 3 W is delivered via mirrors to a beam-expanding telescope then to a periscope, and focused through a lens down onto the sample. The reflected beam is stopped by a beam dump. The Raman scattered light is then collected through the hemisphere by a 50× ULWD (18 mm), 0.55 NA objective (MSPlan, Olympus, Japan) and directed into the spectrometer via a removable mirror in the microscope turret. This mirror can be removed for focusing and alignment, allowing the light to reach a CCTV camera which displays live video on the attached PC. Also located in the turret, a removable 50 % mirror allows illumination of the sample by a lamp. Upon entering the spectrometer the light passes through two edge filters. Next the light passes through an optional half-wave ($\lambda/2$) plate which rotates the plane of polarisation before it passes through an optional polariser. With both $\lambda/2$ waveplate and polariser in place we detect y-polarised light, with just the polariser; x-polarised light. With both optics removed unpolarised light is detected, however as we have seen in section 1.2.8, the grating is polarisation sensitive, hence the different polarisations will not be detected with equal sensitivity. This change in grating efficiency also explains the use of the $\lambda/2$ plate, to ensure the grating is always used in the most efficient way. The light is next focused through a slit and recollected via a lens onto a mirror, then the grating, back on to the

mirror and onto the CCD via a lens. The slit reduces the amount of light not coming from the focal plane of the objective.

2.2 The New Spectrometer

Included in the original plan for this project was the build of a new spectrometer; the reasons are explained in section 2.2.1. The spectrometer (schematic shown in figure 2.2) was designed and constructed from scratch, but built to improve upon the optical arrangement used previously. The build involved a consideration of a number of factors, many of these are discussed in section 1.2.

2.2.1 Build Rational

A commercial Renishaw spectrometer was adapted for TIR-Raman and from use over time, it has become apparent that the setup could be further improved if we re-designed the system. The main problem with the existing spectrometer is that a readout time of around 1 s greatly limits our ability to follow fast kinetic processes including fast surfactant adsorption to interfaces. To overcome this limitation, we chose a faster CCD camera. We already owned a Princeton Instruments device (model number LN/CCD-512TKB), a 512×512 liquid-nitrogen cooled, back-thinned CCD. The advantages of this type of CCD are discussed in section 2.2.2.

The other disadvantage of the Renishaw setup required the cell to be mounted in a vertical position, where the liquid–solid interface to be examined was positioned horizontally at the top of the cell. This orientation meant that should any bubble enter the cell or effervesce out of solution it would, under gravity, migrate towards the top surface. Bubbles on the surface mean that we no longer have a liquid–solid interface (our interface of interest) and greatly reduce our signal levels by increasing scattering. By simply rotating the cell 90°, we are able to eliminate the problem—if any bubbles do nucleate on the surface they are likely to either roll up the interface away from the probe area, or detach from the interface completely and accumulate at the top (previously the side) of the cell where they cannot affect the results. The rotated cell also increases the safety of the system because all laser beams are confined close to the table, below eye level whereas the Renishaw required a tall vertical periscope in order to deliver the beam to the microscope.

In addition to the trapping of bubbles, the original Renishaw design suffers from "focal drift" as can be seen when switching back to the objective view after running an experiment, where the surface is clearly out of focus. The exact origin of the drift has never been fully understood. Focal drift causes a gradual loss of water and/or surfactant signal. Vibration of the sample is likely to cause creep in the mounting components (in particular, the clamping arrangement for the glass cell, which cannot be too tight to avoid breakage). A redesign of the clamping method to the cell has reduced focal drift, however this redesign came at the end of the project and to keep data consistent, we chose to use the pre-existing mounting method, using the same cell throughout the project. The new spectrometer constructed in this project did initially suffer from some periodic focal drift which repeated every ≈ 15 min but the source of this was found and fixed (air-conditioning
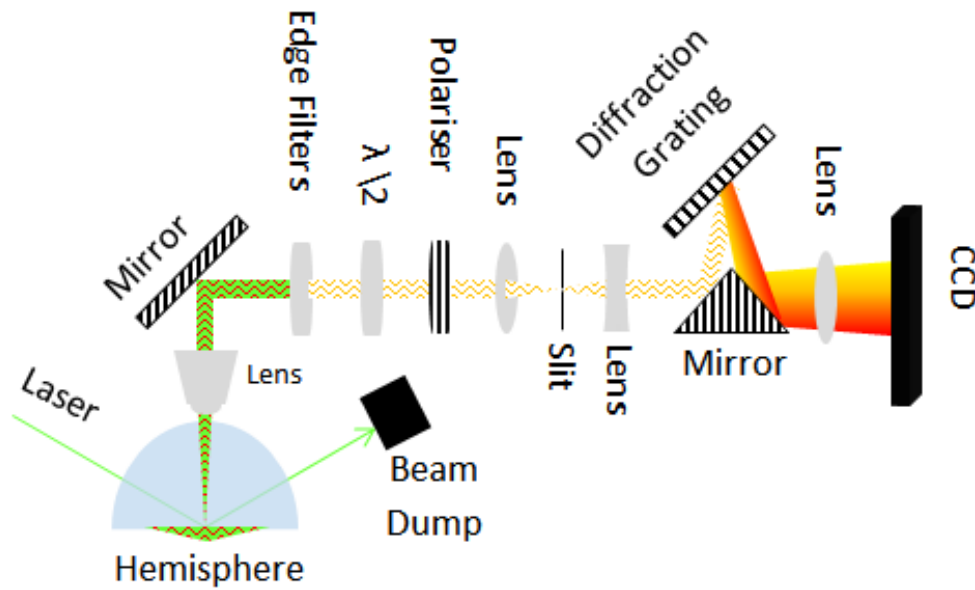
Figure 2.1: Renishaw spectrometer schematic

thermostat).

The redesigned cell mount (shown in figure 2.3) affixes the cell directly to a $3''$ mounting disk using glass adhesive. This assembly then fits directly into the optical mount. This arrangement is much more stable and secure, and less prone to breakage as the glass envelope is no longer under compression.

We managed to isolate one cause of stage vibration for the Renishaw spectrometer, where the stage controller cables were resting on the vibrating water-recirculating bath; however some drift does still occur. The spot also occasionally drifts sideways, showing again that the sample is not as firmly fixed as we would like. Although the apparatus is mounted on an air dampened table, vibrations cannot be eliminated completely. During the first year and a half of the project extensive nearby building works caused great disruption. We did consider using the beam reflected by the hemisphere (TIR) to auto-correct the focal drift through use of a photodiode array, but with the set-up using non-computer controlled stages it would have been hard to control the stages automatically without great expense.

The Renishaw software (WiRE) is unable to be modified to control additional apparatus. By writing our own software the customisation options are greatly expanded and we are able to control other devices, for example the syringe pump and optomechanics (described later).

An open bench design allows for easier customisation and future-proofs the design, for example adding extra optics or changing the gratings. Our addition of a motorised stage to select the incident polarisation and electronically insert neutral density (ND) filters are a useful time-saver. One future possible option we considered, discussed in more detail in section 2.2.4, was recordings both x and y polarisations simultaneously. This technique would not be possible within the existing spectrometer's housing. Adapting the system for imaging was also considered.
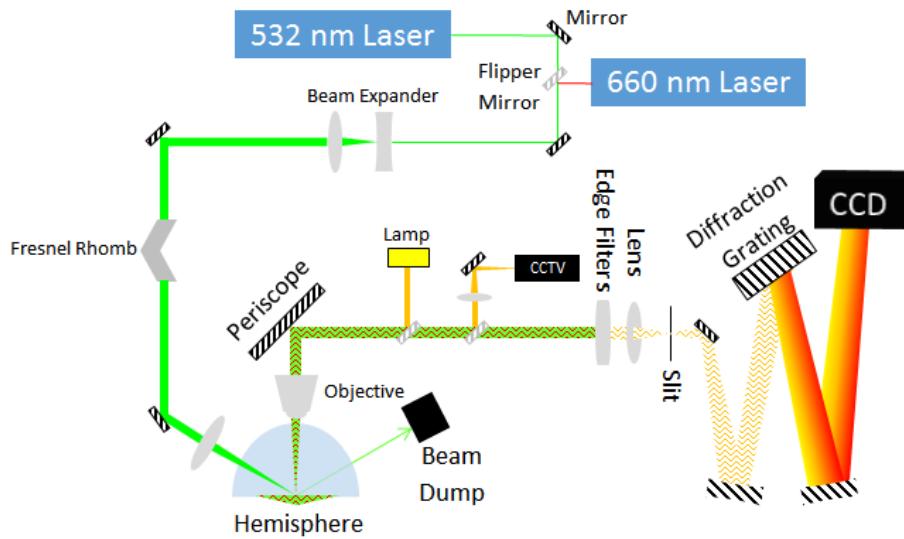
Figure 2.2: New spectrometer schematic

2.2.2 Design and Construction

CCD

Back-thinned CCDs are advantageous because in a traditional front-illumined CCD the electronic components are placed on top of the photocathode; back-thinned CCDs are flipped during manufacture and then reverse thinned by removing some of the substrate.[149,150] The back thinned orientation allows the photons that would normally be reflected or adsorbed by the electronics to reach the photocathode. Back-thinning of the CCD can cause problems due to etaloning, where the thickness of the substrate creates a resonant optical cavity, especially at near infra-red wavelengths, but applying an anti-reflective coating and controlling the thickness so that a destructive resonant cavity is not set up for the wavelengths of interest reduces this effect.[151] The CCD is liquid-nitrogen cooled to reduce noise. The CCD was run at $-100\,°C$ and this was maintained by a heater element incorporated into to the CCD chip, controlled by the CCD driver. This temperature was recommended by the manual[152] to minimise dark charge while maintaining sensitivity, as if too low it decreases the transfer efficiency. When the set temperature is reached, a green LED on the controller lights, and the value is maintained to $\pm 50\,m°C$.[152] Cooling to this temperature took approximately 30 to 45 min. The typical dark charge at this temperature is 3 to 6 electrons/hour/pixel.[152]

The readout time for the new spectrometer is now around 350 ms and could be improved further if necessary by adjusting the binning parameters at the expense of capturing more cosmic rays from skipped regions of the CCD due to the capacity limitation of the shift registers. Replacing the CCD with a more modern camera would also greatly reduce readout time, but was outside our budget.

The CCD controller software, CCD Spectrometric Multichannel Analysis (CSMA) software ran on a Viglen 486 machine (referred to as the CCD computer) under MS-DOS. This was connected to a more modern Dell Optiplex 380 workstation (referred to as the control computer), running Microsoft Windows 7 and National Instruments LabVIEW

Figure 2.3: New cell mount showing the glass cell attached with glass adhesive to a stainless steel mounting plate turned to fit a $3''$ optical mount

software, by a RS-232 null-modem cable for spectral data transfer. An ISA card in the CCD computer was connected by a proprietary serial communications ribbon cable to the CCD driver (model number ST-130), which was in turn connected to the CCD enclosure via a multi-pin cable. The external sync input on the CCD driver (for triggering) was connected to the National Instruments (NI) interface card (described later) via coaxial cable, so that the CCD could be triggered when required.

It is worth noting the quantum efficiency of the detector, the manufacturer's specifications are shown in figure 2.4. The approximate quantum efficiency of the detector for detecting light from C−H bands Stokes shifted by $2900\,\text{cm}^{-1}$ is approximately $75\,\%$ with $532\,\text{nm}$ excitation and $50\,\%$ with $660\,\text{nm}$.

Due to the age of the CCD, there were several dead pixels on the chip: pixels which did not generate a charge upon illumination. These pixels, when binned with vertically adjacent pixels (to improve signal to noise ratio and readout time), were identified as being several hundred counts lower than the surrounding pixels and data from these pixels was replaced (see section 2.2.3). The CCD shutter also suffered from age, sometimes failing to close properly leading to increased counts in subsequent spectra. Luckily the over-exposed frames were easy to identify (due to much higher average intensity) and remove. The software running on such an old computer was also a risk, but in general seemed relatively stable (despite one hard drive failure).

Spectrometer, Grating, and Controller

The spectrograph we obtained (SpectraPro-500i, Acton Research Corporation, USA) has 3 interchangeable gratings. It was of the Czerny-Turner design, see figure 2.5, which uses curved mirrors to provide to focusing, and a plane grating for dispersion.

Three (two 1200, and one $600\,\text{lines}\,\text{mm}^{-1}$) gratings were supplied with the spectrograph, and we purchased one further grating for this project. The new grating's efficiency curve is shown in figure 1.13. The efficiency curve for the other gratings were unknown. As can be seen, the polarisation of light is important, as is the choice of grating, as use
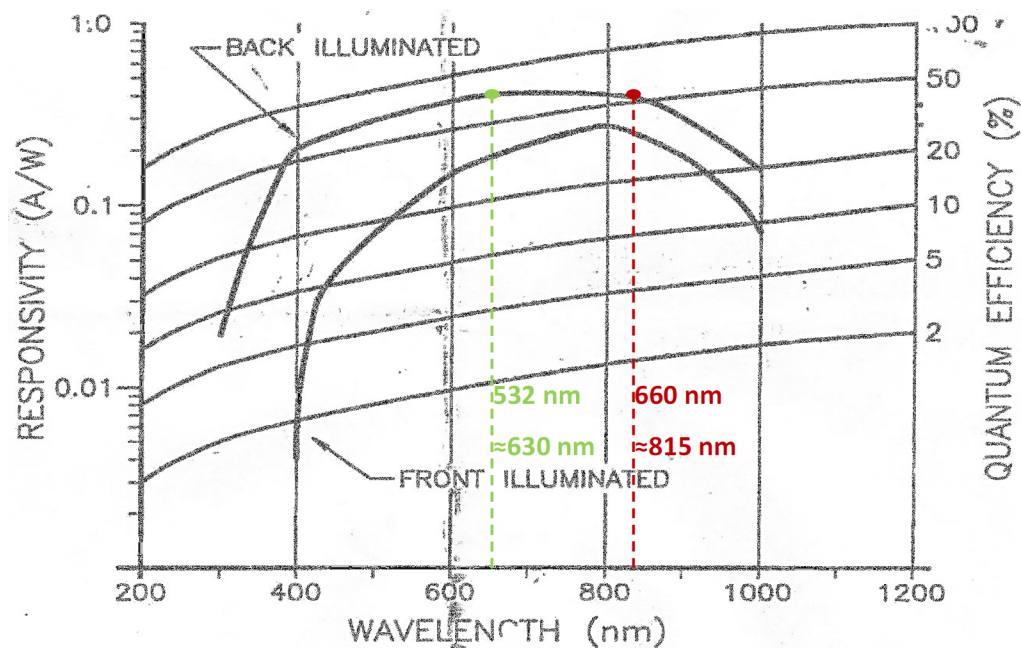
Figure 2.4: CCD quantum efficiency showing stokes shifted light at $2900\,\mathrm{cm}^{-1}$ Raman shift (C−H bands) for $532\,\mathrm{nm}$ and $660\,\mathrm{nm}$ marked. Adapted with permission from reference 153. Copyright 1993 Princeton Instruments Inc.

outside of the optimum spectra range greatly reduces efficiency.

When we acquired the spectrograph, it did not have the original driver electronics, so we had to design and construct a circuit and program to control the grating movement. This was a considerable amount of work as no detail of the hardware's pin-outs or design was available. Special thanks must go to Barry Barker in our electronics workshop for building a replacement controller. The spectrometer itself had four stepper motor windings, two optoswitches that were positioned to monitor when slits on two wheels (connected by a worm gear) did not obstruct the beams from two infra-red light emitting diodes (LEDs). Both optoswitches were pulled high when the beam was unobstructed, which corresponded to grating one being in the M_0 position, which we define as "home". As these optoswitches generated light (LED), they had to be disabled when not in use (the CCD could detect the light they emitted).

The spectrometer was controlled using LabVIEW from National Instruments (NI). The program's graphical user interface (GUI) can be seen in figure 2.6. This graphical programming language controlled a NI PCI-6024E interface card (see figure 2.7 for a full description of the card connections). This card had sixteen 12-bit analogue inputs, two analogue outputs, eight digital inputs or outputs, and two 24-bit counters or timers. The timer was used to generate the pulses to trigger the stepper motor driver board (see appendix A.1) which moved the spectrometer grating. One analogue input was connected to an Analogue Devices AD8495 thermocouple board (circuit digram in appendix A.2), connected to a type K thermocouple which recorded the temperature of the heating/cooling water leaving the cell. The digital input/outputs (I/O) controlled the laser shutter, triggered the CCD camera, and controlled various inputs on the stepper motor driver such as direction, enable drive, enabled half-step and quarter-step (which
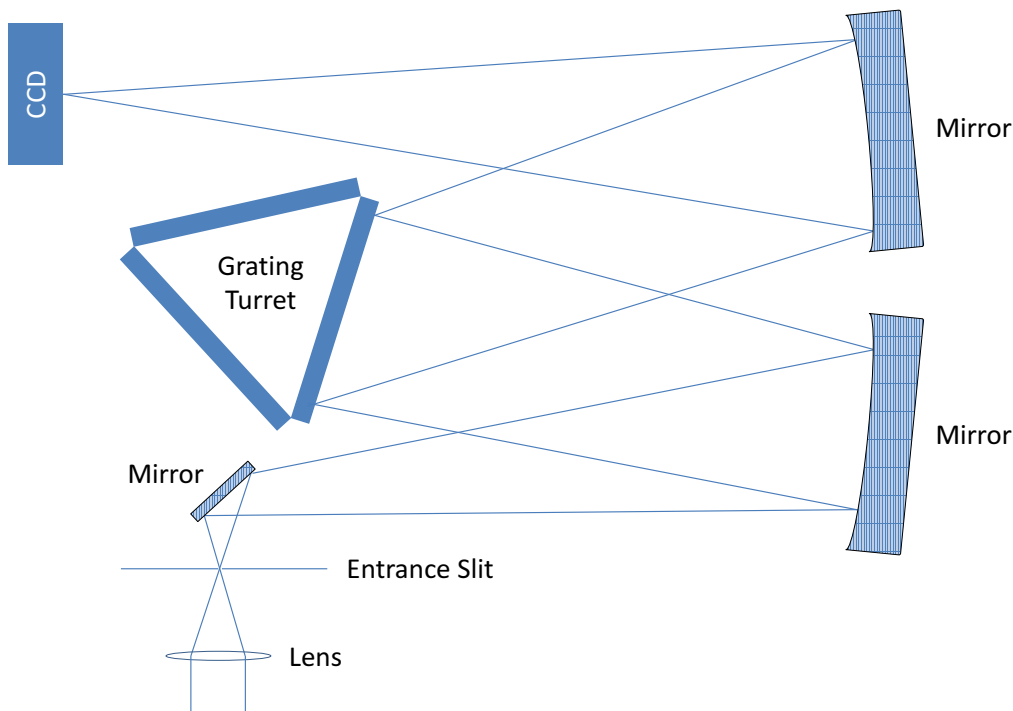
Figure 2.5: Spectrograph schematic (Czerny-Turner design)

when both pulled high, represented eighth-step) modes. The digital inputs monitored the optoswitches. The card was also connected by coaxial cable to two ThorLabs MFF101/M, motorized filter flip mounts, originally designed so that the polarisation entering the spectrometer could be selected remotely, however we never purchased the $\lambda/2$ waveplate or polariser as most of the experiments used unpolarised $(x+y)$ light. The achromatic waveplates that would be needed (due to using both 532 and 660 nm) were also very expensive and the efficiency of commercially available plates would have been poor for 660 nm use. The motorised flippers were instead used to control an ND3 filter in the laser(s) path (used to lower the intensity of the beam to below eye-safe levels ($<1\,\mathrm{mW}$)) and an ND1 filter before the CCTV camera (useful for alignment to prevent saturation of the image sensor). Grounding for the I/O connections was made to the nearest available terminal. The LabVIEW program also controlled the syringe pump (recording volume) via RS-232, electronic rotation stage via USB, and both lasers via RS-232 (recording power).

2.2.3 Experimental Operation

The preparation and general use of the cell and spectrometer for kinetic experiments is covered in section 3.3. This section describes how the spectrometer was programmed and used.

Upon pressing 'go', the control computer signals the syringe pump to start pumping solution through the mixer and into the cell, and simultaneously starts triggering the CCD. The current values for time offset of each trigger pulse (from t=0), the volume added, laser power, and temperature are recorded to a comma separated value (CSV) file. The spectra are recorded separately on the CCD computer (attempts were made to get

Figure 2.6: LabVIEW control program GUI
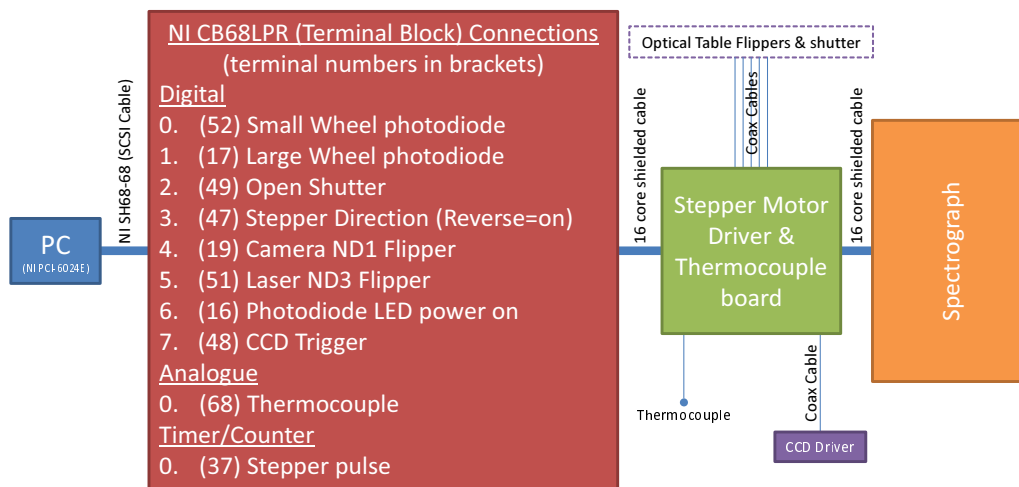
Figure 2.7: Controller wiring schematic

the CSMA program to output the values via RS-232 as they were acquired, but this was deemed too complicated). The CSV filename was appended with the name of the file on the CCD computer (SPE file), normally the day of the month, month and experiment number of that day. The FAT16 file system used by MS-DOS could not handle file names longer than eight characters (excluding extension), or spaces. An example filename for the 3rd experiment taken on 12th June is '12-6-3.SPE'. SPE file are proprietary Princeton Instruments binary files which could be read by a MATLAB script or exported as CSV files.

A single 5 s exposure was selected for kinetic measurements using the in-line mixer, gave a good signal to noise ratio, did not saturate the detector, and was fast enough to monitor the relatively slower changes in concentration. Kinetics measurements used 1 s exposures to maximise time resolution. For single static measurements, a 30-second exposure, accumulated 10 times and summed to give 300 s total exposure.

When the required number of acquisitions are complete, Microsoft Windows 3.11 was loaded and the data compressed into a ZIP file (using WinZIP) with other data sets and transferred from the CCD computer to the control computer via a RS-232 null modem cable using the Kermit transfer protocol and the HyperTerminal program. The SPE files generated by CSMA are extracted and then combined with the CSV files using MATLAB (*mySPEreader.m*, see appendix B.1) and saved as an array for further processing.

To begin processing, anomalous (dead) pixels were removed. The first (1) and last (512) pixels always read high, so these were equated to their adjacent pixel. Target spectra are generated from the highest concentration solution experiment in the set. An average of the first 15 sequential spectra is used to generate a target spectra of water. The final 15 spectra are used to generate a target spectra of surfactant, by subtracting the initial water, multiplied by a scalar to accommodate any drift in water background. An average is taken of all the spectra to locate dead pixels (lower in intensity) on the CCD and the values in these pixels are replaced by the mean of intensity from the two adjacent pixels. Cosmic rays are removed using the *removeCosmicRaysFromTimeSeries.m* program (see appendix B.1) written by David Woods.[1] The program searches for and removes the highest points which are likely to be cosmic rays. The pre-processed data was then viewed in its raw form then input into the factor analysis program, *ADProcesskinetics.m*.

Laser and Optics

The 532 nm laser was a 2 W continuous-wave (CW), frequency-doubled, diode-pumped Nd:YVO$_4$ laser (Spectra-Physics Millennia II). The 660 nm laser was a 1 W CW diode-pumped, solid state laser (Laser Quantum Ignis 660). Laser selection was performed using a manual flip mounted mirror, in addition to selecting the laser in the LabVIEW software. Both lasers were aligned co-axially, with only a small change in delivery lens focus (due to the change in wavelength), and minute changes in spot position required when changing between lasers. Both lasers were fully controllable via RS-232 from the LabVIEW program. After the flip mount, the beam passed through an ND3 filter mounted in electronic flipper and then the beam shutter, both of which were controlled by LabVIEW. The ND3 filter reduced the beams to eye-safe levels (<1 mW) for alignment. A manual cut out switch for the shutter was provided for safety, and the lasers' own interlocks were also incorporated

into the lab's door interlock control system whereby all lasers cut out if an unauthorised person entered. The beam then passed through two lenses to expand the $\approx 1\,$mm beam to approximately $3\,$mm–$4\,$mm, through an alignment iris and then the $\lambda/2$ Fresnel rhomb (ThorLabs, Germany) mounted on a electronic rotation stage (PRM1/MZ8, ThorLabs, Germany). The Fresnel rhomb retarder is used as it provides an achromatic method for rotating the polarisation of incident light, whereas the alternative would be to have one half-wave ($\lambda/2$) plate for each laser wavelength. Another alignment iris is placed before the final beam delivery mirror, with which the angle of incidence is set. A final lens, mounted in a translation stage then focuses the beam down onto the sample, an ellipse $\approx 20{\times}30\,\mu$m in diameter at the surface.

An objective lens (Nikon (MUE21500) 50x, $0.6\,$NA, ULWD, f=$11\,$mm) (mounted on an x, y, z stage), is focused through the hemisphere (on to the liquid-solid interface), to collect the scattered light and pass it into the spectrograph. When the scattered light is reflected 90°, it is also reflected down and then back to its original height via a double periscope assembly. These periscopes are in place to rotate the image by 90° in the optical axis to ensure that the horizontally elongated laser spot arrives vertically elongated on the vertical slit (to maximise both the amount of light entering the spectrometer and the rejection of out-of-focus light). The slit on the spectrograph was set to $50\,\mu$m using a micrometer. Two edge filters remove the unwanted Rayleigh line and the remaining light is focused through the slit into the spectrograph. This slit blocks divergent light, similar to a confocal set-up. Inside the spectrograph curved mirrors expand and reflect light onto the grating, then focus the light onto the CCD detector. A flipper before the edge filters allows light to be diverted through a lens onto a CCTV camera instead of the spectrograph for focusing, alignment and viewing of the sample surface. A second flipper before the camera flipper allows a $100\,$W tungsten microscope illuminator to deliver light to the sample for optical microscopy.

The long-pass edge filters used were the Semrock RazorEdge ultrasteep LP03-532RU-25 and LP02-664RU-25 for the $532\,$nm and $660\,$nm lasers respectively. Two identical filters were used in series to increase the blocking optical density (OD). The $532\,$nm filter had a $5.3\,$nm wide edge at $536.4\,$nm and the $660\,$nm filter had a $6.6\,$nm wide edge at $668.9\,$nm. Both filters had an OD >6 below the target wavelength.

All lenses used were 1 inch ThorLabs N-BK7 plano, spherical lenses with an anti-reflective coating for 350 to $700\,$nm. The 1 inch fused silica broadband dielectric mirrors used were also supplied by ThorLabs and optimised for 400 to $750\,$nm.

Calibration

To calibrate our own grating stepper motor we determined, by electronically counting the number of pulses for a full revolution of the grating turret ($144\,000$), that one pulse turned the grating by 0.0025°. Up to three gratings can be mounted in the spectrometer, meaning that $48\,000$ pulses are required to change grating (120°). The number of pulses to bring the M_0 reflection into the middle of the CCD (pixel 256) from the home position, for each of the three gratings was then found and recorded. From this position "snapshots" (CCD exposures) were taken after moving the grating by 115 pulses. This meant that any spectral peaks appeared in several consecutive "snapshots" which could be used to

later calibrate the spectrometer.

From the CCD manual,[152] we know that the pixel size is 2.70×10^{-5} m. From the spectrograph manual[154] we know the focal length (0.5 m). Using these values, the number of "snapshots" we have taken (to calculate the angle we have moved), and the grating ruling, we can calculate the wavelength of any angle. The angle of dispersion over the CCD, θ_d is:

$$\theta_d = \arcsin \frac{x}{d} = \frac{x}{f} \tag{2.1}$$

where f is the focal length and d is the pixel size. The grating angle from M_0, θ_g is then:

$$\theta_g = E_{n-1} \times \theta_p \times p_f \tag{2.2}$$

where E is the exposure number, θ_p is the pulse angle, and p_f is the number of pulses in the frame.

The grating equation, equation 1.33, relates the angle of incidence to the angle of a wavelength maxima. The angle the light is incident on the grating, θ_i was measured to be 34.7°, so α is:

$$\alpha = \theta_i - \theta_g \tag{2.3}$$

we can therefore calculate α, β and the spectral angle, θ_s and then the wavelength of each pixel (assuming wavelengths from diffraction orders other than one are not incident on the CCD). We then convert this to Raman shift in wavenumber using the following:

$$\Delta w = \left(\frac{1}{\lambda_0} - \frac{1}{\lambda} \right) \tag{2.4}$$

where Δw is the Raman shift in wavenumbers, λ_0 is the excitation wavelength and λ is the spectral wavelength.

To calibrate the spectrometer a mercury-argon lamp (CAL-2000, Ocean Optics Inc., Florida, USA) illuminating a white card was used. This provided diffuse light from a documented calibration emission line spectra between about 250 nm and 920 nm, which can be seen in figure 2.8.[155] We also had the use of a neon glow lamp (type used for electrical indication lamps), but this was harder to use as it was not as bright. A silicon wafer has a sharp Raman peak at $520 \, \mathrm{cm}^{-1}$ which can be used for offset correction. The silicon peak is routinely used on the Renishaw system. Many other materials could also be used for calibration. The Raman peak for acetonitrile is fairly sharp and well defined at a known $2948 \, \mathrm{cm}^{-1}$ therefore this peak can be used to further calibrate the offset of the spectrometer in the $2900 \, \mathrm{cm}^{-1}$ region.[1] Other samples measured included various polymer films such as PTFE, polyethylene and polystyrene.

The calibration lamp lines were then used to fit a 3$^{\mathrm{rd}}$-degree polynomial to our calculated spectra. The results from our calibration were one pulse $\approx$0.0025 nm.

Optical Alignment

Graph paper, with the incident and reflected beam path drawn on at the desired angle (73°), is placed under the cell. By placing a vertical rule on this line with the cell removed the incident beam alignment can be set and checked. When the hemisphere is in place
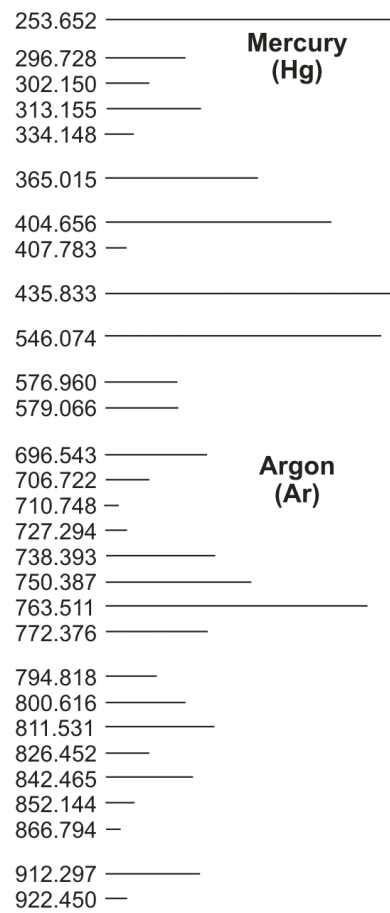
Figure 2.8: Hg-Ar calibration lamp lines. Values for wavelength in nm. Reproduced with permission from reference 155. Copyright 2009 Ocean Optics Inc.

and central (centring method described in section 3.3), the angle of the totally-internally reflected beam can be used to set the bottom of the hemisphere perpendicular to the normal. This rule, when placed along the holes of the table, also allowed the laser beam to be kept parallel with the table and the grid of lines of holes in the table kept the beam straight, or in the case of mirrors, at 90°-bends. Closing the iris before the final delivery mirror reduces the size of the beam and makes it easier to measure the laser spot's position.

Using the back reflection off lenses and filters it is possible to align these optics perpendicular and central to the optical axis. This is important to minimise aberrations. The back reflection can be viewed by placing a card (business card) close to the incident beam, and adjusting the position of the optic until the back reflection passes back down the optical axis.

A bypass mirror, located before the telescope, allows the collimated laser beam to be diverted through the objective (although the sample must be removed and objective rotated out the way for alignment of later components). This alignment beam is used to focus and align the collection optics. Conveniently the use of two lasers allows the alignment to be checked throughout the spectrograph, even with the edge filters in place (normally the filters would block the laser light). Care has to be taken to ensure the use of ND filters and/or low power so as not to damage the filters, slits or CCD.

The final lens is mounted on an x, y, z translation stage to allow the Raman light to be focused tightly through the entrance slit of the spectrograph. The lens and slit are aligned by placing a card just after the slit or at the grating while adjusting the lens' position until the maximum amount of a circle of light passes through the slit. The slit width is decreased iteratively and the lens adjusted again until lens movement in any direction cuts the light passing through. If the slit is too wide then the spectrum background is likely to be higher as divergent light from out of focus parts of the sample will reach the detector. Final adjustment is made by taking repeated spectra and noting the intensity and full-width-at-half-maximum (FWHM) while making small iterative adjustments.

A silicon wafer can be used to check the alignment of the collection optics, spectrograph and CCD. The peak at $520\,\mathrm{cm}^{-1}$ is bright and sharp so it is used to make final corrections to the calibration offset. The CCD is focused on its stage to obtain the maximum signal at the minimum FWHM. The height of the CCD is also adjusted so that the spectrum hits the middle of the chip, while minimising the number of dead pixels due to the age of the CCD.

The CSMA software controls which pixels are "binned". To select the area the whole chip is exposed, then using the cursor the region of interest is selected. By selecting the correct number of rows we minimise the noise and maximise the signal.

After calibration and alignment was complete, the whole system—minus spectrograph and CCD—were boxed-in, using extruded aluminium posts and $5\,\mathrm{mm}$ thick sheets of black plastic. Holes were cut in these sheets, where necessary, to access optomechanics such flippers, micrometers and irises, and allow the cell to be removed. These holes were then covered with removable additional plastic sheets, which overlapped all edges by $10\,\mathrm{mm}$. $10\,\mathrm{mm}$ magnetic tape was then applied to both sides to hold the covers in place. These covers helped reduce noise (by further excluding stray light), reduced dust build-up and increased safety by confining all laser light to within the box. They also helped maintain a

constant temperature of the optics and prevent air currents disturbing the optical bench.

2.2.4 Further Improvements

By constructing our own spectrometer, we provide ourselves with the ability to modify the spectrometer as we see fit. One possible further modification which could be made would be to collect both x and y polarisations simultaneously, using a polarising beam displacement prism and a wedge to introduce a small angular deviation in one polarisation beam path. This was tested successfully with a non-polarising beam displacement prism. The two polarisations would appear as two horizontal stripes, separated by a distance related to the wedge angle. The CSMA software already includes the facility to read multiple stripes.

By replacing the beam dump for the totally-internally reflected beam with a concave mirror, we could in theory double the power at the probe region and further increase signal levels, but may require an expensive Faraday isolator to prevent back-reflected beams damaging or destabilising the lasers.

Modifying the system to perform Raman-imaging ('chemical imaging') is also a possibility. This would allow us to see if surfactant adsorption to the surface was uniform. This would initially require replacement of the manually-controlled electronic stages for cell positioning with computer controlled, indexed stages to allow for z-axis slices to be taken. The use of a pinhole, rather than a slit would improve our resolution in the x-axis (optical axis plane), but lower throughput. We would also need to replace our grating with a variable filter, such as a Fabry-Pérot etalon. These etalons utilise two facing reflecting surfaces to create a resonant optical cavity which filter out unwanted wavelengths by destructive interference of the multiple reflections. Etalons can reduce efficiency however and are expensive. Raman-imaging is typically very slow however, as a full spectrum at each pixel/position is needed, hence following kinetic processes would be difficult. Our group has recently started experimenting using a fixed bandpass filter to "see" only one wavenumber (C−H stretches).

Comparison with Renishaw

To "calibrate" the Renishaw spectrometer, the $520\,\mathrm{cm}^{-1}$ peak of silicon is typically used by the software (this calibration only sets the x-axis value at one point (an offset), so is not a true calibration). Comparing the Renishaw with the new spectrometer, in figure 2.9, we can see that we do achieve higher signal levels when scaling the signal levels to the same laser power; however, as we shall discuss later, the sensitivity is not the same across all wavelengths. It is worth noting that all the spectra have been normalised to a $1\,\mathrm{s}$ exposure at $200\,\mathrm{mW}$. The spot sizes may not be exactly the same. The same objective was used for both spectrometers for this experiment.

Sensitivity is wavelength dependent, as expected since gratings are very wavelength (and polarisation) sensitive. The sensitivity seems to fall below that of the Renishaw in some regions. However, should we ever want to look at different regions at high sensitivity, it is relatively easy to install new gratings in this system (something which is not easily done on the Renishaw, with only one installed grating). The Acton spectrometer allows for selection from up to 3 installed gratings on the turret, allowing fast changeover.
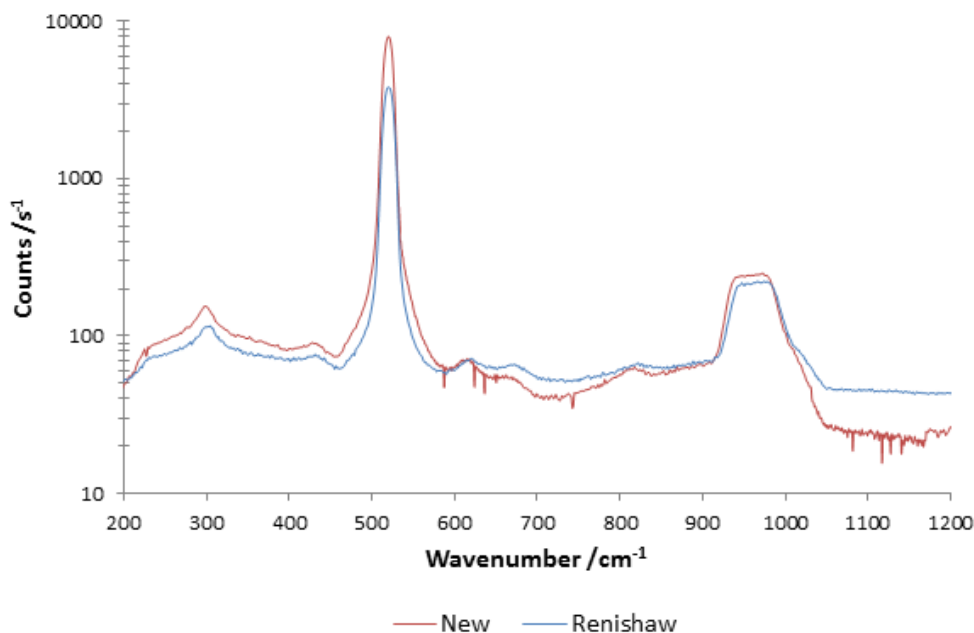
Figure 2.9: Spectrum of silicon wafer taken on both spectrometers, normalised to 1 s at 200 mW, 532 nm

To further test the efficiency and calibration, a few polymers were examined under the spectrometer microscope. The silicon sample only has relatively low wavenumber peaks, compared to where we normally look for our surfactant peaks, $\approx$2900 cm^{-1}; hence the need to find peaks in other wavenumber regions. We used polymer films to investigate these regions. Figure 2.10 shows the spectrum of PTFE which matches well with data recorded on the Renishaw. Again, sensitivity varies with wavelength. The background from the new spectrometer (for example in figure 2.10) is a strange shape because there was stray light reaching one side of the detector (it is possible to see the stitching of the spectra where the counts drop suddenly). This issue was later fixed as the dead pixel removal tool had not yet been developed.

Figure 2.11 shows the literature Raman spectrum of high density polyethylene (HDPE) which matches well with our data (figure 2.12), again signal levels vary depending on wavelength. There also seems to be high background at high wavenumber on the Renishaw, this could be due to surface contamination of the sample. The relative peak intensities of the two peaks at around 2845 cm^{-1} to 2875 cm^{-1} do not match well; this is probably due to the film being orientated differently between the two measurements.

Figure 2.13 shows a spectrum of a polyester (PE) sheet taken on both spectrometers. The signal levels are lower in this spectrum, compared to the previous spectra, however it is common for signal levels to vary on the existing set-up, mostly dependent on the (highly sensitive) position and focus of the excitation beam—to optimise the alignment when using the cell we take a 1 second acquisition and adjust the alignment to obtain $\approx$1500 counts s^{-1} on the water background maximum, when the spectrum is centred at 2900 cm^{-1} and while using a plain silica hemisphere. We can use the water intensity to ensure alignment on the new spectrometer is optimised, in the same way.
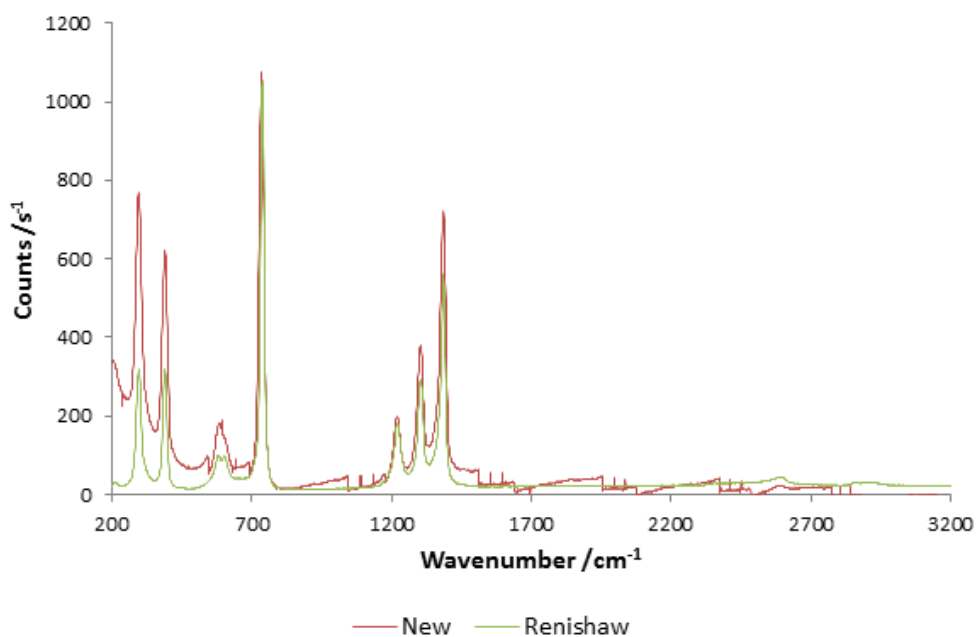
Figure 2.10: Spectrum of PTFE sheet taken on both spectrometers. 200 mW, 532 nm
.
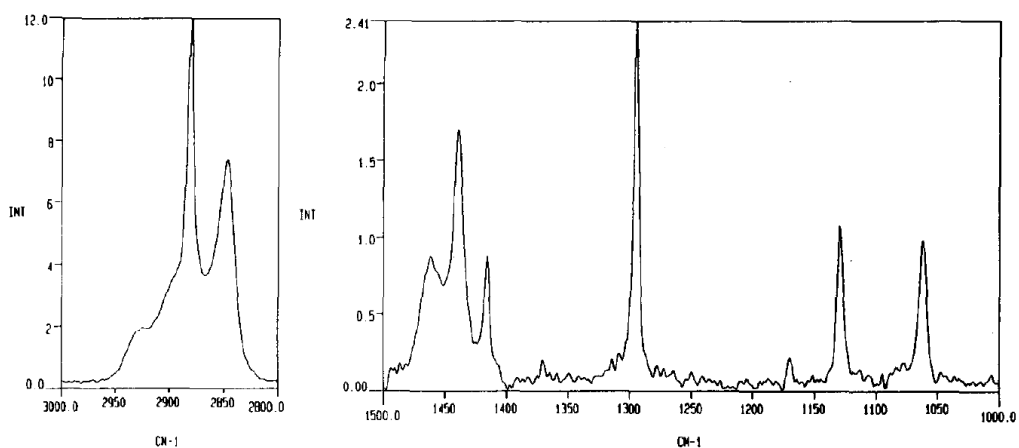
Figure 2.11: Literature spectrum of HDPE. Reprinted with permission from reference
156. Copyright 1995 Elsevier
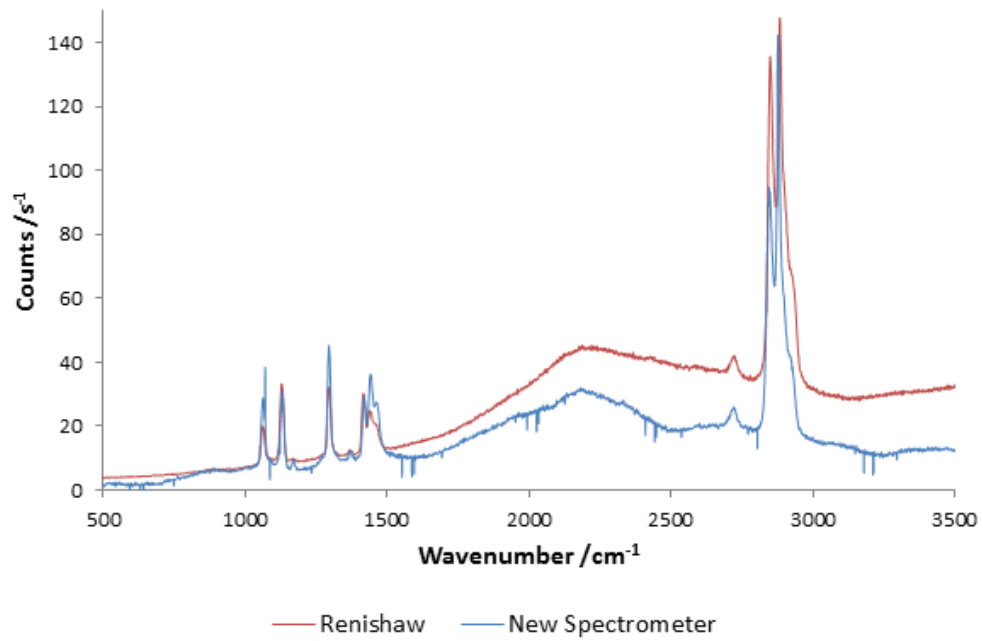
Figure 2.12: Spectrum of HDPE sheet taken on both spectrometers. 200 mW, 532 nm
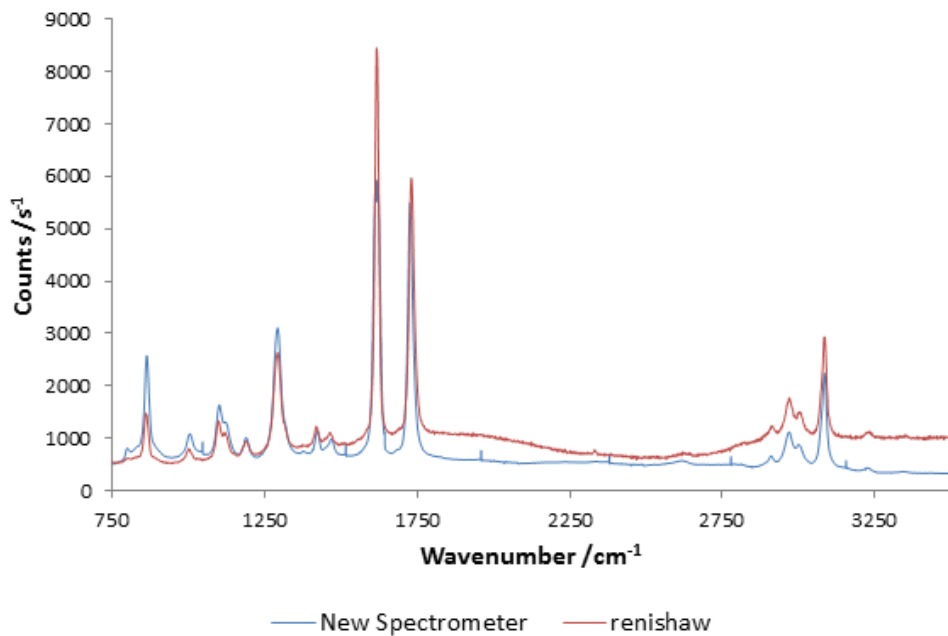
Figure 2.13: Spectrum of polyester sheet taken on both spectrometers. 200 mW, 532 nm

It is worth noting that the above samples are very thin sheets of film, making it hard to use high powers (which burn a hole in the sample), and they are hard to focus on since small air currents cause the substrate to move. This may also be the cause of the relatively high background (already subtracted) in the Renishaw spectrum in figure 2.13.

These extended scans can be performed on the new spectrometer, but are not very efficient (they require a lot of post processing to "stitch" the individual spectra together). Little further work was done to try and optimise the process since all our later experiments required short, repeated exposures where there was not enough time to move the grating, and the area of interest (such as the $C-H$ stretching region at around $2900\,cm^{-1}$) was small. Therefore, spectra did not need "glueing" together often. The Renishaw uses a different extended scan method (rather using stitching) where, we presume (undocumented), the CCD charge is read out in waves while the shutter is open and the grating is moving. This will require direct programming of the CCD, since it is not currently possible to control the shutter using the default program. This could be done in theory, but again, given our applications, is not worth the time.

2.3   Conclusions

Overall, we have designed, built, and commissioned a spectrometer which is more flexible and adaptable than its modified commercial predecessor. Signal levels are comparable to the existing Renishaw system. The simple change in rotating the cell by 90° has greatly improved result reliability, as we will see for the results later, as bubbles on the Renishaw system were the cause of many failed experimental runs. Readout time has been greatly reduced from $1\,s$ to $<400\,ms$ allowing us to follow kinetics with a higher time resolution. The stability of the system has been improved from minutes–hours to often more than a day, minimising alignment time and improving operator efficiency.

The ability to adapt and modify the system means that it can easily be optimised for different purposes, such as dual polarisation read-out, discussed earlier. One later use at the end of my PhD was for studying the gas adsorption to, and reactions on catalysts. The spectrometer was also used to follow the photo-polymerisation of styrene.

Chapter 3

Experimental Details

3.1 Sample Preparation

The following sample preparation techniques were used.

3.1.1 Cleaning

All experiments required stringently clean equipment, both to avoid contamination which would affect experimental results, and to ensure maximum signal could be obtained. Blue powder-free nitrile gloves were worn when handling anything toxic or when there was a risk of contamination from skin oils onto optics or items in contact with surfactant solutions.

All ultra-high purity (UHP) water used during the experiments was from a Milli-Q Gradient A-10 (Merck Millipore, Merck KGaA, Germany) water purification system fed by a Millipore Elix reverse-osmosis system. The conductivity of the water was $>18.2\,\mathrm{M\Omega}$ at $25\,°\mathrm{C}$ and the total organic carbon concentration was $<10\,\mathrm{ppb}$ (both measured by the Millipore system).

The cell, all glassware, attached pipework, o-ring, and valves were cleaned by immersing them overnight in 2–5 % vol. Decon 90 in an UHP water solution. As the Decon is alkaline, it etches glass, so sensitive items were not left in strong solutions for longer periods of time. These sensitive items (particularly volumetric flasks, to minimise the etching of the graduation marks) were cleaned with 5 % Decon 90 for 15 min by sonicating them in a water bath at $50\,°\mathrm{C}$.

The hemisphere was cleaned overnight by covering it with chromosulphuric acid (2–5 % $Na_2Cr_2O_7$ in $\approx$90 % H_2SO_4) solution purchased from Fisher Scientific. The neat chromosulphuric acid was returned to the bottle. Then the cell was thoroughly rinsed with UHP water while disposing of, at least the first three, water rinses as aqueous heavy-metal waste (after later reduction with thiocyanate and neutralisation with sodium carbonate). Between surfactants or experimental runs the assembled cell was rinsed with HPLC grade methanol then UHP water and checked for cleanliness in the spectrometer before use (C−H contamination would be visible in the spectrum if unclean). Anti-scratch coated metal, or plastic tweezers were used when handling the hemisphere and o-rings.

All bench optics (mirrors, lenses, prisms *etc.*) were carefully cleaned first (and

occasionally during their use) to remove dust with compressed purified inert gas, then if necessary, with a fine optical grade lens tissue wetted with HPLC grade methanol or isopropanol (propan-2-ol). First a drop-and-drag method was used then, if this was unsuccessful, forceps used to slowly drag a tightly-folded, wetted lens tissue across the surface. Gloves were essential when handling optics.

3.1.2 Recrystallisation

Recrystallisations were carried out by fully dissolving the sample in a minimum amount of hot solvent using a reflux apparatus to minimise solvent loss. The solution is then left to cool slowly to room temperature, followed by placing in a freezer to ensure complete crystallisation. The solute was removed by vacuum filtration and the filtrate was washed with ice cold solvent to remove remaining impurities while avoiding loss of the pure sample. The recrystallisation was repeated to further increase purity. The process uses a solvent that the product is sparingly soluble in, but impurities are highly soluble. Slow cooling minimises co-crystallisation of the impurities with the product.

3.1.3 Surfactant Samples

The surfactants used along with useful data are listed, in summary, in table 3.1. Supplied purities, where available, are provided.

C_nTAB

C_nTABs purchased from Aldrich, where n=12, 14, 16 were recrystallised three times from acetone and ethanol then left to dry overnight in a vacuum desiccator. $C_{18}TAB$ was used as received.

SDS

Sodium dodecyl sulphate (SDS), purchased from Sigma-Aldrich, was recrystallised twice from ethanol and left to dry overnight in a vacuum desiccator.
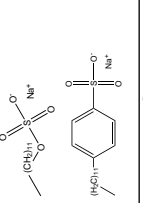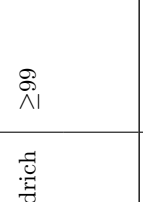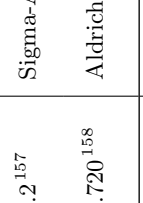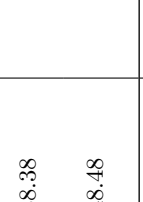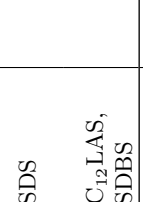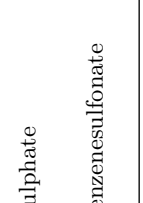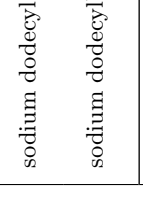
C_nE_ms

Polyethylene oxide alkyl ethers of the form (C_nE_m, where n=12, 14, 16 and m=5, 6, 8), purchased from Sigma-Aldrich, were used as received.

3.1.4 Solution Preparation

The required quantity of surfactant was weighed in a Decon-cleaned glass weighing scoop, then rinsed and dried using a Kimwipe before use on a Mettler Toledo AG135 mass balance, accurate to 0.01 mg. Nitrile gloves were worn throughout the process. The surfactant was then transferred to a Decon-cleaned volumetric flask and UHP water added to rinse the remaining solid into the volumetric flask to maximise transfer. The solution was sonicated for 15 min at room temperature (with the exception of $C_{18}TAB$, which has a Krafft temperature of approx. 38 °C and so was sonicated at 50 °C).

Table 3.1: List of and data for surfactants used

Name	Aliases	RMM/(g mol^{-1})	CMC/mM	Supplier	Purity/ %	Structure	Type
sodium dodecyl sulphate	SDS	288.38	8.2[157]	Sigma-Aldrich	≥99		Anionic
sodium dodecylbenzenesulfonate	C$_{12}$LAS, SDBS	348.48	0.720[158]	Aldrich			Anionic
pentaethylene glycol monododecyl ether	C$_{12}$E$_5$	406.6	0.05[159]	Fluka	≥98.0		Nonionic
hexaethylene glycol monododecyl ether	C$_{12}$E$_6$	450.65	0.089[159]	Fluka	≥98.0		Nonionic
octaethylene glycol monododecyl ether	C$_{12}$E$_8$	538.75	0.08[159]	Sigma	≥98.0		Nonionic
octaethylene glycol monotetradecyl ether	C$_{14}$E$_8$	566.81	0.01[160]	Fluka			Nonionic
hexaethylene glycol monohexadecyl ether	C$_{16}$E$_6$	506.76	0.0017[161]	Fluka	≥99.0		Nonionic
dodecyltrimethylammonium bromide	C$_{12}$TAB, DTAB	308.34	15 [162]	Sigma	≥98		Cationic
tetradecyltrimethylammonium bromide	C$_{14}$TAB, MTAB, TTAB	336.39	4 [162]	Aldrich	≥99		Cationic
hexadecyltrimethylammonium bromide	C$_{16}$TAB, HTAB	364.45	1 [162]	Sigma	≥99		Cationic
octadecyltrimethylammonium bromide	C$_{18}$TAB	392.51	0.34[163]	Sigma	98		Cationic
dihexadecyldimethylammonium bromide	DHDAB, (C$_{16}$)$_2$TAB	574.85	0.078[164]	Tokyo Chemical Industry	>97.0		Cationic

DHDAB Bilayer Preparation

Dihexadecyl dimethylammonium bromide (DHDAB) was supplied by Tokyo Chemical Industry (UK, Oxford) and recrystallized twice from ethyl acetate and twice from acetone (working with our summer project student Joe Beckwith). Further scoping work to determine which surfactant to use and initial work on the Hofmeister Effect was performed by Harris.[38] For the later study with Lambert[165] on Hofmeister series, the purified surfactant was added to degassed UHP water and sonicated for 90 min at 40 °C. The water was degassed by applying a vacuum to the liquid in a Schlenk flask, while in a sonicating bath, for 15 min. The pump is protected by a liquid-nitrogen trap. The elevated temperature was required when dissolving the surfactant as DHDAB has a liquid-crystalline-to-gel phase transition temperature of 28 °C.[166] The degassing helped to eliminate bubbles which could destroy the bilayer. Solutions of 1 mM were used, as this is well above the CMC of 0.078 mM,[164] ensuring that bilayers will form, but not too high that complicated aggregate structures will be formed. The solution was pumped into the cell while taking care to remove any bubbles and left at 35 °C to equilibrate overnight. Experiments with salt solutions were added at 35 °C to avoid transition to the gel phase.

Gel to lamellar phase transitions were measured by monitoring the ratio of the anti-symmetric (d^-) to the symmetric (d^+) methylene stretch peaks in the surfactant Raman spectra. This gave a ratio, d^-/d^+ , where the higher the ratio, the more ordered and gel-like the layers were, at low temperature. The phase transition temperature was indicated by a sharp change in this ratio.

3.1.5   Hemisphere

The hemispheres were made from fused silica and were 10 mm in diameter, supplied by Global Optics UK Ltd.

3.1.6   Flow Cell

The wall-jet flow cell was designed by Eric Tyrode and made by our departmental glass blowers. The cell schematic is shown in figure 3.1 and a photo of the cell with hemisphere (without clamps) is shown in figure 3.2. The design includes a glass envelope through which temperature controlled water supplied from a Grant LDT6/120 recirculating water bath was connected. The temperature of this water leaving the cell was monitored using a thermocouple and recorded with each acquisition throughout the experiment using the LabVIEW program.

The cell had a volume of ≈6 ml and was sealed by pressing, with a clamp, the hemisphere against a ∅10 mm Viton o-ring supplied by Cole-Palmer. The glass inlet tube is ∅≈2 mm and ends ≈0.7 mm (varies depending on clamp pressure on the o-ring) below the surface of the hemisphere. A plastic ∅3″ circular clamp, produced by our departmental mechanical workshop, held both the cell and the hemisphere and served as an adapter so the assembly fitted in a ∅3″ optical mount from ThorLabs, Germany. This was mounted on a post connected to a plastic (male) dovetail, for easy removal and repeatable positioning in the microscope where an aluminium (female) dovetail was positioned on a 3-axis stage. This was the design also used by Woods.
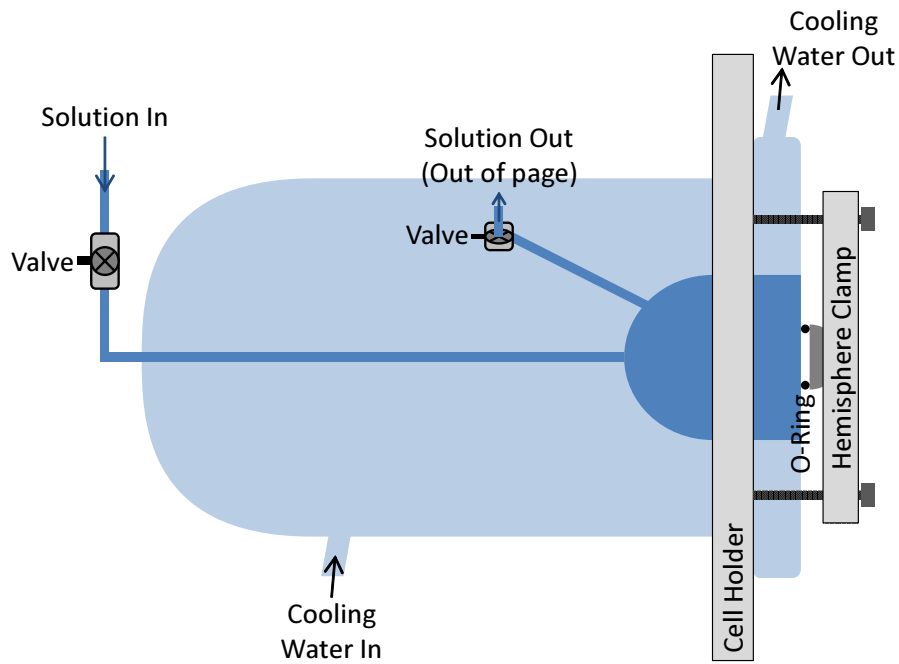
Figure 3.1: Schematic of cell and clamp (not to scale)

The cell is axially symmetric and using the glass inlet tube, we assume there is Poiseuille flow at the exit, so the flow is steady ($\delta/\delta t = 0$) and along the z-axis ($v_r = v_0 = 0$). The velocity distribution is parabolic with respect to r and the flow is fully developed ($\delta v_z/\delta z = 0$). We also assume the concentration of the solution in the tube is uniform. At the hemisphere surface a no-slip boundary condition applies $v_{z=0} = 0$. This results in the mass transport equations reducing to a one-dimensional form along the axis of the tube ($r = 0$) which simplifies mass transport modelling. We discuss these assumptions in more detail in chapter 4.

Figure 3.2: Photo of cell with hemisphere resting on o-ring (no clamps)

3.2 Substrates

The substrate coatings were prepared as follows:

3.2.1 Hydrophobic Silica

The silica hemisphere was made hydrophobic by exposing it to hexamethyldisilazane (figure 3.3) 98 +% (Alfa Aesar, UK) overnight in a dry desiccator purged with nitrogen at room temperature, followed by a UHP water rinse.
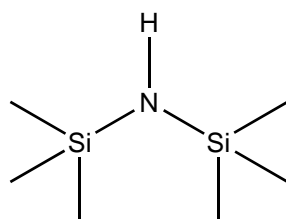
Figure 3.3: Hexamethyldisilazane structure

3.2.2   Zeolite, Kaolinite, Polyester and Haematite

The methods for coating the hemisphere with thin films of zeolite, kaolinite, polyester and haematite are described later in their individual sections in chapter 6.

3.3   General Method

The following method was used with both spectrometers, the only difference being the lack of computer control for the syringe pump with the Renishaw system, so the pump was started manually.

The syringes, two 50 ml SGE Analytical Science syringes were connected via a luer-lock to PTFE tubing of about $^1/_{16}''$ inner diameter, purchased from Cole-Palmer. This tubing was connected to a 3-way valve which allowed flushing of air from the system via a by-pass outlet when changing syringes. The other port on the 3-way valve was connected to the in-line mixer described in section 4.2. The outlet from the mixer was connected via the PTFE tubing to the cell via a valve. Finally on the outlet of the cell a valve was connected to a short length of tubing where waste water could drip into a glass bowl which was emptied when full. The connectors and valves were made by Omnifit and were all for 1.5 mm OD tubing.

To begin, one syringe was filled with the surfactant solution of interest and the other with UHP water. The surfactant syringe was placed into a Harvard Apparatus 11plus syringe pump which was connected by RS-232 to the control computer to allow for remote control and monitoring. The pump has a rated flow rate accuracy of $\pm 0.5\,\%$. The syringe was kept at the same temperature as the cell by surrounding it with a copper sheet to which 2 mm internal-diameter copper pipe was braised. This copper pipe was connected to the recirculating water bath circuit.

The cell was filled with the starting solution slowly from a syringe while holding the cell so that the outlet was at the highest point in order to purge any air from the system. As mentioned above, between different surfactants, the cell was rinsed with water, then methanol, followed by another water rinse to remove any surfactant residue. The cell was then installed on the dovetail mount and pipework was connected.

The pump's pusher was manually slid to near the syringe plunger and then the pump was driven at high speed while the valve directed fluid to a by-pass line to allow for any air and existing fluid in the line to be expelled. This also ensured that any gap between the pusher and plunger was closed so that, upon hitting "go", fluid immediately started flowing (t_0). The delay time for fluid to flow along the pipe to the cell was first measured roughly by watching the meniscus in an empty pipe and then further refined using a solution of acetonitrile in water. Assuming parabolic flow through cylindrical tubing, the velocity in the centre of the cylindrical pipe will be double that of an empty tube (plug flow). This neglects any diffusion in the pipe. This method gave a delay time of 154 s at $0.5\,\text{ml}\,\text{min}^{-1}$ with the original $1/16''$ tubing and the in-line mixer in use. For the shorter pipe, the delay was 102 s. Delay times were scaled with pumping speed when required. After purging the line, the 3-way valve was set to connect the syringe and cell. The lamp was then turned on and mirrors flipped so as to illuminate the sample and view it with the CCTV camera on screen. We then needed to find the centre of the hemisphere (described

below). The valve was set before finding the centre, as the process was likely to shift the position of the cell. Uncertainty in the offset will affect our predicted concentration. The volumes of the mixers were calculated by subtracting the mass when empty from the mass when full of water.

To find the centre of the hemisphere, an iterative process was used. The hemisphere was first moved roughly in line with the objective by observing the light passing through the objective. The cell was moved away, around 1.5 cm from the objective, so that to focus on the surface, the cell had to be moved towards the objective (this was to ensure the first object to come into focus was the "top", curved surface of the cell.) The centre of the hemisphere could be estimated by moving the cell (z-axis) until the top surface was in focus, then moving the cell around in the x and y directions until the surface lost focus. The cell was then moved further away from the objective (z-axis) and the above process repeated until movement in either x or y axes passed through the focal point. This is (approximately) the centre, as the surface is curved, so movement in the two axes results in the surface "falling away" from focus. After finding this point the cell was then moved approximately 0.5 cm (the depth of the hemisphere) in the z-axis, until the "bottom" (flat) surface came into focus. Some fine adjustment of the position, in each of the x and y axes was then needed, to find a 'bright spot'. This spot was the result of a reflection and focusing of the illuminating light back from the curved top surface, which, if the flat surface of the hemisphere was perpendicular to the incident light, was the centre. Depending on how accurately the hemisphere was cut in half (from when it was initially formed as a ball lens) the exact focus of the reflected light and the bottom surface may reside at slightly different depths (trial and error needed to find both). The bottom surface was often difficult to see, especially for uncoated hemispheres as the contrast was poor. Levelling of the cell was performed by measuring the height of the TIR beam and its position above the graph paper using the vertical ruler. Observing the laser spot reflecting on the surface sometimes aided the final focusing of the interface as the reflected spot formed a sharp image when the surface was in focus.

After finding the centre, and focusing on the bottom surface, the laser shutter was opened (and ND3 filter inserted for safety) and small adjustments were made to the delivery mirror to centre the laser spot in the image. Focusing of the delivery lens to obtain as small a spot as possible was also carried out (although if this had been done previously, very little adjustment was needed—the focus was stable for several months). When satisfied with alignment and focus, the illumination and CCTV mirrors, and ND filters were removed, safety covers installed, and laboratory lights extinguished, the experiment was ready.

The experimental details were then entered into the software program. Normally the file name was used to identify the conditions used, for example *"S 700mW 55mM C12TAB in 73Deg 25C 2900cm-1 0.5ml min-1 12-08-2.csv"* translates, in order, to: S-polarised light, 700 mW laser power, 55 mM solution, using C_{12}TAB, "in" experiment, 73° angle of incidence, 25 °C recirculating water bath set temperature, 2900 cm^{-1} spectral centre and a pumping speed of 0.5 ml min^{-1} (and, only for the new spectrometer, the spectral data was stored in the file '12-08-2.SPE'). A set temperature of 25 °C on the recirculating water bath corresponded to (24 ± 1) °C at the cell.

Upon pressing "run program" (or start acquisition for the Renishaw system) the

shutter opened, the CCD began the pre-programmed set of exposures and the pump was started, simultaneously, and continued to run until the experiment was complete (or aborted). During acquisitions the live spectra were displayed on screen allowing for the monitoring of progress (for example to watch for focal drift). Again, typically exposure times of $5\,\mathrm{s}$ were used for isotherms using the mixer, and $1\,\mathrm{s}$ to $5\,\mathrm{s}$ exposures for the kinetic measurements. For the new spectrometer an email was sent on completion to maximise time efficiency.

Before following an "in" experiment with an "out" on the same surfactant (with and without the mixer in use) the cell was removed from its mount, emptied under gravity and then refilled until it overflowed with the solution. This was required to ensure the starting concentration was known. Care was taken to ensure no bubbles remained in the cell. No additional cleaning occurred between solutions of the same surfactant at the same concentration.

It is worth noting that we occasionally observe an anomalous insensitive last pixel at around $3235\,\mathrm{cm}^{-1}$ on the Renishaw system. We see a similar problem with the new spectrometer, discussed in more detail in chapter 2. These pixels do not affect analysis.

3.3.1 Data Processing

Data was processed using PCA in MATLAB, also discussed in more detail in chapter 2.

After processing with PCA, data is copied into Microsoft Excel where the surfactant component is normalised against the water component (background). This helps ensure consistent signal levels across experiments, as well as helping to correct for small changes in focus, laser power, or the laser spot shifting. Because we start recording as soon as the pump is started, we need to account for the offset from the length of time the solution takes to flow through the pipe and/or mixer, so this is subtracted. After obtaining a complete set of data we normalise all data in that set by multiplying the number counts by a scalar so as to match up maximum intensity of the water component weight (at $\approx 3050\,\mathrm{cm}^{-1}$) in each measurement.

To obtain the surface excess values (Γ) for our isotherms, we take one measurement at high concentration, well above the CMC. TFA provides component weights of the refined spectrum, which have no physical meaning. Above the CMC the amount of surfactant present on the surface remains constant and the only increase in component weight is from the bulk surfactant molecules present in the evanescent wave. The number of bulk molecules contributing to the spectrum is the concentration multiplied by the illuminated sample area and the penetration depth of the electric field squared. Provided the spectrum of the bulk is the same as that of the adsorbed species and we can calculate the penetration depth accurately (by assuming the laser beam is not divergent or convergent), we can estimate the contribution to the Raman spectra from molecules in the bulk by taking the gradient of the end of the component weight against concentration graph. We can then subtract this contribution from our component weight to obtain the component weight of the adsorbed surfactant. The penetration depth at $\theta_i = 73°$ is $103\,\mathrm{nm}$ for a silica/water interface. From this depth we can calculate the area and hence the surface excess in $\mathrm{\mu mol\,m}^{-2}$.

Chapter 4

In-line Mixer

4.1 Introduction

The in-line mixer was developed to increase the number of data points (increased concentration resolution) in isotherm experiments, over our previous technique making-up separate solutions of different concentrations. This chapter deals with the design details and use of the mixer, along with the experiments performed to verify the kinetic assumptions. The mixer greatly improved time efficiency as fewer separate concentrations needed to be made-up. Woods did undertake some validation of the mixer's kinetics,[1] but further verification was required; that the equations for first order rate kinetics were correct (equation 1.43a). Additionally sometimes observations, for example slow initial increases, could not be explained by the equations.

4.2 Experimental Details

Two versions of the mixer were created (both by our departmental glass-blowers) the "large mixer" with a volume of 9.48 ml, and the "small mixer" with a volume of 3.45 ml.

Both mixers consist of a hollow glass disk with an inlet and outlet pipe ($\approx 2\,\mathrm{mm}$ inner-diameter), and contained a small ($\approx 3\,\mathrm{mm}$) Teflon-coated magnetic stirrer bar. After filling with solution (in-line with the cell pipework) and ensuring no bubbles were present, the mixer was placed in the centre of a small magnetic stirrer plate (IKA Mini MR standard, IKA-Werke GmbH & Co. KG, Germany). After turning the stirrer plate on to full speed ($\approx 1500\,\mathrm{rpm}$), the correct, free rotation of the magnetic stirrer bar was checked. It is important to check the apparatus to ensure there is minimal tension on the interconnecting pipes (which could lead to detachment and a leak) and that there is minimal vibration being transferred to the cell (which could vibrate the cell out of focus). Figure 4.1 shows a schematic of the large in-line mixer.

As explained earlier, due to the exponential change in concentration, there are fewer data points at early times because the concentration changes more rapidly at the start. Hence, for the higher concentrations during the "out" experiments and for lower concentrations in the "in" experiments, the data points are spaced further apart.

The smaller mixer was constructed to try to improve component separation: variation with concentration is exponential with a time constant of R/V, large changes in concen-
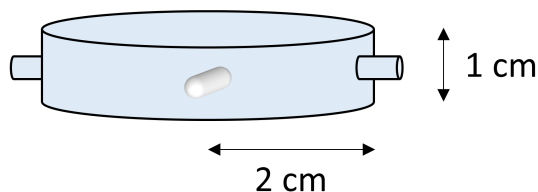
Figure 4.1: Large in-line mixer schematic, with stirrer bar, approximate external dimensions shown

tration were difficult to achieve in an acceptable time. By reducing the volume (V), the concentration changes more rapidly and the reduction in volume is easier to achieve than increasing the flow rate (R). This was a particular problem with our "out" measurements (experiments where the concentration is initially high and decreases exponentially with time), as the surfactant concentration did not decrease sufficiently for desorption to occur when high initial concentrations were used. The small decrease in surfactant signal also meant that our TFA program failed to separate components effectively as the change (drift) in the background signal was often of a similar magnitude to changes in the surfactant signal.

We also designed a static mixer which consisted of a glass envelope encasing a glass rod which had many striations cut into its surface. The idea was that these striations greatly disturbed the liquid by creating a turbulent flow which would mix the solution without any mechanical intervention. However the flow rates used (typically around $0.5\,\text{ml min}^{-1}$) were not fast enough to create the necessary turbulent flow for adequate mixing and hence concentration did not follow our first order kinetics. Additionally the roughly cut surface enhanced the alkaline Decon cleaning surfactant's ability to etch the glassware, limiting the life of the mixer.

During the in-line mixer experiments, spectra are acquired continuously, with a typical acquisition time of $5\,\text{s}$ for 600 acquisitions to give a total experimental time of around $50\,\text{min}$. The exposure time is a balance between improving the signal-to-noise ratio and minimising the change in concentration during the exposure. It is important to ensure, for the "in" experiments, that there is enough solution left to refill the cell (so that the cell can be refilled with the known starting concentration for the "out" measurement). If the "in" and "out" experiments give the same adsorption isotherms, then we can be confident that the rate of change of concentration is sufficiently slow that the surfaces are fully equilibrated. Conversely, hysteresis in the adsorption isotherms is indicative of slow kinetics. Varying the starting concentration (values of $[A]_{in}$ or $[A]_0$) allowed us to focus on different regions in the adsorption isotherm.

4.2.1 Component Separation

Complete separation of components in TFA was often an issue especially when the change in surfactant signal was small. One reason for poor separation was focal drift during long experiments. Focal drift was particularly bad on the Renishaw system, the cause of which was never conclusively determined. Often when viewed with the CCTV camera after the experiments, the whole surface of the hemisphere had drifted out of focus causing the laser spot to move to the side of the field of view (as the laser is delivered at an angle),

reducing signal levels as we are no longer collecting light from where the laser spot hits. One advantage of measurement in the $2900\,\mathrm{cm}^{-1}$ region is that component weight of the water background is obtained from processing the spectra. Loss of this background can also be observed during acquisition, as spectra are displayed live. If the loss is noted to be severe the experiment can be aborted early. If the sample remains in focus, the water component weight should remain approximately constant, as shown in figure 4.2a. The small decrease in the water component weight at the start is associated with the increase in surfactant (as we are displacing water molecules from the surface). Conversely, the water signal can be seen to decrease by over half its initial level in figure 4.2b, showing a loss of focus. To obtain the normalised surfactant component weight we divide by the water component weight at each point in time, as described in section 3.3.1.

Drift would often lead to poor separation of the component spectra. The refined spectra would look like mixtures of the target spectra. For example, figure 4.3 shows an example of the resultant water and surfactant components for $C_{14}TAB$. The water spectrum contains an amount of "surfactant" ($C-H$ bands) around $2800\,\mathrm{cm}^{-1}$ to $2950\,\mathrm{cm}^{-1}$ and the corresponding surfactant spectrum contains "water" signal (spectrum should be flat above $\approx 3000\,\mathrm{cm}^{-1}$). Peak shifts would also make analysis more difficult as we need to include more than two components in the analysis (for example peak from bulk shifts upon adsorption), which was rarely successful.

Several techniques were used to try to improve separation. First the spectral region to be used for TFA was truncated to just include the surfactant peaks around $2650\,\mathrm{cm}^{-1}$ to $3050\,\mathrm{cm}^{-1}$ and attempt to eliminate some of the water background. Second, I attempted to manually review all the spectra in the set to determine if the data only drifted towards the end of the experiment, which could often be discarded if equilibrium had been reached. Having very good target factors with intense peaks and low noise levels aided separation, so, regenerating or re-acquiring these spectra occasionally helped.

After processing, occasionally a high level of background scatter remained resulting in the baseline being offset in one of the components. To overcome this, I took an average of a flat region around $2650\,\mathrm{cm}^{-1}$ and subtracted this from all the spectra (and target spectra). This helped remove the varying baseline and sometimes improved the separation during factor analysis.

Sometimes all attempts to obtain refined spectra that did not visibly mix the target
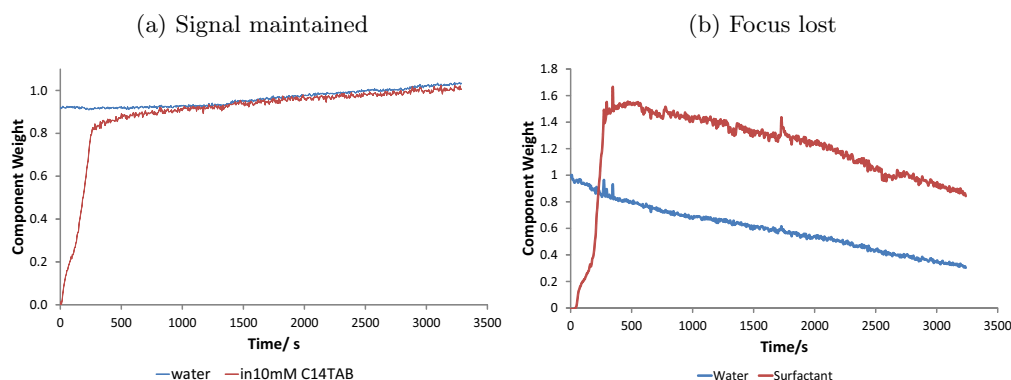
Figure 4.2: Raw component weights of water and surfactant against time showing good signal and signal loss due to drift. $1\,\mathrm{s}$ exposure, $532\,\mathrm{nm}$, new spectrometer, $700\,\mathrm{mW}$
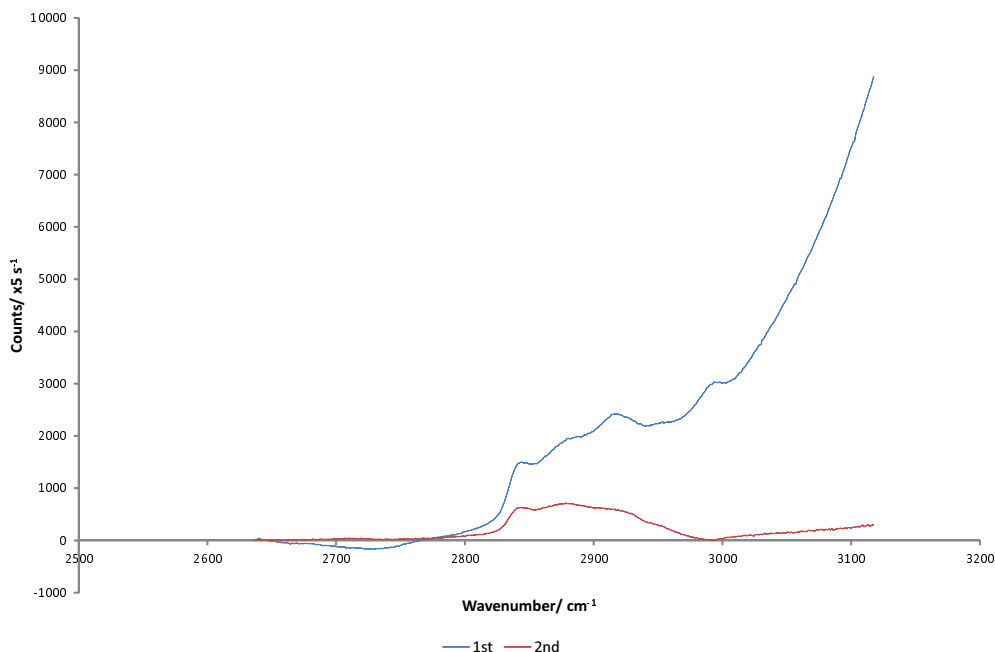
Figure 4.3: Component separation problems ($C_{14}TAB$ on zeolite) showing 1st and 2nd components of PCA, 532 nm, 700 mW

spectra failed and the experiment was discarded. It is not ideal to have a subjective visual criterion for successful TFA, but equally it is meaningless to attempt to interpret component weights which do not represent the actual components and real spectra.

When the data set was not recoverable, it had to be discarded. The new spectrometer greatly reduced the amount of drift and number of failed experiments, compared to the Renishaw system. Any anomalous behaviour within the surfactant signal also resulted in the experiment being discarded.

If the TFA separation was successful (as in figure 4.4, for $C_{12}E_5$ on zeolite—where the zeolite also produces a few small peaks in the water background at around $2925 \, \mathrm{cm}^{-1}$ and $3000 \, \mathrm{cm}^{-1}$) we can confirm this by inspecting the additional components (by viewing the results from TFA analysis (figure 4.5)). While the additional components generated (3rd and 4th) cannot just be attributed to random noise, we can suggest that the major contribution to the 3rd component could be due to a shifting background level (change in scattering from the zeolite on surfactant adsorption) and the 4th component is due to a peak shift which is often seen when comparing the spectra of bulk and adsorbed surfactant molecules.
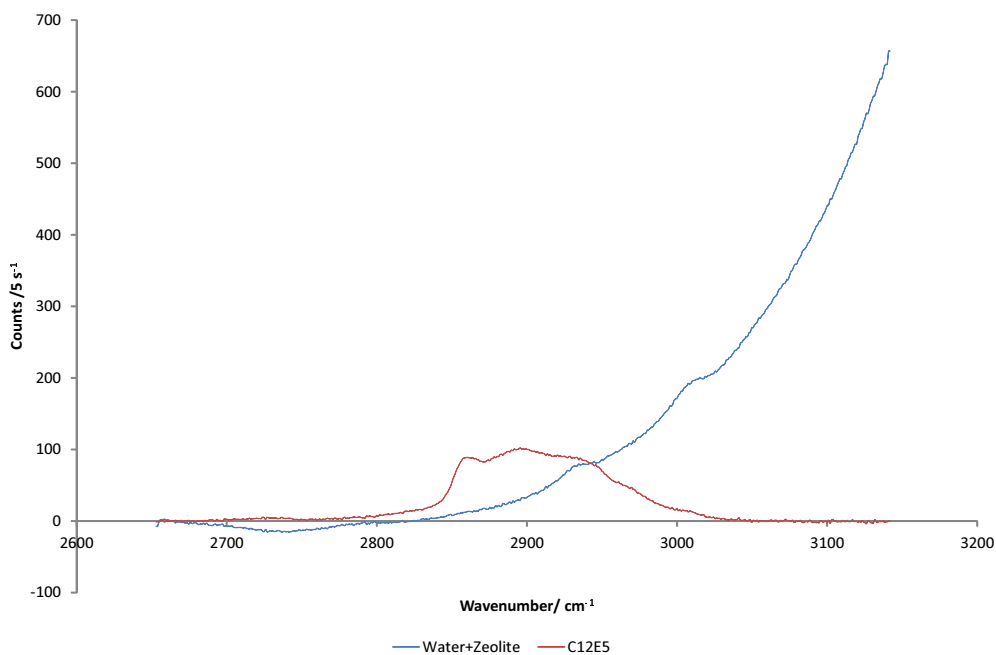
Figure 4.4: TFA components for $C_{12}E_5$ on zeolite, 532 nm, 700 mW
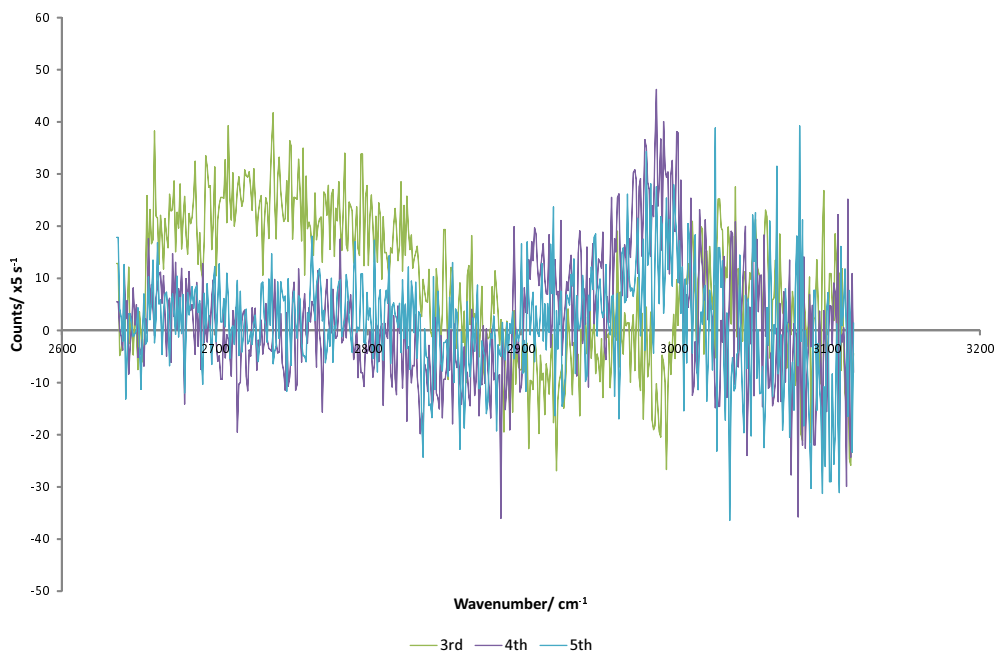
Figure 4.5: Additional (3rd, 4th and 5th) PCA components for $C_{12}E_5$ on zeolite

4.3   Kinetic Validation

To validate our assumptions that the adsorption kinetics of the surfactant to the hemisphere depended only on the concentration provided by the our in-line mixer, we performed our "in" and "out" measurements using species which were Raman active and which we did not expect to adsorb to the silica, so that we only measured the bulk concentration. Confirmation was required to check that the length of the pipe had no effect, that diffusion during pumping to the cell could be ignored and that the delay time (due to pipe length between mixer and cell) was accurate.

Diffusion coefficients for our validation solutes and some surfactants used are shown in table 4.1).

Table 4.1: Diffusion coefficients for validation solutes in water at infinite dilution. Taken from reference 167.

Solute or ion	Diffusion Coefficient (D)/ $10^{-9}\,\mathrm{m}^2\,\mathrm{s}^{-1}$	Temperature (T)/ °C
CH_3OH	1.28	15
Acetonitrile	1.26	15
Sucrose	0.52	25
$C_{12}TA^+$	0.602	25
$C_{14}TA^+$	0.573	25
$C_{16}TA^+$	0.557	25

4.3.1   Acetonitrile

To first check our assumptions for the mixer, a $10\,\%$ vol. $((4.79 \pm 0.01)\,\mathrm{mM})$ solution of HPLC-grade acetonitrile in UHP water was used for "in" and "out" measurements. The results, with our predicted concentration are shown in figure 4.6, with the components from TFA in figure 4.7. The pumping speed was $0.5\,\mathrm{ml\ min^{-1}}$ and the prediction has been scaled to the maximum component weight. Component separation was good but I did encounter a few problems whereby some acetonitrile ended up in the water component—a small amount of acetonitrile is visible in figure 4.7 in the water component and some water is visible in the acetonitrile component. The derivative shape of the acetonitrile peak could suggest a small shift in the CH_3 peak on change in concentration or a shift in the calibration.

Spectra are acquired from when the pump starts. The delay or lag-time in the pipe before the solution reaches the cell is calculated; and $t = 0$ is assigned to the point where the surfactant front (or water front) is predicted to reach the surface. Negative times are displayed to show whether the lag time concentration correction has been successful, *i.e.* the component weight should remain constant until t_0.

As acetonitrile has a slightly higher refractive index (n) compared to that of water (see table 4.2), the penetration depth is increased and therefore to determine precisely the amount of acetonitrile present, the deviation in n needs to be corrected for. The effect can be estimated by calculating the penetration depth for $10\,\%$ acetonitrile in water. For a $10\,\%$ CH_3CN mixture in water, the refractive index, n, is 1.3430 at $20\,$°C.[168] The
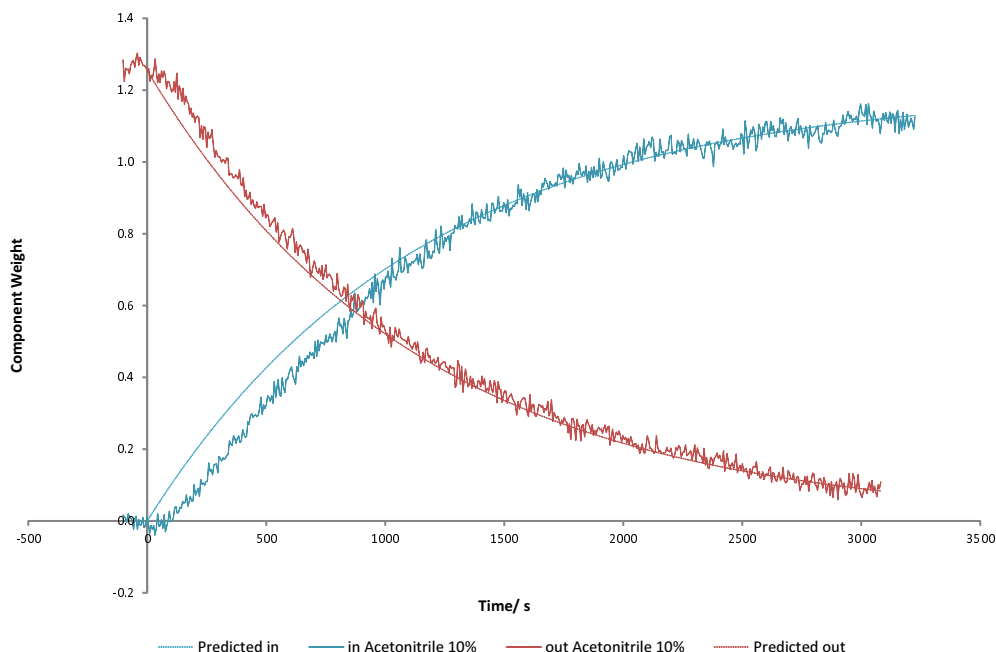
Figure 4.6: Acetonitrile mixing 10 % vol. "in" and "out", with prediction, scaled to component weight at end of "in" and start of "out" experiments. Large mixer. Predictions scaled to maximum component weight

penetration depth increases to 110 nm at 73°. The penetration depth for the silica-water interface is 103 nm so the maximum correction for changing refractive index is 7 %. Woods did show, in previous work in our group, that acetonitrile Raman signal intensity was directly proportional to concentration[1] and when working with Lambert, we were able to repeat this observation (figure 4.8). This would not occur if the acetonitrile adsorbed or there was a substantial change in refractive index. The acetonitrile is not completely removed during the time-scale of this experiment, given the exponential decrease in concentration. On further rinsing with water the acetonitrile is fully removed as expected.

Table 4.2: Refractive indices for validation solutions. Taken from reference 167.

Compound	Refractive Index (n) at 25 °C
Water	1.332 83
Acetonitrile	1.344 23
Methanol	1.3288
Sucrose	1.5376

We can see from the data that the prediction is in good agreement for "in" and "out", as it matches the rates of change well. At early times however, the prediction slightly overestimates the "in" and underestimates the "out" component weights. Acetonitrile peak shift is minimal with increasing concentration, although if the peak does shift it could explain the difference in predicted concentrations, depending on our target. A weak signal would contribute to noise, but should not affect the time constant. The increase in component weight during "in" is approximately linear until around 300 s, therefore ideal
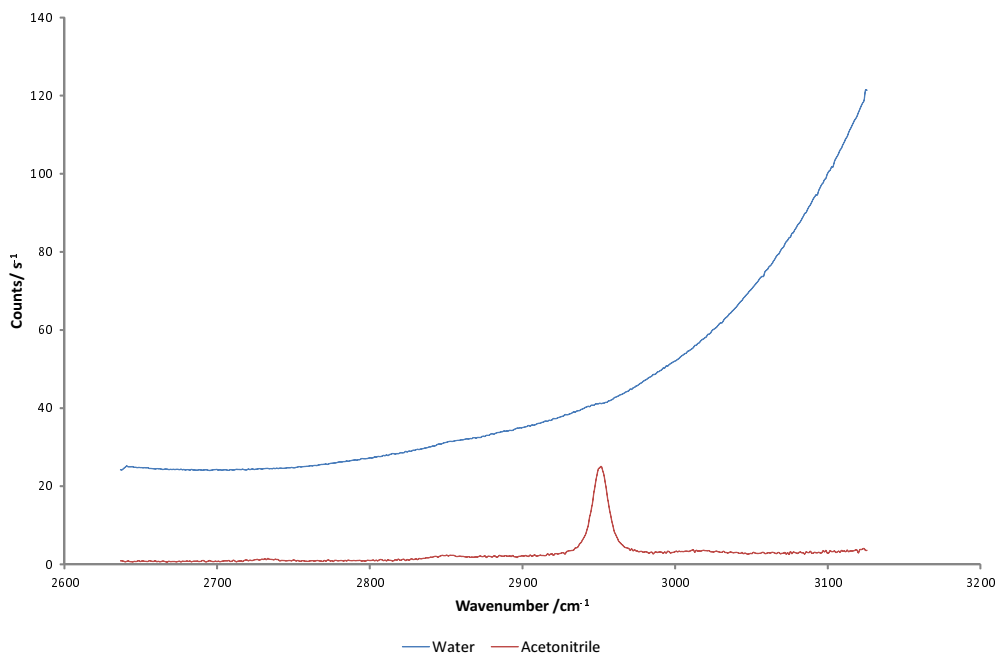
Figure 4.7: Acetonitrile components, 532 nm, 700 mW

mixing is not occurring. The discrepancy could be due to differences in density in the pipe, which we discuss in more detail when looking at sucrose. The diffusion of acetonitrile is rapid, so diffusion away from the interface into the bulk of the cell (which will be at a lower/higher concentration) could also contribute and would result in lower-than-expected component weight.

We moved on to study our mixer with methanol because the total peak area was larger and lower in wavenumber, therefore it is easier to separate our components because there is less overlap with the strong water band.
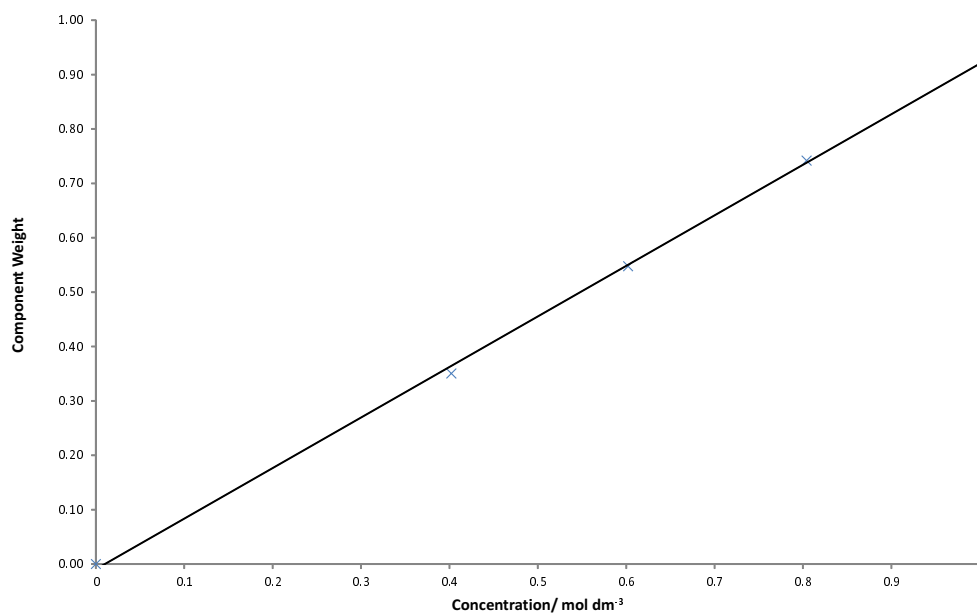
Figure 4.8: Acetonitrile component weight against concentration, from work in collaboration with Lambert

4.3.2   Methanol

HPLC grade methanol (MeOH) of up to 10% (and later deuterated methanol (methanol$-d_4$)) was also used to monitor concentration in the cell. MeOH has Raman-active bands at $2845\,cm^{-1}$ (CH_3 symmetric stretch) and $2955\,cm^{-1}$ (Fermi resonance modes of CH_3 bending overtones).[169] Good separation of the components occurred, the result of which can be seen in figure 4.9 and there does not appear to be any mixing of the two components.

Again, if we keep the concentration low we should minimise the effect of this change in n. For a 10% solution of MeOH in water the refractive index is 1.3364[170] at $25\,°C$, the penetration depth is $104\,nm$ at $73°$. This is a much smaller change in depth than for acetonitrile.

Figure 4.10 shows the change in component weight on change in concentration, for four different concentrations listed in table 4.3. The predicted kinetics have been used to convert the time into concentration at the surface. "In" measurements show some initial lag in increase in component weight and the "out" measurements show an initial lag in the decrease in component weight. There is also some hysteresis indicating that

Table 4.3: Methanol concentrations for validation

Sample Name	Concentration/ mM
0.5 %	125.5 ± 0.2
1 %	270.1 ± 0.3
2 %	525.8 ± 0.6
5 %	1260 ± 2
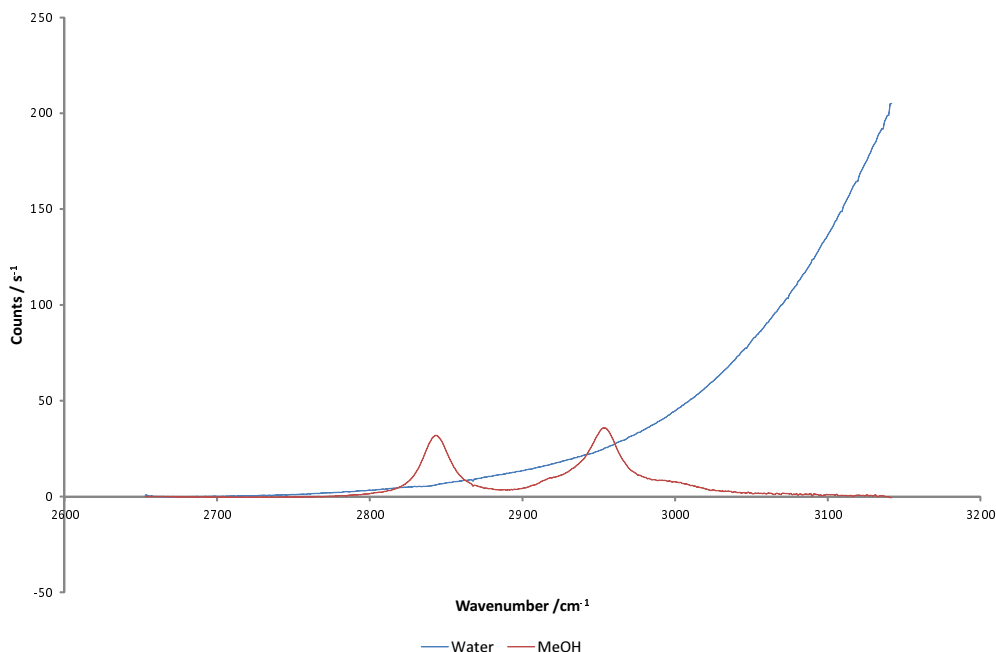
Figure 4.9: MeOH and water components, 532 nm, 700 mW

our data are not following the predicted kinetic model. MeOH is removed during "out" experiments, but for the higher concentrations the time-frame of the experiment does not allow for the amount to reach zero because it decreases exponentially.

To understand the reasons behind the deviations in figure 4.10, we studied the effect of flow rate, the reasoning being that the axial diffusion would be less significant at higher flow rates, while mixing would be more efficient at lower flow rates.

Figure 4.11 shows the effect of changing the pumping speed against time. Figure 4.12 shows the same data, calculating the predicted concentration as before, using the known volume of the mixer and the flow rate. The methanol concentration was (248.4 ± 0.2) mM. There appears to be minimal effect when increasing the pumping speed to $2 \, \text{ml} \, \text{min}^{-1}$, therefore we can rule out incomplete mixing in the mixer as a factor. Additionally, any change in the viscosity or diffusion constant on change in solute concentration will only affect the rate of transport in the final diffusion layer. Our results in figure 4.12 show excellent agreement in slope, but have small offsets due to imperfect component separation, where there is a non-zero component weight for MeOH in pure water.

At high concentrations (>500 mM) we saw some odd behaviour, such as that shown in figure 4.13, where oscillations appeared at predicted concentrations above around 700 mM during the "in" measurement but not the "out". The "in" measurement does reach the same maximum component weight as the starting point in the "out" measurement. The water component remained constant so this odd behaviour in the MeOH component weight is not due to some external factor, such as a change in focus. The origin of these oscillations, with a time period of around 80 s was never identified but may be associated with hydrodynamic instabilities in the flow cell. The hydrophobic inner wall of the pipe may attract air bubbles, which might require a high enough capillary pressure to overcome. However, large air bubbles would normally be obvious. Small air bubbles in the mixer

79
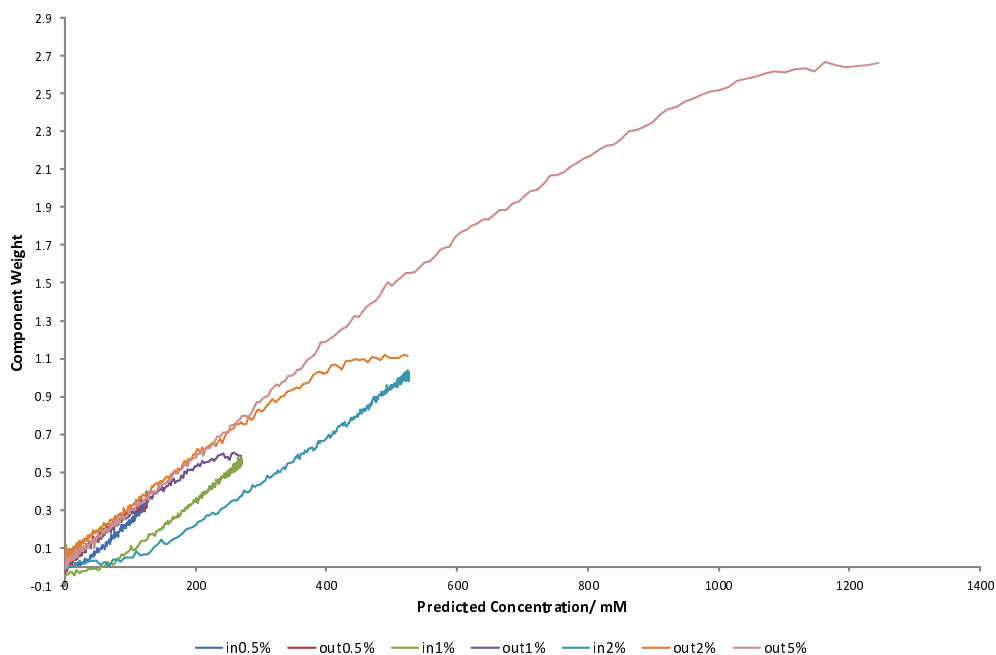
Figure 4.10: Effect of concentration showing component weight of MeOH against predicted concentration. $0.5 \, \mathrm{ml \, min^{-1}}$ small mixer. % vol. shown in legend
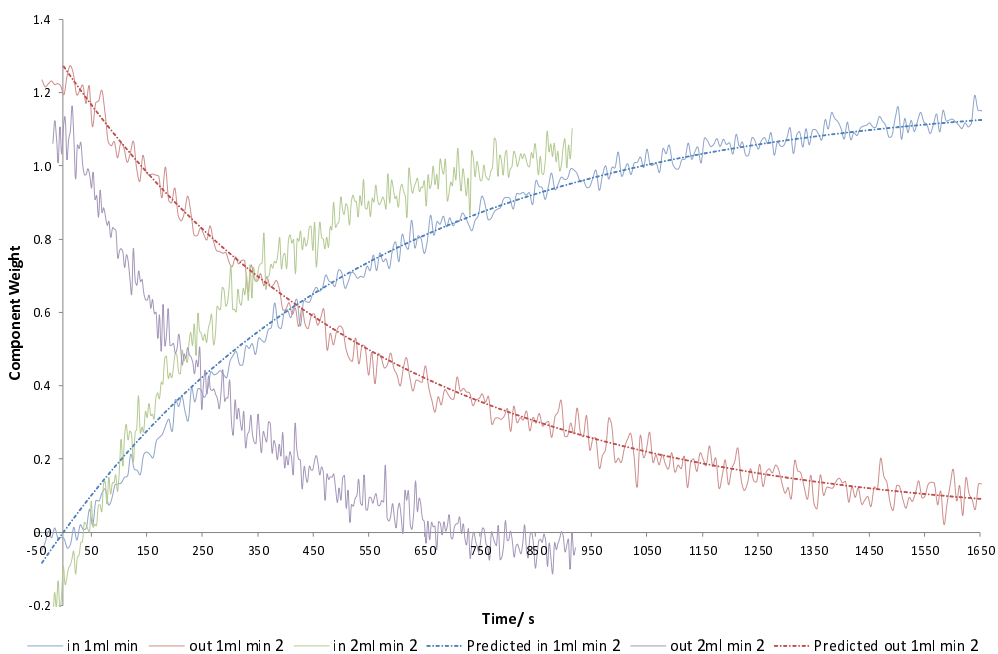
Figure 4.11: Effect of flow rate of MeOH against time. $248 \, \mathrm{mM}$ ($\approx 0.8\,\%$). Large Mixer. Flow rate shown in legend. Predictions scaled to maximum component weight

often occur but these often revolve with the stirrer bar and would only affect the kinetics by lowering the mixer's volume. Woods also observed a similar phenomena in acetonitrile, but on desorption (figure 4.14).
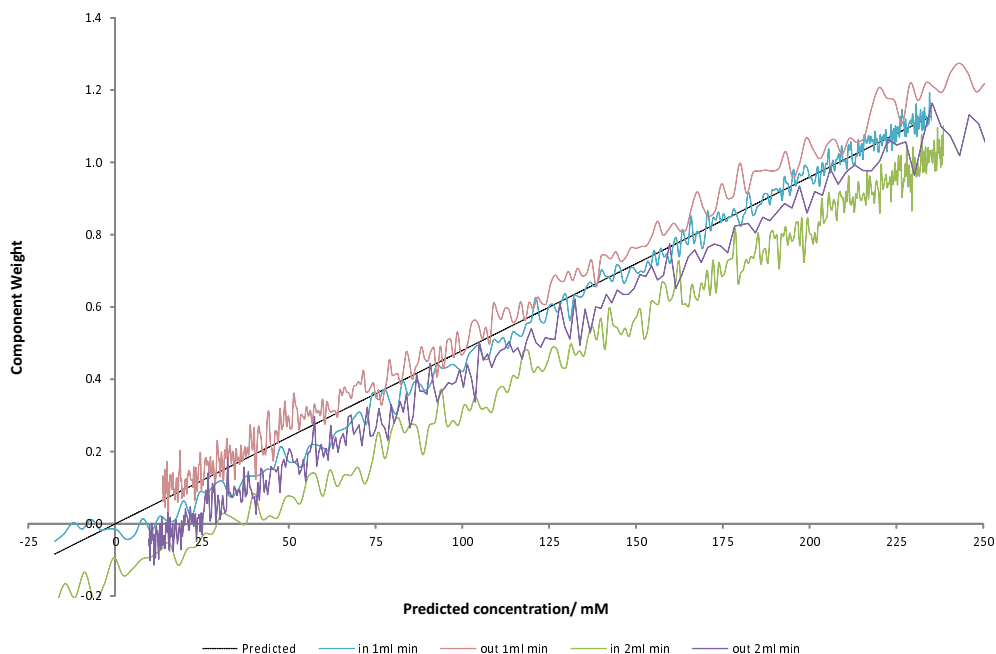
Figure 4.12: Effect of flow rate of MeOH, plotted against predicted concentration. 248 mM (≈0.8 %). Large mixer. Flow rate in legend
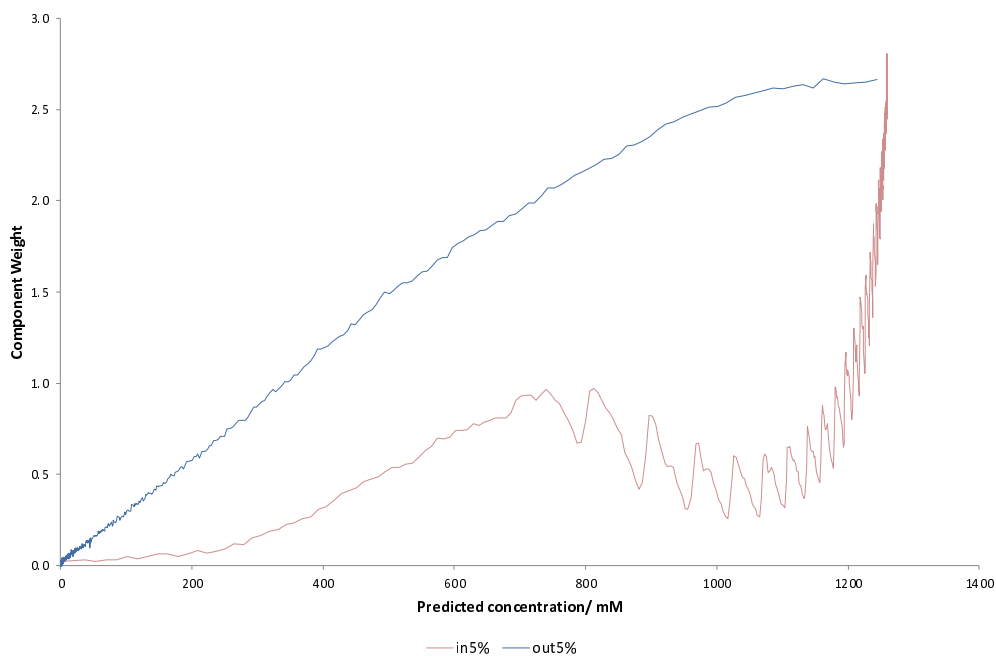
Figure 4.13: Oscillations observed at high MeOH concentration. The oscillations are periodic in time, but compressed when plotted against concentration. $0.5 \, \text{ml} \, \text{min}^{-1}$. Small mixer

(a) 0.4 mL min^{-1}

(b) 0.5 mL min^{-1}

(c) 0.7 mL min^{-1}

(d) 1.0 mL min^{-1}

(e) 2.0 mL min^{-1}
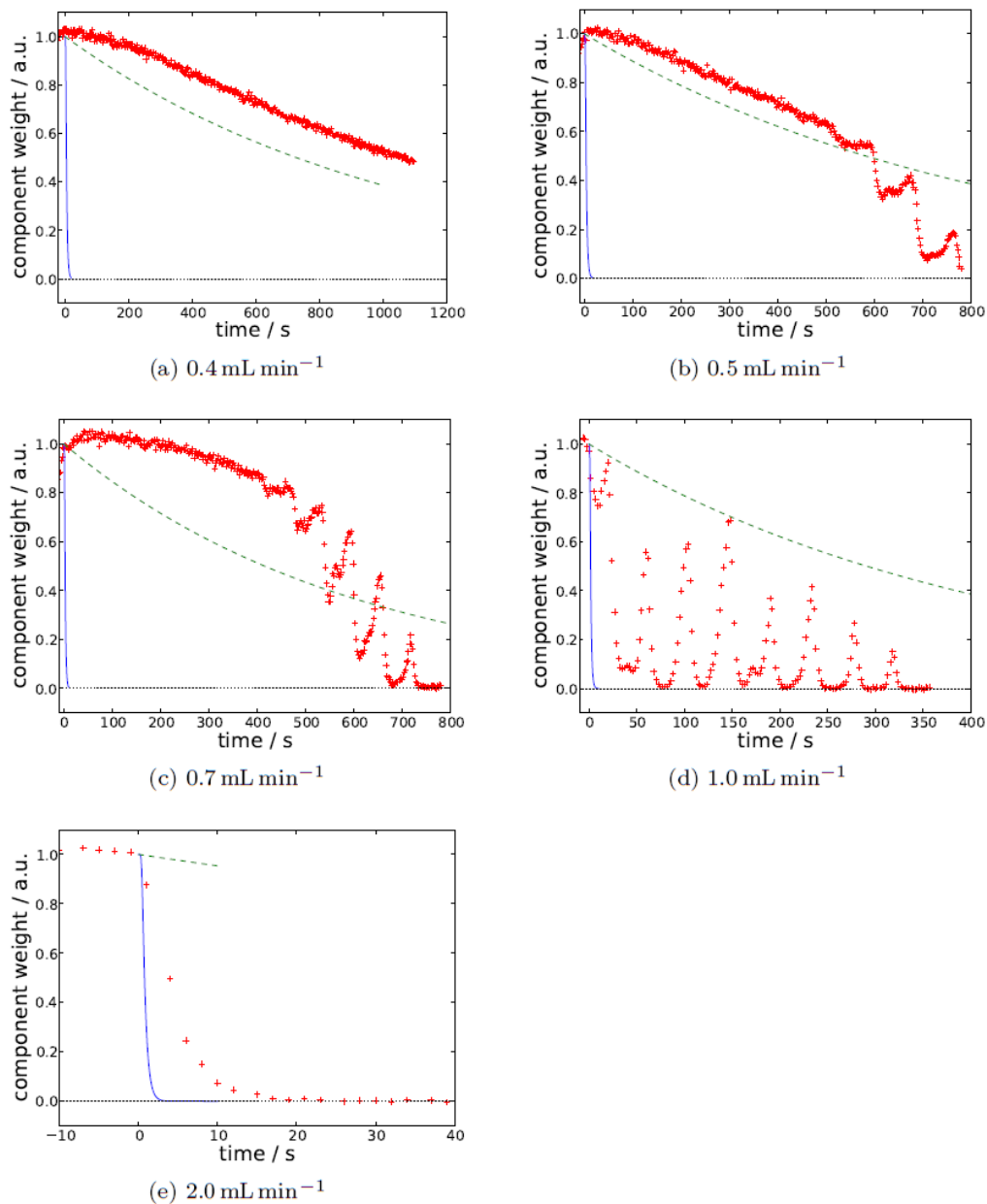
Figure 4.14: Oscillations observed by Woods at high acetonitrile concentration. Experimental (points), convection-diffusion modelled (solid blue lines) and instantaneous mixing modelled (dashed green lines) transport of acetonitrile away from the surface at a variety of different flow rates. Taken from reference 1

Deuterated-Methanol

We used deuterated-methanol (methanol$-d_4$ or CD_3OD) (99.8 % D) (Cambridge Isotope Laboratories, Inc., USA) briefly to look in the $2150\,cm^{-1}$ region where there is a much lower background. We can neglect the difference in rate of diffusion of CD_3OH in water (OD will replaced by OH in water due to diffusional isotherm exchange) as the Stokes-Einstein equation (equation 4.1) gives the diffusion D, for a particle of radius a in a medium at temperature T, with viscosity η, a non-dependence on mass:

$$D = \frac{k_B T}{6\pi\eta a} \tag{4.1}$$

The components used are shown in figure 4.15. Methanol$-d_4$ has Raman active peaks at around $2075\,cm^{-1}$, $2130\,cm^{-1}$, and $2250\,cm^{-1}$. Figure 4.16 shows the kinetic results (no mixer) using $\approx 1\,\%$ methanol$-d_4$ ((384.9 ± 0.5) mM). We can see that methanol$-d_4$ is completely removed on rinsing. During the first $20\,s$ there is some lag, in both "in" and "out" which could be due to the solute having to diffuse into/away from the boundary layer and hence the concentration at the surface does not initially equilibrate to the bulk concentration. The initial slopes ($0.16\,s^{-1}$ for in and $0.13\,s^{-1}$ for out) are probably equal within experimental error.

In our model we assume instantaneous appearance of the bulk solution at the interface, neglecting diffusion across the boundary layer. If diffusion is occurring we would need to account for this. However, from earlier models by Woods, we know that transport across the boundary layer is rapid—figure 4.17 shows the results from the model of acetonitrile transport at the surface.[1] We can see that the limiting value for the component weight is expected to be reached within $5\,s$, for a pumping speed of $1\,ml\,min^{-1}$, or $10\,s$ for $0.5\,ml\,min^{-1}$. Our data show slower than expected adsorption after this initial lag. His data also show better agreement with the model for "in" measurements than these measurements and diffusion in our system is taking around $100\,s$. Diffusion constants for acetonitrile and methanol are approximately the same, but mixtures of methanol and water have a higher viscosity than either solvent, so the diffusion coefficient may be lower than expected from a pure solvent, even in dilute solution. The pipes used in our results are approximately the same length as what Woods used. The mixing of methanol and other polar molecules is not ideal, and the use of a marker that does mix ideally would allow for a better understanding of the mixing and diffusion process.

Switching back to using the mixer, to slowly increase the concentration, figure 4.18 shows the change in methanol$-d_4$ component weight against time, scaled to maximum component weight (using the same $\approx 1\,\%$ solution) and figure 4.19 shows the data plotted against predicted concentration. Some initial data from the "out" measurement is missing due to file corruption. These data are very good in terms of the separation of the components, mostly due to the lack of any significant background or water spectrum which could vary. Figure 4.19 shows excellent agreement between "out" experiment and the prediction. The "in" measurement underestimates the component weight due to the non-zero component of methanol in pure water.

The slopes for "in" and "out" agree well, but not perfectly. The kinetics are likely to be valid and the small deviation from prediction could be due to the offset in the background, although any error in measuring the mixer volume will also affect this value.
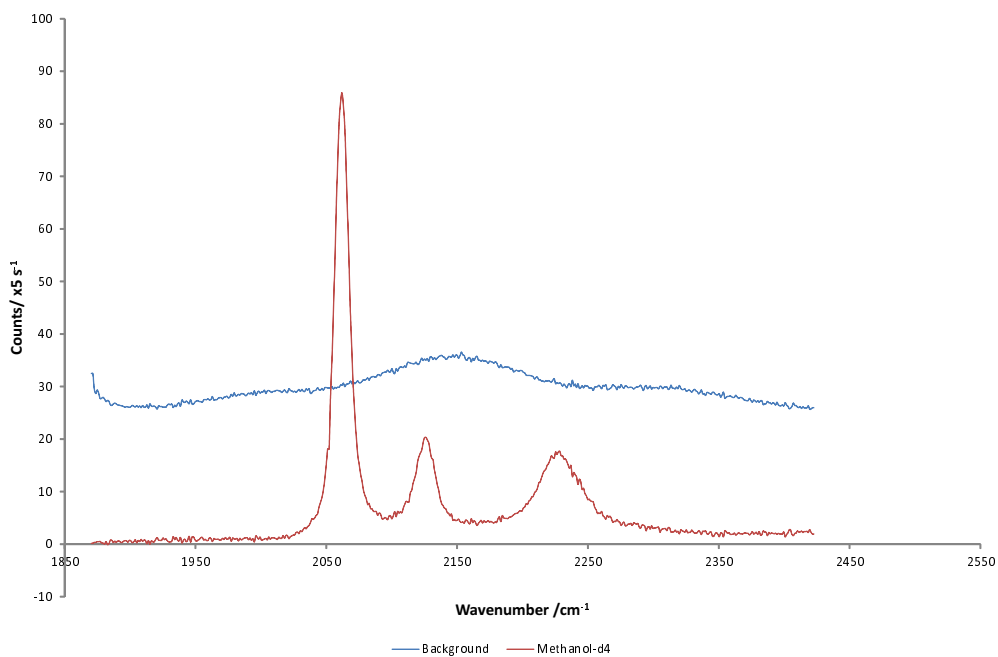
Figure 4.15: Methanol$-$d$_4$ components for $1\,\%$ solution in water, $532\,\mathrm{nm}$, $700\,\mathrm{mW}$

It is difficult to determine the mixer volume accurately as there will be some mixing in the pipe just before the solution enters the main mixer tank. Changing the design of the mixer to have very narrow inlets and outlets may improve our results by restricting mixing to the defined tank volume. Adding an offset of around 0.04 to the predicted component weight for "in" (the y offset) provides a better fit. Looking at the component separation in figure 4.15, we do not observe any poor separation (the strong d$-$MeOh peaks are not visible in the background) which is often a cause of component weight offset.
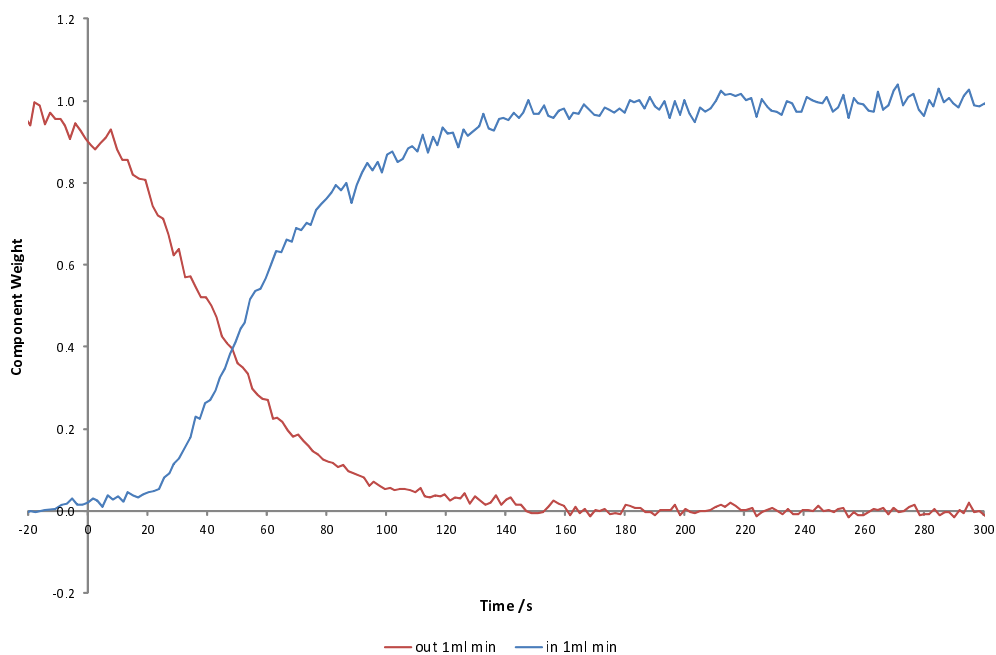
Figure 4.16: Methanol$-$d$_4$ kinetics without mixer

(a) $0.5\,\mathrm{ml\,min^{-1}}$ (b) $1.0\,\mathrm{ml\,min^{-1}}$
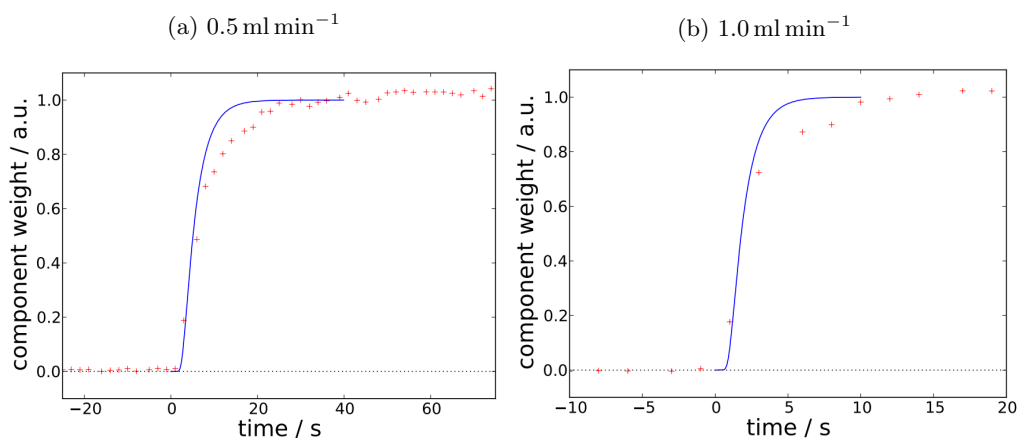
Figure 4.17: Experimental (points) and modelled (lines) transport of acetonitrile to the surface at a variety of different flow rates. The experimental data has been offset on the x-axis to match the modelled data. Taken from reference 1

86
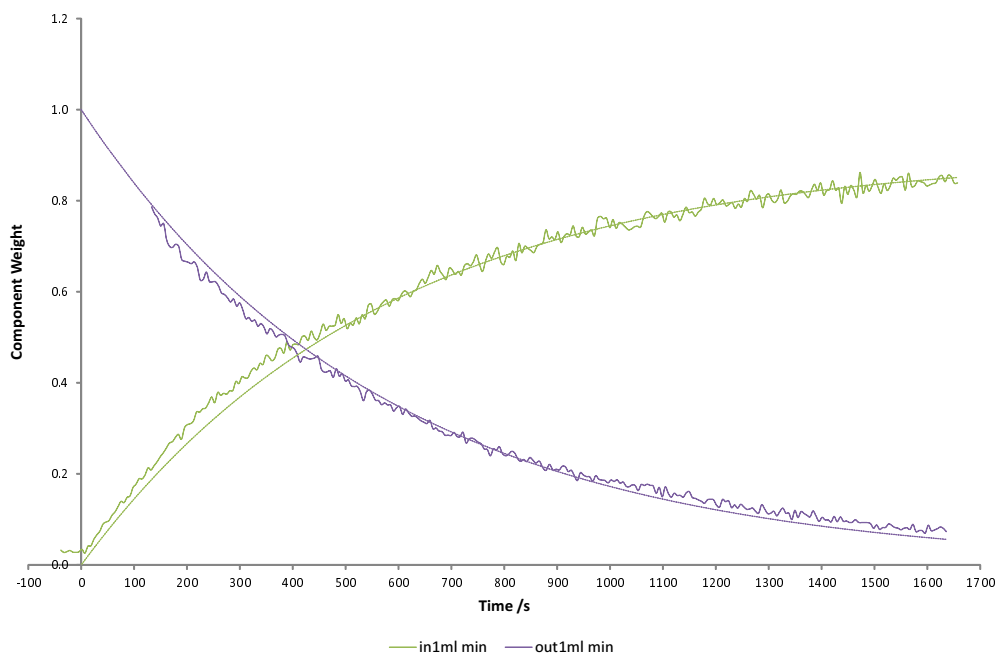
Figure 4.18: Methanol$-$d$_4$ component weight against time, with prediction (dashed lines), using the large mixer, $\approx$1 % wt. solution, scaled to maximum component weight
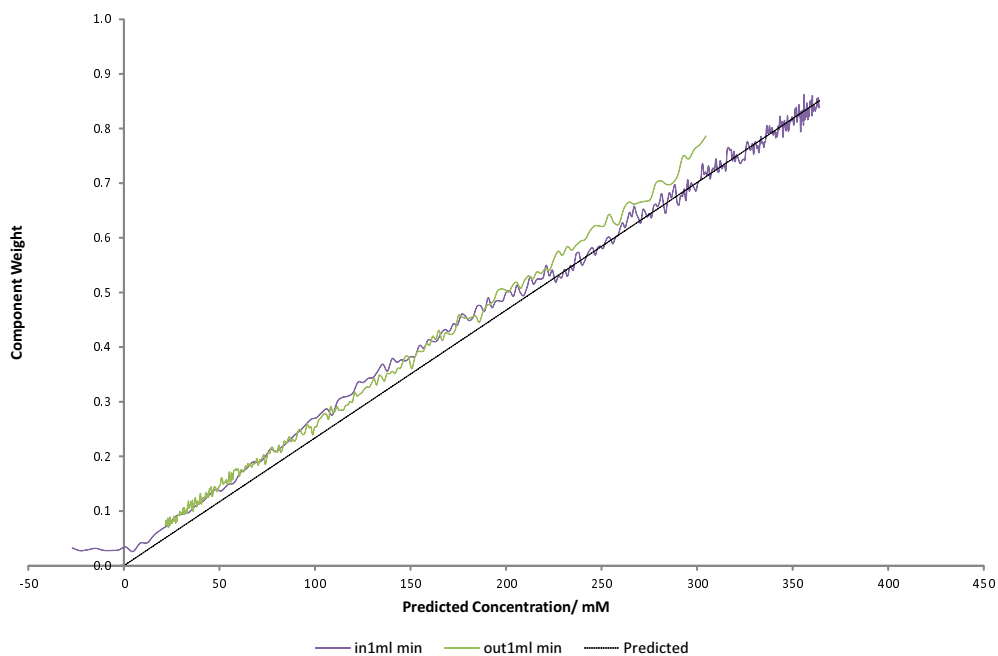
Figure 4.19: Methanol$-$d$_4$ component weight against predicted concentration, with prediction (dashed line), using the large mixer, $\approx$1 % wt. solution

4.3.3   Sucrose

In order to match more closely the diffusion coefficient of a typical surfactant molecule, to see how surfactants might behave in our system, we performed experiments using sucrose. Diffusion coefficients for some of the solutes and ions we have used are shown previously in table 4.1.[167] Methanol and acetonitrile have much higher diffusion coefficients (around double that of the C_nTABs) and hence we are more likely to see the effects of diffusion within the pipework with these smaller molecules.

Figure 4.20 shows the components of a 2 % wt. sucrose solution on silica in the $2900\,cm^{-1}$ region. There is a broad $C-H$ signal around $2900\,cm^{-1}$ for sucrose. Component separation is good.

Figure 4.21 shows what happens when we alter the flow rate and mixer speed and figure 4.22 shows the same data against calculated predicted concentration. The concentration of the 5 % wt. solution was $(145.72 \pm 0.03)\,mM$. We vary the pump and mixer speeds as described in the legend. We vary the mixer's speed with "normal" being $(1500\,rpm)$ and "half mix" being $\approx 750\,rpm$. We can see that there is still some degree of non-linearity at the start of the experiments, which we suspect is still from diffusion in the pipe. The main problem, is that sucrose is not reliably removable, which is not expected.

The inability to rinse out the sucrose (which should not adsorb to silica) suggests that the flow of the capillary in the cell is not axisymmetric but bypasses the stagnation point, possibly due to density differences between the fluid being pumped in and the (denser) sucrose solution in the cell. This effect could have been exacerbated in the new design by rotating the cell, as before the solution exit point was at the base with the capillary vertical, promoting the removal of denser solutions from the cell. Now the pipe and cell are horizontal, denser solutions will pool along the bottom. There may also be impurities in the sucrose.

To try and improve the results, we shortened the length of pipe between the mixer and cell to see if this reduced the diffusion before the solution entered the cell. Practically there are limits to how short the pipe could be as the mixer and stirrer plate were located outside the laser enclosure. Changing the pumping rate or shortening the pipe did not appear to have any effect; the component weight was still below the predicted value at early times (low concentrations) during "in" measurements.
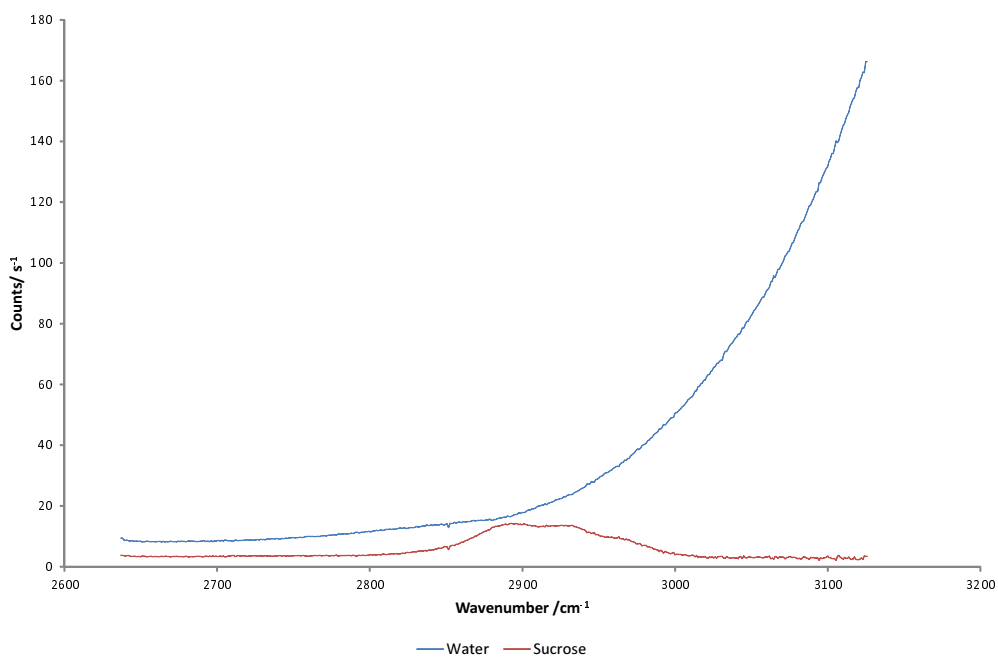
Figure 4.20: Sucrose and water components from "in2%normal", 532 nm, 700 mW
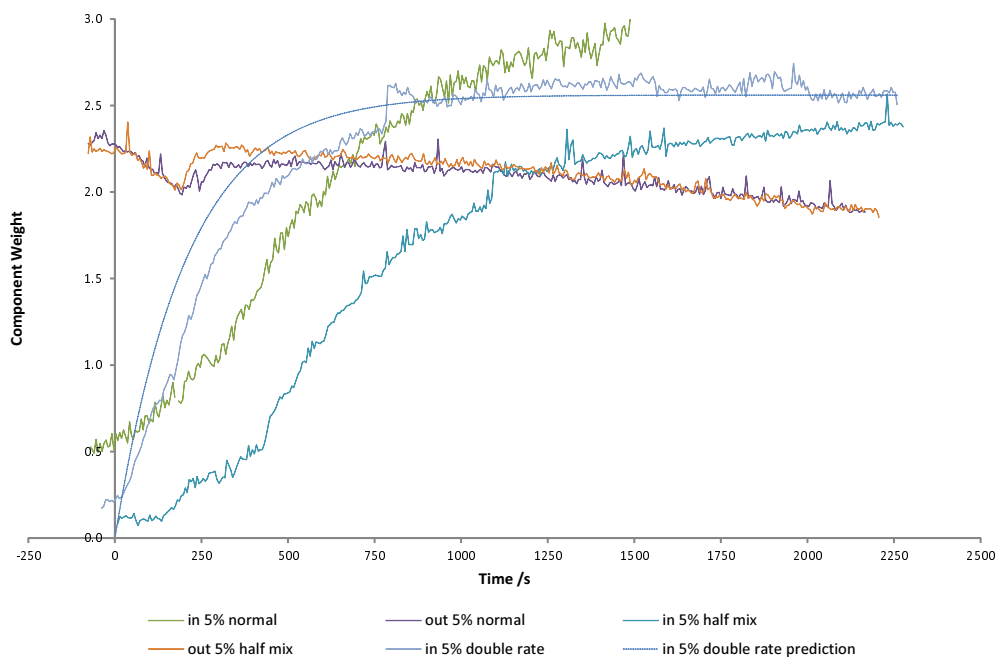
Figure 4.21: Sucrose 5 % wt. effect of mixer speed and flow rate against time. Prediction for "in5% double rate" shown. Small mixer, "half mix" is half mixing speed, "double rate" is $1 \, \text{ml} \, \text{min}^{-1}$
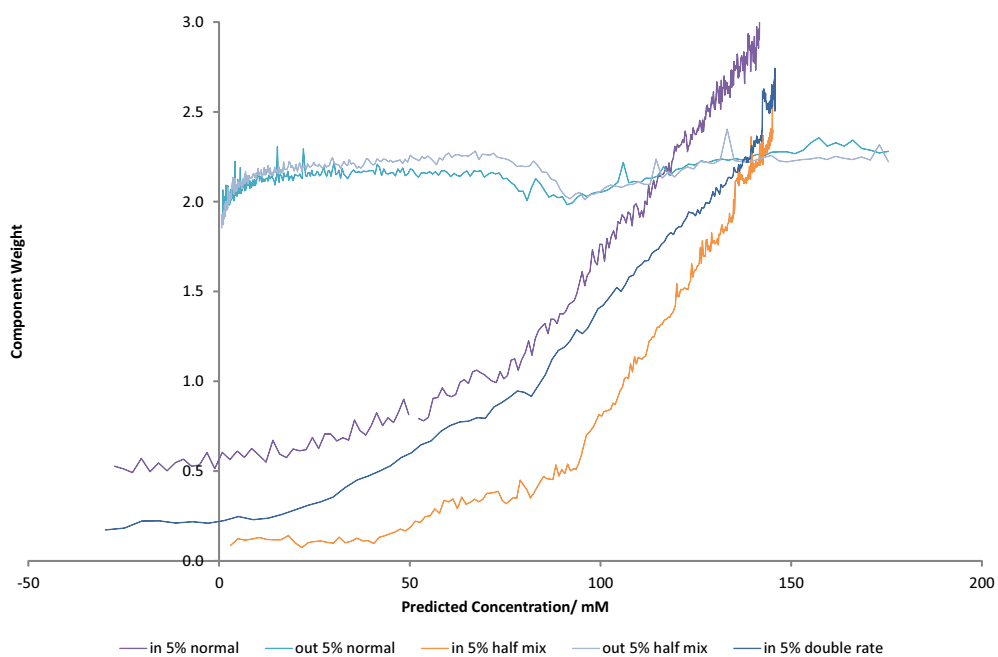
Figure 4.22: Sucrose 5 % wt. effect of mixer speed and flow rate against predicted concentration. Small mixer, "half mix" is half mixing speed, "double rate" is $1\,\mathrm{ml\,min^{-1}}$

4.4   Conclusions

Overall our in-line mixer has shown confusing results. While the data from acetonitrile, methanol and deuterated methanol show fairly good agreement with our predictions after some time, we suspect rapid diffusion of these small molecules in the pipe results in our assumptions about the concentration profile in the pipe matching the flow pattern being invalid. Looking at just "in" data, we can see there is initial lag in increase in concentration, but this could again be due to a delay in diffusion into the boundary layer resulting in a delay in reaching equilibrium. Diffusion of solute in the pipe to the mixer before starting the pump would result in the concentration increasing more rapidly than our prediction. Using a mixer with a more confined mixing volume or studying molecules which behave more like an ideal mixture in water may improve results. Woods suggests sodium tosylate or D_2O, in H_2O.[1]

Our experiments with sucrose, to try a solute which more closely match the diffusion coefficient of a surfactant, were mostly unsuccessful due to the solute not rinsing away and suspected density gradients. The reason for the sucrose not reliably desorbing is unknown. Impurities in the sucrose could be surface active and recrystallisation may be one way of purifying the compound, but the signal from an impurity is not likely to be as large as we have seen. Changes in the flow within the pipe and cell due to the difference in density are more likely. We could further investigate mixing by using other Raman-active, non-surface-active solutes with similar diffusion coefficients to surfactants.

The unexpected behaviour at early times could be explained by the following; the parabolic flow profile inside the pipe is depicted in figure 4.23. As the concentration changes, concentration contours will form along the same parabolic profile in the absence of diffusion. If axial diffusion occurs it will slightly broaden the concentration profile, as the concentration will rise slower as adsorption will occur sooner, but the bulk concentration will reach the limiting value later. However, if radial diffusion occurs the change in concentration profile will be more significant, especially in the case of not using the mixer, where the concentration gradients are much higher. Radial diffusion is more important than axial diffusion. Rapid radial diffusion would give rise to a "plug flow" profile, which gives the same concentration variation as Poiseuille flow, but would double the time taken for the adsorbate to reach the surface (since the axial velocity is twice the mean velocity). Again, the differences in density may also affect the concentration profiles. All these effects should be less significant for our more dilute surfactant solutions and the higher the diffusion coefficient, the larger the errors will be from neglecting diffusion in the pipe. For a typical surfactant, with $D = 5 \times 10^{-10}\,\mathrm{m^2\,s^{-1}}$, the rms distance that a molecule diffuses in 100 s is $\sqrt{2Dt}$ =0.3 mm, so axial diffusion is negligible and even radial diffusion is less than the radius of the pipe.

Our in-line mixer is reliable provided concentrations are kept low ($\approx$100 mM). It is difficult to determine whether pumping rate affects the diffusion. Slowing the mixer down does slightly decrease the mixing efficiency. We have seen that there is a delay in molecules diffusing in/out of the boundary layer and hence the concentration in our probe region does not match the predicted bulk concentration. Often the drift in the focus and/or background complicates analysis; our d−MeOH data shows better reproducibility due to the lack of any changing background, but there are advantages to normalising
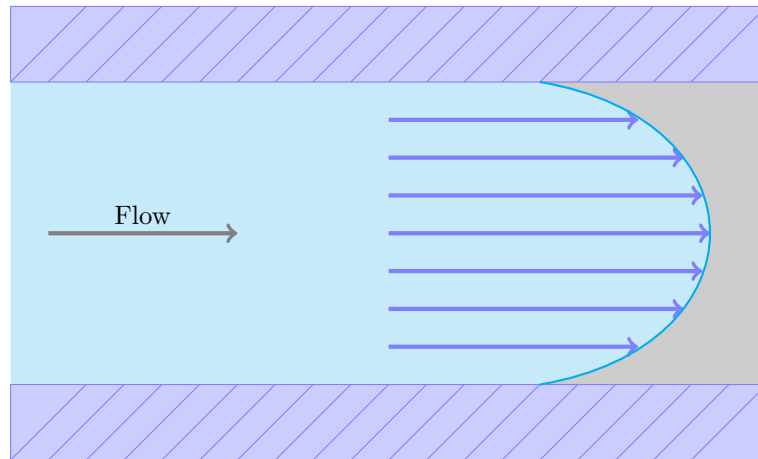
Figure 4.23: Schematic of the side view of parabolic flow profile in a pipe

against the background as we can correct for drifts when calculating surface coverages.

Chapter 5

Adsorption of Surfactants onto Silica

5.1   Introduction

This chapter is primarily concerned with the adsorption of common cationic and nonionic surfactants to acid-washed silica. It also includes a brief summary and further analysis of collaborative work studying the Hofmeister effect on bilayers of double-chained cationic surfactants carried out by undergraduate project students under my guidance.

Surfactant adsorption onto silica is of great importance to many technological processes including detergency, cosmetics, personal care applications, food products and pharmaceuticals. Silica is a commonly used model for a polar, negatively charged surface. For example, understanding surfactant adsorption to surfaces such as silica is important in enhanced oil recovery, used to maximise the extraction of oil from a well. In this process two interfaces are involved, the oil/water interface and the oil/solid interface. Increasing the wetability of the reservoir improves oil extraction.[171] The surface area of the reservoir can be large when surface is porous rock, sand or clay which can result in up to two-thirds of oil remaining in the reservoir after initial extraction.[171] Silica is a model surface for these reservoirs and the adsorption of $C_{16}TAB$ on SiO_2 films has also been investigated by Bi *et al.* as a model for oil recovery.[171] Forming stable colloidal suspensions is also important for mineral processing.

We begin by looking at the quaternary (4°) ammonium bromide surfactants on silica, initially varying alkyl chain length (single-chained) TAB (trimethyl ammonium bromide) followed by one (double chained) DAB (dimethyl ammonium bromide) surfactant.

We are interested in determining the amount of surfactant on the surface, termed surface excess (Γ) in an adsorption isotherm (constant temperature). The speed at which the surfactant adsorbs, along with the profile (shape) during adsorption are of interest as they may reveal the mechanisms behind the adsorption process. Many physical and chemical parameters may change the composition and behaviour of surfactants at an interface, including the hydrophilicity, temperature, pH, salt concentration, size and charge of counterions, surface roughness, and surface charge. For example, figure 5.1 shows C_nTAB adsorption onto alumina at pH 10 (above the isoelectric point, so the

surface possesses a negative charge).[172]

Unless otherwise stated, the following experiments on silica were all performed at $25\,°C$, $73°$ angle of incidence and with $700\,mW$, $532\,nm$ laser excitation. The pumping speed was $0.5\,ml\,min^{-1}$.
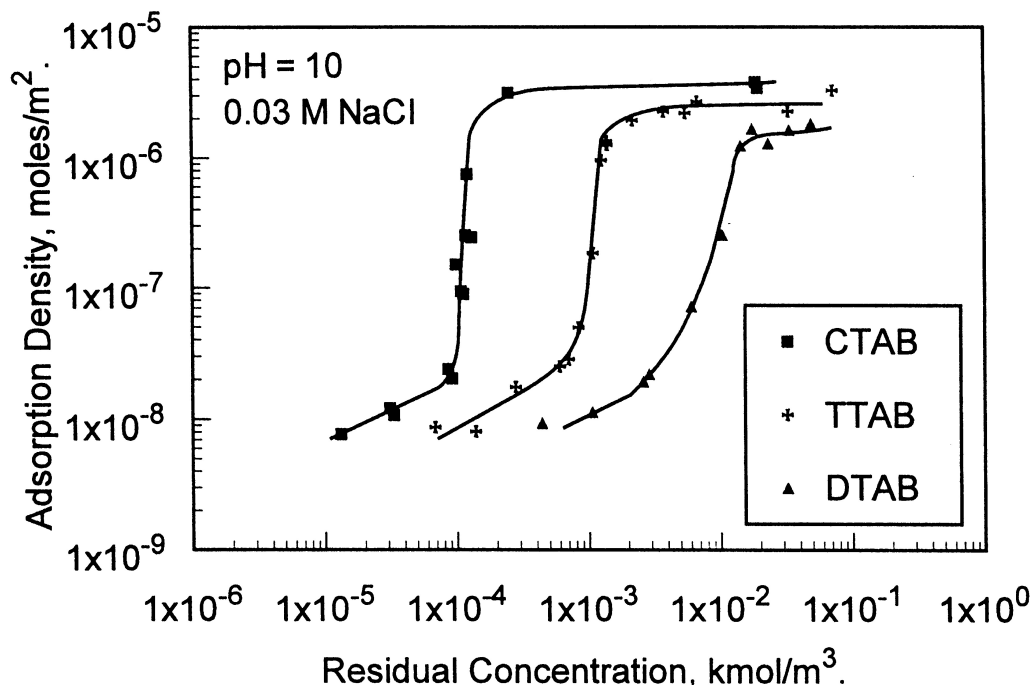
Figure 5.1: Adsorption isotherms for C_nTABs on alumina (CTAB (C_{16}TAB), TTAB (C_{14}TAB) and DTAB (C_{12}TAB)) on alumina at pH 10, with $0.03\,M$ NaCl present. Reproduced with permission from reference 172. Copyright 1997 American Chemical Society

5.2   Single-Chained 4° Ammonium Bromides

5.2.1   Introduction

The series of C_{12}, C_{14}, C_{16} and C_{18} TABs were studied on plain, acid washed silica using the in-line mixer. Initially data was difficult to obtain because of the limitations with the Renishaw set-up due to focal drift over the extended time period when using the mixer and bubbles adhering to the surface. The new spectrometer constructed during the project allowed for greater data reliability. However, with all the mixer experiments, successful separation of the components was often difficult, particularly for the "out" measurements. Where separation has not been perfect, it is often seen as an offset in the y-axis, where the surfactant component does not start at zero for "in" measurements. For "out" measurements, poor separation can result in the surface excess starting at a different maximum concentration to that which was reached during the "in" measurement, despite using the same target factors. That said, the cell is emptied and refilled between "in" and "out" measurements, so some variation may be observed if the layer has not reached equilibrium. As mentioned earlier, silica is a model soil (stain) as it is the major component of the earth's crust.

5.2.2 Results

In these results, we are interested in the initial "in" slopes and general shape, in order to determine if there is any diffusion in the pipe or mixing is incomplete, and we are looking to see if these isotherms start at zero surface excess, to observe if our component separation and data analysis were correct. Later in the isotherm trace, we are looking at Γ_{max} at saturation, if there is any overshoot at the CMC, and comparing Γ_{max} to literature values, where available. For the "out" measurements, we are observing the consistency and determining if there is any hysteresis or residual adsorption.

As we have already explained in section 4.3.1, due to all spectra being obtained from when the pump starts, we have corrected for the lag time in the pipe before the solution reaches the cell; hence we calculate "negative" concentrations.

C_{12}TAB

C_{12}TAB or dodecyltrimethylammonium bromide was the lowest molecular weight and the highest CMC TAB under investigation, at 15 mM.[162] The concentrations used are shown in table 5.1. Separation of the components (see figure 5.2) is good, however given the lower number of alkyl groups, there is less surfactant signal compared to the longer chains. Figure 5.3 shows the results using the large mixer when we were unable to obtain only one reliable "out" measurement. Figure 5.4 does show reproducibility and the "in30mM" result agrees with the literature CMC value. As C_{12}TAB has a relatively high CMC, there is a large bulk contribution to the spectra, hence it is critical to have an accurate subtraction of the bulk signal in order for the results to be accurate. On the "out" measurement the concentration does not decrease far enough for complete desorption as we are using the large mixer. The components for the "out" measurements show good separation, so we should see Γ decreasing continually with decreasing concentration, therefore we are not just observing a change in concentration and perhaps impurities are affecting results (around 7 mM). The "out" measurements in figure 5.3 and figure 5.4 could also indicate irreversible adsorption. This behaviour is observed on glass, but is not expected on silica (although this could be due to impurities remaining on the substrate).

The initial slope of the "in" reproducibility experiments in figure 5.4 are fairly constant until an increase which occurs when the surface excess reaches around 4 µmol m^{-2}. The slope then increases to the overshoot, followed by a more rapid decrease to reach $\Gamma_{equilibrium}$ of around, at a mean across all experiments of around 6 µmol m^{-2}. This overshoot can be explained by the surfactant adsorbing up until the normal surface excess, but the impurities continue adsorbing until the CMC is reached when they rapidly desorb into micelles. Out measurements were largely unsuccessful when analysed with TFA due to the lack of any significant decrease in concentration, but complete desorption did not occur in the experimental time-frame, despite our predicted final concentration being well below the CMC. This suggests adsorption is not completely reversible (or impurities are present).

In all C_{12}TAB experiments there is a noticeable overshoot in Γ at the CMC on the way "in". This overshoot has been observed in other work on these TABs.[173,174] This maximum is suspected to be due to impurity in the sample which is more surface active than the surfactant under investigation. Above the CMC, these impurities would be
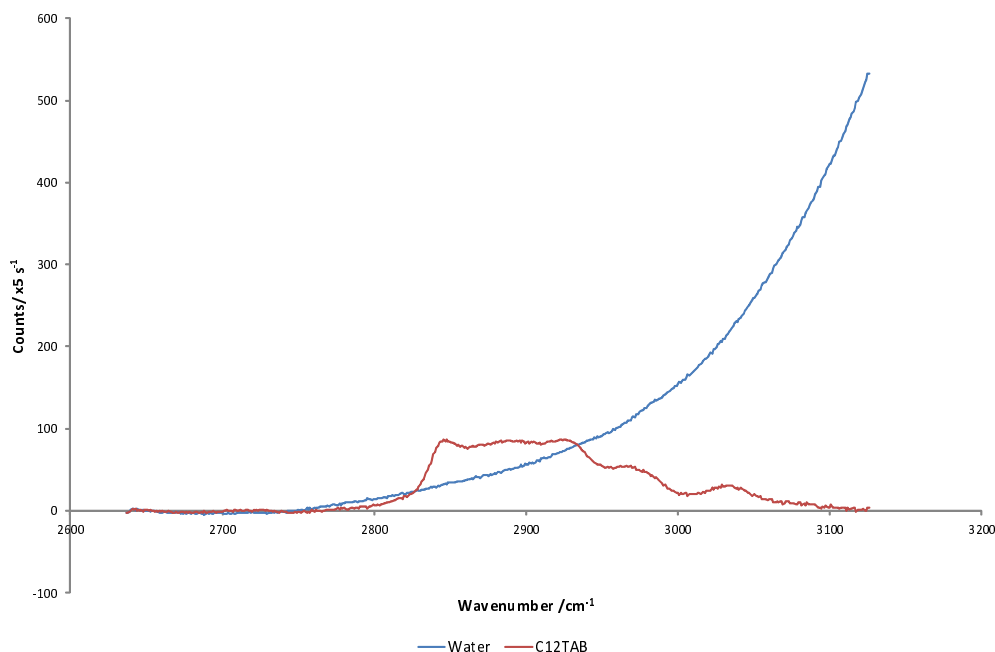
Figure 5.2: C_{12}TAB components for "in30mM", 532 nm, 700 mW

Table 5.1: C_{12}TAB concentrations

Sample Name	Concentration/ mM
C12TAB-20mM2 (small mixer)	20.45 ± 0.03
C12TAB-20mM3 (small mixer)	20.00 ± 0.02
C12TAB-30mM (large mixer)	29.69 ± 0.01
C12TAB-55mM (large mixer)	55.51 ± 0.07
C12TAB-2	20.02 ± 0.02
C12TAB-3	19.98 ± 0.02

solubilised in micelles.[173] On "out" experiments these impurities would also remain in micelles, until the concentration dropped below the CMC when they would then partition into the surface layer. With our results, however, further purification by additional recrystallisation did not eliminate the overshoot. Impurities in the sample could consist of C_nTAB homologues or other surface active impurity. If these impurities are more surface active than our target surfactant then we will observe more impurity than surfactant in our probe region.

Later analysis of our sample by accurate mass ultra-performance liquid chromatography with electro-spray ionisation mass spectrometry (LC-ESI-MS) (Acquity UPLC (Waters Ltd, UK)), in HPLC-grade methanol (figure 5.5) does show additional mass peaks that were not C_{12}TAB. The measured mass 228.2696 m/z is consistent with the empirical formula $C_{15}H_{34}N$ with an accuracy of 2.2 ppm or 0.5 mDa. This is accepted as the molecular ion $C_{12}TA^+$. The chromatography results show the sample is mostly C_{12}TAB, but there is some C_{13}TAB and large amount of C_{14}TAB present in the sample. Similar analysis for other nearby homologous surfactants showed the presence of smaller amounts of C_{10}TAB and C_{11}TAB; hence, despite multiple recrystallisation steps, our sample
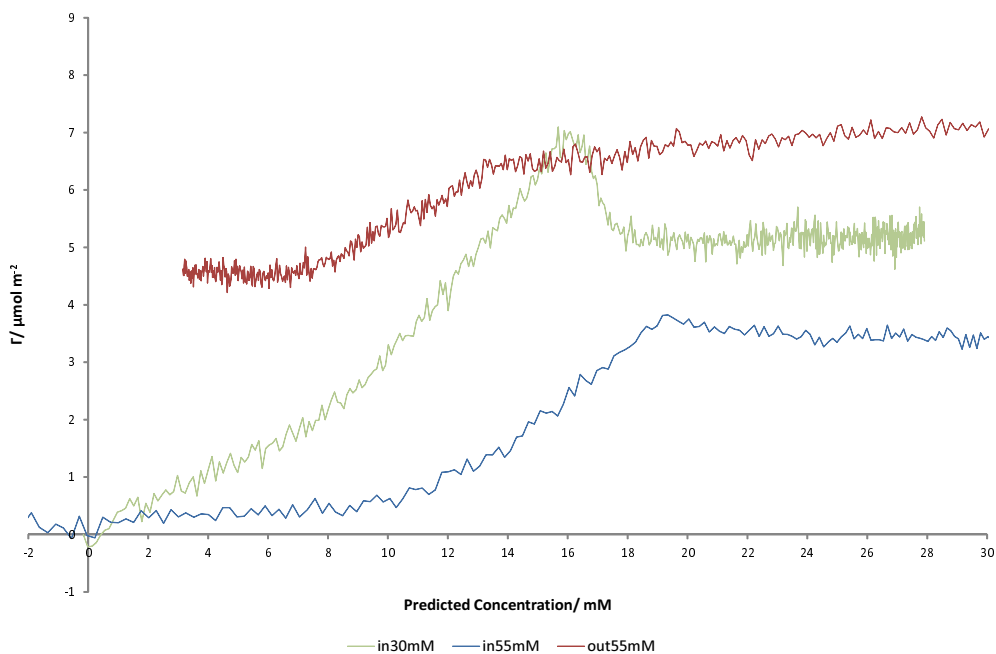
Figure 5.3: C_{12}TAB isotherm on silica (large mixer)

remains very impure. The stated purity was $\geq 98\%$, but our mass spectrometry results suggest the sample to be much more impure than this and hence this is why our isotherms were poor. The identity of the broad peak at around 2.8 min in the first graph in figure 5.5 is unknown. Mixtures of two chain lengths of CTABs are known to affect the CMC.[162,175]
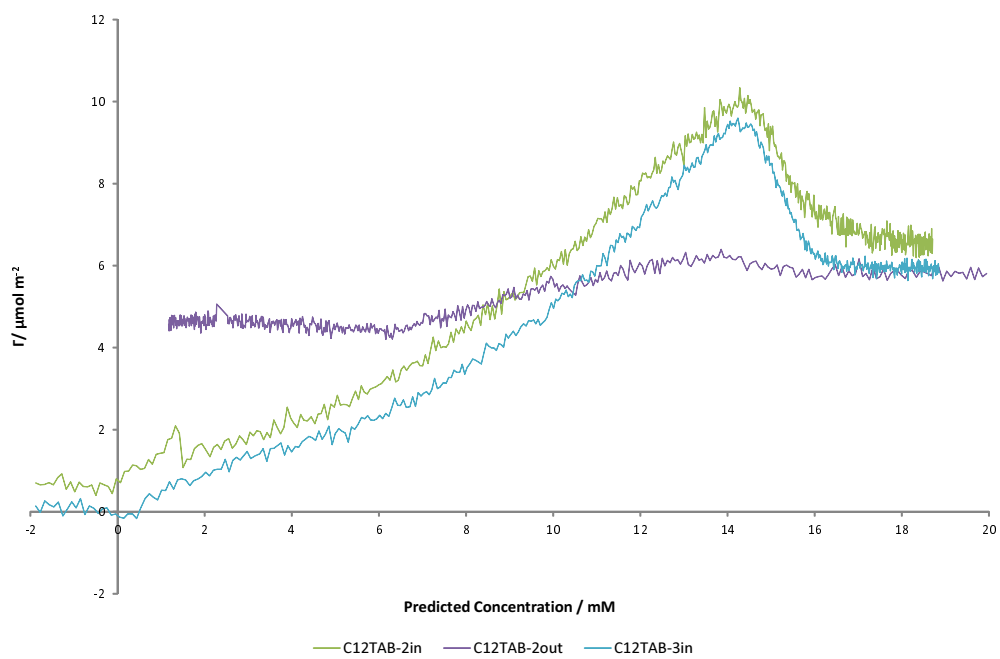
Figure 5.4: C_{12}TAB isotherm reproducibility on silica (large mixer)
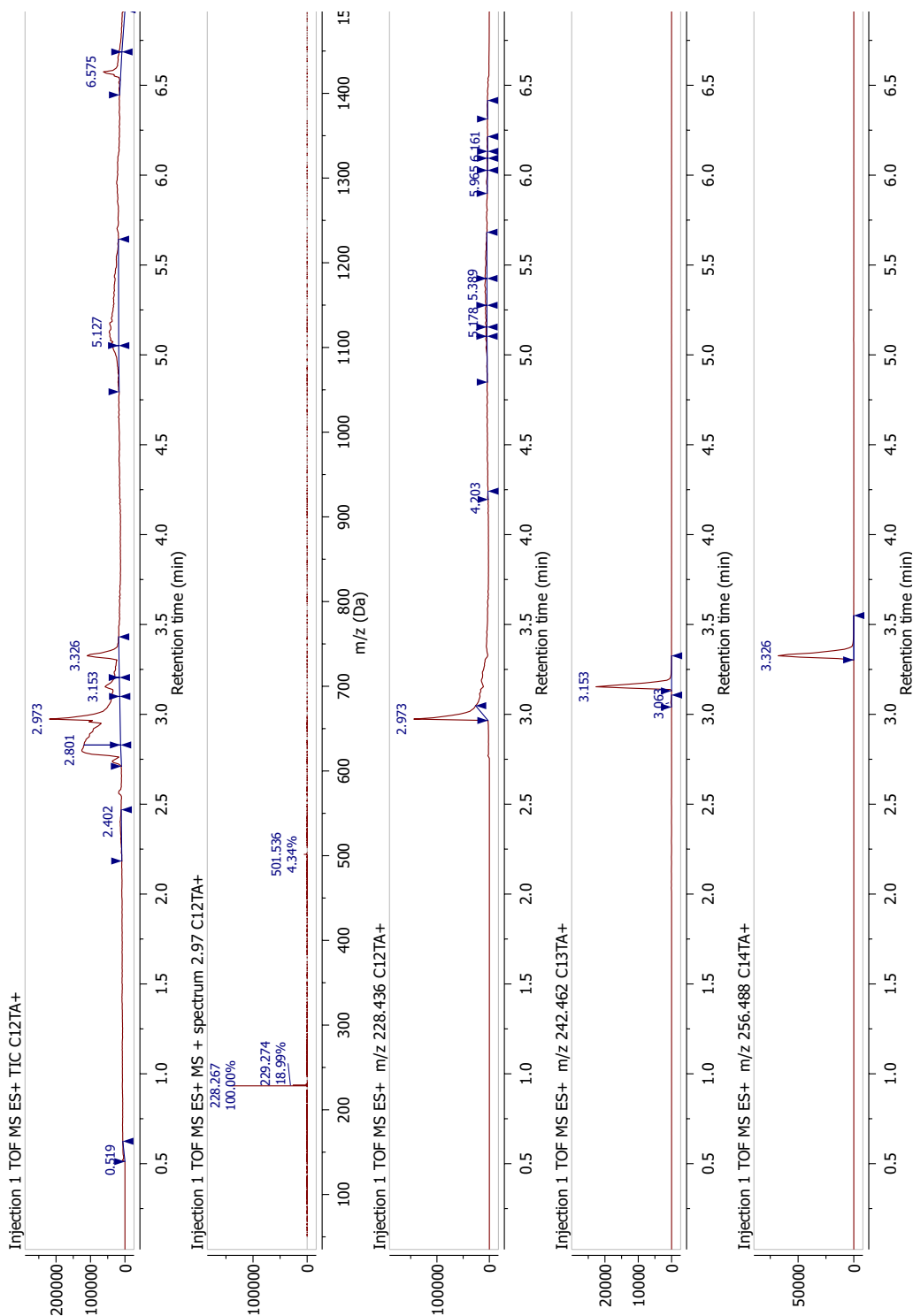
Figure 5.5: C_{12}TAB UPLC+ESI mass spectrometry, in MeOH. Showing from left (top when rotated) to right: the chromatogram, largest peak (2.97 min) mass spectrum, and mass chromatograms for C_{12}TA$^+$, C_{13}TA$^+$ and C_{14}TA$^+$

C$_{14}$TAB

C$_{14}$TAB or tetradecyltrimethylammonium bromide has a CMC of 4 mM.[162] Component separation was typically good (figure 5.6). Table 5.2 shows the concentrations used. The CMC in figure 5.7, using the small mixer matches with the literature at around 4 mM, with the exception of the highest concentration (in 20 mM), where again the concentration rises rapidly which decreases the precision (during 5 s acquisitions) of this initial data. The accuracy could be lower due to diffusion or kinetic limitations at the surface. There is some hysteresis on the "out" measurements and the surfactant does not completely desorb from the surface. Overall, reproducibility is good; however, the calculated time offset for "in10mM" is wrong and adjusting for this brings the isotherm curve further out of line with the CMC. This was perhaps caused by an error when making up the concentration or a bubble in the pipe. The initial "in" slopes in figure 5.7 start with an abrupt jump to around 1 μmol m^{-2}, before a more gradual increase to the plateau. There is no maximum before the plateau so we do not appear to have the same contamination issue that we saw with C$_{12}$TAB (with the exception of in 5 mM). Our bulk subtraction has worked well. Surface excess at the plateau is variable, at around 6.5 μmol m^{-2}. There is good consistency for the "out" measurements which give a residual adsorption of around 2 μmol m^{-2}. Correct component separation has resulted in zero surfactant adsorbed at 0 mM (with the exception of "in10mM").

Figure 5.8 shows the data from our large mixer, with the concentrations used also shown in table 5.2. Reproducibility is poor and there is probably some contamination demonstrated by the surface excess maximum. Our bulk subtraction is also unsatisfactory, as the plateau has a negative gradient because we are subtracting too much bulk contribution. Our time offsets are good agreement with there being zero surfactant at $t = 0$. Again, using the large mixer, our concentration does not drop far enough to determine if there is residual adsorption and there is a lack of reproducibility for the "out" data. Our "out" data does show that our concentrations are what we predict, since desorption starts at the same concentration ($\approx$2.5 mM).

Table 5.2: C$_{14}$TAB concentrations

Sample Name	Concentration/ mM
C14TAB-5mM	5.02 $\pm$ 0.01
C14TAB-10mM	10.04 $\pm$ 0.01
C14TAB-20mM	19.61 $\pm$ 0.02
C14TAB-50mM	49.62 $\pm$ 0.06
C14TAB-10mM3	10.34 $\pm$ 0.01
C14TAB-5mM (large mixer)	5.006 $\pm$ 0.008
C14TAB-10mM (large mixer)	10.02 $\pm$ 0.01
C14TAB-10mMrepeat (large mixer)	10.01 $\pm$ 0.01
C14TAB-20mM (large mixer)	19.91 $\pm$ 0.02
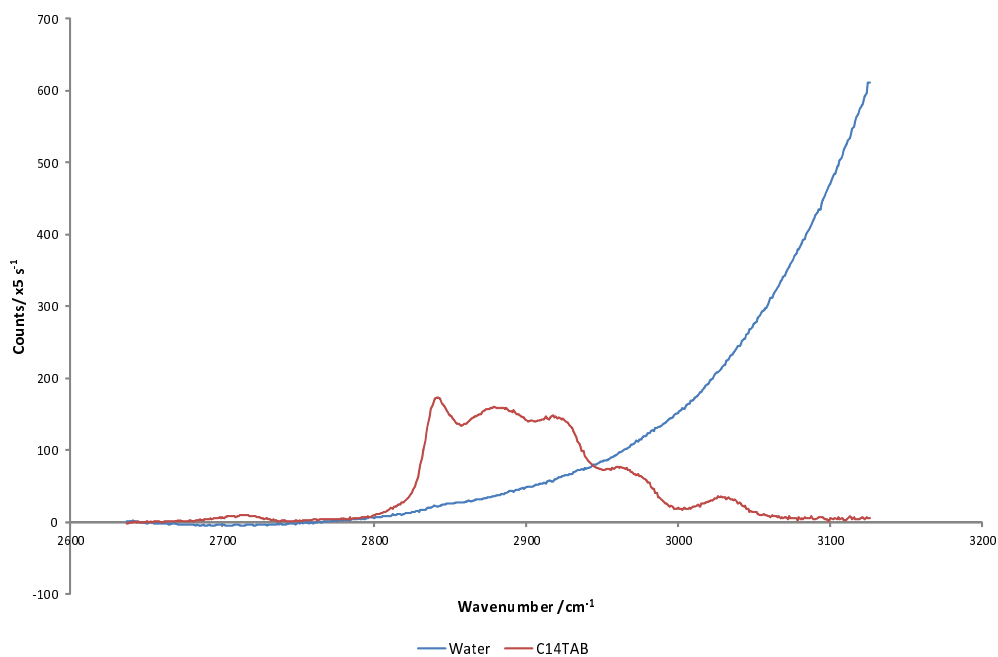
Figure 5.6: C$_{14}$TAB components, for "in5mM", 532 nm, 700 mW
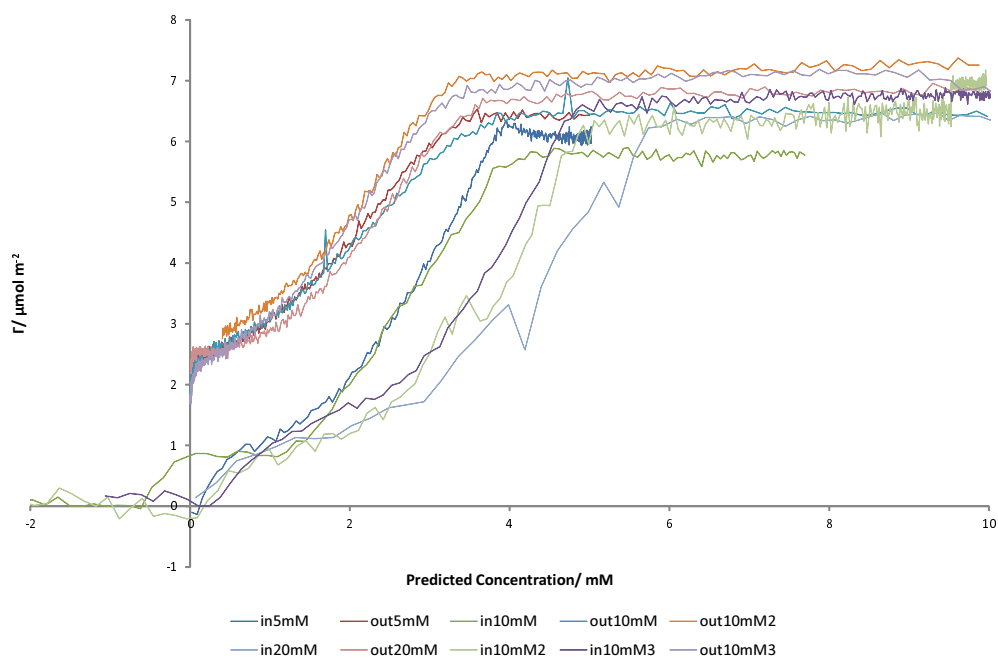
Figure 5.7: C$_{14}$TAB isotherm on silica (small mixer)
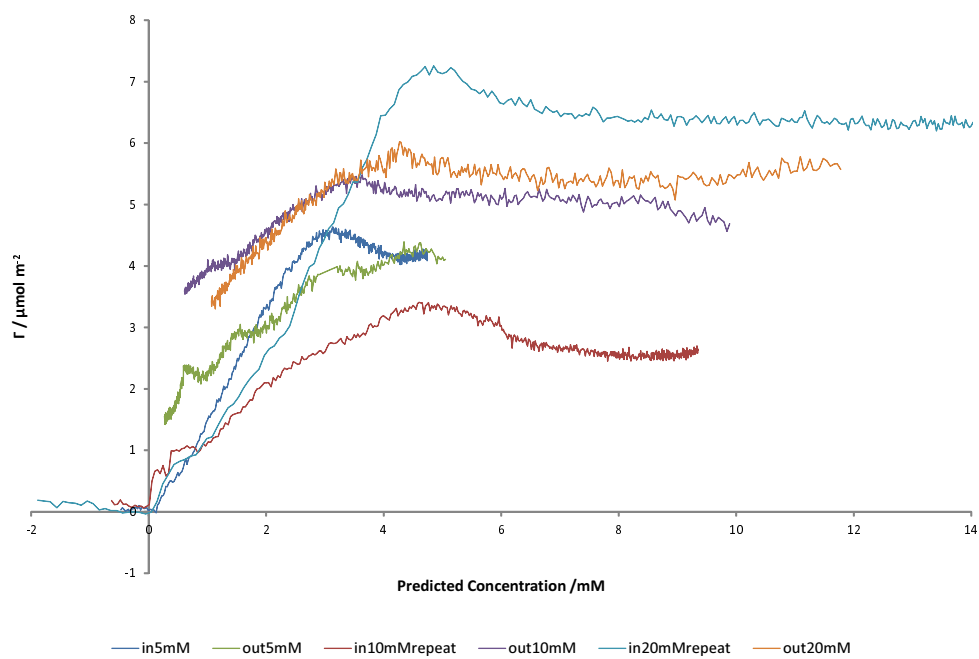
Figure 5.8: C_{14}TAB isotherm on silica (large mixer)

C$_{16}$TAB

C$_{16}$TAB or hexadecyltrimethylammonium bromide has a CMC of 1 mM.[162] Figure 5.9 shows the components have separated well (although not as good as C$_{12}$TAB or C$_{14}$TAB— the peaks appear to shift to lower wavenumber with increase in concentration, due to interactions between adjacent chains), and a comparatively strong (the strongest TAB so far) C−H region (expected as the chains are longer). Our results fit well with the CMC value. Concentrations used are shown in table 5.3. Figure 5.10 also shows these results are in agreement with the CMC for two out of the three "in" experiments when using the large mixer. Again, with the highest concentration solution, the rate of change in concentration at the start is high and therefore we know the concentration with lower precision, or it could be due to diffusion and/or kinetic limitations. As the gradient of the line above the CMC is near-zero, bulk subtraction to obtain the surface excess was successful. There is some overshoot on the "in" 2 mM and 5 mM solutions, possibly due to contamination. The experiments that do not match with the CMC could be down to our kinetic assumptions or an inaccuracy in t_0. Similar results are seen with the smaller mixer (figure 5.11). There was some data loss when the laser interlock was tripped at around 5.5 to 6.5 mM during "in10mM". Again, the two highest concentration "in" measurements fail to match the CMC. With the smaller mixer there does not seem to be any noticeable overshoot, despite using the same recrystallised, solid surfactant sample so the contamination must be related to cleanliness. Gradients also match well across the concentration range studied (excluding the higher concentrations). Using the smaller mixer, we were able to reduce the concentration far enough to determine the residual surface excess to be around 1 μmol m^{-2}.

Figure 5.12 shows reproducible data for the "in" experiments. It can be seen that our time offsets for "3in" and "4in" are not perfect, but after correcting for this the isotherms match well. There is possibly some overshoot in surface excess in "2in". The concentrations used are shown in the bottom section of table 5.3. Our "out" experiments do not seem to be as reproducible, with experiments "2out" and "3out" ending in different surface excess values to "4out" and "5out". The two pairs were taken on different days, but the experimental conditions should have been identical, so the cause is unknown. The data we have suggests there to be a slow initial rate of adsorption below ≈1 mM, then increasing until reaching a plateau of around 6 mM. Again our bulk subtraction is excellent as the plateau is very flat. "3in" does not appear to be clean, as we do not start at zero. Our other experiments, however, do appear to have separated well, giving a surface excess of 0 mM at the start. Again, because of the large mixer, our concentration did not drop low enough in the experimental window in the "out" measurement to observe complete desorption.
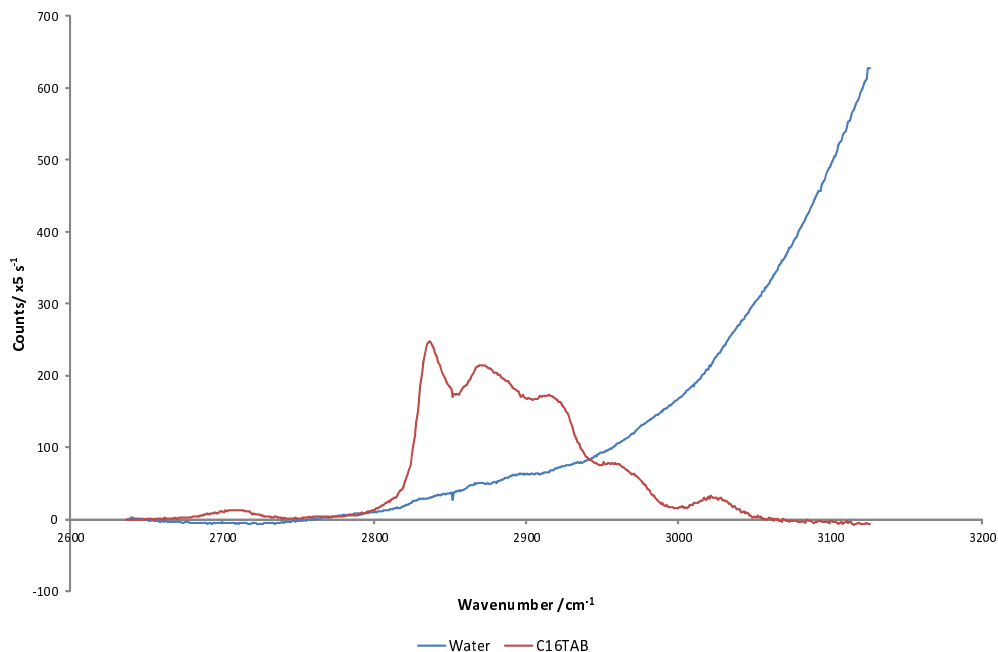
Figure 5.9: $C_{16}TAB$ components for "out2mM", $532\,nm$, $700\,mW$

Table 5.3: $C_{16}TAB$ concentrations

Sample Name	Concentration/ mM
C16TAB-2mM	2.01 ± 0.01
C16TAB-10mM	10.10 ± 0.01
C16TAB-55mM	54.94 ± 0.07
C16TAB-2mM (small mixer)	2.09 ± 0.01
C16TAB-5mM (small mixer)	5.39 ± 0.01
C16TAB-8mM (small mixer)	8.03 ± 0.01
C16TAB-10mM (small mixer)	10.14 ± 0.01
C16TAB-30mM (small mixer-in)	29.96 ± 0.04
C16TAB-30mM (small mixer-out)	30.19 ± 0.04
C16TAB-45mM (small mixer)	45.13 ± 0.04
C16TAB-2	5.043 ± 0.008
C16TAB-3	5.032 ± 0.008
C14TAB-4	5.024 ± 0.008
C14TAB-5	5.006 ± 0.008
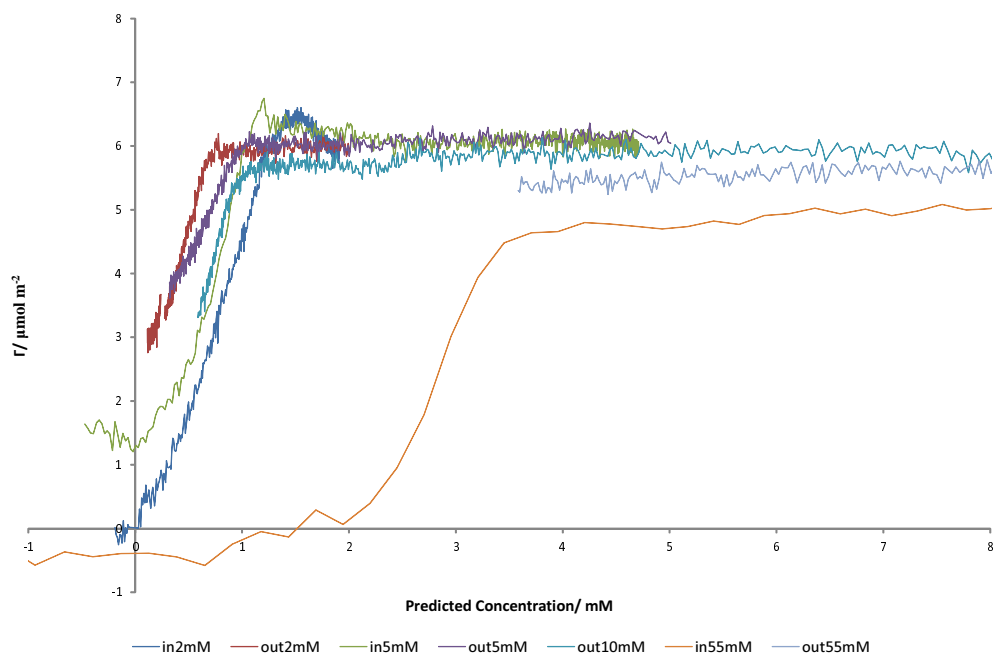
Figure 5.10: C_{16}TAB isotherm on silica (large mixer)
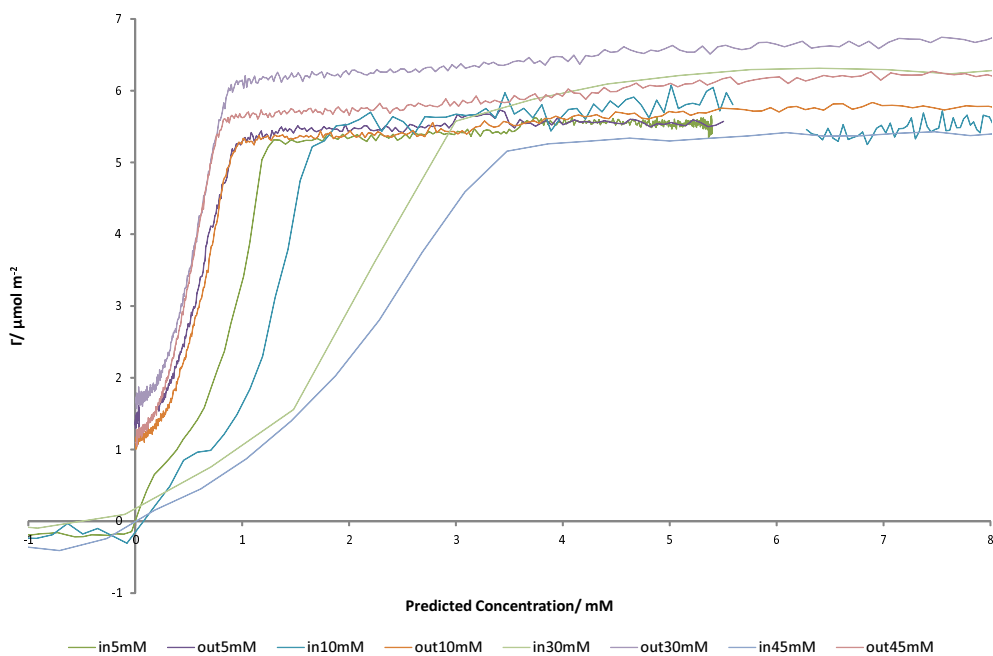
Figure 5.11: C_{16}TAB isotherm on silica (small mixer)
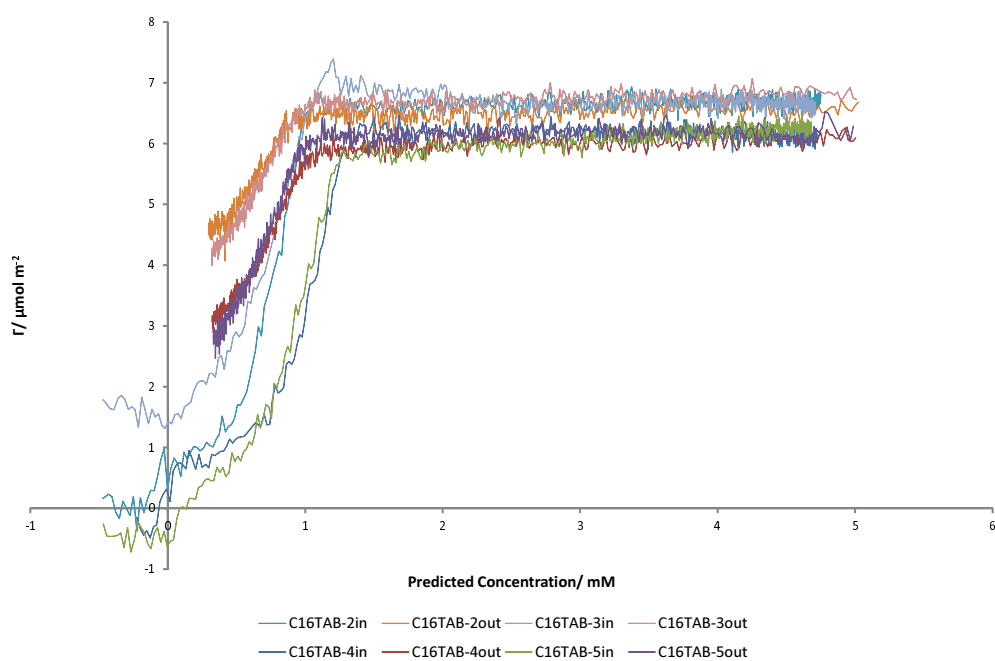
Figure 5.12: C_{16}TAB isotherm reproducibility on silica (large mixer) (5 mM)

$C_{18}TAB$

As a quick trial we undertook a brief experiment with C_{18}TAB. The surfactant has a CMC of 0.34 mM, and has a Krafft temperature of $\approx 38\,°C$ in water.[163] To overcome the problem of crystallisation, the experiments were performed at $(42 \pm 1)\,°C$, however maintaining this temperature consistently was difficult and considerable focal drift occurred, despite equilibrating for 60 min prior to the experiment (our water bath was set to $50\,°C$, so there are clearly considerable heat losses). "Bubble wrap" insulation was added to the syringe and pipe, and the mixer was placed on a hotplate stirrer to reduce heat loss. The drift resulted in the components not separating that well (see figure 5.13). Expansion or drift of the optics, cell, clamps and stages may also occur with time. Additionally the $C-H$ peaks are less intense against the water background compared to the other TABs despite the increase in number of $C-H$ groups. We would predict Γ_{max} to be slightly higher due to the increase in chain length (more $C-H$ bonds present), but the increase in temperature would lower the predicted Γ_{max}. The lower counts could also be due to loss of focus. Figure 5.14 shows one experiment ("in" and "out") performed with (1.019 ± 0.005) mM C_{18}TAB. These results do not match the literature CMC value well. The "out" curve is better, but the reason for the increase during the "in" at high concentration is unknown; however, looking at the water component it is clear that we have lost $\approx 70\,\%$ of our original water component weight. The surfactant is not removed during the experiment, even after observing the raw data. The component weight remains at a minimum for over 20 min, which could be an impurity stuck to the surface. The high Krafft temperature could cause the surfactant to crash out of solution while in the pipe between the heated mixer and cell. If the flow rate is low or stopped, the solution will cool. This would result in a lower than predicted concentration at the surface on the "in" measurement (not what is observed). For the "out" measurement, if the surfactant had crashed out in the pipe while waiting for the temperature to equilibrate it will take longer to remove, then upon starting the pump again the fresh warm solution redissolves the surfactant. Better insulation or heating of the pipe may improve stability, along with recrystallisation of the surfactant, if we had wanted to investigate C_{18}TAB further.
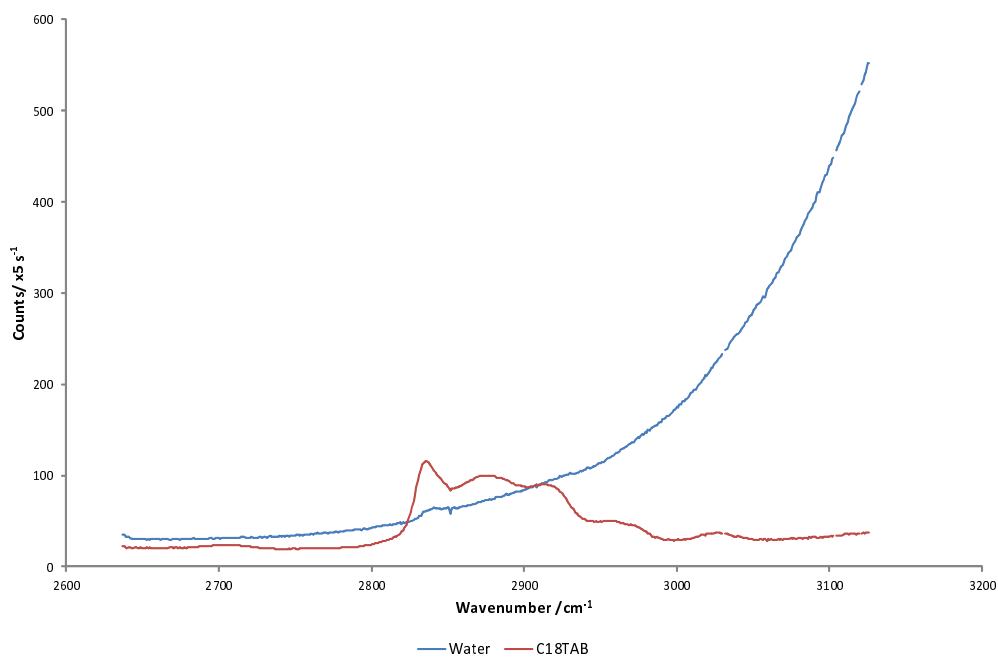
Figure 5.13: C_{18}TAB components, 532 nm, 700 mW
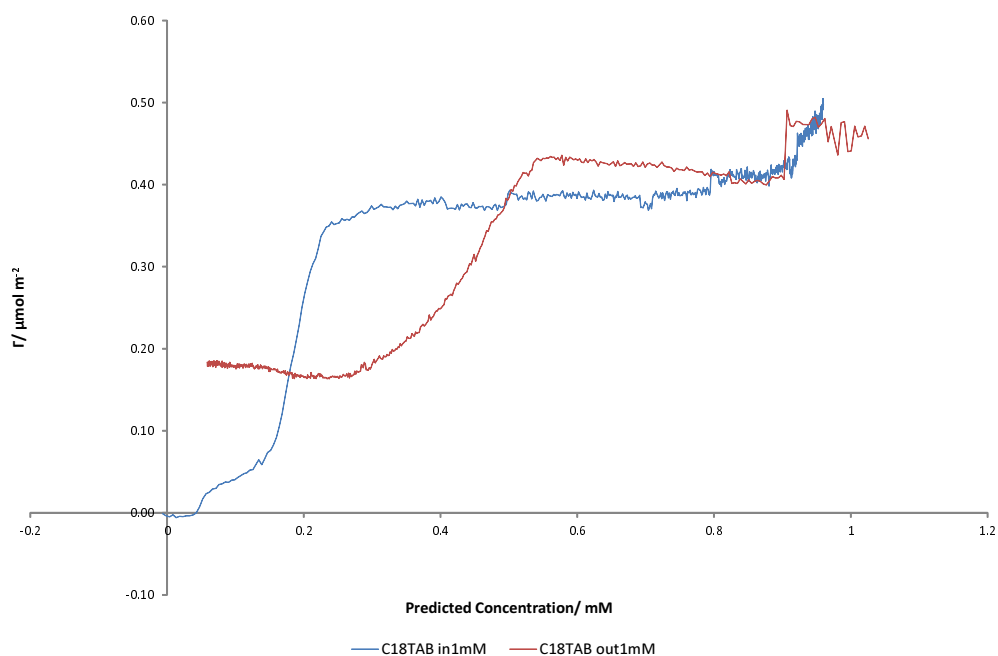
Figure 5.14: C_{18}TAB component weights on silica against predicted concentration (big mixer)

5.2.3   Discussion

Overall we have shown that when component separation in TFA is good we have reproducible results which match our CMC values, however proper separation does not occur as often as we would like. We were unable to eliminate the overshoot for C_{12}TAB. We suspect this was due to impurities despite multiple attempts to purify by recrystallisation.

In many experiments, the gradients at different concentrations are not the same. We have shown when discussing the mixer that diffusion in the pipe for a typical surfactant is negligible. The "in" and "out" gradients are closest for C_{16}TAB but hysteresis is present in all isotherms. Hysteresis arises from slow kinetics at the surface, especially if desorption is slow.

Earlier work by Woods used a Frumkin adsorption isotherm to model the adsorption kinetics in a wall-jet cell.[1] He found good agreement with the predicted kinetic adsorption rate for C_{14}TAB below flow rates of $1\,ml\,min^{-1}$ for a $1.2\,mM$ solution when acquiring spectra at $0.5\,Hz$. He investigated how fast surfactants could diffuse in our system. He determined the limiting flux densities for different CMCs, in figure 5.15, assuming a perfect sink boundary condition.[1] From this data, of the three main TABs we have investigated, our lowest CMC surfactant, C_{16}TAB (at $1\,mM$) would have the lowest flux at $12.8\,\mu mol\,m^{-2}\,s^{-1}$.[1] On the high concentration experiments (to determine the bulk subtraction), we are likely to be reaching the flux limit when the concentration is changing quickly at the beginning and this is another source of error for early times. Given Γ_{max}, we would only need $0.5\,s$ at J_{max} to deliver enough material to the surface to reach equilibrium at the lower concentrations we are using, so the flux does not provide a limitation when using our $5\,s$ acquisitions on non-bulk concentrations.

Literature data from Tyrode *et al.* shows a surface excess of around 2.9 to $3.2\,molecules\,nm^{-2}$ for C_{16}TAB,[9] which, converted, is around 5.0 to $5.3\,\mu mol\,m^{-2}$. Woods estimated the systematic error in the absolute surface excess in our system to be $25\,\%$,[1] so our results do match literature values within this error. The shape (see figure 1.3), a "Langmuir-S shape" is also comparable to those obtained previously. The data also matches well with data ($4.5\,\mu mol\,m^{-2}$) on SiO_2 obtained by Furst *et al.*, with $0.01\,M$ KBr electrolyte present. The group also noted *c.a.* $15\,\%$ ($0.7\,\mu mol\,m^{-2}$) remaining attached after rinsing with $0.01\,M$ KBr, when using $0.2\,mM$ C_{16}TAB, but complete removal by the same concentration of KBr when using $0.8\,mM$ C_{16}TAB. They attributed this behaviour to impurities in the surfactant (as we have seen with C_{12}TAB). This does not match up with our results within error, but our final concentration is never zero.

Figure 5.16 shows kinetic data for the C_nTABs measured using reflectometry from the work of Biswas and Chattoraj. They showed that the adsorption follows a two-step first order rate process with two different process rate constants.[113] While these data are kinetic data on a different substrate (powdered silica, mesh 60-120), and at very low concentration (very early times in adsorption), we can see a similar trend on both adsorption rate and equilibrium surface excess. A monolayer for C_{16}TAB would equate to a surface excess of around $4\,\mu mol\,m^{-2}$, they only reach $0.2\,mM$, well below the CMC.

Figure 5.17 shows selected combined isotherm results for C_nTABs, where n=12, 14 and 16 from our TIR-Raman experiments. We can see that there is a slight increase in Γ_{max}
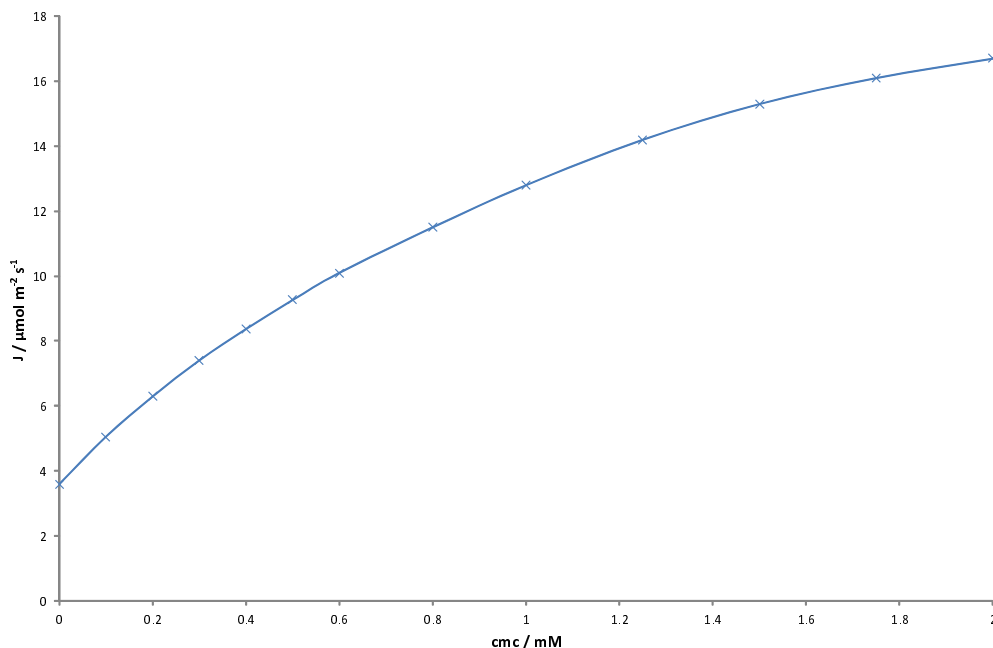
Figure 5.15: Limiting flux to the surface (calculated using $J = D\frac{\mathrm{d}c}{\mathrm{d}z}$ at $z = 0$), for a variety of different CMCs. Adapted with permission from data in reference 1. Copyright Woods 2011

at equilibrium on increase in chain length (due to increased chain-chain interactions), giving approximate mean values of $5.4\,\mu\mathrm{mol\,m^{-2}}$, $6.0\,\mu\mathrm{mol\,m^{-2}}$, and $6.7\,\mu\mathrm{mol\,m^{-2}}$ for C_{12}TAB, C_{14}TAB, and C_{16}TAB respectively. Fan *et al.* studied the adsorption of the same homologous series on alumina, at pH 10 (figure 5.1). Although this is a different substrate, we can see that the shapes of the curves are similar even though the adsorption mechanism will be different. They also found Γ to increase with increasing chain length. Their surface excess values, in the presence of $0.03\,\mathrm{M}$ NaCl, were *c.a.* $0.5\,\mu\mathrm{mol\,m^{-2}}$, $1\,\mu\mathrm{mol\,m^{-2}}$ and $2\,\mu\mathrm{mol\,m^{-2}}$ for C_{12}TAB, C_{14}TAB, and C_{16}TAB respectively.[172] Alumina normally possesses a positive surface charge, but in their case at high pH, it will be negative. Vanjara and Dixit found a similar trend in results when increasing chain length with these same surfactants in $1\,\mathrm{mM}$ KCl on (hydrophobic) PTFE.[176]

Comparing our data on the C_{n}TAB homologues, we can see that the initial slope before maximum surface excess is reached is slower for C_{12}TAB. The log-log plot represents chemical potential linearly on the x-axis, so the gradient on this graph represents the measure of cooperative interactions between surfactant molecules, where favourable interactions are represented by a steeper gradient. On a linear axis, for C_{12}TAB, there appears to be a change in gradient around $7\,\mathrm{mM}$ during the "in" experiments. There may be an initial plateau at very low concentration, but this is hard to confirm with the results we obtained. C_{14}TAB also appears to show a similar profile: initially steep, then reducing, and finally an "exponential-like" increase in Γ. This is consistent with literature results mentioned above.[9]

Overall, our "out" measurements for C_{14}TAB and C_{16}TAB are consistent for the point at which the surface excess begins to decrease across different concentration solutions, however the final surface excess does vary for a particular concentration. This suggests
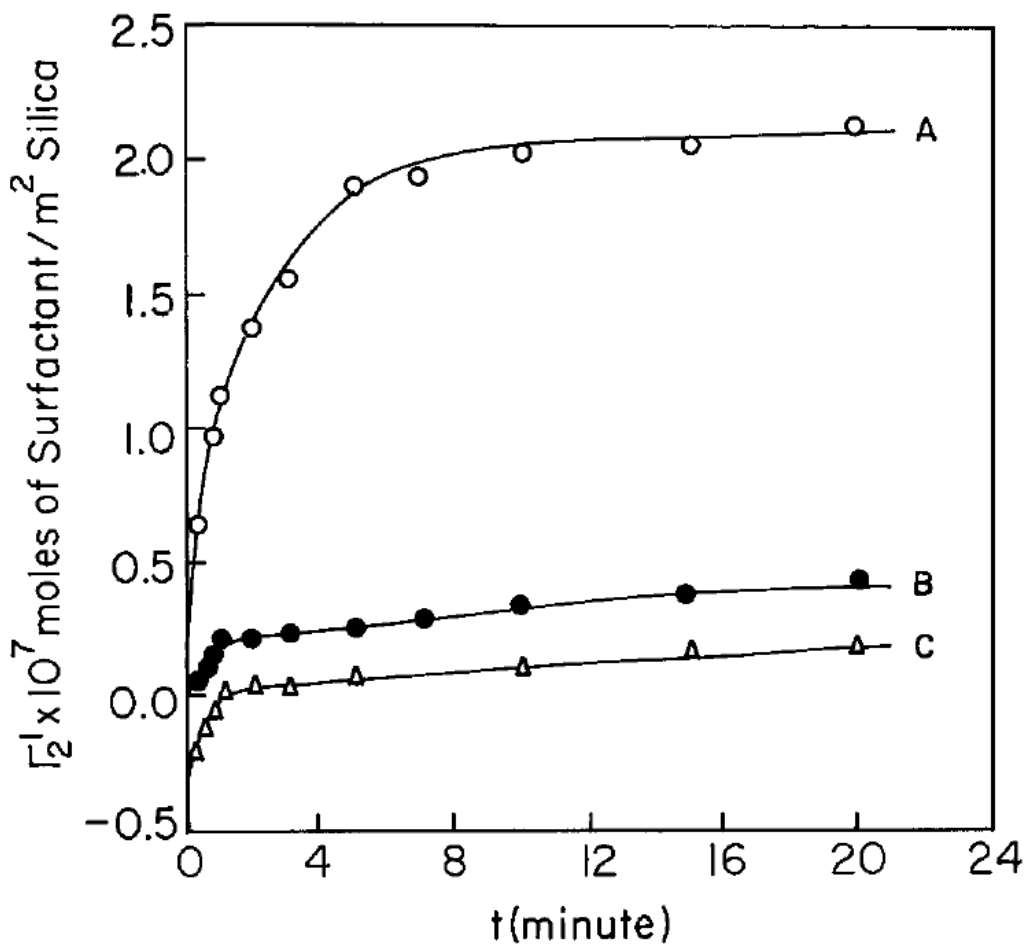
Figure 5.16: Plot of Γ *vs.* time for $C_{12}TAB$ (C), $C_{14}TAB$ (B) and $C_{16}TAB$ (A) at silica-water interface at pH 5, 318 K, 0.03 mM. Reproduced with permission from reference 113. Copyright 1998 Elsevier

that we do have precise control of the solution concentration, but something else is affecting the affinity of the surfactant for the surface. When good data was obtained, for C_{14} and $C_{16}TAB$, our results match well with the literature CMC values.
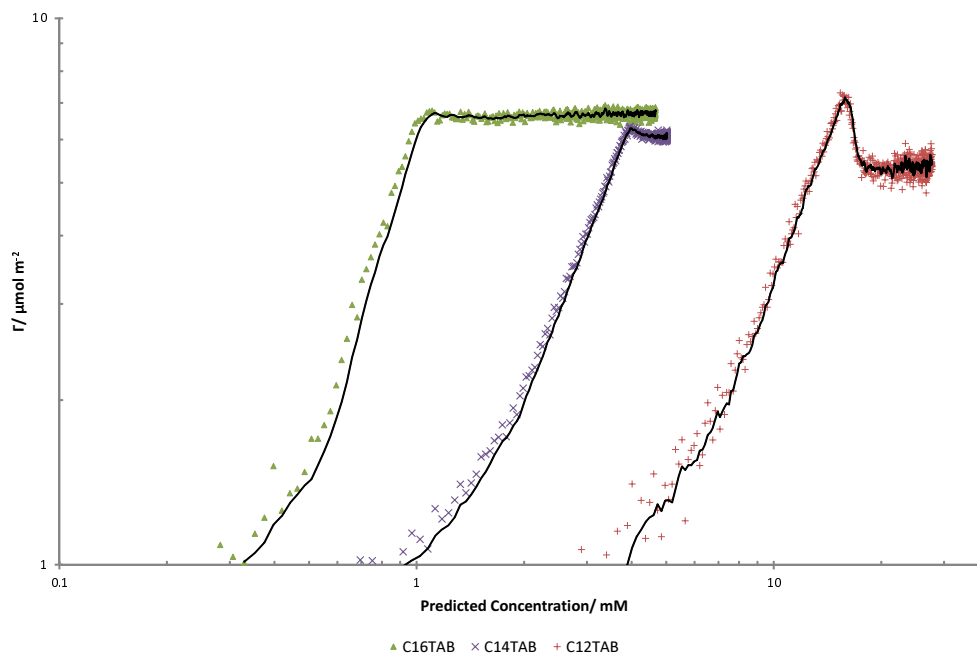
Figure 5.17: Combined C_nTAB adsorption isotherms on silica, trend-lines are 5-point moving averages

5.3 Double-Chained 4° Ammonium Bromides

5.3.1 Introduction

Supervising and collaborating with our 4th year MChem students Jack Harris and Michelle Lambert, over two consecutive years, we undertook an investigation to see if the presence of different anion salts had an affect on bilayers of double-chained quaternary ammonium surfactants and their phase transition temperature. Purification of the double chained ammonium bromides by recrystallisation was performed with Joe Beckwith during his summer project.[177]

Following initial training by me, the experimental results were obtained by Harris and Lambert. I wrote the MATLAB programs for the peak ratio analysis and carried out most of the factor analysis of their data. The conclusions presented here are my interpretation of their results.

We also wanted to determine if the Hofmeister series had any effect on the competitive displacement of anions in the bilayer. To do this, first we had to find a stable bilayer. Beckwith focused mainly on finding out which bilayers (of the general formula $CH_3(CH_2)_{(n-1)}N^+(CH_3)_2Br^-$, where n=12, 14, 16 and 18) were stable and Harris, the effect of temperature on the behaviour of these layers and their phase transition. Lambert studied the binding of Raman-active anions (such as thiocyanate (SCN^-) and sulphate (SO_4^{2-})) and the exchange of these ions in surfactant layers.

All experiments were performed on the Renishaw spectrometer (since the new spectrometer was still under construction).

DHDAB is a model membrane for biological bilayers (cell membranes and vesicles). Cell membranes separate the contents from the surrounding environment and research on

bilayers is important for nano-compartmentalisation and drug delivery. Studying model bilayer systems to find similar molecules to mimic biological systems and also allow for the development of targeted drug delivery systems, where a vesicle protects the drug until it reaches its target site. Ion exchange into bilayers is of interest as many organisms rely on the interactions of ions with bilayers, such as nerve impulses and chemical signalling.

5.3.2 Results

Firstly, we will look at the phase transition results on DHDAB (n=16). Prior to this work, Beckwith determined this surfactant to be the double-chained ammonium bromide most resistant to water rinsing from silica, that it provided a strong Raman signal, and an easily accessible phase transition temperature.

Phase Changes

The temperature at which the transition of the bilayer from gel to fluid phase was studied. Higher temperatures result in the chains being in the higher-energy gauche conformation, where the chains are packed less orderly, which is termed the fluid phase. Lowering the temperature increases order and the surfactant enters a gel phase. The process can be monitored by observing the change in spectra of the methylene stretches in the alkyl chains of the adsorbed bilayer. Figure 5.18 shows the spectra at various temperatures, normalised to the water intensity of the highest temperature. The two C−H peaks, d^- (symmetric) and d^+ (anti-symmetric) at around $2852 \, \text{cm}^{-1}$ and $2890 \, \text{cm}^{-1}$ respectively, are used to monitor the phase transition. There is also a change in the shoulder at $2930 \, \text{cm}^{-1}$ (the Fermi resonance of the symmetric stretch) which is not used for our analysis (because it changes less). While the peaks would shift to higher wavenumber on increase in temperature, due to the expected increase in bond vibrational energy at higher temperature, but for these C−H stretches, the population of the $v = 1$ is negligible (and $v = 1 \rightarrow 2$, if it was populated, would be at lower wavenumber due to anharmonicity) therefore this is not the main cause of the shift. The peak shift at these temperatures is likely due to coupling of vibrational modes in the all-trans chains: orbitals on adjacent chains overlap and this causes broadening. The C−H groups in adjacent chains are out of phase with each other and the dipole moments add, leading to the symmetric stretch increasing in frequency and the antisymmetric stretch decreasing in frequency. The ratio of these two peaks will be hereon in referred to as the d^-/d^+ ratio. The ratios were calculated from a MATLAB script which took the maximum intensity of the spectra within two ranges centred on each of the symmetric and anti-symmetric peaks. Figure 5.19 shows the results from temperature ramp experiments performed on a DHDAB bilayer. A lower ratio of d^-/d^+ (≈ 1.05) indicated the bilayer was in the fluid phase and higher ratios (≈ 1.45) showed that the bilayer was in the gel phase. Results are shown with and without surfactant present (just water) in the bulk. There is hysteresis upon heating and cooling. We attributed this to supercooling of the bilayer when, without a seed for the phase change to occur, the phase change occurs at a lower temperature. Super-heating of solids has been shown by Bai and Li not to follow classical nucleation theory unless under extreme conditions, such as high pressure.[178] This is why we used the heating curve to determine the phase transition temperature as it was likely to be closer to the

true temperature. It is also worth noting that the temperature we recorded is not the temperature of the bilayer, but the temperature of the cooling water in the cell (as his newer cell had a port for a thermocouple), however, we performed rough calculations using the thermal conductivity of glass and water which suggested that the difference was too small to affect the results.

The lack of a sharp phase transition was attributed to the size of the area probed by the laser beam, where the phase transition travels over the area under investigation. However, we suspect that the surfactant forms domains on the surface of different sizes and these transition at slightly different temperatures. If the broad transition was due to the phase change travelling over the surface, we would have seen a sharper phase transition when changing the temperature at a slower rate ($0.22\,°\mathrm{Cmin}^{-1}$). Alternatively, the delay could be due to interactions with the substrate. The nearly identical curves with and without bulk surfactant present showed us that the bilayers are stable to heating and cooling, and do not lose material. The reported literature value for the phase transition temperature of DHDAB is $28\,°\mathrm{C}$,[179] which is in agreement with the results.
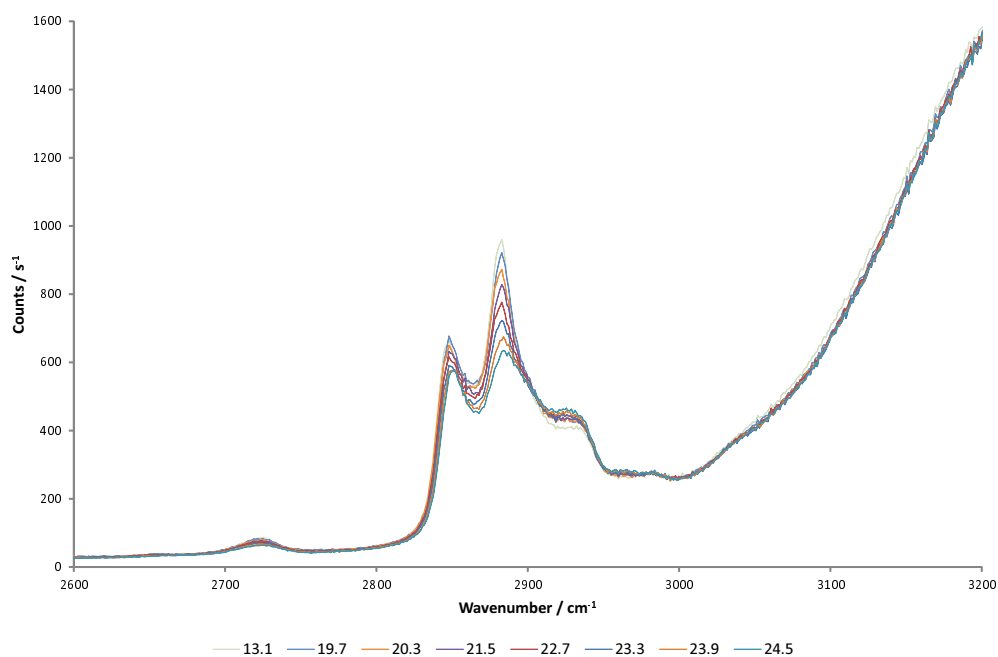
Figure 5.18: DHDAB spectra at different temperatures (temperature in °C in legend). Normalised to spectrum obtained at highest temperature, 532 nm, 700 mW
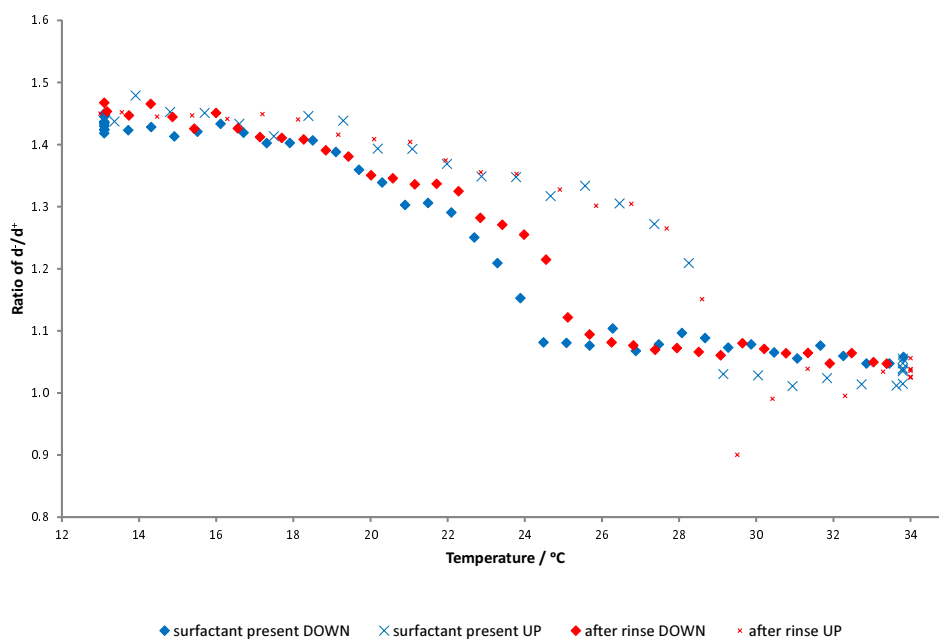
Figure 5.19: Temperature ramp d^-/d^+ ratio for DHDAB with excess surfactant (surfactant present) and after rinsing with water (after rinse). The crosses show the heating curves (UP) and the diamonds show the cooling path of the temperature ramp (DOWN).

Effect of Sodium Ions

We were interested in how the presence of other ions affected the bilayer and its phase transition temperature, in the absence of DHDAB in the bulk. As before, these layers were formed overnight at 35 °C. To see if the additional sodium (Na^+) ions in solution had any effect we started by adding sodium bromide (DHDAB has a bromide (Br^-) counter ion) to an already formed bilayer. High (≈ 100 mM) concentrations of NaBr caused the bilayer to crystallise due to the salt raising the Krafft point (T_k). Below T_k, the bilayer is metastable with respect to the crystal. Figure 5.20 shows the same temperature ramp experiment performed with 1 mM NaBr solution present in the bulk along with the results from figure 5.19 above.

Due to time constraints we did not fully investigate the overall lowering of d^-/d^+, but proposed that the Na^+ cations might displace the cationic surfactant and disrupt the packing and decrease the ratio. We would expect the addition of salt to reduce the electrostatic repulsions between the head-groups and increase the packing, thereby increasing the ratio. If the surfactant was being displaced we would observe a weaker spectrum (which is not observed), therefore this effect must be due to some other unknown factor. The bilayer may crack as it shrinks on cooling (resulting in a weaker spectrum), which we may not observe in the probed region.

The slow change in ratio at constant temperature at around 17 °C on the cooling cycle with the NaBr present suggests the system was slower to reach equilibrium. After decreasing the rate of temperature change to 0.22 °C min^{-1}, we observe a phase transition temperature similar to when just surfactant was present, although still with some lag when constant temperature is reached. Overall the phase temperature on cooling appears to occur at the same point (≈ 24 °C). The presence of sodium ions slows down the rate of reorganisation, which could indicate our expected reduced electrostatic repulsion, to form regions of closer-packed chains which grow in size, slowly, over the substrate. Further experiments at static temperatures, where the bilayer is allowed to fully equilibrate, may provide better insight.

Other Hofmeister Ions

The main aim of our investigation was to see if the range of salts in the Hofmeister series had any effect on the phase transition temperature and whether one anion displaced or competed with another. The cation was Na^+ throughout. We decided initially to use thiocyanate (SCN^-) as the most extreme "salting-in" and sulphate (SO_4^{2-}) as the most extreme "salting-out" salts. Both anions have the advantage of being Raman active, so we should be able to observe their presence in the bilayer. The ionic strength was maintained when changing the salt and the bilayer formed overnight at 35 °C, as before.

Figure 5.21 shows that SO_4^{2-} lowers the d^-/d^+ ratio below the melting temperature of the pure bilayer, similar to the behaviour of Br^-. The cell was filled with salt solution at 35 °C before cooling to 10 °C, then starting the temperature increase while monitoring the Raman spectra. In the presence of SO_4^{2-} there does not appear to be a definitive phase change, but a gradual increase in the d^-/d^+ ratio. The change in this ratio on adding the anion was large and rapid. He concluded that this could be due to the formation of intermediate phases, similar to an effect seen by Goto *et al.* on their studies on dioctadecyl
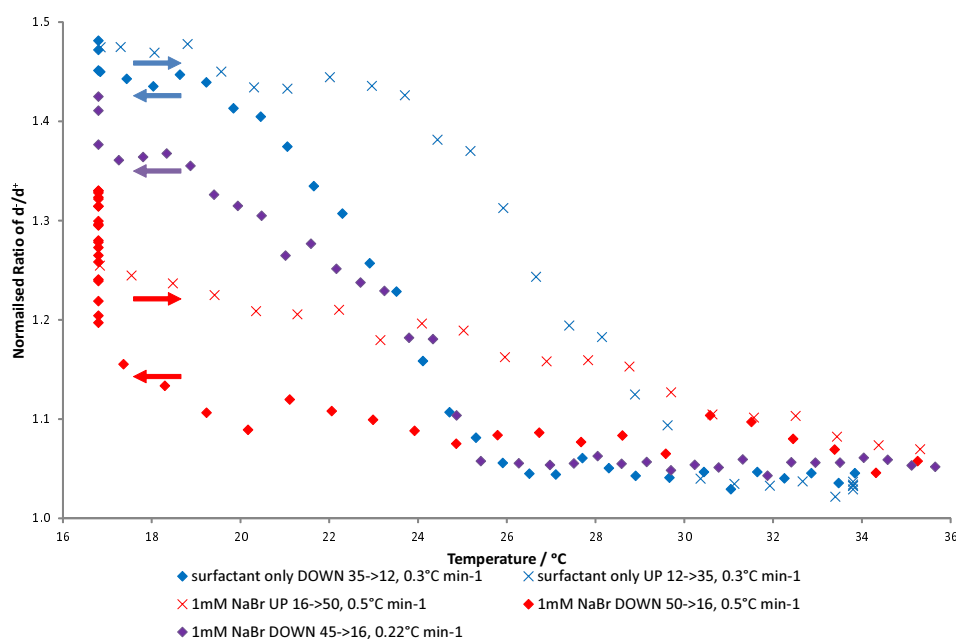
Figure 5.20: Temperature ramp measurements for preformed DHDAB bilayer in the presence of $1\,\text{mM}$ NaBr solution. The crosses and diamonds represent the heating (UP) and cooling (DOWN) curves respectively. The rate of temperature change, direction and the starting and ending temperature (T_{start} to T_{end}) is also shown in the legend. The horizontal arrows are to show the direction of temperature change clearly. A temperature ramp for just surfactant present (blue markers) is shown for comparison.

dimethylammonium bromide (DODAB, n=18).[180] They proposed that a fluid crystal phase co-existed with the gel phase near the transition temperature. However, further study with a lower rate of temperature change is needed to investigate this behaviour fully.

In contrast to both $SO_4{}^{2-}$ and just having surfactant present, SCN^- lowers the phase transition temperature to $\approx 18\,°C$, nearly $10\,°C$ lower. The range from maximum to minimum peak ratio is also lower. This means that the kinetic barrier to phase transition is lower, however the phase change does occur over a wider temperature range, but this could again be due to differences in phase transition temperatures between domains. Determination of the phase transition temperature for DHDAB in the presence of other salts is needed to determine if the Hofmeister series does play a role in this behaviour.

At the end of the project we performed brief experiments to show that after rinsing with water, SCN^- could be detected in the bilayer at around $2050\,\text{cm}^{-1}$ by Raman spectroscopy, as shown in figure 5.22. The weak peak and fast ($\approx 50\,\text{s}$) adsorption meant that later attempts at following the kinetics of adsorption were limited to around $10\,\text{s}$ time resolution. We observe the SCN^- peak in the $20\,\text{mM}$ solution, with contributions from the bulk also in the evanescent wave present before the rinse. Further discussion on SCN^- peak intensity is presented later on figure 5.24. Although from our work on the mixer, we have seen that our cell does not always rinse completely. I would not expect water to remove the SCN^- as charge neutrality is required, but other species present in the water, such as carbonate, could displace the SCN^-.
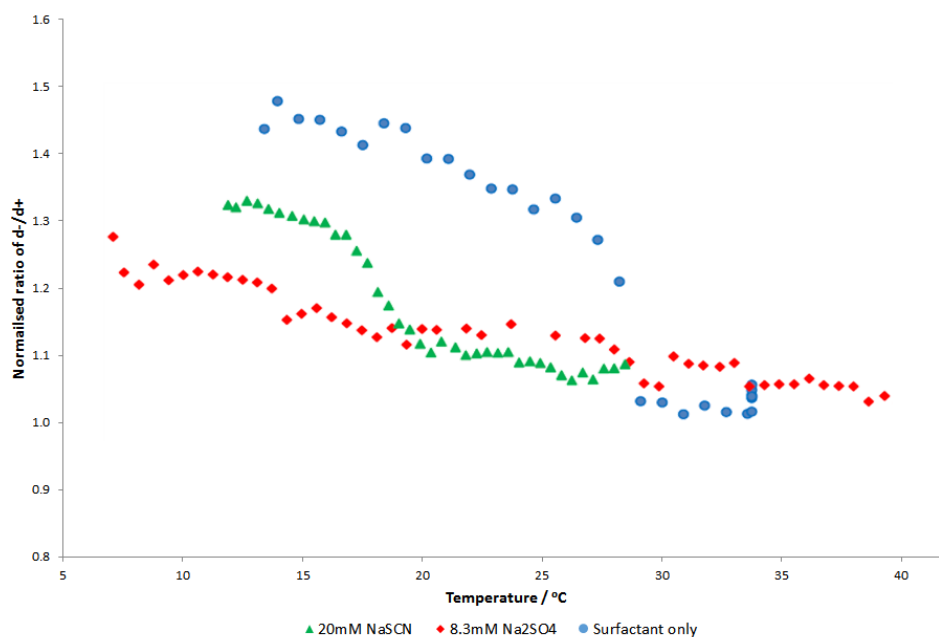
Figure 5.21: Plots of d^-/d^+ peak ratio from temperature ramp (increase) experiments for DHDAB bilayer preformed at 35 °C in the presence of 20 mM NaSCN and 8.3 mM Na$_2$SO$_4$, in pure water (no bulk surfactant). Data from the temperature ramp experiment with bulk surfactant present is shown for comparison.

Using a Br$^-$ solution it was possible to completely remove the SCN$^-$ anions (but not with pure water). Upon rinsing with pure water and re-adding SCN$^-$ solution, the peak at 2050 cm^{-1} reappeared although, as Br$^-$ is not Raman active, we were unable to determine if all the Br$^-$ had been removed, but the intensity of the SCN$^-$ peak relative to the background returned to the same value. Comparing their hydrodynamic size, R_H, of Br$^-$ and SCN$^-$ at 1.77 Å [181] and 1.60 Å [182] respectively, we can see they are close and are likely to have similar diffusion rate and could replace Br$^-$ by SCN$^-$ in the Stern layer.

Further to the above, similar experiments with SCN$^-$ and SO$_4{}^{2-}$ were performed. While the SO$_4{}^{2-}$ anions initially removed the SCN$^-$ peak, after addition of the SO$_4{}^{2-}$ stopped, the SCN$^-$ peak reappeared showing that SCN$^-$ ions are diffusing back to near the surface. The hydrodynamic radius of SO$_4{}^{2-}$ is larger at 2.31 Å, [183] so he attributed the effect to the size of the hydration shell of SO$_4{}^{2-}$ when dissolved in the water, but as the Hofmeister effect is not just dependent on size, there must be a favourable interaction of SCN$^-$ with the bilayer.

The effect of SO$_4{}^{2-}$ being unable to fully replace SCN$^-$, unlike the interchange with Br$^-$ could be due to the Hofmeister effect, as SO$_4{}^{2-}$ is at the opposite end to the other two anions.

To further our understanding of the effects of ions on bilayers of dichain quaternary ammonium surfactants, Lambert undertook additional studies on DHDAB. After continuing the previous work on SCN$^-$, specifically looking at the kinetics of salt entering the layer, we also looked at the Raman-active sodium salts of azide (N$_3{}^-$), nitrate (NO$_3{}^-$), acetate (C$_2$H$_3$O$_2{}^-$) and deutero-acetate (C$_2$D$_3$O$_2{}^-$).

Some experiments used an increased laser power of 1500 mW to improve the signal to
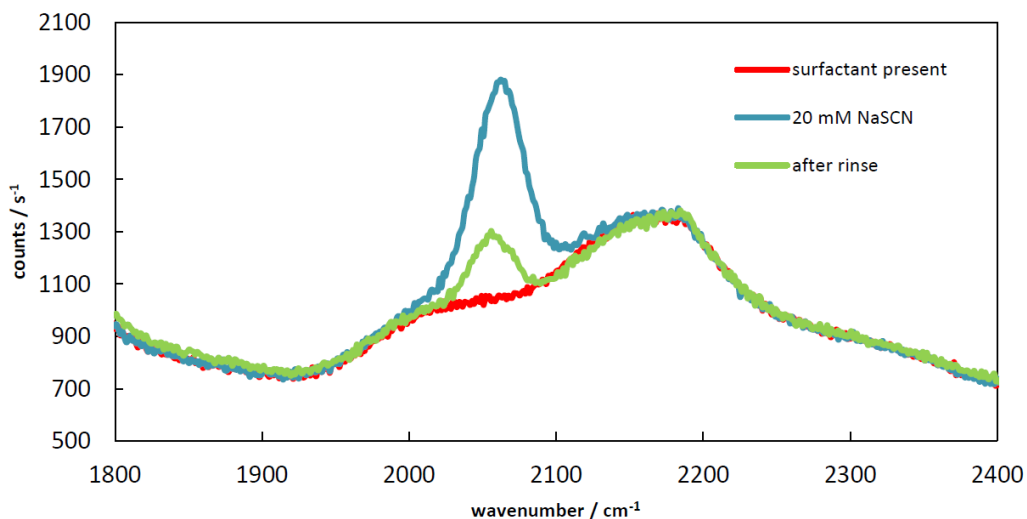
Figure 5.22: Raman spectra of DHDAB and DHDAB with $20\,\mathrm{mM}$ SCN$^-$ at $35\,°\mathrm{C}$ before and after rinse with $100\,\mathrm{ml}$ of UHP water. $300\,\mathrm{s}$ exposure, $532\,\mathrm{nm}$, $1500\,\mathrm{mW}$

noise ratio. We checked to ensure laser power did not influence the bilayer.

We attempted to monitor the kinetics of SCN$^-$ adsorption into the bilayer with TFA, with the ideal components given in figure 5.23. However, the peak was found to shift up in wavenumber by nearly $10\,\mathrm{cm}^{-1}$ on increase in concentration and this limited the technique's use. A reason for this shift was not discussed, but it may have been due to bound SCN$^-$ having a different Raman shift to the bulk, perhaps due to the Stark effect. Alternatively the frequency of bound SCN$^-$ could have shifted as more Br$^-$ was replaced.

Due to the two different spectral windows (around $2100\,\mathrm{cm}^{-1}$ and $2900\,\mathrm{cm}^{-1}$) needed to view both the anion and bilayer respectively, we were only able to monitor them kinetically, separately. We did take longer ($10\,\mathrm{s}$) exposures to check the integrity of bilayer, before and after each run. Twenty $30\,\mathrm{s}$ static exposures were used to observe the SCN$^-$ peak in the same way. This allowed us to see if the SCN$^-$ caused a change in the bilayer structure on addition/removal.

Problems of focal drift plagued experiments as before, but without a strong water background, as in the $2900\,\mathrm{cm}^{-1}$ region, we added $15\,\mathrm{mM}$ acetonitrile to act as an internal reference to all solutions. Acetonitrile has a peak at $2253\,\mathrm{cm}^{-1}$ and hence it can be viewed simultaneously with the SCN$^-$ peak. Being a polar, aprotic molecule we did not expect it to affect the bilayer (although this was not checked).

Varying the amount of SCN$^-$ concentration in the bulk, with the bilayer present, we acquired the data in figure 5.24. The repeat of the $1\,\mathrm{mM}$ solution after the $40\,\mathrm{mM}$ solution shows that the peak returns to its original height. We intended to perform TFA to produce an isotherm and determine the maximum ion concentration in the bilayer, before the only bulk signal increased. However, due to the large peak shift, TFA was unable to separate the components.

It is difficult to tell if there are separate peaks for bound and free SCN$^-$, but it is possible that the bound ion peak occurs at a lower wavenumber. Performing further analysis on the small amount of data in the work, to determine the peak areas from the data in figure 5.24, we obtain the data shown in figure 5.25. We can again see that
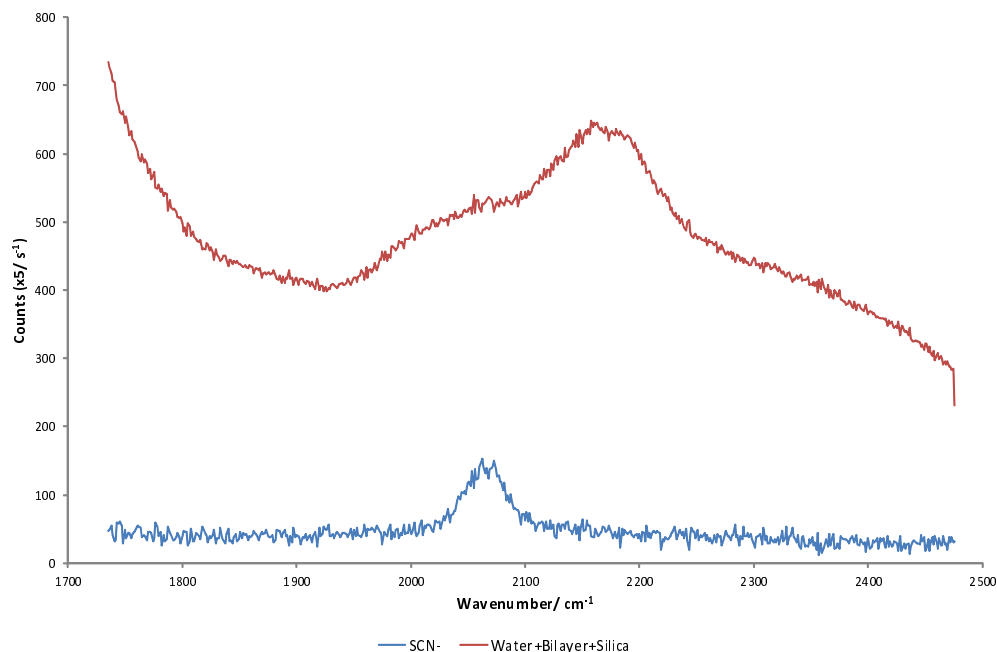
Figure 5.23: SCN^- components, using NaSCN in a capillary to generate the pure salt target, 532 nm, 700 mW

the peak height returns to its original level after increasing the concentration, showing that the binding is fully reversible. With limited data, it is hard to make any conclusive comments, but if the increase is linear with concentration, then the increase is likely due to just an increase in the bulk concentration and adsorption is complete by 1 mM.

We undertook further experiments to monitor the displacement of Br^- by SCN^- by increasing ("inc") and decreasing ("dec") the mole fraction while keeping a constant salt concentration of 1 mM and a constant temperature of 35 °C. The results (figure 5.26) differed from what Harris obtained—where the SCN^- ion peak is displaced by Br^-—but when returning to pure SCN^- the peak did not reappear in the spectra. We did observe a phase change when monitoring the 2900 cm^{-1} region and a change in the d^-/d^+ ratio which might cause this difference between the two sets of results. If the bilayer changes to fluid phase, then the increased packing might prevent the ions from diffusing.

Alternatively, other ions such as hydroxide (OH^-) or bicarbonate (HCO_3^-) could be involved. There could even be trace ion contamination from the silica substrate or glass cell. As we are only able to see one of the ions, it is unclear what is happening.

To overcome only knowing what it happening to one ion, scoping experiments using different Raman active salts, first in a capillary, and then on the bilayer were performed. These showed that SO_4^{2-} only had low intensity peaks, NO_3^- and N_3^- had peaks which overlapped the background from the silica substrate, and were thus difficult to monitor. The peaks from deutero-acetate ($CD_3CO_2^-$) overlapped with the DHDAB spectra. $CD_3CO_2^-$ was detectable in the DHDAB bilayer (peaks at 2115 cm^{-1} and 2190 cm^{-1}), but was weaker than SCN^-. $CD_3CO_2^-$ also has the advantage that it is visible in the same region as SCN^- and hence we should be able to monitor both peaks simultaneously. Figure 5.27 shows the spectra for 20 mM solutions of (Na^+) $CD_3CO_2^-$ and SCN^- taken from a capillary.
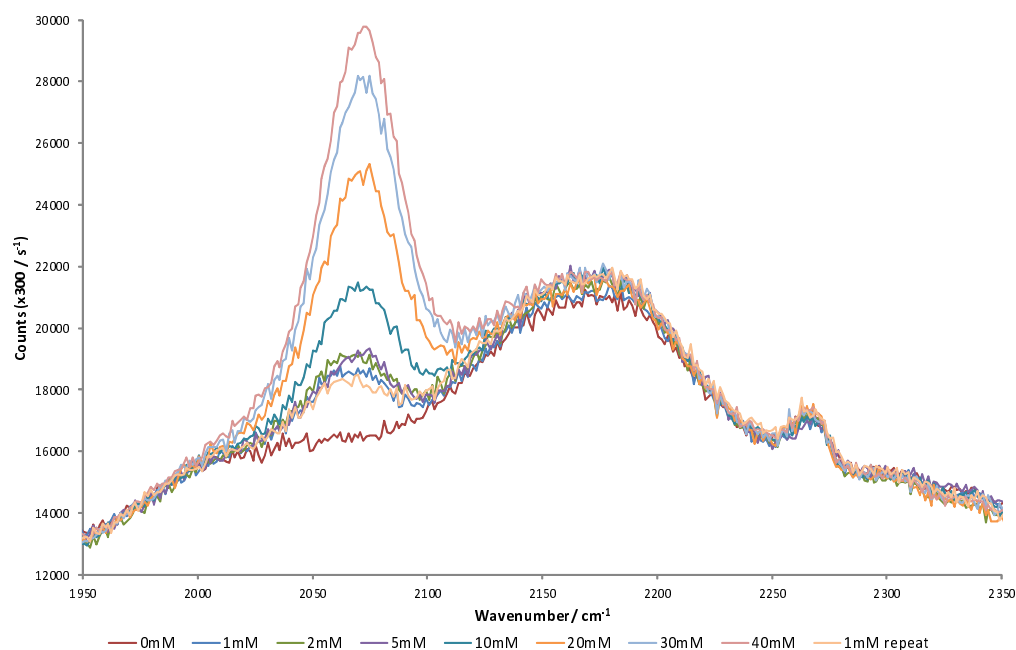
Figure 5.24: SCN$^-$ spectra on increasing SCN$^-$ concentration. 35 °C, 700 mW, 30×10 s exposure, 532 nm

Using both $C_2D_3O_2{}^-$ and SCN$^-$ we repeated our displacement experiment, by varying the mole fraction, while keeping the concentration at 1 mM. This data was analysed by TFA using the components in figure 5.28.

Figure 5.29 shows the results from TFA analysis. $CD_3CO_2{}^-$ appears to remove SCN$^-$. On replacement with SCN$^-$ the signal returns, to almost identical levels. However, we are unable to see $CD_3CO_2{}^-$ in the bilayer at this concentration: two factors were required for the analysis. Neither increasing or decreasing the mole fraction gives zero component weight for zero SCN$^-$ concentration, possibly due to the background varying. No firm conclusions could be drawn on the relative binding affinities of the two anions.

5.3.3 Discussion

No firm conclusions on the Hofmeister effect can be drawn from their work due the limitations in studying few Raman active ions in the spectral window of the silica substrate. We have shown that we can monitor some ions in the bilayer, and that some ions replace others. Iodide would have been interesting to study, but caused crystallisation of the bilayer and while the temperature could have been increased, we know from other experiments that we lose focus quickly at higher temperatures. It is still unknown whether order of replacement is related to the Hofmeister series. Replacing the silica hemisphere an alternate substrate, may allow the use of other Raman active anions. Use of calcium fluoride (CaF_2) may improve results, as this crystalline material has a background in the region of interest consisting of only one sharp peak (at 321 cm^{-1}). A pure CaF_2 substrate has a positive surface charge, hence DHDAB may not adhere. Later work creating silica coated CaF_2 hemispheres to minimise background while still presenting a silica substrate resulted in unacceptable fluorescence. Other Raman active ions, such as cyanide (CN$^-$)
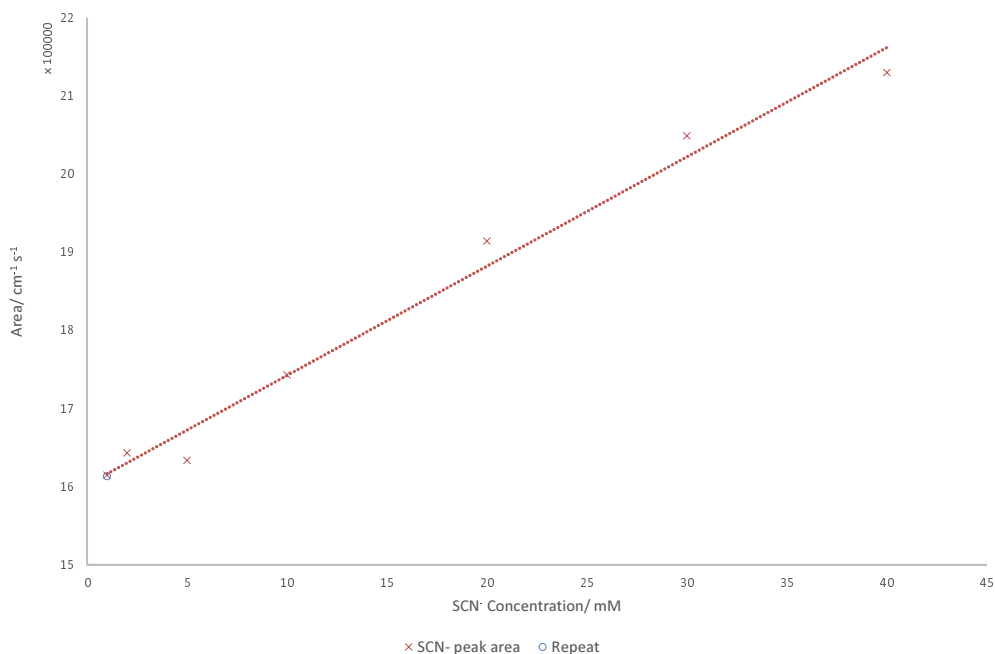
Figure 5.25: Peak area after background subtraction against bulk SCN^- concentration in the presence of DHDAB bilayer at 35 °C, "repeat" is the result after returning the concentration to 1 mM. Error data unavailable

were considered, but this ion was ruled out due to its toxicity.

Further analysis and discussion of their results has added some reasoning for the slow transitions in the phase transition experiments with the possible formation of different sized domains and a better explanation for the reappearance of SCN^- peaks after rinsing with SO_4^{2-}. We were able to propose the difference in wavenumber between bound and unbound SCN^- peaks was due to the Stark effect, and produce further analysis on SCN^- adsorption to the bilayer, but were limited in our conclusions by the small amount of data available.
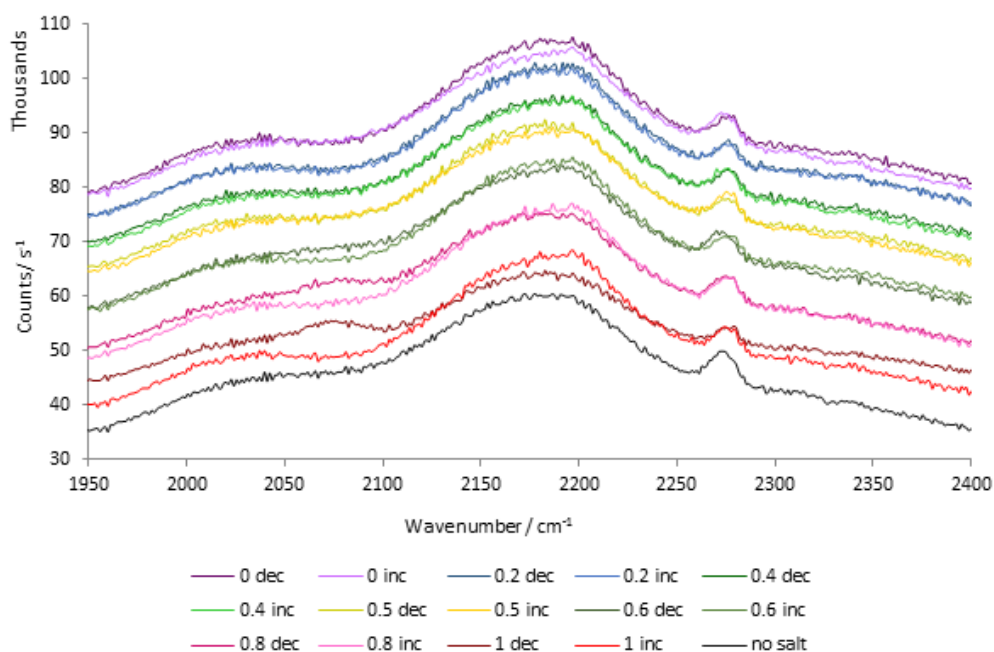
Figure 5.26: Spectra with varying ratios of SCN^- and Br^-, legend shows SCN^- mole fraction. Overall concentration 1 mM, 30×10 s exposure. y-axis offset. The notation 'dec' being the first experiment where SCN^- concentration was decreased and 'inc' the second experiment where the mole fraction was increased again. 35 °C, 1 mM, 532 nm, 1500 mW
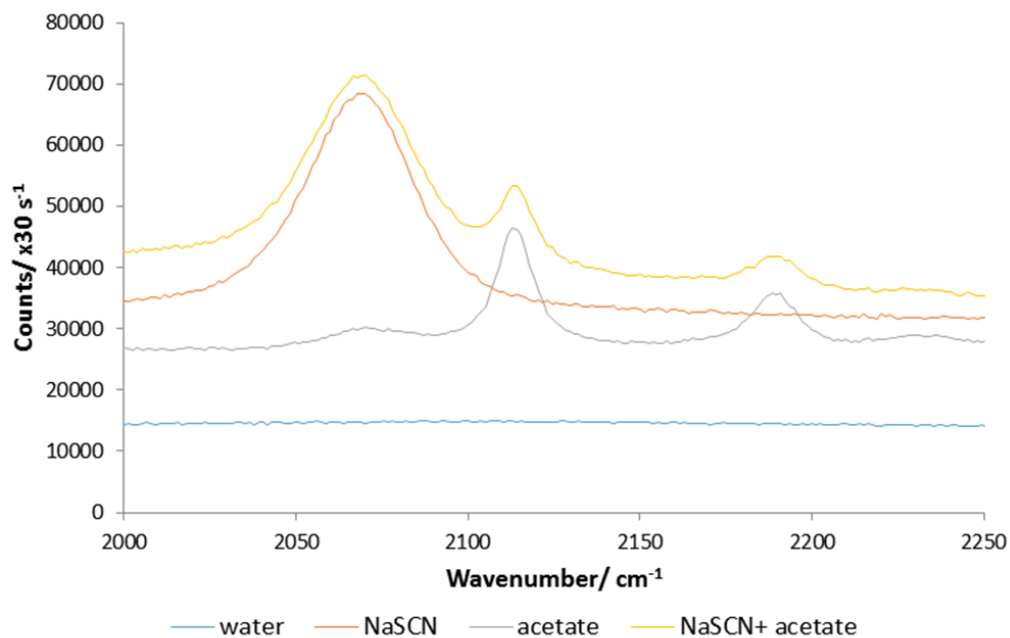
Figure 5.27: $CD_3CO_2^-$ and SCN^- spectra from a capillary (20 mM), 200 mW, 10 mM, 532 mW
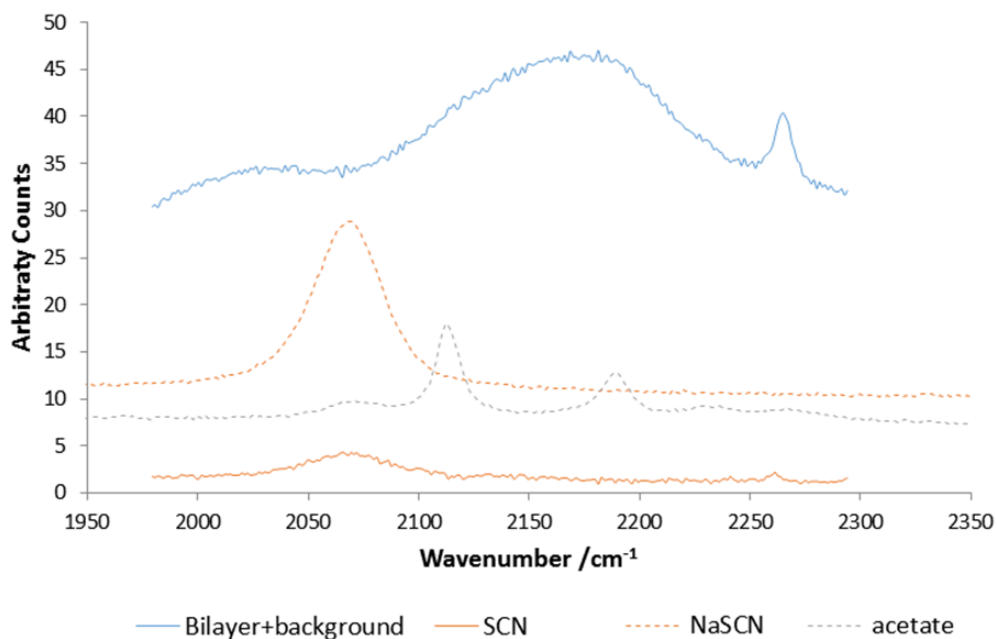
Figure 5.28: Target factors used for SCN^- and $CD_3CO_2^-$ analysis with capillary SCN^- and $CD_3CO_2^-$ peaks overlaid (dashed, not to y-scale), acetonitrile present in SCN^- component. 532 nm, 1500 mW
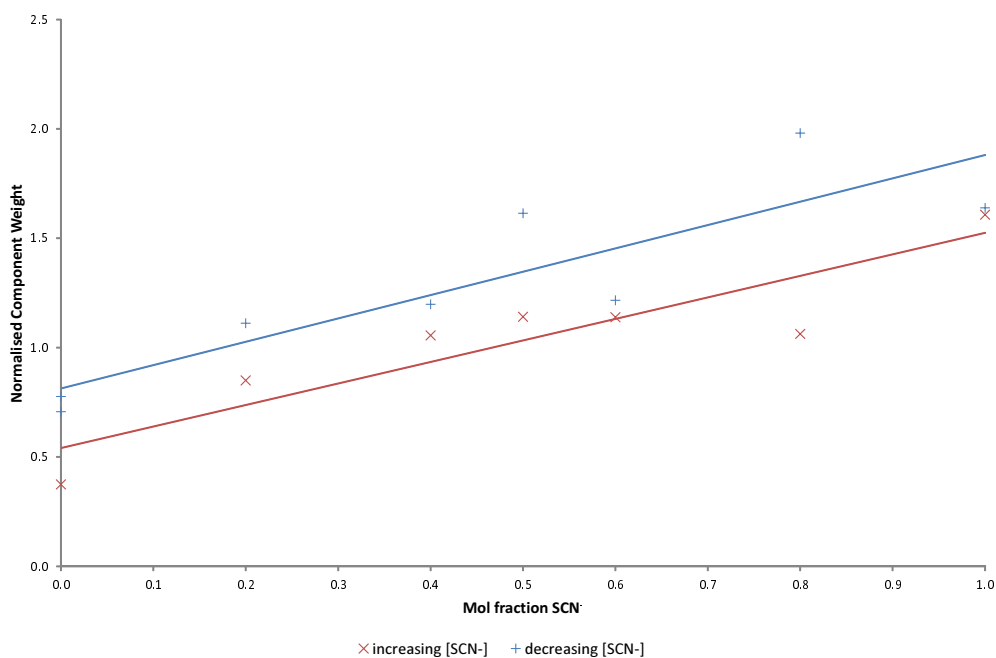
Figure 5.29: The component weight of SCN^- with $COOCD_3^-$ as a function of its concentration. The component weight is normalised to the water signal.

5.4 $\mathbf{C_{12}}$LAS & $\mathbf{C_{12}E_6}$ multicomponent systems

5.4.1   Introduction

Surfactants, as discussed in the introduction, are often utilised as detergents. Different surfactants adhere better to some substrates over others. Often to improve adsorption surfactant mixtures are used. For example, the anionic surfactant sodium dodecylbenzenesulfonate, commonly known as C_{12}LAS (or just LAS or SDBS), does not adsorb from water to hydrophilic, negatively charged surfaces such as silica. The addition of a nonionic surfactant is thought to enhance LAS adsorption. We planned to see how the presence and relative amount of nonionic surfactant (polyethylene oxide alkyl ethers, of the form C_nE_m) affected adsorption of LAS. We investigated LAS and $C_{12}E_6$ individually and as mixtures of both at different ratios ($2:1$, $3:1$, $1:1$ and $1:3$ (C_{12}LAS : $C_{12}E_6$)), absorbing onto hydrophilic and hydrophobic silica. By subtracting the amount of nonionic surfactant, we would be able to determine the amount of LAS adsorbed. These experiments were performed to investigate the behaviour of typical laundry detergents and follow on from Woods' work where he was able to resolve a mixed binary system consisting of C_{16}TAB and Triton X-100 (TX-100), another nonionic surfactant.[1] TIR-Raman was chosen as the technique probes only (very close to) the surface of interest and allows for monitoring of the system in real time and this technique was shown by Woods to work well for this mixture.

     The behaviour of mixtures of nonionic and anionic surfactants are also of interest because surfactant mixtures are also often used for commercial processes such as flotation of minerals, oil recovery and in paints.

5.4.2   Results

All experiments were performed on the Renishaw spectrometer as the new spectrometer was still under construction. To estimate the percentage of a bilayer, we look at the raw C−H counts at $2900\,\text{cm}^{-1}$ against the water background at $3125\,\text{cm}^{-1}$, and compare this ratio to our known C−H to H_2O ratio for C_{16}TAB on silica. This estimate assumes that a bilayer of C_{12}LAS and $C_{12}E_6$ has the same intensity at $2900\,\text{cm}^{-1}$ as a bilayer of C_{16}TAB (which is not a complete bilayer).

Hydrophobic Silica Isotherms

Despite several attempts, no satisfactory data resulted from isotherms for the individual surfactants on hydrophobic silica owing to focal drift when using the mixer with the Renishaw system as longer experimental times increased the likelihood of drift. The difficulty of bubbles attaching to the surface also hindered success. More on the problems of a hydrophobic surface and the Renishaw system will be discussed later.

i)   *C_{12}LAS on Hydrophilic Silica*

     The CMC ($0.7\,\text{mM}$)[158] fits with the data in figure 5.30, which shows desorption of a $(0.926 \pm 0.003)\,\text{mM}$ solution of C_{12}LAS from a hydrophilic (acid-washed) silica using

the large in-line mixer. Component separation (inset) was poor. Four other attempts to obtain satisfactory data at different concentrations and to monitor adsorption with the Renishaw system failed. The step at around 0.15 mM coincided with a drop in water and surfactant component weights (possibly due to a bubble passing through the system).

Above the CMC, any increase in surfactant signal can be ascribed to surfactant in the bulk solution within the evanescent wave, but as we did not successfully measure far above the CMC, bulk correction to work out surface excess will be very inaccurate. Rough estimates give a large area per molecule of 500 Å, but we would not expect pure LAS to absorb to a hydrophilic silica surface. As the surfactant-coated surface is charged, it may repel the charged surfactant in the bulk and affect the bulk signal however, at 1 mM concentration the Debye length is just 10 nm, much lower than our penetration depth ($\approx$100 nm) and so this effect will be minimal. Additionally, any impurities in the $C_{12}LAS$ would produce a peak around the CMC which could also affect the slope of this line and hence the calibration. LAS is a bulk commercial surfactant and therefore it is likely to contain many impurities. Additionally, commercial LASs are a mixture of linear alkyl chains consisting of 10–13 carbon atoms and the phenyl ring is randomly distributed in all possible positions (except 1-phenyl).[40] We may only be observing impurities absorbed. The linear slope below the CMC is unusual and indicative of impurities desorbing. Looking at the raw data and comparing to results from our $C_{12}TAB$ measurements using the C$-$H band intensity relative to the background we can see that we get approximately the same signal, so around a monolayer. To obtain a reliable calibration we would need to obtain better data at much higher concentrations too. Looking at the raw data, the total adsorbed amount of $C_{12}LAS$ is around half that of what we would see for $C_{16}TAB$ on silica which suggests the formation of about a monolayer of something.

ii)   ***$C_{12}E_6$ on Hydrophilic Silica***

None of the $C_{12}E_6$ isotherms produced acceptable data and experiments were plagued with problems with bubbles. This is despite degassing the water by drawing a vacuum, avoiding agitation and being thorough in checking for bubbles in the pipes. As the CMC of the surfactant is so low, the bulk signal should be minimal and little correction is needed to remove the contribution from the data. However, at low concentration the flux is very low, therefore longer times are required to reach equilibrium and the use of the mixer at low concentrations may result in our kinetic assumptions may be wrong. Additionally, monitoring signal at low concentrations is limited by sensitivity.
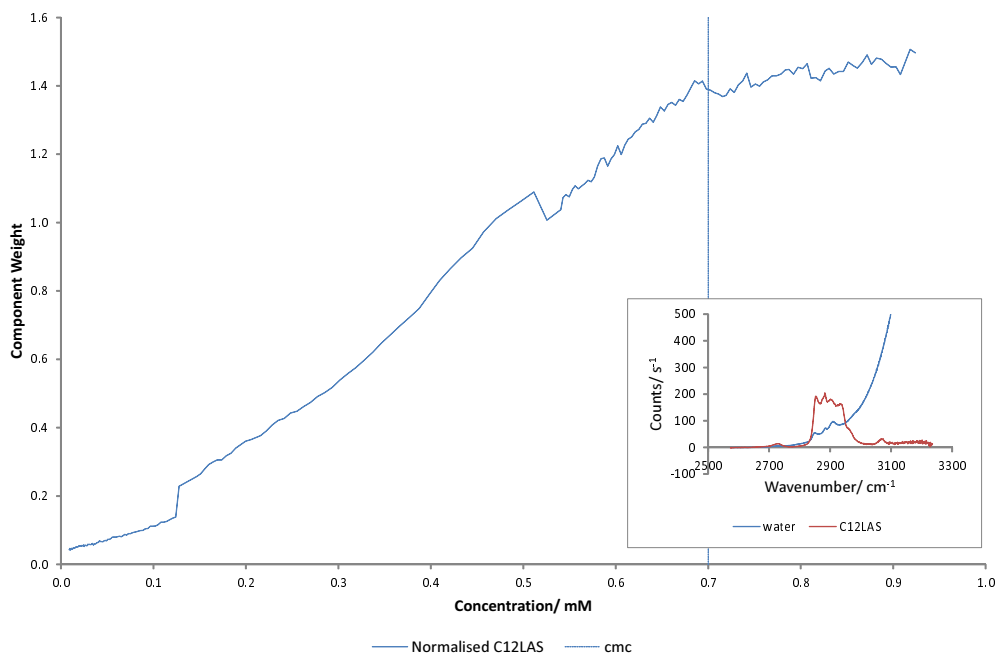
Figure 5.30: C_{12}LAS desorption from hydrophobic silica, (large mixer), $0.5\,\mathrm{ml\,min^{-1}}$, $5\,\mathrm{s}$ acquisition, $700\,\mathrm{mW}$ with y-axis truncated components inset ($300\,\mathrm{s}$ acquisition), $532\,\mathrm{nm}$

Hydrophobic Silica Kinetics

Preliminary kinetic measurements with C_{12}LAS and $C_{12}E_6$ were undertaken on silica made hydrophobic with hexamethyldisilazane. There is limited data available due to problems of bubbles. Attempts to follow SDS adsorption on hydrophobic silica also failed as the solution formed bubbles easily. The hydrophobic surface also caused an additional problem that any bubbles that did form attached to the surface and were very difficult to remove, this combined with the orientation of the cell when using the Renishaw system exacerbated the problem. To minimise the chance of forming a bubble: when mixing the solutions, care was taken to minimise agitation and pulsed sonication was used on the solutions to help to remove dissolved gases. The use of vacuum on the water would additionally help to minimise the number of bubbles effervescing out of solution and sticking to the surface, although we had not yet developed this solution.

i) $C_{12}LAS$

Figure 5.31 shows the adsorption and desorption kinetics for C_{12}LAS on hydrophobic silica recorded on the in-line mixer. The components are shown in figure 5.32. The components separate well and the peaks from the silane attached to the surface can be seen in the water spectrum at around $2910\,\mathrm{cm^{-1}}$. We also would expect a broad peak at around $3020\,\mathrm{cm^{-1}}$, but this is masked by the water signal. This experiment also confirms that the hydrophobic silane coating is not removed by the surfactant. The concentration used was $(1.915 \pm 0.002)\,\mathrm{mM}$. The equilibrium adsorbed amount is around $60\,\%$ that of C_{16}TAB on hydrophilic silica, suggesting around a monolayer has adsorbed.

The adsorption appears to be very fast (too fast for our Renishaw spectrometer to

follow with an exposure time of 1 s and a readout time of $\approx$1 s) after an initial delay and the desorption slower. The initial increase on desorption is odd, but also observed by Woods.[1] Also, the amount of surfactant decreases between experiments; perhaps a bubble passed over the surfaced during rinsing, although the surfactant components are almost identical in each direction.

ii)   **$C_{12}E_6$**

Figure 5.33 shows the kinetics for $C_{12}E_6$ adsorption to the substrate. Adsorption is rapid and a step function. The surfactant does not desorb on rinsing with water, as expected due to the very low CMC. It is possible that a bubble went through the cell resulting in an jump in component weight at around 38 s, although unusually the same event occurs at the same time on the way "out", so it could be due to an impurity. Concentration was (0.926 ± 0.003) mm, well above the CMC of 0.089 mm.[159] The adsorbed amount was around half that of the amount of C_{16}TAB adsorbed to hydrophobic silica, which is consistent with the expected monolayer adsorbed (tail-group first).

The TFA components displayed (figure 5.34) show good separation, although often in other experiments (not shown) the separation was poor, particularly if the water background varied substantially (possibly due to bubbles or focal drift).

Overall, while we were able to obtain an estimate of the adsorbed amount, bubbles sticking to the surface and repeated issues of contamination meant that many kinetic experiments were unsuccessful. If we had had more time we could have investigated this system on the new spectrometer. C_{12}LAS adsorption is slower than $C_{12}E_6$.
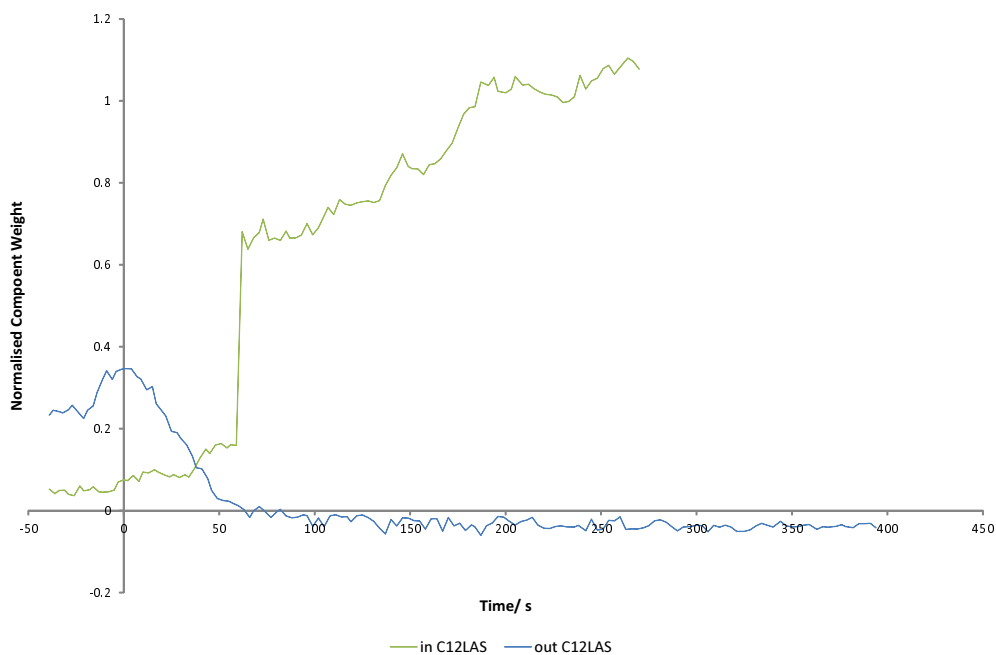
Figure 5.31: Kinetics of $\approx 1.9\,\text{mM}$ C_{12}LAS on hydrophobic silica, $1\,\text{s}$ acquisitions, $0.5\,\text{ml min}^{-1}$ pumping speed
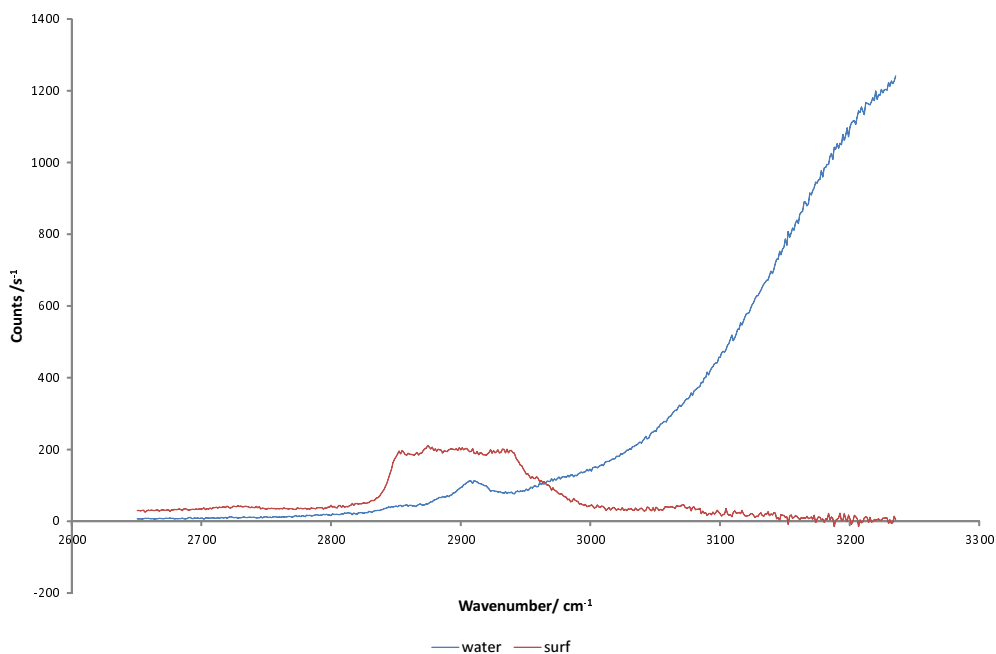
Figure 5.32: Refined components for kinetics of C_{12}LAS on hydrophobic silica, $1\,\text{s}$ exposure, $532\,\text{nm}$, $700\,\text{mW}$
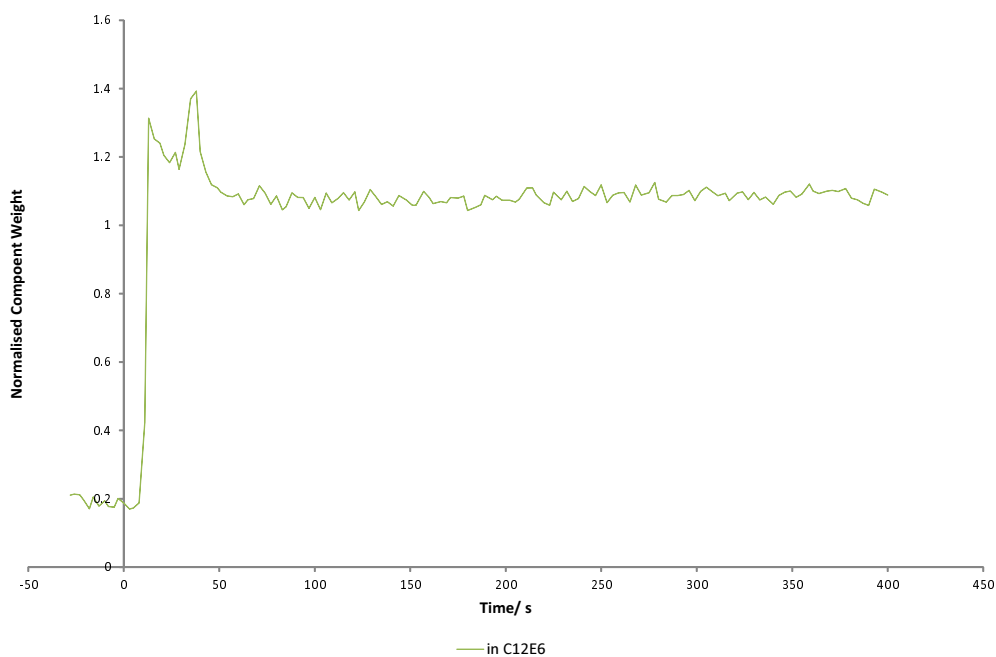
Figure 5.33: Kinetics of ≈ 0.93 mM $C_{12}E_6$ on hydrophobic silica, 1 s acquisitions, 0.5 ml min^{-1} pumping speed
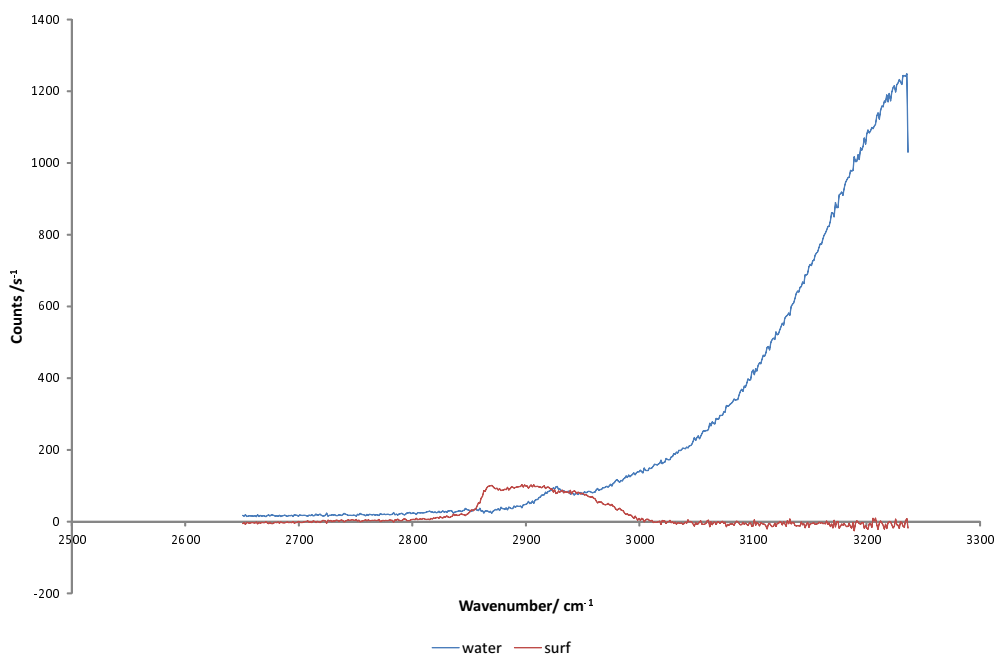
Figure 5.34: Components for kinetics of $C_{12}E_6$ adsorption on hydrophobic silica, 532 nm, 700 mW

Kinetics of Adsorption of $C_{12}LAS/C_{12}E_6$ Mixtures

These experiments are used as a way to study how the anionic $C_{12}LAS$ adsorbs to hydrophobic silica in the presence of a nonionic surfactant, to see if the adsorption is cooperative and investigate whether adsorption is enhanced by screening by the nonionic surfactant. Some textiles, for example polyester, are hydrophobic and by studying how surfactant mixtures adsorb we may be able to design better detergents. Again, we should be able to determine the amount of $C_{12}LAS$ adsorbed by subtracting the amount of $C_{12}E_6$ adsorbed. TIR-Raman, as we have seen, allows us to investigate adsorbed species and largely ignore bulk contributions and we have seen that our hydrophobic surface is not removed by surfactants. The ratio used to describe the mixture is the mass ratio of $C_{12}LAS : C_{12}E_6$.

Two-component (water + surfactants) analysis of the adsorption and desorption kinetics on hydrophobic silica was carried out to study the effects of the concentration and mixing ratio. The $C_{12}LAS/C_{12}E_6$ solutions were used in ascending concentration order, to minimise the effect of hysteresis from incomplete rinsing (by water). Component separation was often unsuccessful using either 2 (or 3) components. A two component model (water and surfactants) were more likely to separate, implying cooperative adsorption. As the maximum adsorbed amount varies and we cannot accurately convert to surface excess, it is difficult to compare the rates of adsorption or desorption quantitatively.

The surfactant with the higher monomer concentration in the mixture might be expected to adhere to the surface first, as the transport of micelles is generally slower than monomers, but our cooperative adsorption model would suggest that they both adsorb simultaneously.

The concentrations used in the following binary surfactant mixture experiments are shown in table 5.4.

3 : 1 *Mixture*

For the desorption of a 3 : 1 mixture of $C_{12}LAS$ to $C_{12}E_6$, component separation was good, typically looking like figure 5.35. Figure 5.36 shows the adsorption curves for a 3 : 1 mixture. The three highest concentrations all show similar rates of adsorption (note that these are probably all above the CMC of the mixture). The lowest concentration, which is probably below the CMC, adsorbs at a slower rate. Despite good component separation, the component weight offset at the start was poor. The 1.38 mM data was much noisier, despite Raman signal levels being the same, the noise seems to be in the background, so perhaps this was due to stray light. The adsorbed amount is the same for all concentrations, if we ignore the offset in component weight at the start. The kinetics of adsorption are all the same and fast, on the experimental time-scale, with the exception of the lowest concentration. The adsorption ended with around 90 % of a bilayer on the surface, which is very high and the overestimate probably results from our assumption about the intensity of C−H stretches for the mixture being the same as $C_{16}TAB$ on hydrophilic silica. The rate of adsorption is the highest of all the mixtures.

Figure 5.37 show data from experiments in which a pre-adsorbed layer is rinsed with pure water. Although there is an unusual increase around 50 s in the 0.22 mM data, the four curves suggest that the initial concentration is not important in determining the rate

Table 5.4: $C_{12}LAS$ and $C_{12}E_6$ concentrations

Sample Name	$C_{12}LAS$ Concentration/ mM	$C_{12}E_6$ Concentration/ mM
3 : 1 0.11 mM	0.1100 ± 0.0007	0.0277 ± 0.0002
3 : 1 0.22 mM	0.220 ± 0.001	0.0554 ± 0.0005
3 : 1 1.38 mM	1.375 ± 0.006	0.346 ± 0.003
3 : 1 1.93 mM	1.93 ± 0.01	0.485 ± 0.004
2 : 1 0.08 mM	0.080 ± 0.001	0.0308 ± 0.0004
2 : 1 0.16 mM	0.161 ± 0.001	0.0616 ± 0.0005
2 : 1 0.32 mM	0.315 ± 0.003	0.121 ± 0.001
2 : 1 0.77 mM	0.766 ± 0.007	0.293 ± 0.003
2 : 1 1.46 mM	1.46 ± 0.01	0.560 ± 0.005
2 : 1 8.04 mM	8.04 ± 0.03	3.08 ± 0.01
1 : 1 0.10 mM	0.1010 ± 0.0006	0.0858 ± 0.0005
1 : 1 0.20 mM	0.202 ± 0.001	0.172 ± 0.001
1 : 1 1.01 mM	1.010 ± 0.005	0.858 ± 0.005
1 : 1 5.05 mM	5.050 ± 0.007	4.290 ± 0.006
1 : 3 0.03 mM	0.0316 ± 0.0004	0.070 ± 0.001
1 : 3 0.06 mM	0.0632 ± 0.0004	0.140 ± 0.001
1 : 3 0.63 mM	0.631 ± 0.003	1.399 ± 0.008
1 : 3 3.16 mM	3.158 ± 0.008	6.99 ± 0.01

of desorption, which is to be expected when the adsorbed amount is the same. Rate of desorption is also the highest of all the mixtures.
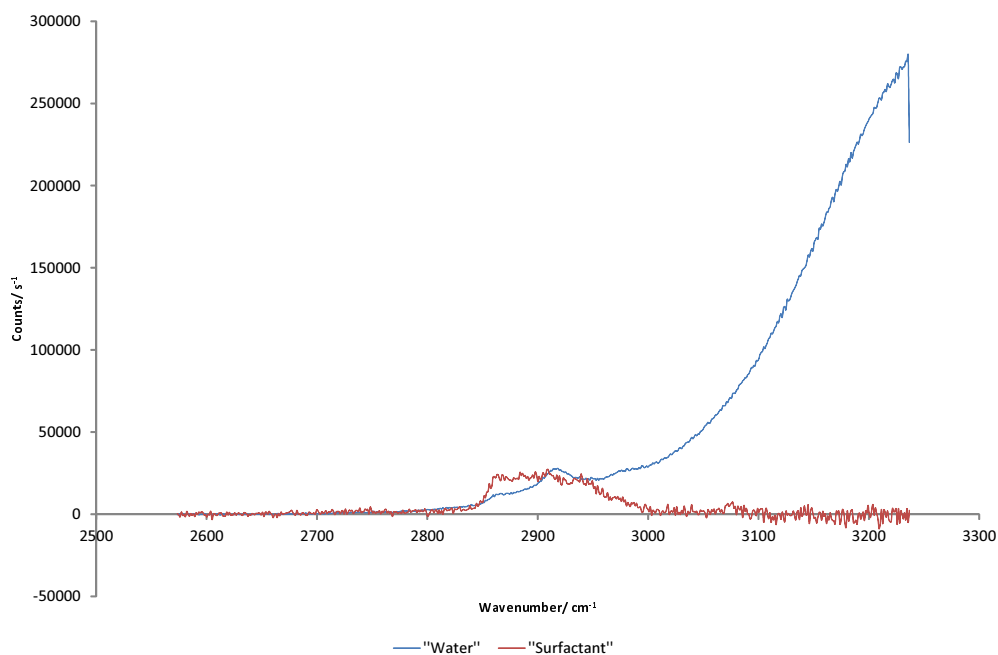
Figure 5.35: 3 : 1 adsorption onto hydrophobic silica components, 532 nm, 700 mW

Figure 5.36: 3 : 1 adsorption of $C_{12}LAS$:$C_{12}E_6$ on hydrophobic silica, $C_{12}LAS$ concentration shown in legend. 0.5 ml min^{-1}

Figure 5.37: 3 : 1 desorption of C_{12}LAS:$C_{12}E_6$ on hydrophobic silica, C_{12}LAS concentration shown in legend. 0.5 ml min^{-1}

2 : 1 **Mixture**

Adsorption and desorption experiments for six different concentrations were attempted for the 2 : 1 mixture and these are shown in figure 5.38 and figure 5.39 respectively. The increase in component weight for the 0.32 mM solution is due to a loss in water signal (most likely due to a bubble). Our starting component weights for desorption do not match the end points in figure 5.38. For the 8.04 mM solution this mismatch is due to poor component separation. For the remaining solutions, this could have been due to the refilling of the cell with fresh surfactant solution removing or adding an impurity. The rate of adsorption was the slowest of all mixtures and the adsorbed amount was much lower at $\approx 10\%$ of a bilayer.

One might expect faster rates of adsorption for higher concentrations; however, the data do not always show this and some show the complete opposite. For example, figure 5.38 shows the highest concentration being the slowest to adsorb, we need to bear in mind, however, that C_{12}LAS has a higher CMC than $C_{12}E_6$. At low concentrations, the micelles are richer in $C_{12}E_6$ than at higher concentrations. Consequently, the monomer concentration of $C_{12}E_6$ in equilibrium with the micelles is higher at low total concentrations than it is at high total concentrations (where the micelle composition mimics the total concentration). If the monomer concentration of $C_{12}E_6$ is important in determining the adsorption rate, then it would make sense to have slower kinetics at higher concentrations.

Later work by Ci Yan in our group on the adsorption of $C_{16}E_8$ micelles at the air-water interface in an overflowing cylinder (OFC) has shown that addition of just 5% of an ionic surfactant nearly switches off the adsorption process as negatively charged micelles are repelled from a negatively charged surface.[184] These results show the importance of the monomer composition in determining adsorption kinetics on like-charged surfaces.

The rate of desorption does not appear to be concentration sensitive. Apart from the highest concentration, all the ratio mixtures appear to be fairly concentration insensitive. For similar surface excesses, although possibly different compositions, the desorption rates are similar. The results also show that desorption is slower than adsorption, at the same flow rate. Further work to investigate different flow rates could probe if flow rate is a factor in determining the kinetics. Although, with the Renishaw spectrometer set up, we would be unable to study higher flow rates due to the limited time resolution. The new spectrometer should resolve this issue. At lower flow rates, the decreased flux may become an issue, along with an increasing contribution from diffusion within the cell back to the surface. Desorption rate varied, but was among the slowest.
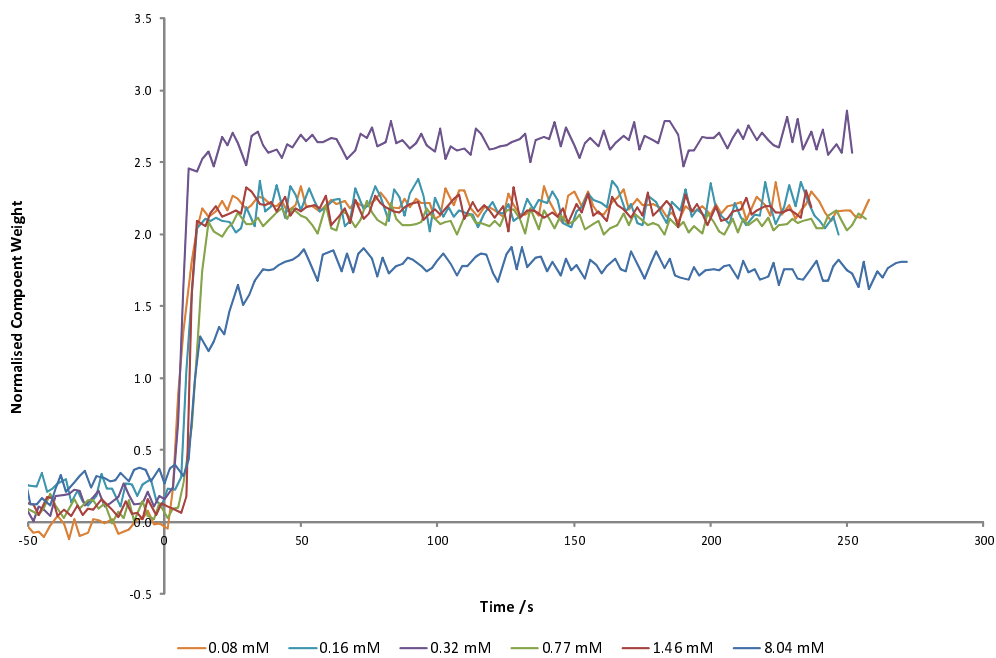
Figure 5.38: $2:1$ adsorption of $C_{12}LAS$:$C_{12}E_6$ on hydrophobic silica, $C_{12}LAS$ concentration shown in legend. $0.5\,\mathrm{ml\ min^{-1}}$
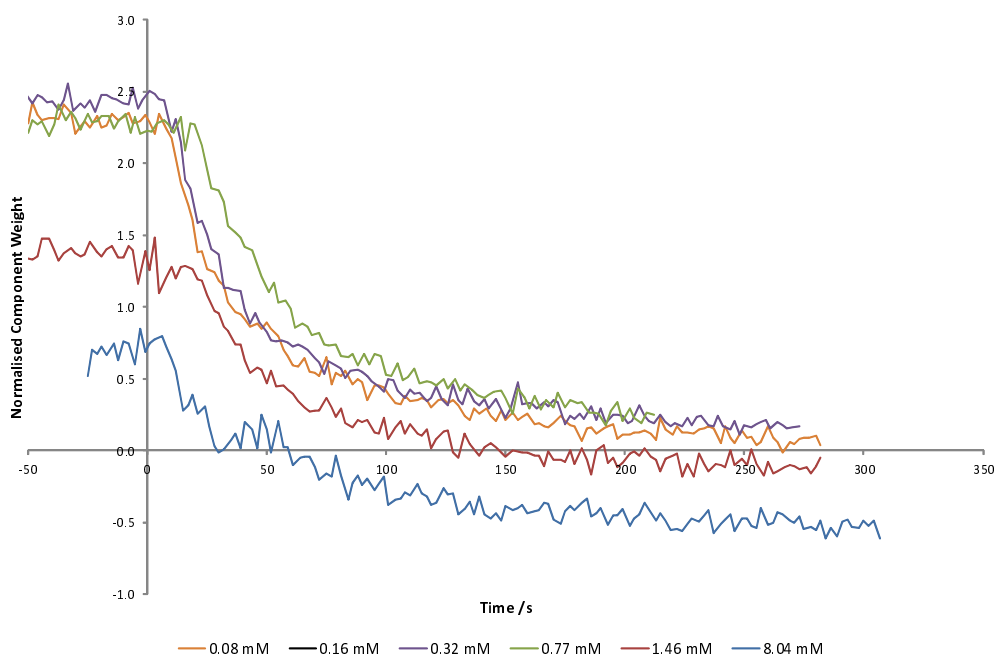
Figure 5.39: $2:1$ desorption of $C_{12}LAS$:$C_{12}E_6$ on hydrophobic silica, $C_{12}LAS$ concentration shown in legend. $0.5\,\mathrm{ml\ min^{-1}}$

1 : 1 **Mixture**

Figure 5.40 shows the adsorption curves for a range of equimolar concentrations. For the 1.01 mM concentration, the adsorption is too fast to be resolved properly with the 2 s time resolution of the spectrometer. The highest and lowest concentrations appear to show slower kinetics than the intermediate concentrations. The three higher concentrations yield the same final signal, which is lower for the lowest surfactant concentration. Different initial signal levels were found in the desorption experiments shown in figure 5.41, highlighting the need for improved reproducibility. The rate of adsorption was much slower than for 3 : 1 solution and around 10 % of a bilayer is present on the surface.

Figure 5.41 shows the 1 : 1 desorption data. It is difficult to conclude much from these data. The increase in component weight at around 50 s in the 5.05 mM solution is probably an artefact, although the water component remains constant. The rate of desorption is slightly slower than for the 3 : 1 mixture.
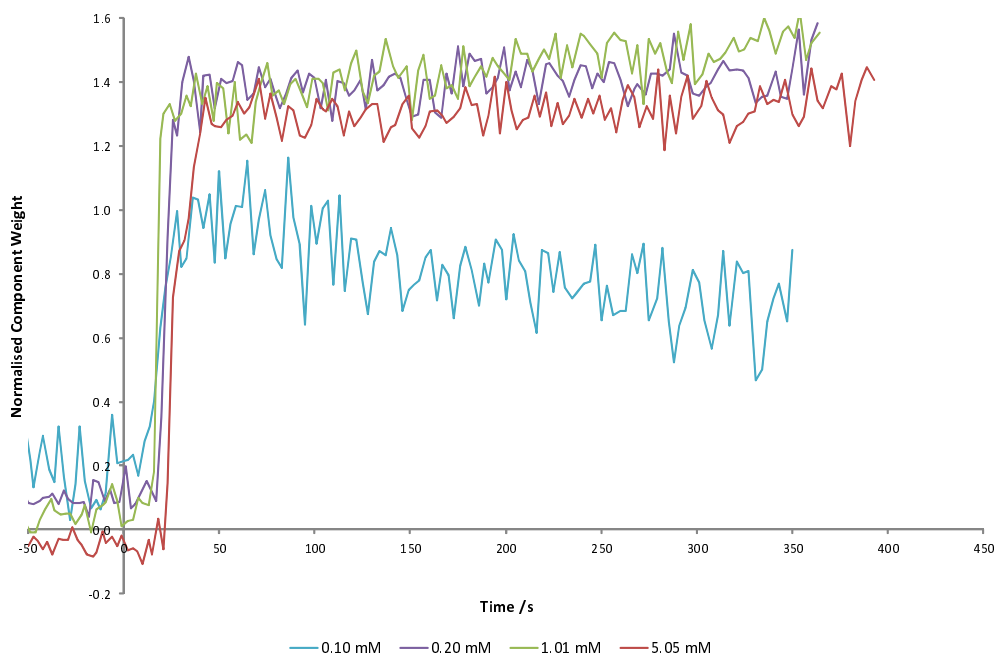
Figure 5.40: 1 : 1 adsorption of $C_{12}LAS$:$C_{12}E_6$ on hydrophobic silica, $C_{12}LAS$ concentration shown in legend. $0.5\,\mathrm{ml\ min}^{-1}$
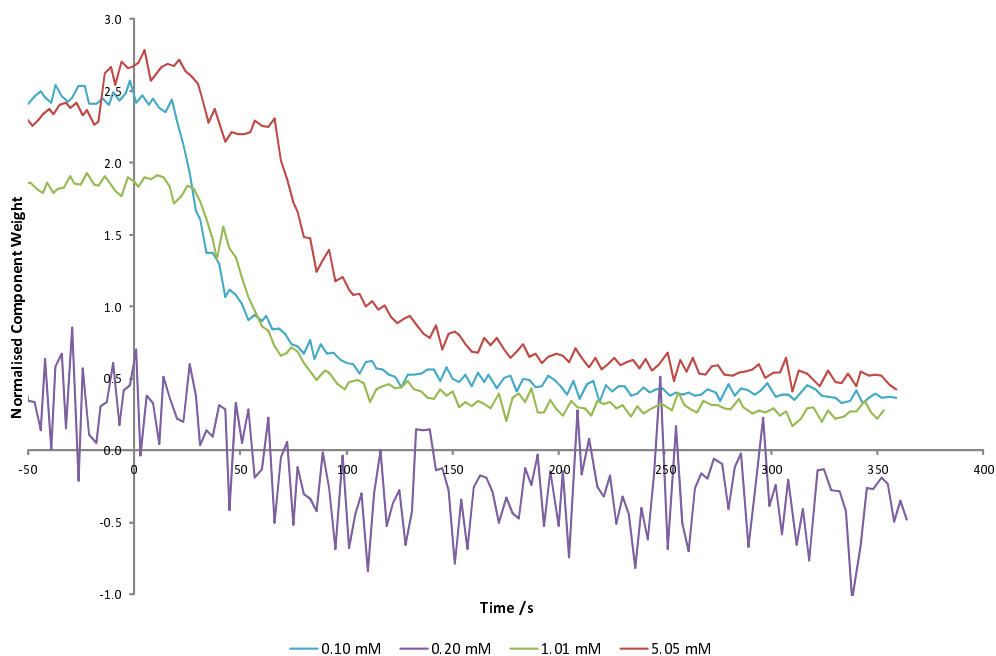
Figure 5.41: 1 : 1 desorption of $C_{12}LAS$:$C_{12}E_6$ on hydrophobic silica, $C_{12}LAS$ concentration shown in legend. $0.5\,\mathrm{ml\ min}^{-1}$

138

1 : 3 **Mixture**

For the $C_{12}E_6$-rich mixture, we have only obtained two good data sets, which are shown in figure 5.42. Although the data is of poor quality we can estimate that we have around 90 % of a bilayer present and the rate of adsorption is approximately the same as the 1 : 1 mixture.

For this mixture, figure 5.43 shows almost identical desorption rates across the concentration range and about the same as for the 2 : 1 mixture.
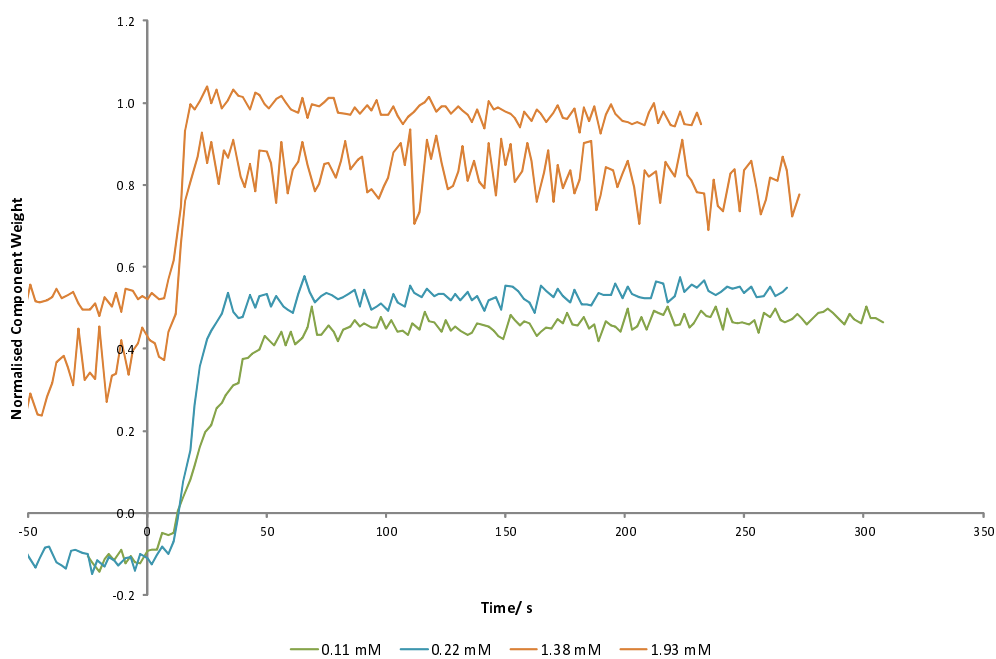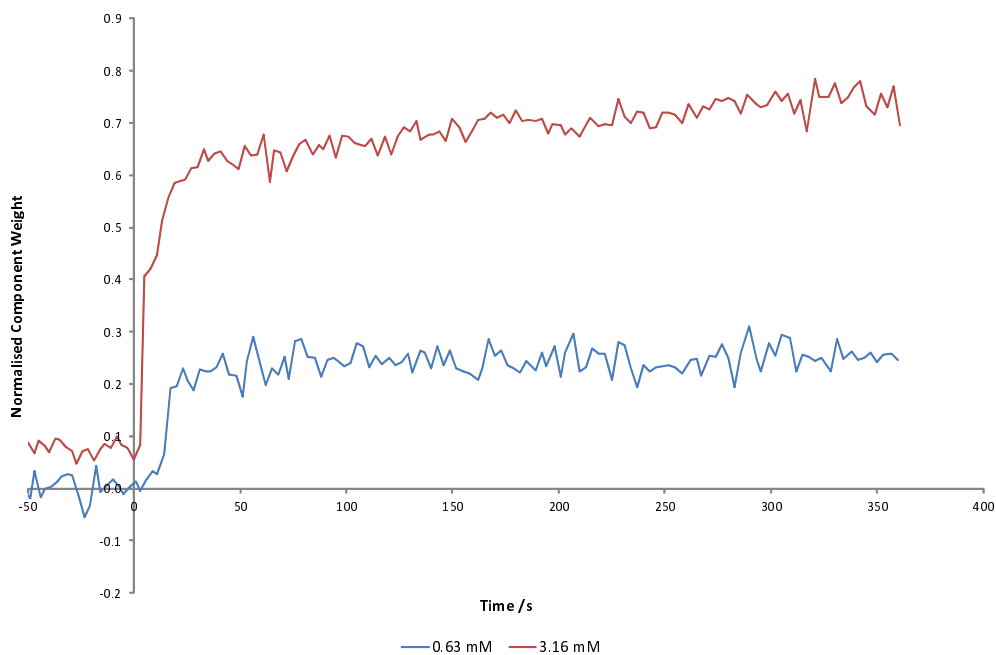
Figure 5.42: $1:3$ adsorption of $C_{12}LAS:C_{12}E_6$ on hydrophobic silica, $C_{12}LAS$ concentration shown in legend. $0.5\,\text{ml min}^{-1}$
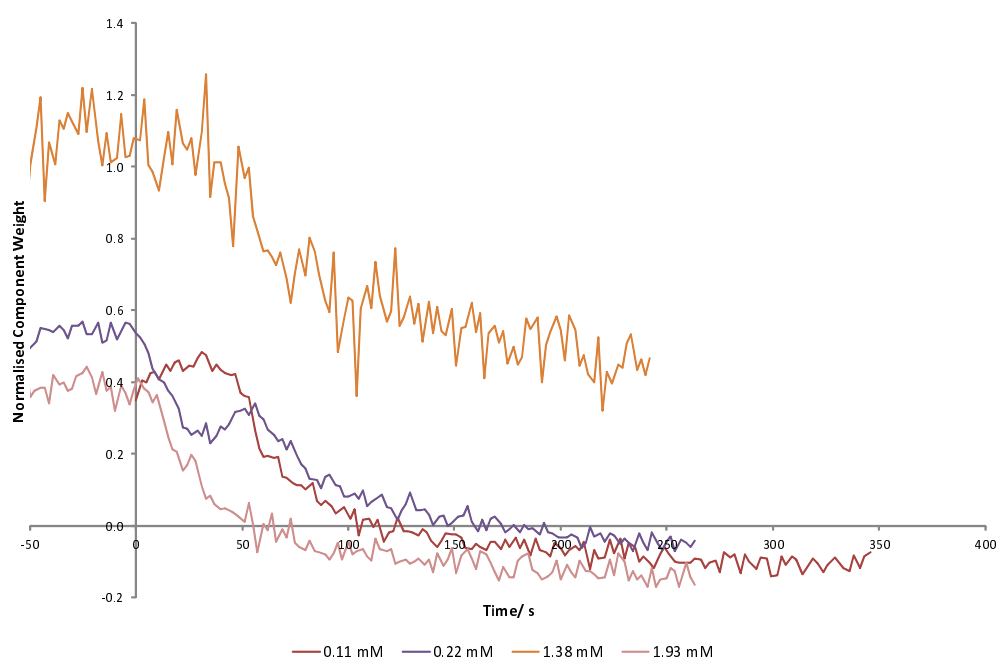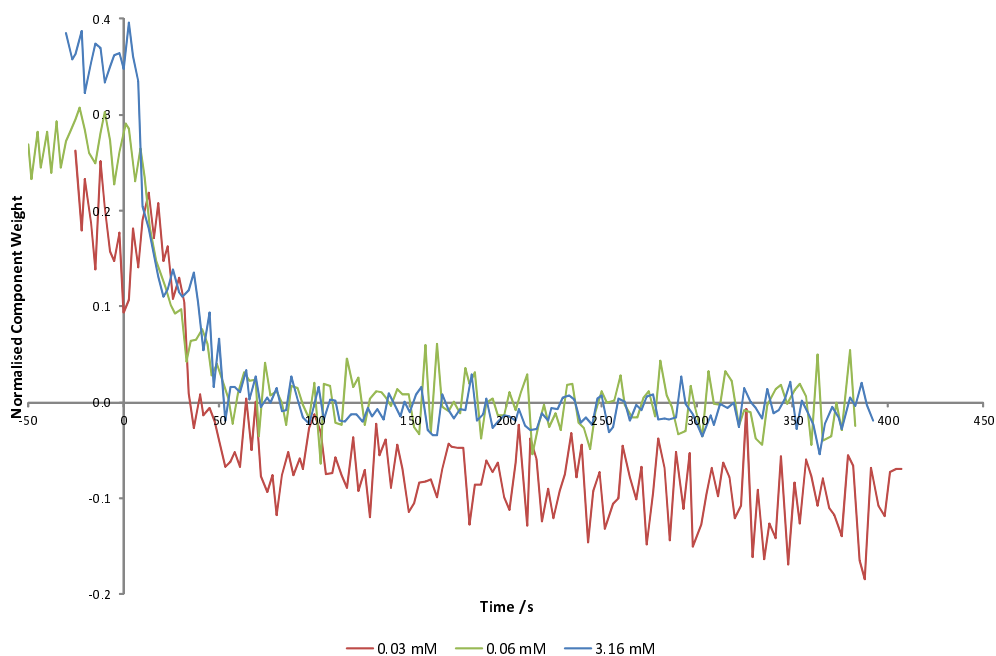

Figure 5.43: $1:3$ desorption of $C_{12}LAS:C_{12}E_6$ on hydrophobic silica, $C_{12}LAS$ concentration shown in legend. $0.5\,\text{ml min}^{-1}$

5.4.3   Discussion

While we have estimated rates of adsorption/desorption, many of the adsorption rates are much faster than the time resolution of our Renishaw spectrometer, hence there will be a very large error associated with them. The summary results for adsorbed amounts are tabulated in table 5.5.

Our adsorbed amounts of the single surfactant solutions form near monolayer coverage, which is expected on the hydrophobic substrate. The adsorption rate of $C_{12}E_6$ is around half that of C_{12}LAS. When in a mixture, the equilibrium amount of the 3 : 1 solution was the highest (at nearly a complete bilayer), followed by less-than-monolayers of the 1 : 3, 1 : 1 then 2 : 1 mixtures. We would expect all to give a monolayer on a hydrophobic surface, but again our assumption that the C$-$H counts would be the same for these surfactants as for C_{16}TAB is a poor estimate. It is difficult to explain the wildly varying adsorbed amounts.

In general rates of adsorption and desorption were faster for the mixtures with the highest surface coverage, which is expected as these interactions are more favourable.

Given that C_{12}LAS has a slightly higher affinity for the surface (more adsorption of surfactant on its own), this could explain why the most C_{12}LAS-rich mixture adsorbs the most. The more-favourable formation of mixed micelles could be the reason for why when the mixture changes to 2 : 1 adsorption almost stops. The nonionic may repel the surface if not all the silanol groups have reacted with the silane leaving some negative charge on the substrate, so any aggregate which results in the head-group orientated towards these groups on the substrate will be unfavourable. If the $C_{12}E_6$ head-groups orientate into the water, they could hydrogen bond with water molecules, making a mixed bilayer even more favourable.

It is worth noting, the 1 : 1 (by mass) mixture contains more moles of C_{12}LAS as it has a lower relative molecular mass (348.48 g mol^{-1} compared to 450.65 g mol^{-1} for $C_{12}E_6$). Also $C_{12}E_6$ has a lower CMC (0.089 mM [159]) compared to C_{12}LAS (0.72 mM [158]) therefore there will be fewer $C_{12}E_6$ molecules in the bulk at low concentrations. $C_{12}E_6$ is an impure mixture and therefore the presence of many other homologues will affect results (although we do not observe any overshoot in adsorption in any of the mixtures).

As we are unable to separate the two surfactants, it is difficult to determine anything about the adsorbed structure and if the ratio of the adsorbed species matches the bulk mixture.

While there is some contribution to the C$-$H stretch from the hydrophobic silane

Table 5.5: Summary of binary mixture coverage, referenced to C_{16}TAB on silica

Mixture	Bilayer Estimate (%)
3 : 1	90
2 : 1	10
1 : 1	15
1 : 3	30
Pure $C_{12}E_6$	50
Pure C_{12}LAS	60

coating, this contribution appears in the water/background component.

As we were using the Renishaw system we encountered our usual difficulties with focal drift. In addition, the surfactant creates a hydrophobic monolayer which is difficult to study for a number of reasons: any bubbles which form stick to the surface and are very difficult to remove without emptying and re-filling the cell, sometimes several times at varying speeds, and this is often not possible with the limited volume of solution, and cost of surfactants used. Due to the stagnation point at the centre of the hemisphere (where our objective is focused and we collect data), there are no shear forces to detach bubbles from this region. The presence of air bubbles on the surface contribute to signal loss and affect the hydrodynamics of the flow. The interface under investigation will no longer be liquid–solid, but also a mixture of liquid–vapour and solid–vapour. Air bubbles give rise to very poor reproducibility of data. The hydrophobic surface is also difficult to clean as any contaminants (such as surfactants or other contaminants) do not wash away easily.

The C_{12}LAS/$C_{12}E_6$ system proved difficult to study; separation of the two surfactants in the spectra was poor as they are spectrally quite similar (see figure 5.44). The $C_{12}E_6$ data is noisier due to the concentration being lower. There is a peak around $3075\,\mathrm{cm}^{-1}$ in the C_{12}LAS which is not present in the $C_{12}E_6$ spectra, which is due to the aromatic C−H stretches. This is masked by the water band. The spectra are very similar in all other regions and any peaks which are present in the $C_{12}E_6$ spectra are largely masked by the ones from C_{12}LAS. The fingerprint region (figure 5.45) is dominated by the peaks from the silica substrate. Overall the amount of C_{12}LAS adsorbed is low and the weak, broad peak makes detection difficult.

To conclude, LAS has unique peaks at $1000\,\mathrm{cm}^{-1}$ and $3075\,\mathrm{cm}^{-1}$, but these are not strong enough to use to quantify LAS on its own. $C_{12}E_6$ has no unique peaks so cannot be distinguished from LAS in the aliphatic C−H region. A solution may be to deuterate one chain, but these are often expensive.

In a different wavenumber region, C_{12}LAS does however, show a small peak at around $1450\,\mathrm{cm}^{-1}$ that is not present in the $C_{12}E_6$, although this CH_2 peak should be in both surfactants, but is probably absent due to the low concentration used. There is also a C−C stretch from the aromatic ring at around $1600\,\mathrm{cm}^{-1}$, although this is somewhat masked by the silica. Earlier unpublished work in the group by Tom Curwen related the amount of adsorption to how the silica was washed and hence this could explain some of the variation we observe.

Analysing the Raman spectra with three components (corresponding to the two surfactants and (water + background)) has been unsuccessful: the target factor analysis returns a single component for both surfactants.

When forcing an analysis with three components (water, C_{12}LAS and $C_{12}E_6$) we obtained a large number of "subtraction artefacts" shown in figure 5.46.

The investigation of these multicomponent systems was suspended due to the difficulties in obtaining good data on the old Renishaw spectrometer and were not revisited on completion of the new spectrometer due to lack of time.

Additional work on the new spectrometer, or other suitable spectrometer, would be needed to confirm and refine our conclusions.
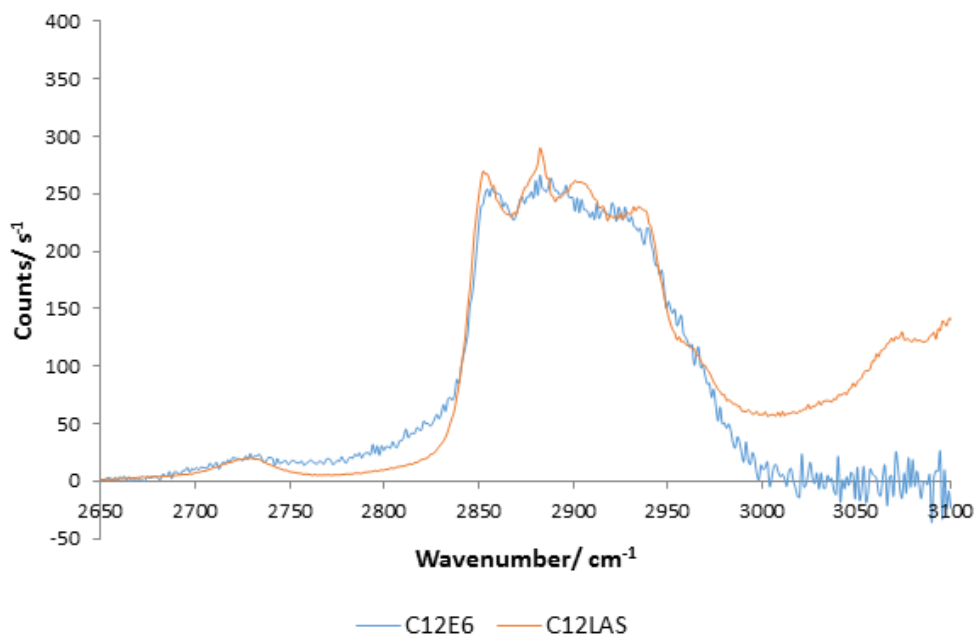
Figure 5.44: C_{12}LAS and $C_{12}E_6$ spectra, taken in a capillary, 532 nm, 700 mW

5.5 Conclusions

We have shown that TIR-Raman is a powerful technique for investigating adsorbed mono- and bi- layers on silica as we only probe the region close to the interface.

For our isotherms of C_nTAB on plain hydrophilic silica, when component separation was successful, we were able to produce good data which fit well with literature values. C_{16}TAB produced the most reliable data for all measurements due to stronger C−H bands and lower impurities. We have also shown that the rate of adsorption of these surfactants in the flow cell is not flux limited. The trend on increase in chain length also matches well with literature data on other substrates.

We were able to monitor how a bilayer transitions between phases and this provided good insight into how ions interact with a DHDAB bilayer. Monitoring the ratio of the d^- to d^+ peaks was a good method of following phase transitions in the bilayer. We were able to draw some additional conclusions from the collaborative study. The TIR-Raman technique has and will continue to be used to study bilayers of various surfactants and lipids on silica. Further investigation into the effect of other ions present in water, for example hydroxide or bicarbonate may assist in the understanding of bilayer ion replacement.

Our work on binary surfactant solutions with C_{12}LAS and $C_{12}E_6$ was plagued with component separation issues due to the similarity of the two molecules' spectra in the $2900 \, \text{cm}^{-1}$ region, the adherence of bubbles and contaminants, and our common focal drift problems encountered on the Renishaw spectrometer. The binary system would have been useful to investigate as a model mixed ionic/non-ionic system, but it proved difficult to obtain reliable results. Studying the system with a deuterated surfactant may allow further investigation, although this would be expensive. However, with a deuterated
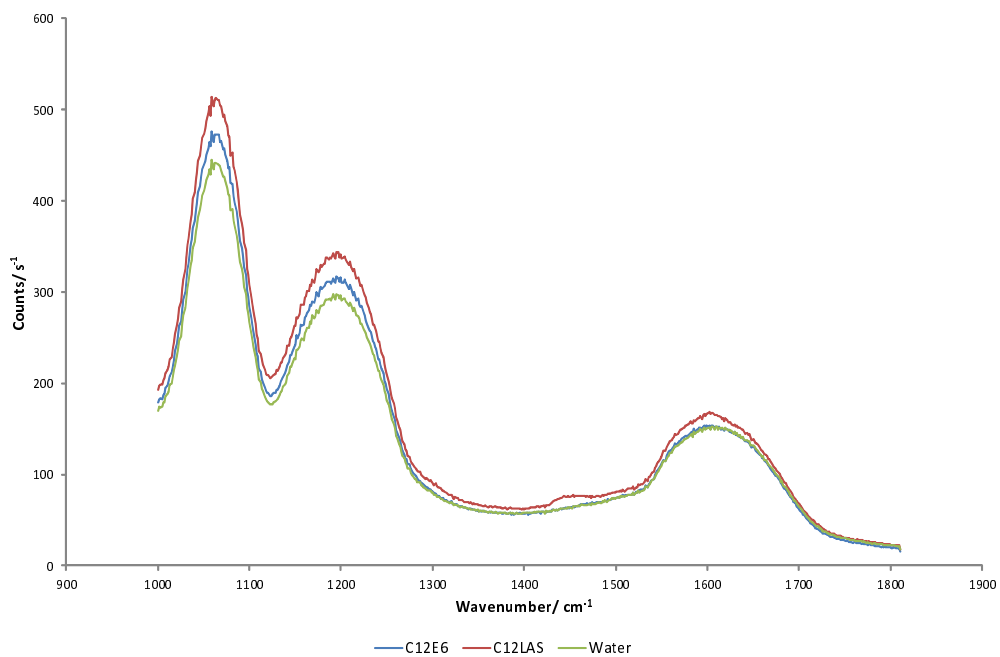
Figure 5.45: Water, $C_{12}LAS$ and $C_{12}E_6$ fingerprint region, acquired in a capillary, 532 nm, 20 mW

surfactant, we may not be able to follow both surfactants simultaneously unless we change our spectral range by swapping the grating.
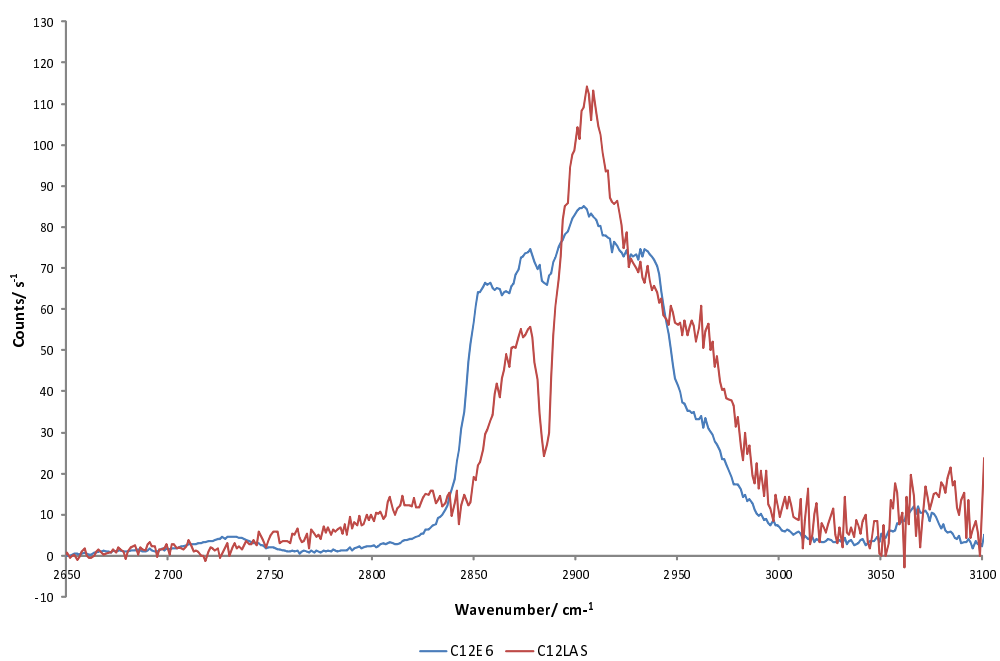
Figure 5.46: Subtraction artefacts from forcing 3 component analysis

Chapter 6

Adsorption of Surfactants onto Thin Films

6.1 Introduction

We were also interested in how surfactants behaved on thin films of various substrates as the adsorption of surfactants to these surfaces is of great interest in many industrial, commercial and domestic processes including ore extraction, purification and laundry detergents. Understanding how the nature of surfactant and substrate affect adsorption behaviour can, for example, increase yields when mining and improve cleaning effectiveness.

We studied the adsorption using the same TIR-Raman technique Woods used to study surfactant adsorption to cellulose and mica. He was only successful with the former, as the formation of bubbles at the laser spot resulted in damage to the substrate and/or hemisphere. We investigated other substrates (zeolite, kaolinite, polyester and haematite) to see if we could determine the thermodynamics and kinetics of adsorption for various surfactants, first trying to develop a reproducible coating technique on the hemisphere before following the adsorption of surfactants to the thin film surface using TIR-Raman.

TIR-Raman, combined with the formation of a thin film of target substrate on a silica hemisphere allows for real-time measurement of the adsorption kinetics and adsorbed amount to that substrate. In the $C-H$ region under investigation we know there is very little contribution from the silica and the small penetration depth of the TIR technique allows for only the interface to be probed. Provided an even, uniform coverage of a thin film of the target substrate can be formed and there is a minimum Raman contribution from the coating, we can monitor adsorption to that substrate.

Each section begins with an introduction on the substrate and our study characterising the deposited layer using various experimental techniques is presented. We then present the data acquired by TIR-Raman on how surfactants behave at the surface. When we are able to "see" through the substrate (in all cases other than haematite) we have obtained some results. Most measurements follow the kinetics of adsorption and desorption to the substrate, but we have also obtained some isotherms, again using our in-line mixer technique.

The coatings affect the penetration depth if there is change in index of refraction. In

general we need to use a three-layer optical model to determine the depth of electric field in the evanescent wave. If $n_{silica} \geq n_{film} \geq n_{H_2O}$ and $\theta > \theta_c(SiO_2/film)$, the decay of the electric field is slower in the film than in water and TIR occurs at the silica-film interface. For $\theta_c(SiO_2/H_2O) < \theta < \theta_c(SiO_2/film)$ or if $n_{film} > n_{silica}$, the light is transmitted through the film and total-internal reflection occurs at the film-water interface. For example, zeolite has a slightly higher refractive index (≈ 1.5) than silica (≈ 1.46), so TIR occurs at the zeolite-water interface (assuming a uniform film layer) and the penetration depth is lower, at $\approx 82\,nm$. Increasing the excitation wavelength (to our 660 nm laser) on the same substrate increases the penetration depth to $\approx 102\,nm$, since the refractive indices only vary slowly with wavelength. Experiments in this chapter, unless otherwise stated used 532 nm excitation and the new spectrometer system.

The kaolinite, zeolite and haematite substrates we selected are used as model soils and polyester is a common textile. By studying these systems we can better understand adsorption processes which could lead to the development of improved detergents: adsorption of the detergent to the soil, followed by a low barrier for removal of that soil from a substrate such as polyester would make fabric washing more efficient.

6.2 Zeolite

6.2.1 Introduction

Surfactant adsorption to a zeolite layer on silica was studied as a model surface. Zeolites are abundant and fairly low-cost, and can be found impure in soils, particularly in volcanic regions where ash reacts with alkaline groundwater and so it is a model soil of fabrics and can be a model for the more common aluminosilicates.[185] They are also often used as sorbents known as "molecular sieves", for example in environmental clean-up operations such as for extracting radioactive species,[186] heavy metal and inorganic ions,[136] and aromatic hydrocarbons.[187,188] These molecular sieves can also be used to remove surfactants from wastewater as, when left untreated, they can cause the build-up of foams in rivers and lakes, reducing the oxygen concentration of the water thereby harming aquatic life.[131,185] Other common uses of zeolites include pet litter, animal feed, horticultural applications (soil conditioners and growth media) and synthetic zeolites are used as catalysts and in detergents. Calcining of zeolites drives off water and causes reorganisation of the molecular structure.[189]

6.2.2 Experimental

The zeolite (structure shown in figure 1.16) substrate was prepared, according to the method described by Lee *et al.*, by rubbing zeolite powder, purchased from Sigma (CAS Number 1318-02-1), with a gloved finger and then placing the hemisphere in a furnace for calcining at 500 °C for 24 h.[123] Information on which type of zeolite purchased was not provided. From the manufacturers' specifications, the pore size is typically 4 Å and the particle size is $<45\,\mu m$.

6.2.3   Substrate Characterisation

The zeolite coating does scatter the laser light more than other surfaces we have looked at (which results in a higher background), probably due to the large particles scattering the light. The edge filters block most of this light so we can still obtain spectra of adsorbed species however, the microscope's CCTV camera often bleaches when using full power during alignment, so we used an ND filter in front of this camera for laser alignment and to prevent damage.

Figure 6.1 shows the ^{29}Si solid-solid state NMR for bulk zeolite purchased from Sigma Aldrich. Comparing the peak with data from literature (figure 6.2), with peak at $\delta = -89.26$ ppm, agrees with the sample being Na-zeolite A,[190] (also known as Linde Type A (LTA)) with the peak shift indicating that the silicon atom is surrounded by three aluminium atoms, the smaller peak at $\delta = -94.46$ ppm is a silicon atom surrounded by two aluminium atoms, hence the Si/Al ratio is close to one.

The Raman spectrum of bulk zeolite powder, taken on the Renishaw spectrometer, is shown in figure 6.3. There is a lot of fluorescence in the bulk sample. Comparing our data with literature spectra of zeolite shown in figure 6.4 again suggests zeolite A, with a Si/Al ratio between 1.0 and 1.2.[191] The strong band at around 490 cm^{-1} is assigned to the oxygen atoms in a four-membered ring.[191] The bands at around 975 cm^{-1}, 1040 cm^{-1}, and 1105 cm^{-1} are due to the Si$-$O$^-$ stretches of silicon atoms connected to non-bonded oxygen atoms.[191] The band at 696 cm^{-1} is assigned to an Al$-$O stretch.[191]

The spectrum of the silica hemisphere, in water, after coating with zeolite and calcining is shown in figure 6.5. The two peaks at around 2925 cm^{-1} and 3000 cm^{-1} are of an unknown origin as they do not appear in the bulk powder spectrum (although they could be masked by the fluorescence). They are not removed on rinsing with water, methanol or Decon, but their shift suggests some form of C$-$H contamination. One contaminant we have encountered before in the lab are silicone oils (they are used as a lubricant during the manufacture of many items) so we investigated if they could have been the result of Si$-$Me peaks. The Raman peaks for CH$_3$ stretches adjacent to Si are at 2940 cm^{-1} and 2888 cm^{-1}, but PDMS contains two Me groups per Si atom, so we would expect the peaks to be lower. As our peaks do not match, the source of this contamination is unknown. However, the peaks are not removed on surfactant addition or rinsing with solvents such as methanol, so they can be treated as part if the substrate spectrum; they could even be used to show the zeolite layer is not changing or being removed. We can also see a high level of background due to increased scattering or fluorescence.

Figure 6.6 shows a scanning electron microscope (SEM) micrograph of a layer of zeolite on a glass slide (coated with carbon for conductivity). The layer and sinter are fairly uniform with the exception of the hole near the centre. Provided we probe regions on the hemisphere where the surface looks complete we should be studying a zeolite surface. For a better understanding we would need to know the film thickness. The particle size of <45 μm is large on the scale of SEM, so although the value is a maximum, the surface preparation results in a uniform film. Calcining is performed to obtain a more reactive phase, with the loss of structural water and reorganisation and aggregation of the structure to form Si$-$O$-$Si bridges and remove organics from the pores.[192] Calcining can also cause cracking of a zeolite film.[192,193]

911/3580
APD Sigma Zeolite

File: 15/cba_20140519_01

Pulse Sequence: onepul

Date May 19 2014
Probe 6.0_MM_PENCIL
Spectrometer: VNMRS

Observe Si29
Frequency 79.435 MHz
Spectral width 40322.6 Hz
Acquisition time 30.0 ms
Recycle 10.0 sec
No. repetitions 184

Direct excitation
Pulse duration 6.2 us
TPPM decoupling at 45.5 kHz
Spin-rate 6800 Hz

FT size 32768
Ambient temperature

-89.361

-94.472

Figure 6.1: Solid-state (^{29}Si) NMR of zeolite-A
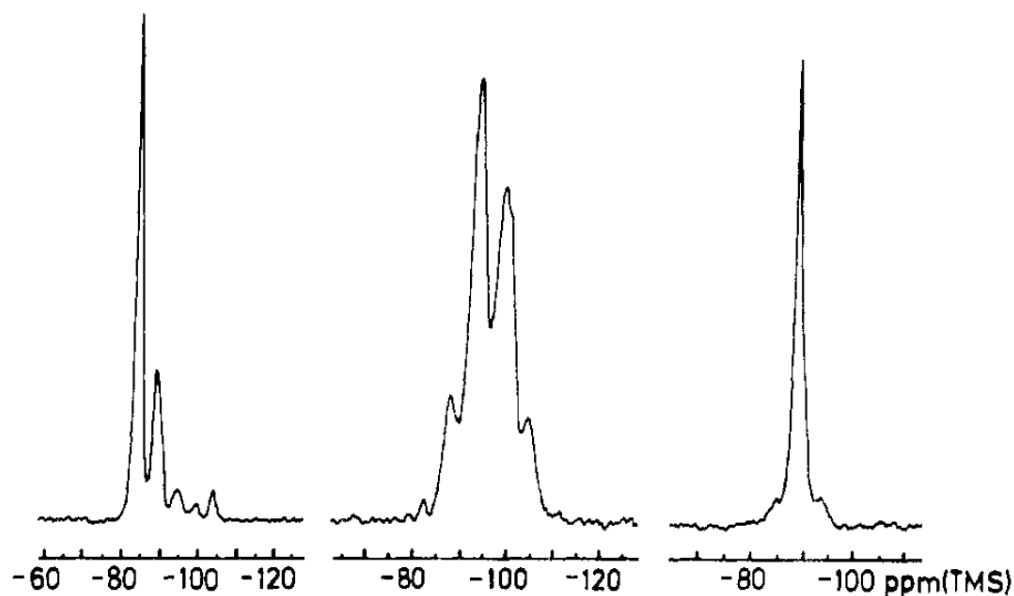
Figure 6.2: ^{29}Si NMR spectra of NaX, NaY, and NaA zeolites, from left to right. Reprinted with permission from American Chemical Society from reference 190. Copyright 1981 American Chemical Society

Streaming Potential Results

Approximate streaming potential data kindly provided by Ian Tucker (Unilever Research and Development, Port Sunlight UK) showed a marked reduction in ζ potential for zeolite ($\approx -35\,\text{mV}$), compared to $\approx -80\,\text{mV}$ for silica (at pH 7).[35]

6.2.4 Surfactant Adsorption

Concentrations for the following surfactant adsorption isotherms using the in-line mixer are shown in table 6.1; and kinetics, where the concentration is fixed, are in table 6.2.

Table 6.1: Surfactant concentrations for use with in-line mixer to determine zeolite isotherms

Sample Name	Concentration/ mM
C_{14}TAB-5mM (small mixer)	5.060 ± 0.008
C_{14}TAB-10mM (small mixer)	10.07 ± 0.01
C_{14}TAB-15mM (small mixer)	15.23 ± 0.02
C_{14}TAB-20mM (small mixer)	20.07 ± 0.03
C_{14}TAB-30mM (small mixer)	29.32 ± 0.03
C_{14}TAB-40mM (small mixer)	39.86 ± 0.05
C_{14}TAB-4mM (large mixer)	3.995 ± 0.008
C_{14}TAB-7.5mM (large mixer)	7.54 ± 0.01
C_{14}TAB-10mM (large mixer)	10.05 ± 0.01
$C_{16}E_6$-2mM	2.001 ± 0.005
$C_{16}E_6$-5mM	5.012 ± 0.007
SDS-10mM	10.04 ± 0.01

150
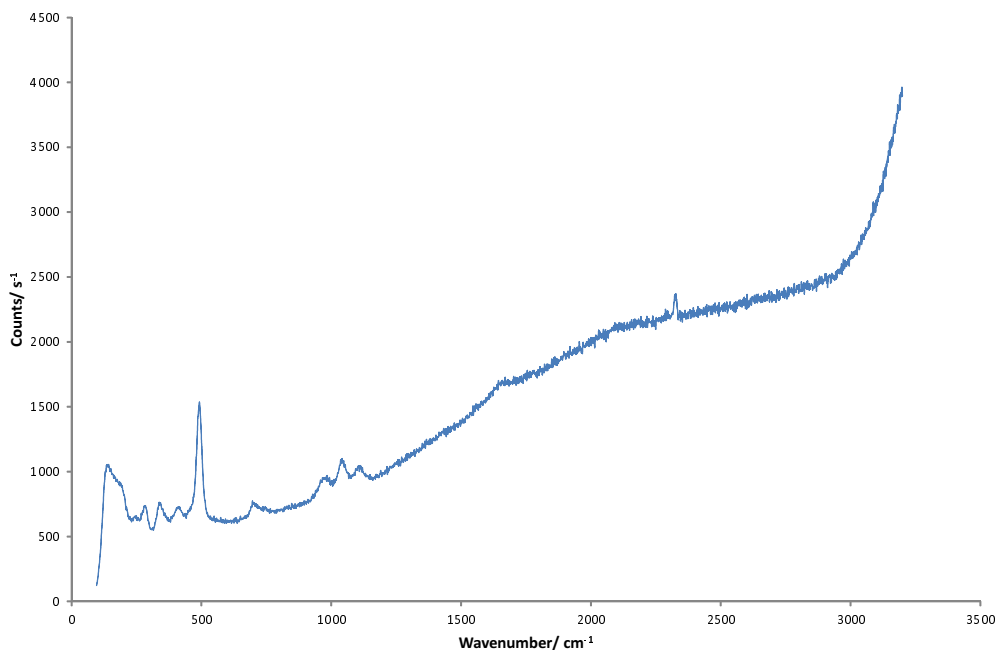
Figure 6.3: Zeolite powder Raman spectrum, 150 mW, 5 s exposure, 532 nm

C_nTABs

Isotherms

Isotherms of a few surfactants (LAS, $C_{12}E_6$, $C_{14}TAC$ (chloride)) adsorbing to zeolite A have been previously studied, although $C_{12}TAC$ was measured at below the CMC.[132] The increase in component weight of $C_{14}TAB$ adsorption on zeolite against concentration using the small mixer is shown in figure 6.7. Data for the large mixer is shown in figure 6.8. An example of the refined spectra from figure 6.8 is available in figure 6.9. TFA on the zeolite isotherms followed by conversion to surface excess is shown in figure 6.7. The component separation is good, but the data and bulk subtraction are poor because the background varies greatly, and the $C_{14}TAB$ signal in the raw spectra is weak, resulting in varying maximum component weight. We observe a linear adsorption isotherm profile, consistent

Table 6.2: Surfactant concentrations for zeolite kinetics

Sample Name	Concentration/ mM
$C_{16}TAB$-4mM	3.578 ± 0.007
$C_{16}TAB$-8mM	$8.15 \ \pm 0.01$
$C_{12}E_5$-1mM	1.397 ± 0.005
$C_{12}E_8$-1mM	0.943 ± 0.004
$C_{12}E_8$-4mM	4.529 ± 0.007
$C_{14}E_8$-1mM	1.080 ± 0.004
$C_{16}E_6$-1mM(1)	1.223 ± 0.004
$C_{16}E_6$-1mM(2)	0.983 ± 0.004
$C_{16}E_6$-2mM	2.009 ± 0.005
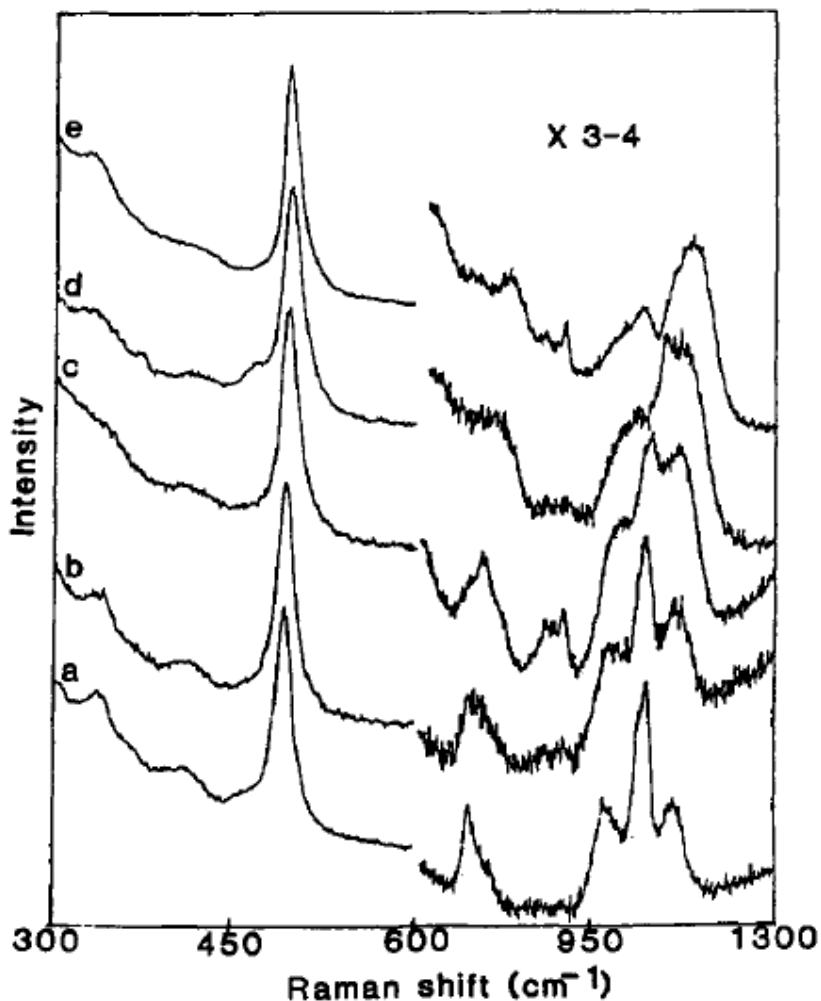
Figure 6.4: Raman spectra of calcined and Na^+-exchanged zeolite samples: (a) Si/Al = 1.0; (b) Si/Al = 1.2; (c) Si/Al = 1.4; (d) Si/Al = 2.0; (e) Si/Al = 2.7. Laser line = 457.9 nm. Reprinted with permission from reference 191. Copyright 1988 American Chemical Society

with a C (constant partition) class adsorption isotherm for microporous substrates.[15] However, Luo *et al.* found the C_{16}TAB isotherm on zeolite A to be S-shaped.[194] On natural Chilean Na-zeolite, Taffarel and Rubio found an L class isotherm;[131] the isotherm class depends on the type and nature of zeolite used.

A clearer view of the data from the large mixer, by scaling a mean of 10 consecutive raw spectra, is shown in figure 6.10. The "start" refers to pure water on zeolite coated silica hemisphere; "in end" refers to after ≈ 3300 s of pumping the target concentration solution into the mixer at $0.5 \, \mathrm{ml \, min^{-1}}$; and "out end" refers to the end of the "out" rinse. These spectra have been scaled so that the background at around $2650 \, \mathrm{cm^{-1}}$ and $3100 \, \mathrm{cm^{-1}}$ overlaps. In the average data, we observe maximum adsorption for the $4 \, \mathrm{mM}$ solution, which could be expected for a non-homogeneous substrate at the CMC, although we do not observe this overshoot using other concentrations in the isotherm.[15] We rarely observe a maxima in other C_{14}TAB isotherms on silica, but impurities are also a possible cause. Due to the non-uniform nature of the substrate, the variation in Γ_{max} is most likely due to differences between probed areas.
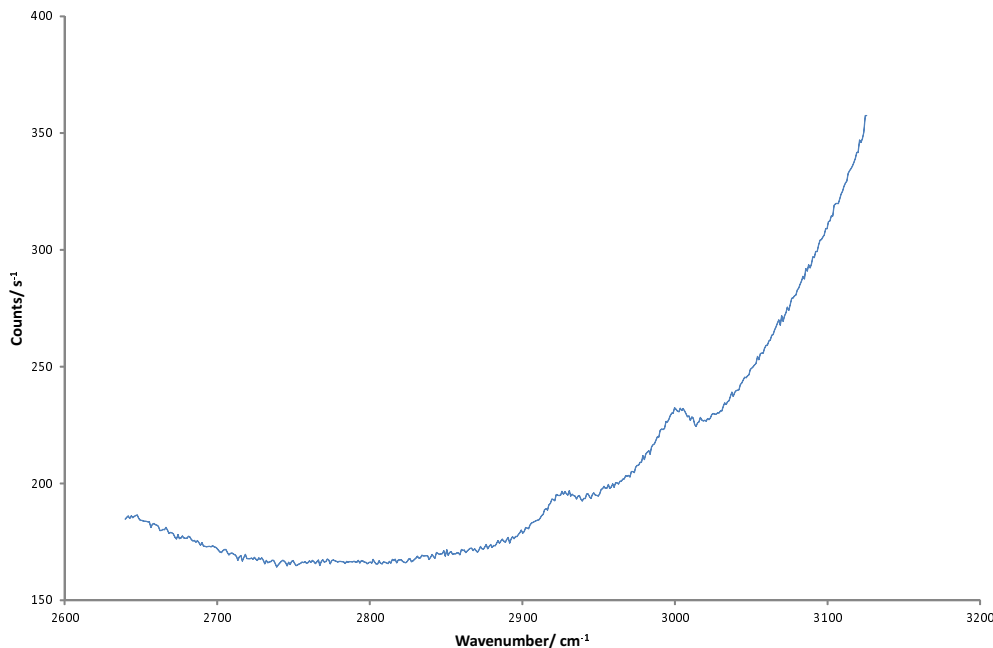
Figure 6.5: Raman spectrum of silica hemisphere coated in zeolite, in water. 700 mW, 5 s exposure, average over 10 consecutive acquisitions, 532 nm

The intensity of the C_{14}TAB peaks returns nearly to the level at the start, showing that the surfactant is not fully removed on the experimental timescale, but further rinsing with water does result in complete removal. Looking at the raw number of counts for the C_{14}TAB C−H bands against water on zeolite compared to silica, at the same concentration, above the CMC, we have ≈40 % decrease in the amount of surfactant on the surface. To calculate this percentage we have subtracted the increased background as we assume that this arises from the substrate scattering light, which we know varies. The ≈40 % reduction in ζ potential over that of silica will lead to weaker electrostatic attraction to the charged cationic head-group. The increased surface roughness could also contribute to the reduction, by inhibiting close-packing.

The literature value for a vertical monolayer of C_{14}TAC on zeolite A is $35 \, \text{Å}^2 \, \text{molecule}^{-1}$ which when converted is $4.7 \, \mu\text{mol} \, \text{m}^{-2}$.[132] Our value comes in at around half this, but again we know our surface is not uniform this results in our coverage being patchy.

By monitoring the ζ potential as a function of C_nTAB concentration it is possible to determine when the potential changes sign, indicating the probable change between monolayer and bilayer coverage and this may be a useful additional area of investigation.[131] A study by Taffarel and Rubio found that the zeta potential changes sign at 100 % external cation exchange capacity (0.136 meq. CTAB g^{-1} zeolite).[131]

As it was difficult to obtain good isotherms on zeolite we switched to studying the kinetics of adsorption.
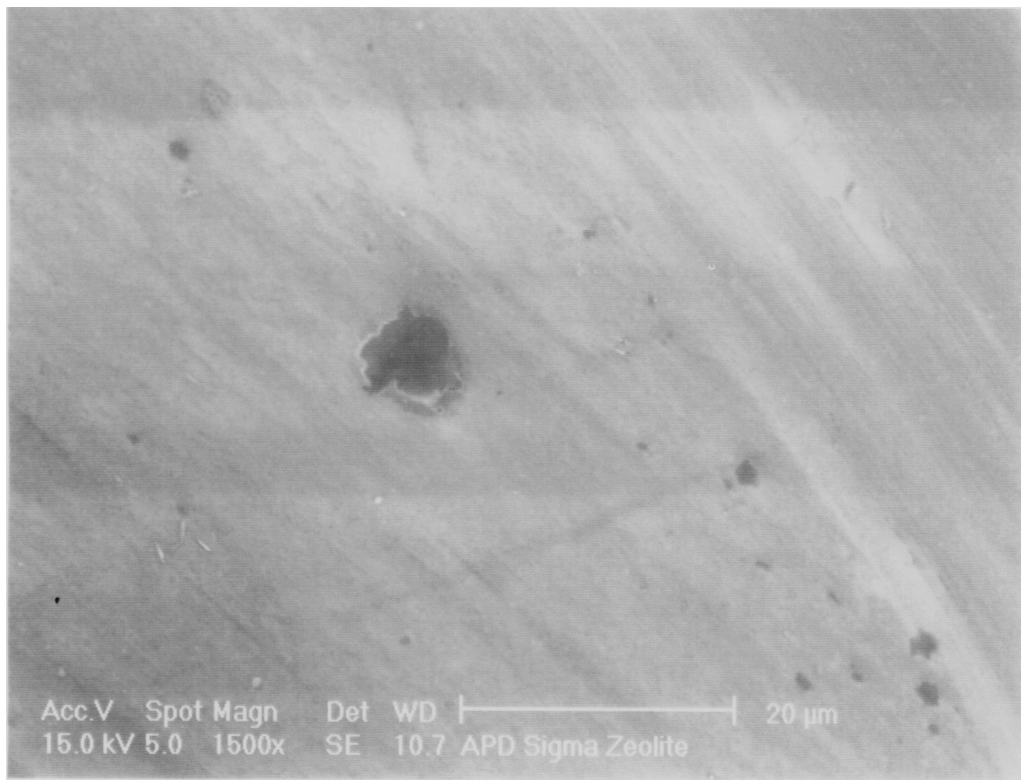
Figure 6.6: 1500× magnification SEM image of calcined zeolite A sample on glass slide, carbon coated
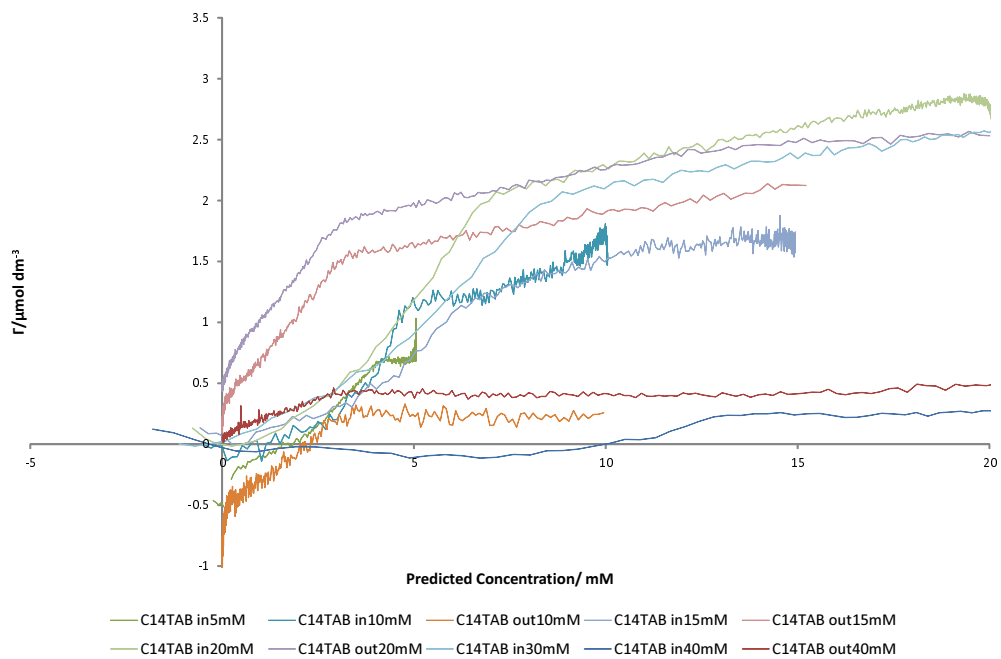
Figure 6.7: C_{14}TAB isotherm on zeolite (small mixer)

154
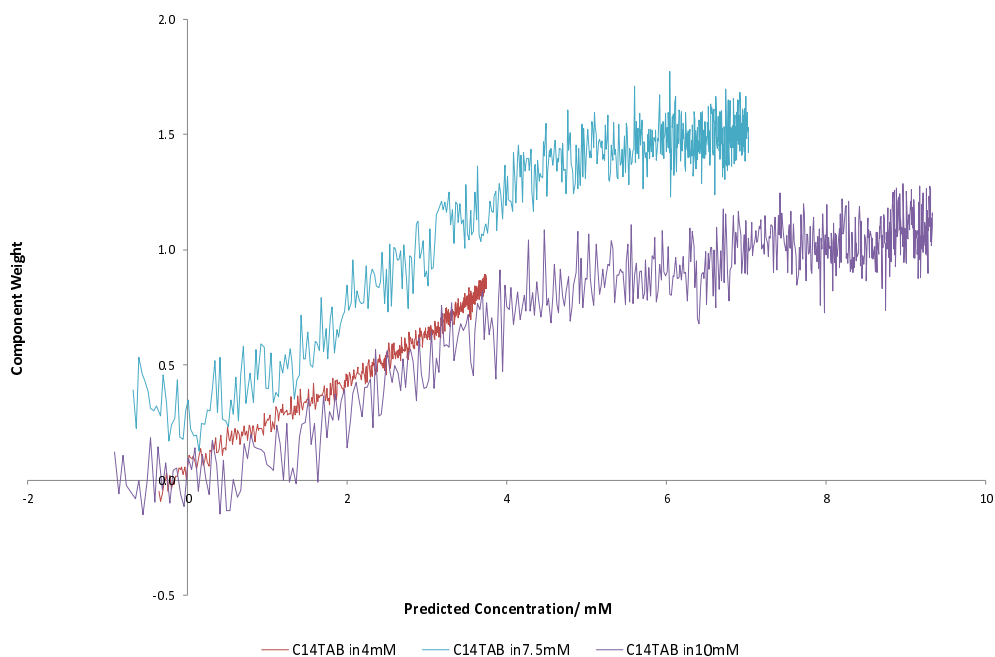
Figure 6.8: Component weights against predicted concentration for $C_{14}TAB$ adsorption to zeolite, $700\,mW$, $5\,s$ exposure, large mixer
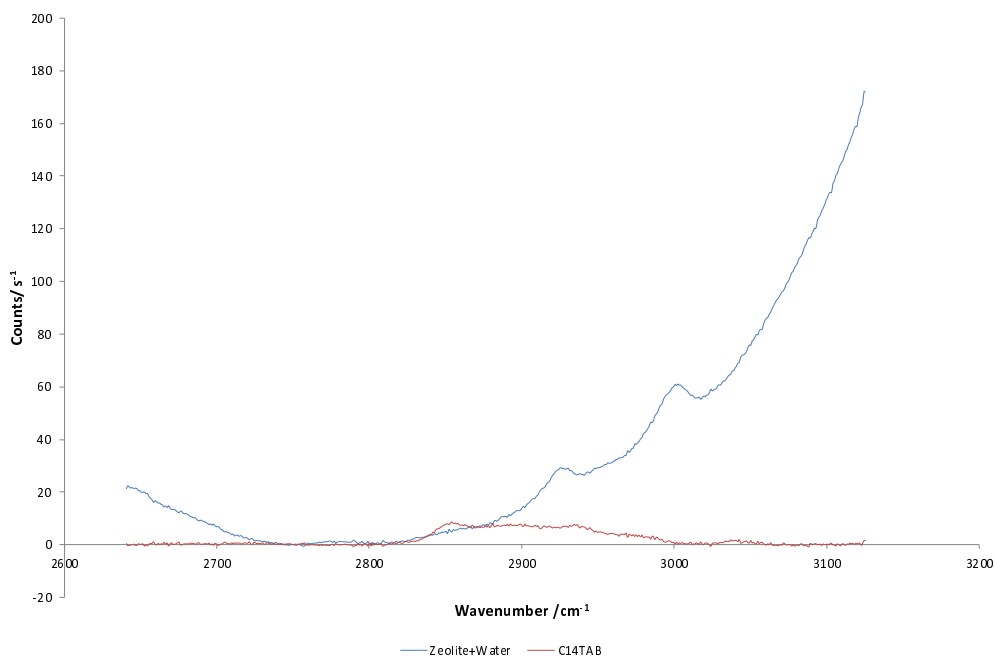
Figure 6.9: Components for "C14TAB in10mM" adsorption onto zeolite in figure 6.8, $532\,nm$, $700\,mW$
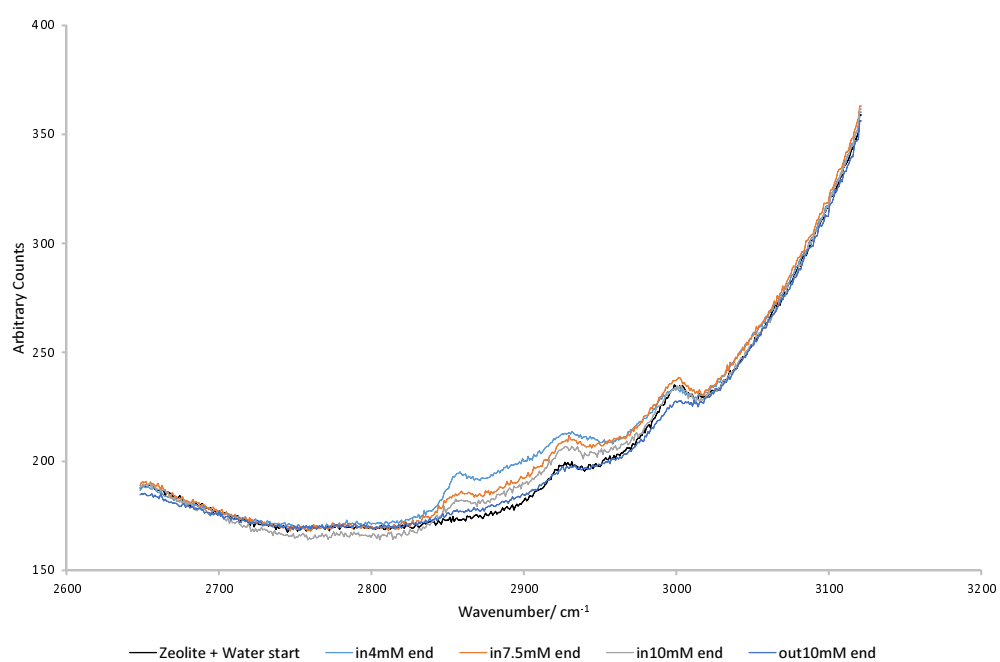
Figure 6.10: Average of 10 consecutive spectra for "start" and "end" of C_{14}TAB "in" adsorption to zeolite with target concentration in legend, $700\,mW$, $5\,s$ exposure, $532\,nm$

Kinetics

As $C_{16}TAB$ gave more reproducible data than $C_{14}TAB$ on plain silica, we changed to $C_{16}TAB$ for zeolite. Figure 6.11 shows the adsorption and desorption kinetics for $C_{16}TAB$ on zeolite, using isotherm $C_{12}TAB$ data from silica (figure 5.11) to convert the component weight into surface excess. This is a rough estimate of surface excess, as we do not have a well defined surface area and our penetration depth will be lower than for silica/water. Looking at the raw counts for $C_{16}TAB$ on zeolite against water, we have around half (a monolayer) the amount adsorbed compared to silica. We are probably observing patchy bilayers/admicelles on the surface. Subtraction of the bulk contribution was not included when calculating Γ. The surface coverage reaches equilibrium in $\approx 35\,\text{s}$ independent of concentration. Experiments marked "1ml/min" were performed at twice the pumping speed (at $1\,\text{ml min}^{-1}$), but the rate of adsorption does not change (not diffusion controlled). There still were some component separation problems, indicated by the y-axis offsets. This is most likely caused by the (large, relative to surfactant signal) background varying. Desorption is slower and is dependent on concentration, although the data are less reproducible due to variable background from variations between probed areas. From figure 5.15 the flux limit is around $13\,\mu\text{mol m}^{-2}\,\text{s}^{-1}$ for $C_{16}TAB$ with a CMC of $1\,\text{mM}$, well above the rates observed here, hence the adsorption process is not diffusion-limited.

SDS

Figure 6.12 shows the results from the adsorption and desorption of a $(10.00 \pm 0.01)\,\text{mM}$ SDS surfactant solution ("SDS (2)" is a repeat) to the zeolite layer. Figure 6.13 shows the components. SDS does not significantly adsorb to silica and we would not expect it to adsorb to a negatively charged zeolite surface. SDS adsorption was also investigated and found to be minimal by Taffarel and Rubio, who were using $C_{16}TAB$-modified zeolite to remove $C_{12}LAS$ from wastewater.[131] The adsorption is around $1\,\%$ of what we would see for $C_{16}TAB$ on silica. Adsorption and desorption are quite slow, with a long lag, and occur at around the same rate. The negative counts in the SDS component will result in an increased component weight.

We also attempted to see if a cationic electrolyte would reduce the repulsion between the negatively charged surface and anionic surfactant head-group, as zeolite is used industrially as a cationic exchange medium. Experiments were performed in the presence of a $CaCl_2$ solution already in the cell, with the same salt concentration in the surfactant solution (to exchange the sodium ions in the zeolite with the calcium). The results are not shown as the salt caused the SDS to precipitate out of solution on the surface (or form $Ca-SDS$ complexes) as the salt lowers the Krafft point of the solution. The surfactant did then redissolve on addition of more solution.
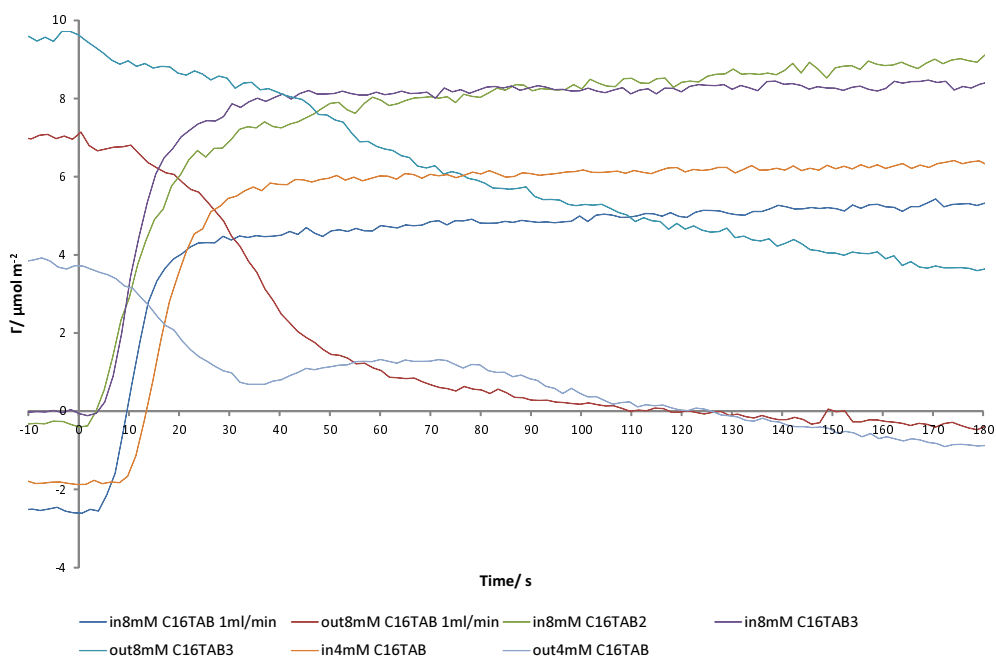
Figure 6.11: C_{16}TAB adsorption and desorption kinetics for zeolite, 700 mW, 5 s exposure, 0.5 ml min^{-1} pumping speed for all, except those labelled "1ml/min" (1 ml min^{-1}) Conversion to surface excess from C_{16}TAB isotherm on silica (small mixer)
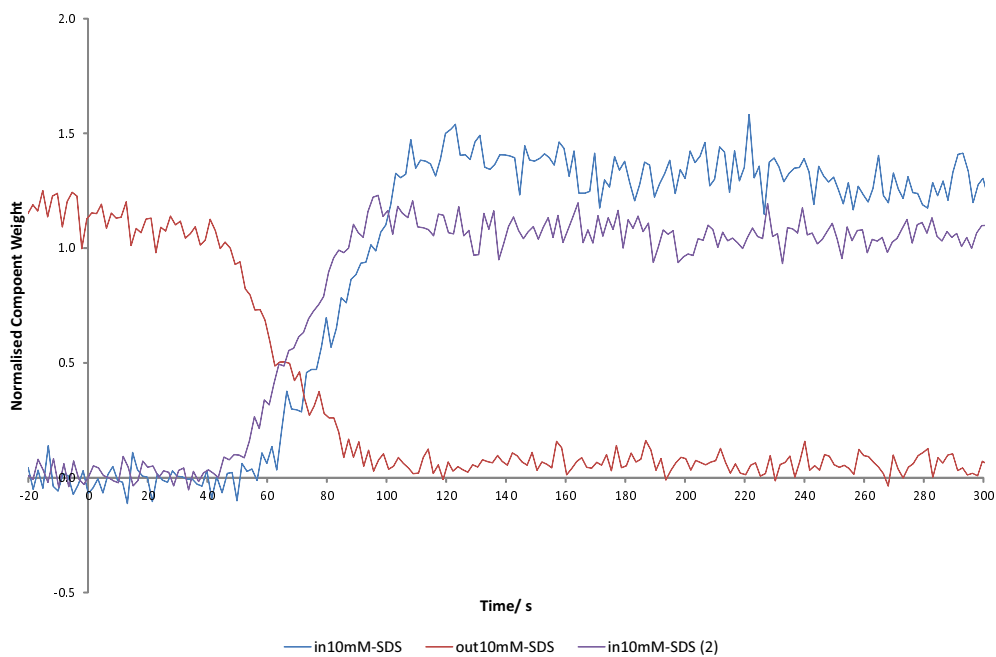
Figure 6.12: SDS kinetic adsorption to zeolite, 0.5 ml min^{-1}, 700 mW
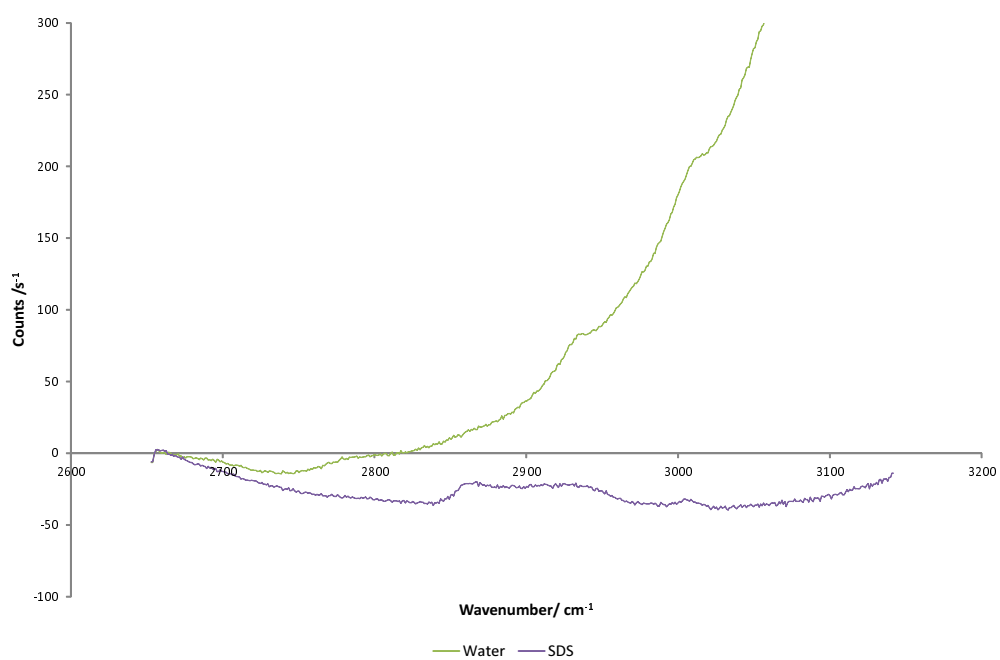
Figure 6.13: Components for SDS kinetic adsorption to zeolite, $700\,\mathrm{mW}$, $1\,\mathrm{s}$ acquisition, $532\,\mathrm{nm}$

Polyethylene Oxide Alkyl Ethers

We looked at various polyethylene oxide alkyl ethers (C_nE_ms) nonionic surfactant homologues adsorbing to zeolite. Anionic surfactant adsorption to zeolites are of interest as they have been found to inhibit particle growth during synthesis of synthetic zeolites;[133] the smaller (nm) particles exhibit higher cationic exchange rates compared to larger (µm) particles.[195] As discussed in section 1.2.1, the longer the tail-group, typically the higher Γ_{max}. This is because there is increased attraction between the longer hydrophobic groups. Increasing the length, and therefore the area of the head-group, results in a decreased Γ_{max}. The tail-group also affects the CMC, with longer chained molecules having a lower CMC. The packing of the surfactant is also related to the preferred curvature of the aggregate, via the surfactant packing parameter P. We know that for hydrophilic surfaces, as the length of the head-group increases the shape of the isotherm becomes more sigmoidal and the adsorbed amount decreases.[196]

Isotherms

Due to low CMCs we can only essentially record kinetic experiments for the C_nE_ms using our set-up, as it takes a long time to reach equilibrium using the mixer and there may be surface depletion effects. The low concentrations would also make it difficult to see the surfactant in the bulk, needed to perform the conversion into surface excess.

Kinetics

To see if head-group and tail-group size affect the kinetics of adsorption and desorption, we perform experiments with different sized C_nE_m surfactants. By varying the head- and tail-group size we can investigate what effect the size has on the rate of adsorption. Increasing the tail-group size will have the largest effect in lowering the CMC.

$C_{12}E_5$

$C_{12}E_5$ has the shortest head-group and a CMC of $0.05\,\text{mM}$[159]. We would therefore expect the molecules to pack close and lead to a larger Γ_{max}. Figure 6.14 shows the kinetic adsorption of $C_{12}E_5$ to zeolite with the components inset. The rate of desorption is about a quarter the rate of adsorption, a step function). The components are almost identical, with the exception of the normal speed ($0.5\,\text{ml min}^{-1}$) $1\,\text{mM}$ solution, in red, with an additional peak at $\approx 3010\,\text{cm}^{-1}$. This could be due to an impurity. The two recorded at $1\,\text{ml min}^{-1}$ used twice the pumping speed, and hence adsorption starts at around half the time of the normal speed experiments. Comparing the average equilibrium amount adsorbed for $C_{12}E_5$ with $C_{14}TAB$ on zeolite, there is around 3 times more $C_{12}E_6$, and $C_{16}TAB$ adsorption is around $80\,\%$ that of $C_{12}E_5$.
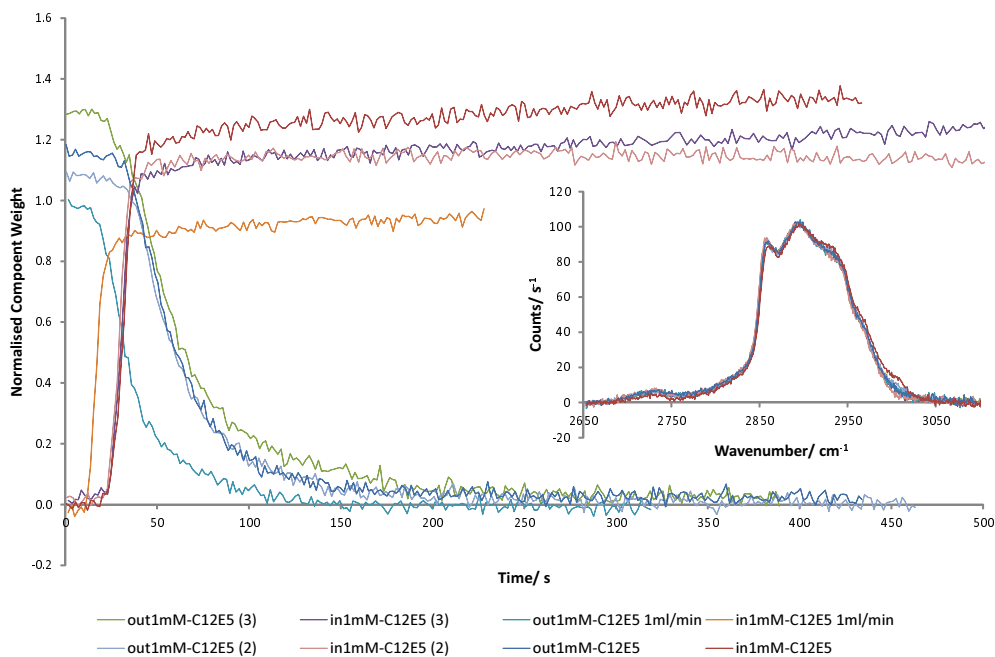
Figure 6.14: $C_{12}E_5$ kinetic adsorption to zeolite $700\,\mathrm{mW}$, $1\,\mathrm{s}$ acquisition, $0.5\,\mathrm{ml\ min^{-1}}$ for all except "1ml/min" ($1\,\mathrm{ml\ min^{-1}}$), with surfactant components inset, $532\,\mathrm{nm}$

$C_{12}E_8$

$C_{12}E_8$ has a CMC of $0.08\,\mathrm{mM}$ and has a larger head-group, so we would expect lower Γ_{max} than for $C_{12}E_5$. Figure 6.15 shows the results from $C_{12}E_8$ kinetic adsorption. Again, the series labelled as "double" used twice the pumping speed, hence desorption occurs at half the time (adsorption starts early but then decreases, possibly due to a bubble). Our maximum component weight varies greatly. Since the (non-normalised) surfactant components, shown in figure 6.16, are nearly identical (because the target spectra used is the same for each measurement), the increase in component weight is real and corresponds to a varying amount on the surface (Γ_{max}). This suggests that the amount of surfactant adsorbed is highly dependent on the area we probe (the surface is not uniform). While care is taken to always observe the same area, clearly variations occur. The maximum adsorption is far less reproducible than $C_{12}E_5$, probably due to a lower signal to noise ratio resulting from less surfactant adsorbed. The amount of $C_{12}E_8$ adsorbed is around $30\,\%$ that of $C_{12}E_5$. The approximate rates for adsorption and desorption were slower than for $C_{12}E_5$ and, due to the longer head-group, are more sigmoidal.
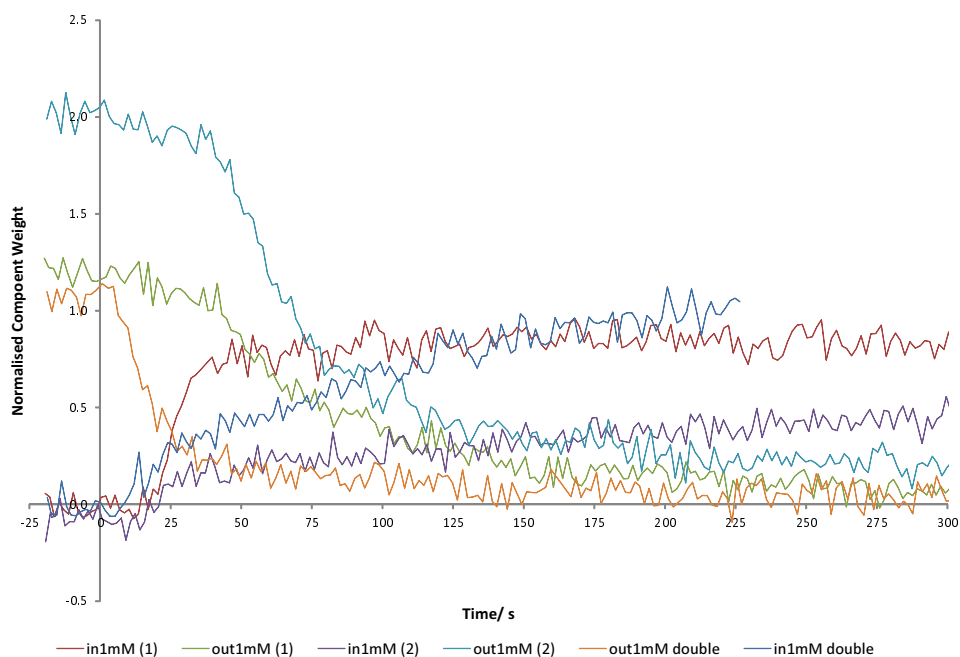
Figure 6.15: $C_{12}E_8$ kinetic adsorption to zeolite, $700\,\mathrm{mW}$, $1\,\mathrm{s}$ acquisition, $0.5\,\mathrm{ml}\,\mathrm{min}^{-1}$ for all except "double" $(1\,\mathrm{ml}\,\mathrm{min}^{-1})$
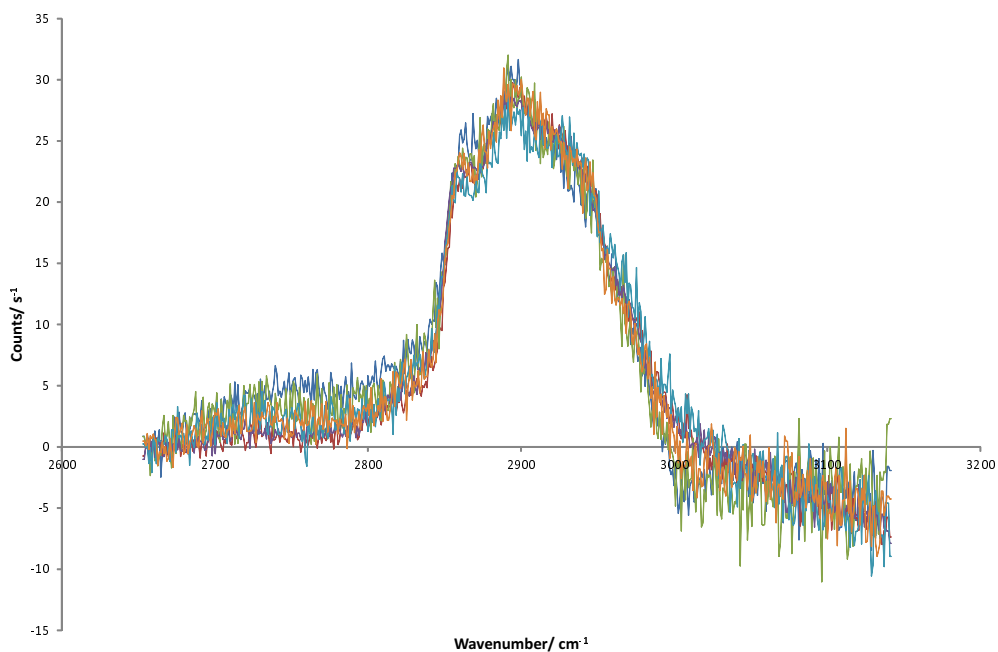
Figure 6.16: Refined surfactant spectra for $C_{12}E_8$ kinetic adsorption to zeolite, $700\,\mathrm{mW}$, $1\,\mathrm{s}$ acquisition, $532\,\mathrm{nm}$

162

$C_{14}E_8$

$C_{14}E_8$ has the same sized head-group, but longer tail-group than $C_{12}E_8$, therefore we would predict increased affinity for the surface. Figure 6.17 shows the kinetic adsorption and desorption for $C_{14}E_8$. Despite there being limited data, the results are of good quality and component separation is excellent. We can see that adsorption and desorption occurs more slowly, and desorption is not complete within the experimental time-frame. Increased tail-group size leads to more favourable chain–chain interactions on the surface and in micelles, leading to a decrease in the rate. The surfactant is removed on rinsing with ≈100 ml of water. We would expect there to be a longer induction time (time before the surfactant starts desorbing) due to the time it takes for the concentration to fall from 1 mM to below the CMC (0.01 mM) before desorption occurs. Looking again at the number of counts, the amount of $C_{14}E_8$ on the surface is around 80 % that of $C_{12}E_5$, and nearly 3 times as much as $C_{12}E_8$ are so our predicted trend on increasing tail-group size is correct. The decrease in adsorbed amount, compared to $C_{12}E_5$, is due to a longer head-group requiring more area on the surface. A competing factor, increasing peak height, is that the larger head-group of $C_{14}E_8$ contributes more $C-H$ bonds to the spectra from fewer molecules adsorbed.
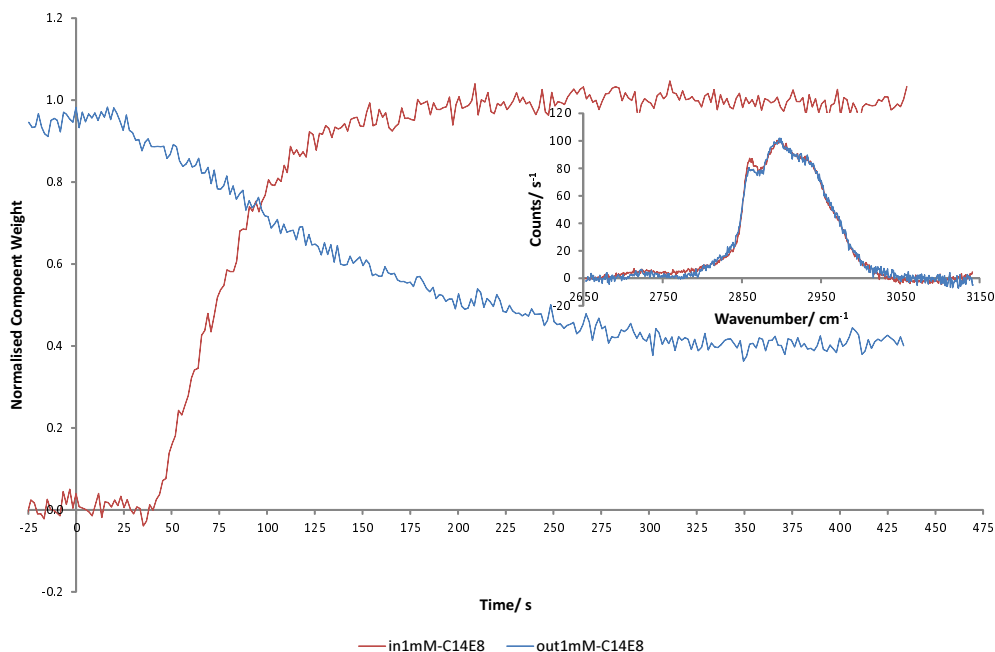
Figure 6.17: $C_{14}E_8$ kinetic adsorption to zeolite $700\,mW$, $1\,s$ acquisition, $0.5\,ml\,min^{-1}$, with surfactant components inset, $532\,nm$

$C_{16}E_6$

Figure 6.18 shows the kinetics for $C_{16}E_6$ adsorption to zeolite. $C_{16}E_6$ has the longest tail-group size and the lowest CMC of the surfactants investigated ($0.0017\,mM$). The component separation was poor for adsorption and desorption however we can see that removal does not occur during rinsing, instead the component weight increases. The increase on rinsing could be plausible as diluting can cause deposition of surfactants. The CMC is very low, hence most of the surfactant will be in micellar form. If only monomers adsorb, the micelles may need to break down first (kinetic delay). Additionally, micelles diffuse more slowly than monomers due to their size. Additionally $C_{16}E_6$ forms rod-like micelles in solution that diffuse slower than spheres. Comparing the refined spectra with those for $C_{14}E_8$ and looking at the d^-/d^+ ratio we can see that peaks represent a more ordered structure. The hydrocarbon chains are more vertical and the head-groups are less randomly arranged. The increased ordering could also be indicative of an impurity adsorbing. Given the change in spectra, it is likely that adsorption of an impurity (possibly hexadecanol) is being observed and not the $C_{16}E_6$. The amount of C−H adsorbed is around $85\,\%$ of $C_{12}E_8$.

164
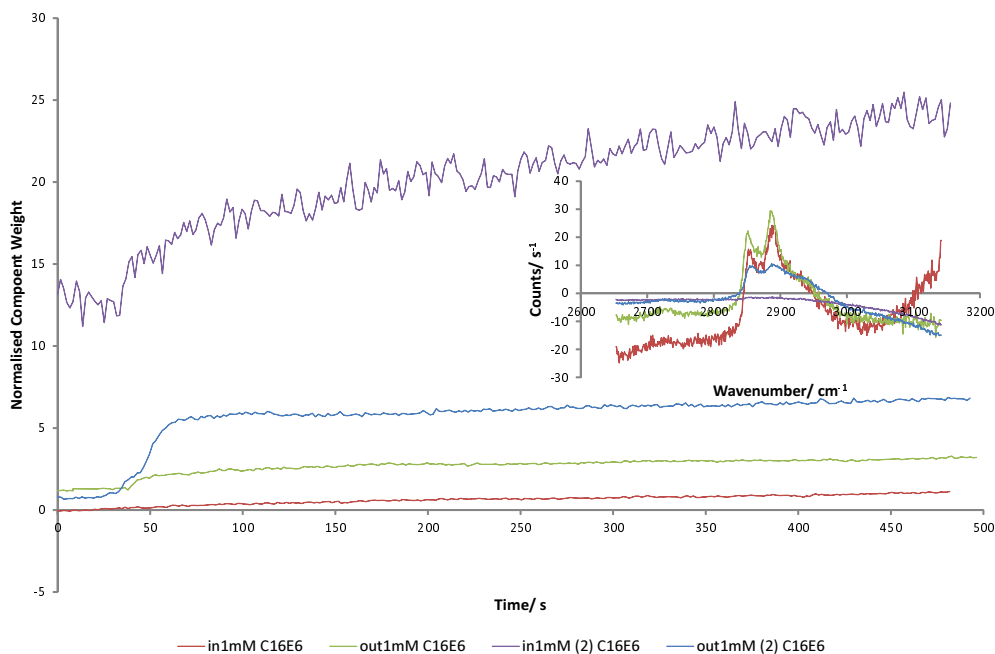
Figure 6.18: $C_{16}E_6$ kinetic adsorption to zeolite, $700\,\text{mW}$, $1\,\text{s}$ acquisition, $0.5\,\text{ml min}^{-1}$, with surfactant components inset, $532\,\text{nm}$

Kinetics Discussion

In summary, the kinetics of C_nE_m surfactants adsorption to zeolite follows our predicted trends based on head- and tail-group size, with increasing sigmoidal shape and decreased surface coverage on increase in head-group size, and increased adsorption with a decrease in rate on increase in tail-group length (although we only really have two lengths of each to compare). The amounts are comparable to that of monolayer of $C_{16}\text{TAB}$ on silica. While there is some variation of the equilibrium adsorbed amount (due to inhomogeneity of the zeolite substrate) making accurate determination of the surface excess difficult, it is possible to follow the trends. Component separation is generally good. Although, to compare these fully we would need to convert our component weight data into surface excess. To calculate the surface excess we need to determine the surface area of zeolite accessible to the surfactant solution per unit area of the substrate.

6.2.5   Discussion

Overall we have shown that we can monitor both the kinetics and an isotherm for various surfactants adsorbing to a zeolite substrate using TIR-Raman spectroscopy. The timescales of adsorption kinetics for the surfactants studied on this substrate ($\approx 10\,\text{s}$) are easily measurable with our new spectrometer set-up (as they would also be with slower spectrometers, such as the Renishaw spectrometer). The substrate layer does not appear to change or be removed by surfactants.

Our results are consistent with the zeolite layer possessing a negative charge; where nonionic and cationic surfactants can adsorb to the surface. We have seen that one anionic surfactant (SDS) adsorbs very little, therefore we did not investigate other anionics.

Among the nonionic polyethylene oxide alkyl ethers, $C_{14}E_8$ and $C_{12}E_5$ produced

the most reliable results. $C_{12}E_5$ and $C_{12}E_8$ desorbed on rinsing; $C_{16}E_6$ and $C_{14}E_8$ did not fully desorb on rinsing. Increasing the head-group (E) size has been seen to decrease adsorption on silica and cellulose,[197] which matches our results. Lengthening the hydrophilic head-group chain also increases the hydrophilicity of the surfactant and might decrease its adsorption if the adsorption is driven by the hydrophobic effect. If the surfactant forms a complex with Na^+ or K^+ ions, then adsorption would increase on increase in head-group size. We have seen the surfactants with the shorter tail-group desorb. The shorter chained surfactants have higher CMCs and desorption will only occur below the CMC. Therefore, it takes longer for the concentration of longer chain surfactants to drop low enough for desorption to take place. When desorption does occur, the process is slow because dc/dz is very small and flux J is $J = -\Delta dc/dz$, where c is the concentration and z is the distance from the surface.

Nonionic adsorption is governed by the preferred curvature of the aggregate, following equation 1.11 which relates the tail-group area and length, and head-group area. For the nonionic surfactants used, $C_{12}E_8$ and $C_{12}E_5$ both form spherical aggregates, but $C_{12}E_5$ with the smaller head-group allows for a smaller curvature and more adsorption.

There is more variation in the amount adsorbed on zeolite compared to silica, which may be due to the surface not being uniform or having a well defined surface area. By exchanging the cation in the zeolite layer it may be possible to investigate if the cation exchange properties of zeolite affect adsorption of cationic and anionic surfactants by changing the cation to adjust the screening of the substrate charge. However, this experiment caused precipitation when using $CaCl_2$ and SDS. It is difficult to determine the effect of surface charge from our data due to the surface area of the zeolite being unknown, but comparing $C_{16}TAB$ adsorption on silica and zeolite (where the component separation has been successful) we see around half the amount adsorbed for zeolite. Both substrates possess a negative surface charge therefore electrostatics are likely to be a driving factor. To further investigate this we would need to compare with other substrates of differing ζ potentials.

6.3 Kaolinite

6.3.1 Introduction

Adsorption kinetics of an anionic and two nonionic (C_nE_m) surfactants on another silicate, kaolinite was studied. As kaolinite is often found in clay mud, it is a model soil (dirt) on fabrics in clay-rich regions. The structure of the mineral can be found in figure 1.17. After calcining, kaolinite forms a more reactive phase (metakaolinite) after loss of structural water with reorganization of the structure. Only a fraction of AlO_6 octahedra are retained, with the rest transformed into more reactive tetra- and penta-coordinated units.[198] Adsorption of other nonionics (polyoxyethylenic surfactants such as Triton-X100) have been previously studied and found to be highly dependent on the type and morphology of kaolinite and that the amount adsorbed decreases with increasing head-group size.[199,200] Decreased skin flotation (increased hydrophilicity) of kaolinite was observed after adsorption of mixtures of SDS and $C_{12}E_8$, as the $C_{12}E_8$ reversed orientation.[201] The affinity of kaolinite for adsorbing cations is lower than that

of zeolite.[119]

6.3.2   Experimental

The kaolinite substrate purchased from Sigma was prepared and calcined using the same method as zeolite in section 6.2.2, above.

6.3.3   Surface Characterisation

Figure 6.19 shows the Raman spectrum of kaolinite powder taken on the Renishaw spectrometer. Figure 6.20 shows the literature Raman spectrum.[202] There is a lot of fluorescence in the powder spectrum, so it is hard to identify the peaks but we do observe a peak at around $147\,cm^{-1}$ which is close to that of kaolinite type KGa-2 in the literature, at $142.7\,cm^{-1}$ assigned to the $O-Al-O$ symmetric bend.[202] The $200\,cm^{-1}$ to $1000\,cm^{-1}$ fingerprint region is largely obscured, but the peak at $637\,cm^{-1}$ matches the $636.5\,cm^{-1}$ band in the literature, assigned to the $Si-O-Si$ stretch.[202] The thickness of the kaolinite coating is unknown.

Figure 6.21 shows the TIR-Raman spectrum of kaolinite on the hemisphere, averaged over ten 1 second acquisitions. The spectrum looks identical to that of water and no peaks are obvious, however the increase in background counts (due to increased scattering) does demonstrate that there is something present in the probed region, which is not removed by rinsing or surfactant. We should observe peaks in the hydroxyl region (figure 6.20b), but these are probably obscured by the large background from increased light scattering. Neither of the peaks (at $2920\,cm^{-1}$ and $3000\,cm^{-1}$) seen in the hemisphere spectrum for zeolite (figure 6.5) are observed for kaolinite.
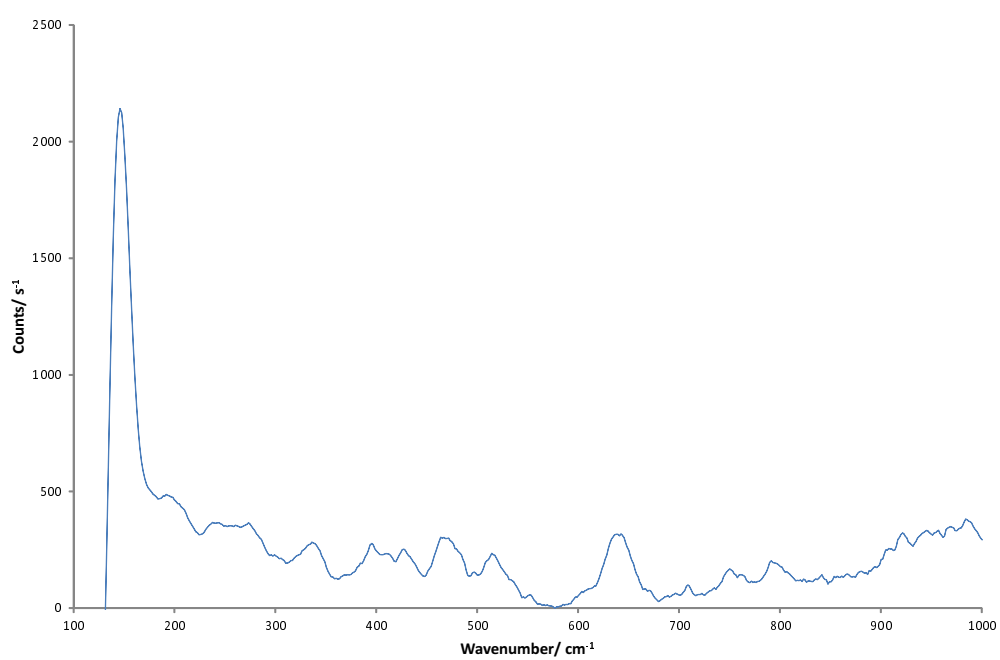
Figure 6.19: Raman spectrum of kaolinite powder, 50 mW, 10 s, background subtracted, 532 nm.
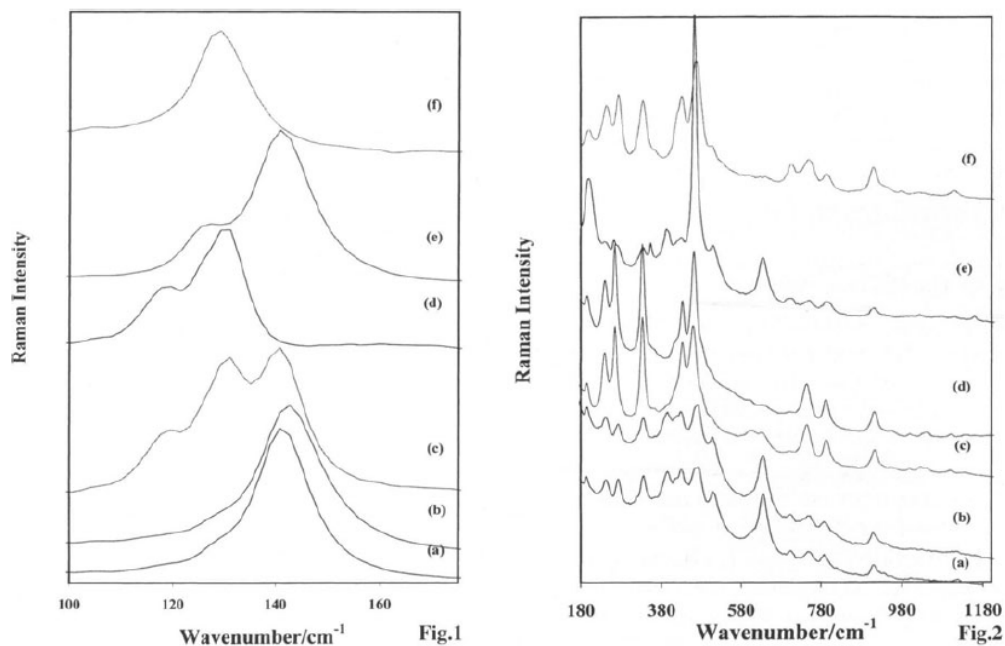
(a) $100 \, \mathrm{cm}^{-1}$ to $150 \, \mathrm{cm}^{-1}$ and $200 \, \mathrm{cm}^{-1}$ to $1200 \, \mathrm{cm}^{-1}$
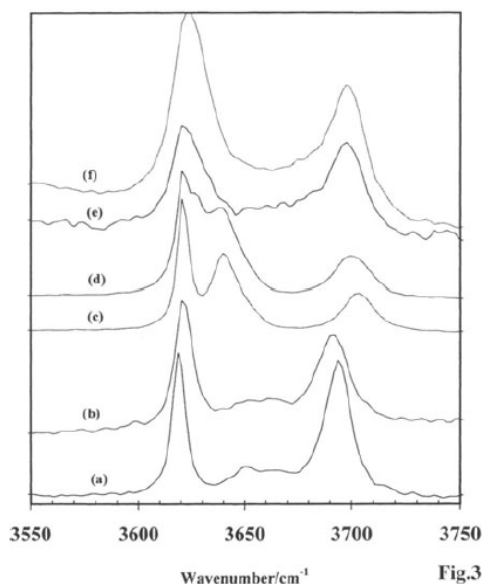
(b) Hydroxyl stretching region

Figure 6.20: The literature FT-Raman spectra of (a) kaolinite (KGa-1); (b) kaolinite (KGa-2); (c) dickite (San Juanito); (d) dickite (Sainte Claire); (e) halloysite (Eureka); and (f) halloysite (New Zealand). Reprinted with permission from reference 202. Copyright 1997 Springer
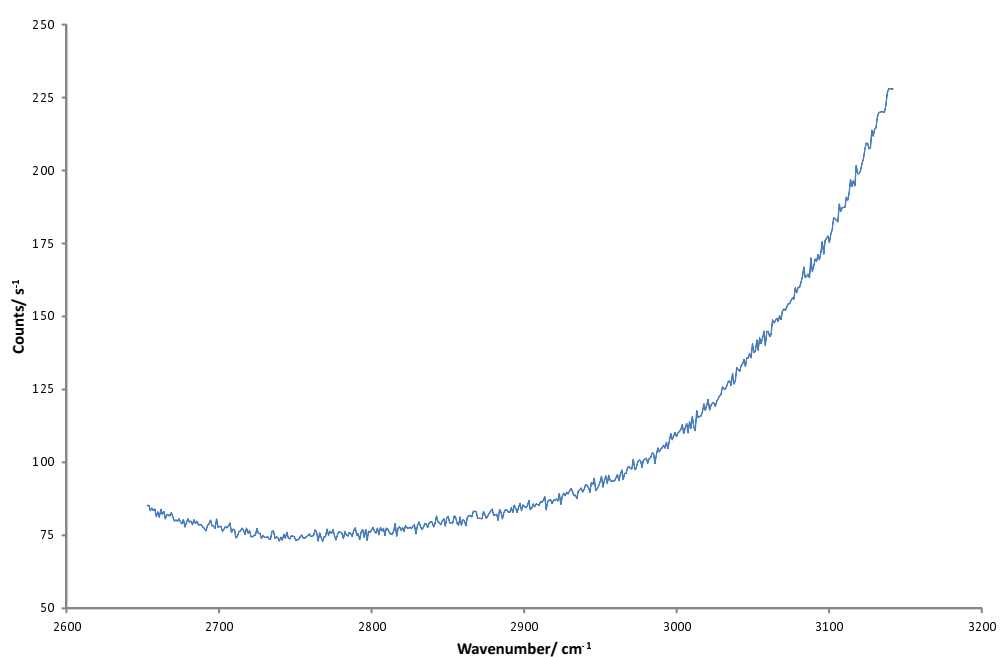
Figure 6.21: Spectrum of kaolinite on hemisphere in water, $700\,\mathrm{mW}$, $1\,\mathrm{s}$ acquisition, $532\,\mathrm{nm}$

6.3.4 Surfactant Adsorption

SDS Kinetics

SDS $((10.04 \pm 0.01)\,\text{mM})$ showed very minimal adsorption to kaolinite and PCA analysis of the kinetics was not possible. The SDS is just visible in figure 6.22, which shows the mean of 10 consecutive spectra before and after addition of SDS to the cell. We know that kaolinite has a lower affinity for cations than zeolite but is weakly positively charged, so we would not expect much adsorption.[201]

Polyethylene Oxide Alkyl Ether Kinetics

We used $(1.56 \pm 0.01)\,\text{mM}$ $C_{12}E_5$ and $(1.981 \pm 0.005)\,\text{mM}$ $C_{12}E_6$. Figure 6.23 shows the kinetics for $C_{12}E_5$ and $C_{12}E_6$ on kaolinite. The components are shown in figure 6.24, normalised to water, there is some variation in the background between measurements which could be due to measuring a different region. It is likely that a bubble passed through around $160\,\text{s}$ during "out $C_{12}E_6$".
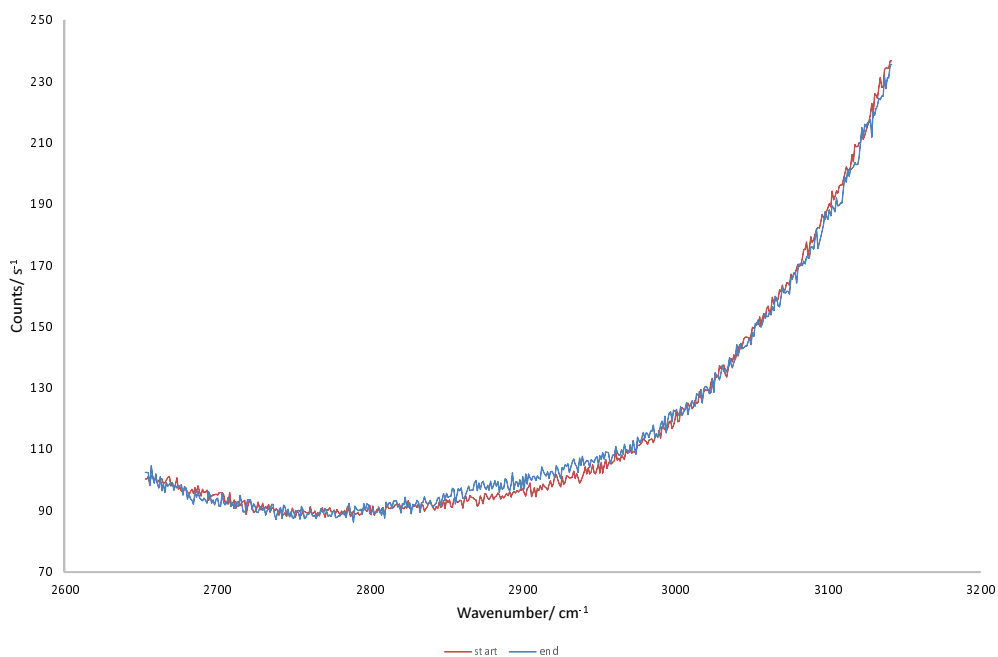
Figure 6.22: Mean of 10 consecutive spectra before ("start") and after ("end") SDS addition to kaolinite, $700\,mW$, $1\,s$ acquisition, $0.5\,ml\,min^{-1}$, $532\,nm$
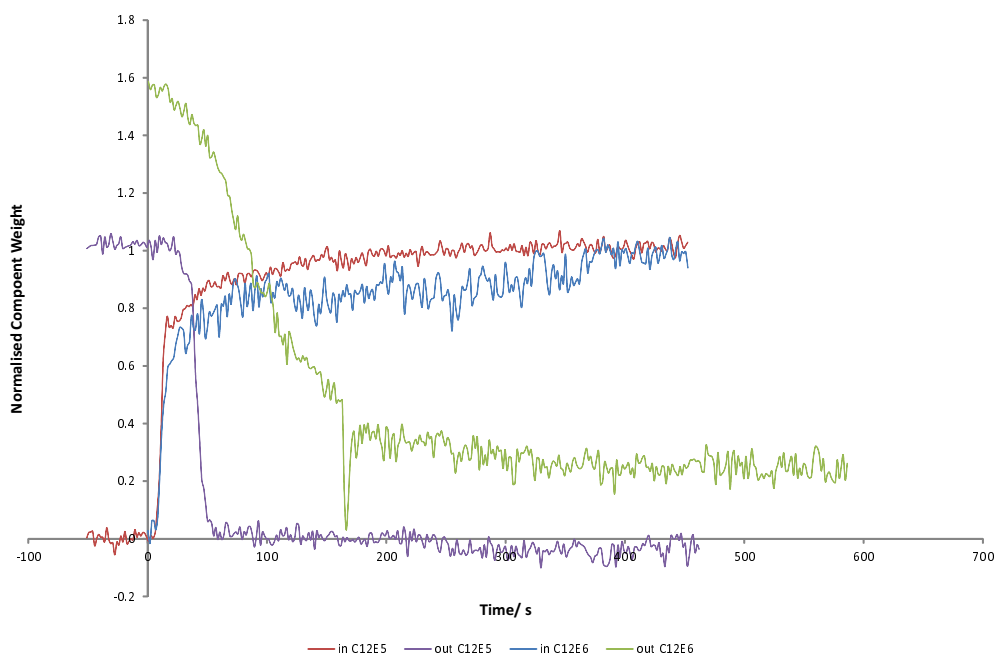
Figure 6.23: $C_{12}E_5$ and $C_{12}E_6$ kinetic adsorption to kaolinite, $700\,mW$, $1\,s$ acquisition, $0.5\,ml\,min^{-1}$
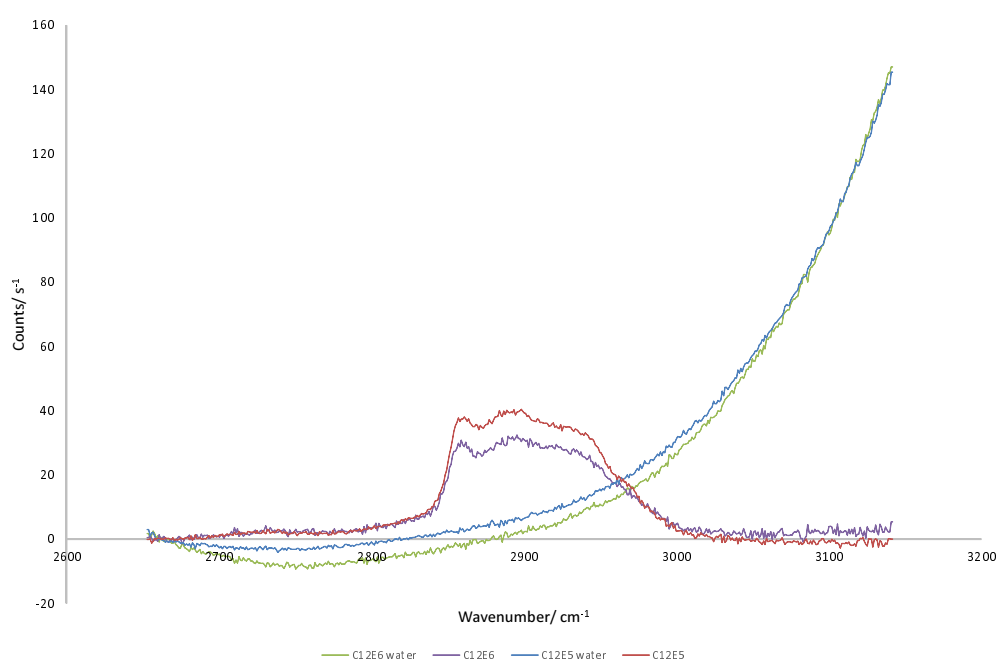
Figure 6.24: Components for $C_{12}E_5$ and $C_{12}E_6$ adsorption to kaolinite, normalised to water at $3100\,cm^{-1}$. $700\,mW$, $1\,s$ acquisition, $0.5\,ml\,min^{-1}$, $532\,nm$

Kinetics Discussion

The rate of adsorption is fast for the nonionics and appears to be identical for both surfactants, but we are approaching the limit of time resolution for the spectrometer. Desorption takes around twice as long as adsorption for $C_{12}E_5$ and much longer for $C_{12}E_6$. There also appears to be two rates of desorption for $C_{12}E_6$, with the rate decreasing at around 100 s, at about half the maximum component weight, which could be removal of the outer layer of a bilayer or could be due to the unknown surface roughness, heterogeneous surface charge[139] and porosity of the substrate. The varying surface charge may affect adsorption if the head-group is complexed with cations and this could be the reason for a decrease in $C_{12}E_6$ adsorption rate after around 100 s.

Comparing the raw, water normalised data for the two surfactants in figure 6.25, we have around 80 % of the adsorbed amount of $C_{12}E_5$ for $C_{12}E_6$. The bulk concentration is higher for $C_{12}E_6$, but the contribution from the bulk signal will be minimal at these low concentrations. The slightly larger head-group of $C_{12}E_6$ occupies more area, leading to lower surface excess. We would only expect a small change, as the EO head-group size is only increasing by one (OCH_2CH_2) unit.
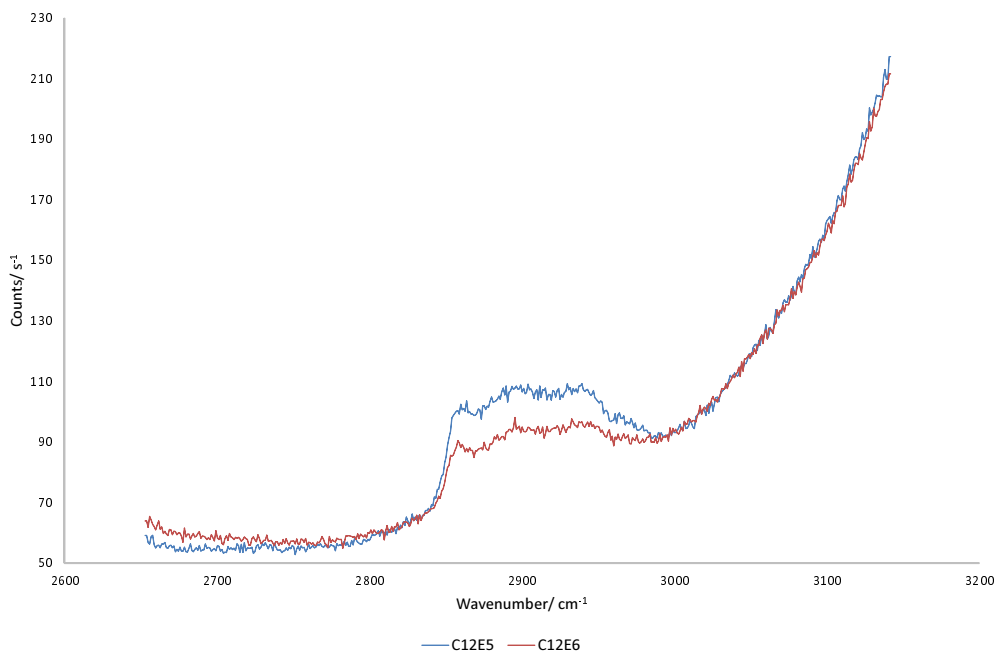
Figure 6.25: Mean of 10 spectra from end of kinetic experiment of $C_{12}E_5$ and $C_{12}E_6$ adsorption to kaolinite, normalised to water. 700 mW, 1 s acquisition, 0.5 ml min^{-1}, 532 nm

6.3.5 Discussion

Again, we have demonstrated that we are able to form, and monitor the adsorption kinetics of a small number of surfactants (an anionic and two nonionic) to, the kaolinite surface using TIR-Raman and that our coating on the silica hemisphere is not modified or removed by the surfactant. SDS showed very minimal adsorption despite a minimal positive surface charge.

We do not have sufficient data to accurately estimate Γ as we need to obtain bulk data to convert from component weight, but we can compare with our $C_{16}TAB$ data and estimate that we have around the same amount of $C_{12}E_5$ as $C_{14}TAB$ on silica ($\approx 6\,\mu M\,m^{-2}$).

As we have shown that this is a valid technique, it would be interesting to study a wider range of surfactants on the kaolinite substrate, although we need better characterisation of the surface, including determining the thickness of the layer and area available for adsorption. The variability of the surface and background does limit our ability to make accurate quantitative measurements.

6.4 Silicate Mineral Substrates Discussion

Figure 6.26 compares the intensity of the components for $C_{12}E_5$ on kaolinite and zeolite after normalising to the water component intensity; $\approx 30\,\%$ less surfactant adsorbs onto zeolite, although the surface areas of these substrates is not well defined, so we may just be observing different accessible areas of the substrate rather than chemical differences between the surfaces. Kaolinite has a lower affinity for adsorbing cations.[119] Therefore,

the increased number of adsorbed cations on the zeolite could reduce the adsorption of the slightly positive C_nE_m nonionic surfactants, by electrostatic repulsion. Binding of alkali metal cations from the substrate surface to the C_nE_m head-groups may also affect the charge on the head-group. We also observe around 2 times less water/background signal for the kaolinite when compared to zeolite which could be due to less scattering from the surface or due to having a less water in the kaolinite (again, we do not know the thickness of either substrate).

Rates of adsorption for $C_{12}E_5$ on both substrates are similar, and with limited data it is difficult to make firm conclusions, but from the data we do have, adsorption is fractionally faster on zeolite, but again this is likely dependent on the area probed.

It may be useful to try different cation electrolyte solutions (adsorbed into the zeolite pores), and investigate different pH levels to determine the effect on adsorption.
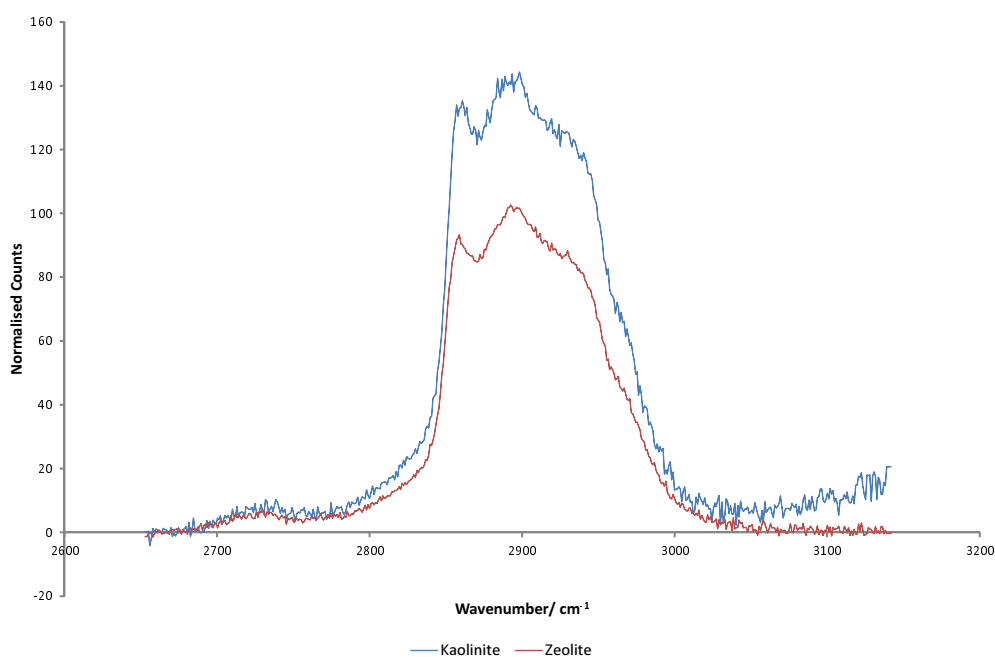
Figure 6.26: Comparison of $C_{12}E_5$ adsorption on kaolinite and zeolite, 700 mW, 1 s acquisition, normalised to water components at $\approx 3050\,\text{cm}^{-1}$, 532 nm

6.5   Polyester

6.5.1   Introduction

We studied the adsorption of surfactants to a spin-coated polyester layer. This work followed on from the work by Woods, who studied cellulose using the TIR-Raman technique.[1] Polyesters are semi-crystalline polymers commonly used in fabrics in the clothing industry and hence the behaviour of surfactants on this surface was of interest to us as surfactants are often used as detergents and for dyeing. Unlike natural fibres such as cotton, they are hydrophobic.

We formed and then looked briefly at a non-ionic and a cationic surfactant adsorbing to polyester. A combination of time constraints and removal of the layer by surfactants meant that we did not study this substrate in depth.

6.5.2   Experimental

Polyester, supplied by Domino UK Ltd., was spin coated onto the hemisphere from two drops (50 µL) of a solution of 50 mg of polyester in 5 ml of chloroform, at a speed of 4000 rpm using a Cammax Precima spin coater.

6.5.3   Surface Characterisation

The spin-coated polyester film was measured before the surfactant adsorption experiments. The thickness of the film was measured to be around 10 nm, using a spectrophotometer (nkd-6000, Aquila Instruments Ltd., UK). The obtained transmittance-reflectance curves (350 nm to 1000 nm wavelength range) were fitted, using the software provided, to a Cauchy model for dielectric materials using a modified Levenberg-Marquardt algorithm.

The Raman spectrum of a polyester coated hemisphere in water taken on the new spectrometer is shown in figure 6.27. The two strong bands at $1618\,\mathrm{cm^{-1}}$ and $1730\,\mathrm{cm^{-1}}$ match with literature values.[203] The spectra also suggest the layer is fairly amorphous. The Raman spectrum of polyester with water subtracted and a water spectrum, both on a silica hemisphere, are shown in figure 6.28. The main aliphatic C−H stretch is at $\approx 2970\,\mathrm{cm^{-1}}$ and the aromatic C−H stretch is at $\approx 3080\,\mathrm{cm^{-1}}$.

Initially the polyester thickness was found to be poorly reproducible (wildly varying C−H intensity against water), however we were able to improve the consistency with practice and more precise measurement of the deposited liquid volume. This was important as the polyester film was sometimes removed by surfactants and so we could not reuse the same layer, unlike our other substrates.

The polyester is suspected to be polyethylene terephthalate (PET). Analysis of our bulk sample by size exclusion chromatography, compared to a set of linear polystyrene standards, suggests a rather low number-average molecular weight of around $5200\,\mathrm{gmol^{-1}}$ (≈ 31 repeat units) and a polydispersity of 1.9. From literature, the refractive index n, is ≈ 1.65 at $532\,\mathrm{nm}$,[204] however, it is worth noting that PET is birefringent in sheet form and therefore refractive index depends on the dimension being measured and, that there is also a slight index grading in the thickness direction.[204,205] Using this refractive index, we obtain a penetration depth of $\approx 50\,\mathrm{nm}$, around half that of our silica/water interface.
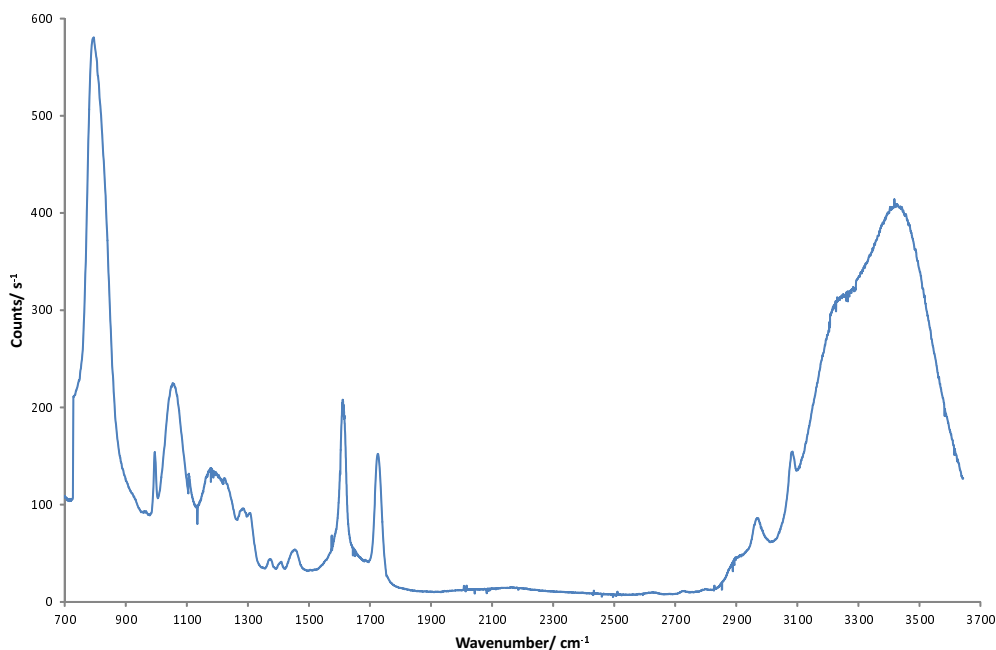
Figure 6.27: Spectrum of polyester on hemisphere, 700 mW, 20 s exposure, new spectrometer, 532 nm

The surface coating of polyester on the hemisphere, (a semi-crystalline polymer), appears to form domains (see figure 6.29) which may indicate uneven coverage; however spectra taken over a number of areas appear to be consistent (although the laser spot is often larger than the domains). The domains are likely to be stress fractures that developed during drying.

6.5.4   Surfactant Adsorption

C_{14}TAB

Figure 6.30 shows a sample of the data for a polyester layer before ("start") and after ("end") addition of (9.944 ± 0.004) mM C_{14}TAB normalised to water. We can see that the polyester appears to be partially removed in the latter spectrum as the aromatic and aliphatic polyester peaks have reduced in intensity. We also observe large variations in the intensity of the polyester peaks with repeated coatings. TFA did not yield any successful results, even when attempting the analysis with three components. Looking at the raw data, there appears to be some minimal initial adsorption of the surfactant to the surface, but this could be to the polyester or to the silica underneath if we are observing the layer being removed. Adsorption to the silica could detach the polyester layer. Under the optical microscope, we still observe the domains, which suggests the marks are either not formed from polyester or the polyester does not detach completely. Spectra from the edge of the domains are the same as from the centre. Again, the laser spot often covers an area larger than one domain, so we are unlikely to see variations in the two areas. Due to operator error the data is not centred on the usual $2900 \, \text{cm}^{-1}$ region.

Due to the problem of the possible removal of the polyester coating, work was not
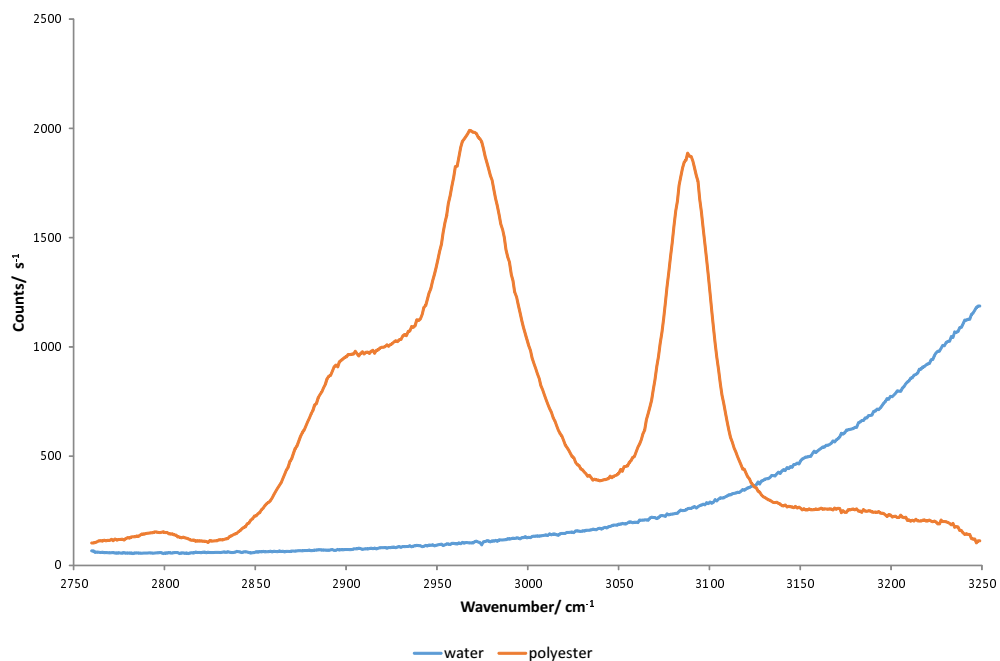
Figure 6.28: C−H region spectrum of polyester on hemisphere with water subtracted, and water on silica hemisphere, 700 mW, 5 s exposure, 532 nm

continued with C_nTABs.
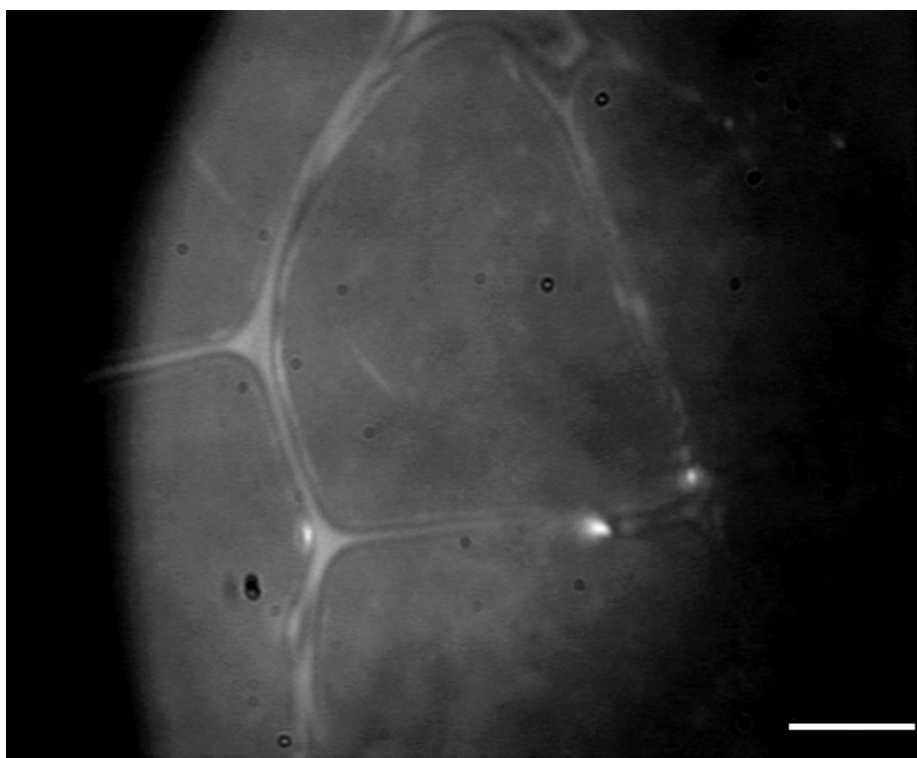
Figure 6.29: Optical microscope image showing surface domains of 10 nm polyester film, scale bar = 10 µm
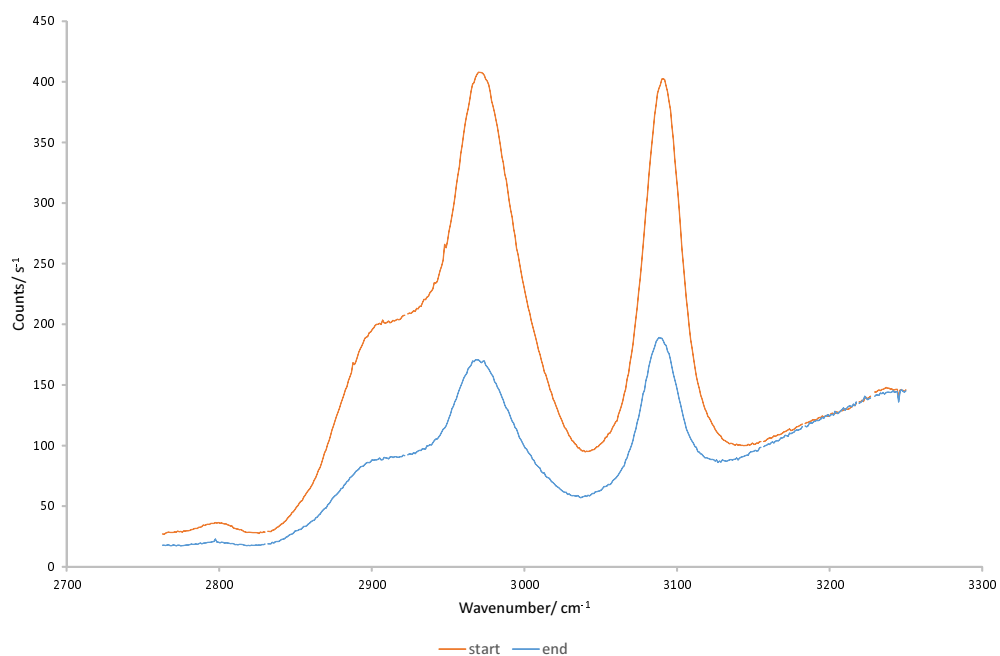
Figure 6.30: Spectra before (start) and after addition (end) of 10 mM C_{14}TAB to polyester layer, 5 s exposure, normalised to counts at $3200\,\mathrm{cm}^{-1}$, 532 nm

$C_{16}E_6$

We have limited data for $C_{16}E_6$ on polyester. While we were able to obtain fairly good separation using two component TFA, shown in figure 6.31, we were unable to obtain good, reproducible data for time or concentration. We observe some drift in the polyester peaks (shown by the additional peak in the surfactant component). As TFA was not successful, the start and end of one set of "in" data, is shown in figure 6.32. We did not see any surfactant desorption on the experimental time-scale. We can see partial loss of the polyester layer on adsorption and the surfactant peak is very strong equating to around 3.5 times a bilayer of $C_{16}TAB$, which is not very realistic, although our water signal will be lower due to the presence of the polyester layer which will result in an increase in the estimate for surfactant coverage. There is also a large loss of water during the experiment, which could be due to focal drift. We do not know the area of the substrate layer, or the roughness which could encourage to the formation of larger aggregates.

Analysis of a different set of data using three components: $C_{16}E_6$, polyester, and water (after excluding the shifting aromatic peak from the analysis), shown in figure 6.33, using the small in-line mixer and (2.060 ± 0.005) mM $C_{16}E_6$ produced the results shown in figure 6.34, with the data normalised to the water component weight in figure 6.35. The data is still poor, and there is a loss of water signal from ≈ 1100 s. We can see some adsorption of surfactant, well above the CMC $(0.0017$ mM$)$ and loss of polyester above around 1.5 mM. The surfactant spectrum looks very different to our previous data and shows a much less ordered surfactant layer, which could be an impurity. Our "out" experiments did not show any desorption and some even showed an increase in surfactant component, which could be deposition of the surfactant as a monolayer onto the hydrophobic surface, such as the way fabric conditioners adsorb to fabrics on rinsing.
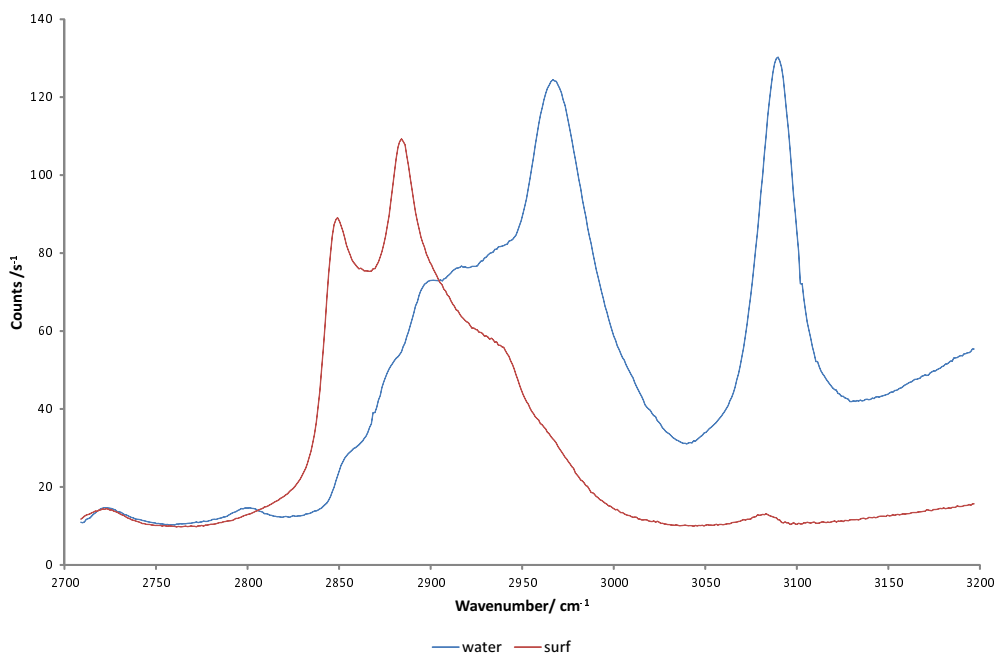
Figure 6.31: Refined spectra for $C_{16}E_6$ adsorption to a polyester layer, 532 nm, 700 mW
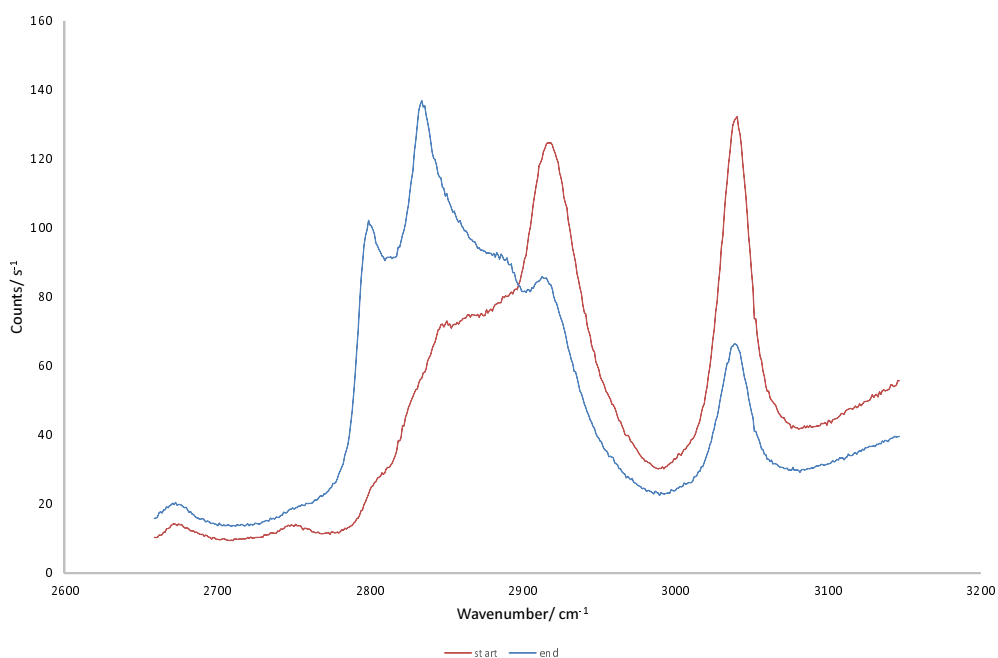
Figure 6.32: Start and end of $C_{16}E_6$ adsorption to a polyester layer using the small in-line mixer, (1.808 ± 0.005) mM. Average of 10 consecutive 5 s spectra, 532 nm, 700 mW

182
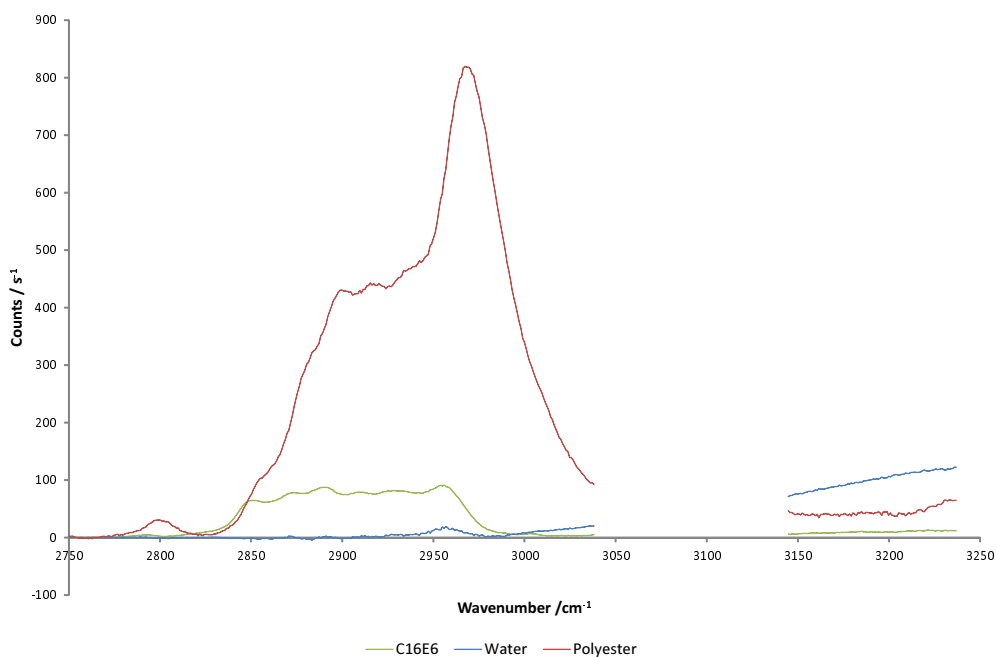
Figure 6.33: 3 components used for analysis of polyester and $C_{16}E_6$ isotherm, normalised to water, 700 mW, 5 s exposure, excluding aromatic peak, 532 nm
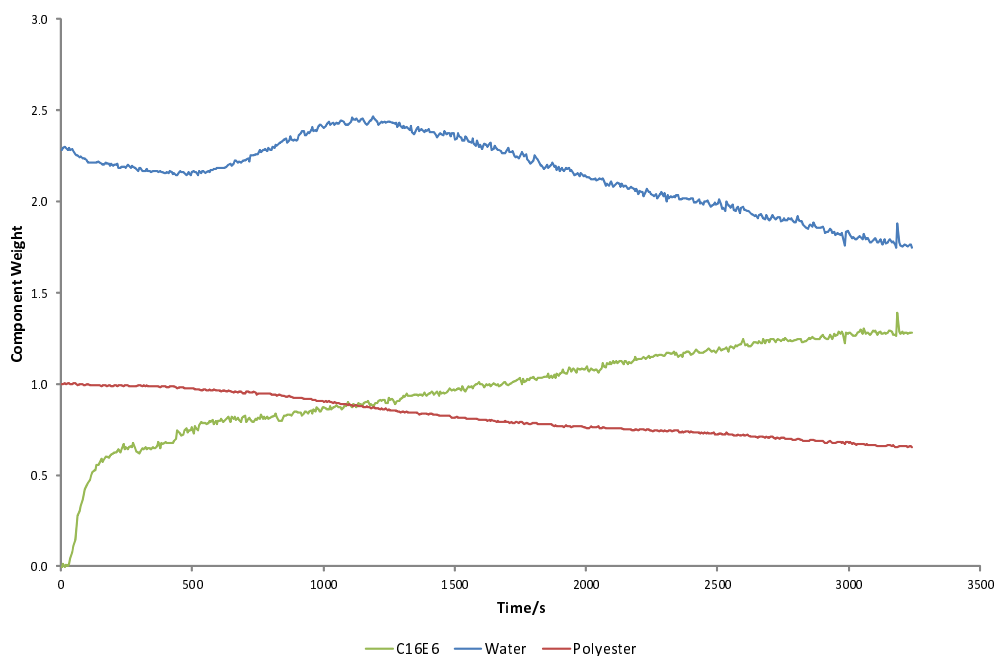
Figure 6.34: Component weight against time using 3 component analysis of $C_{16}E_6$ isotherm on polyester layer using the small in-line mixer, (8.40 ± 0.04) mM
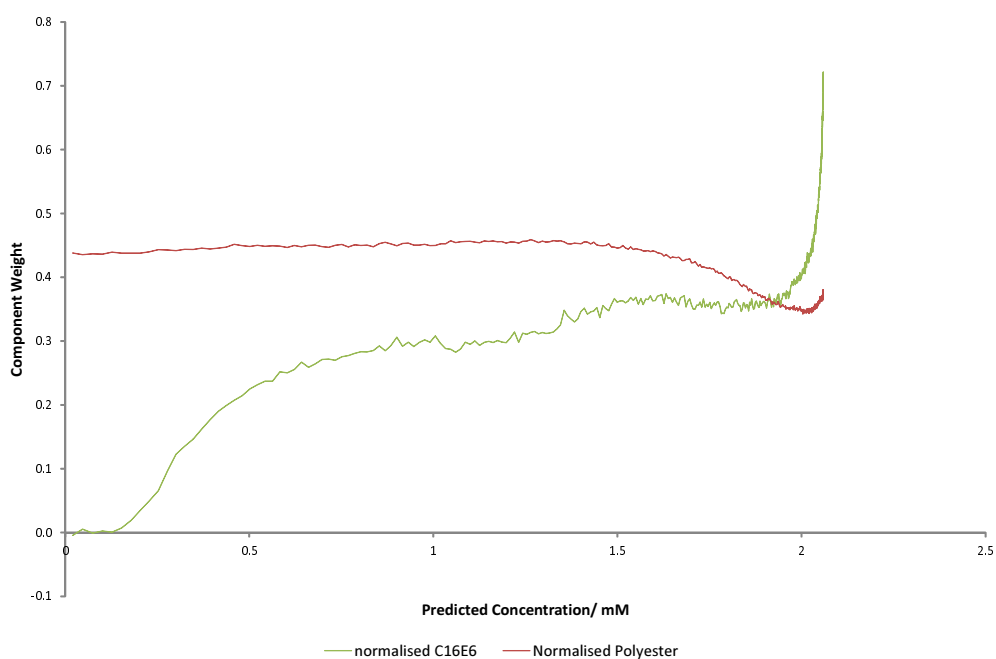
Figure 6.35: Components of $C_{16}E_6$ and polyester isotherm on polyester layer using the small in-line mixer against predicted concentration, (8.40 ± 0.04) mM, normalised to the water component

6.5.5 Discussion

Our initial experiments on polyester showed that we were able to measure a surfactant signal through a layer of polyester spin-coated on our hemisphere, but our surfactant data is limited as the layer was not reproducible and removed by surfactants. Further work, including finding a better method of attaching the polyester layer, is required to investigate this substrate further. Our analysis using three components for PCA demonstrates the use of this technique on more complicated systems.

While it is difficult to determine the amount of surfactant on the surface, we can see from the d^-/d^+ ratio that $C_{16}E_6$ on the surface forms an ordered structure on the surface, although this could be the same impurity that we observed on zeolite. It is difficult to comment on the structure of $C_{14}TAB$ as not much has adsorbed.

Future work could investigate silanizing the surface, to make the silica hydrophobic, before applying the layer of polyester. This pre-treatment may prevent domains from forming and prevent the removal of the layer. It may also be worth trying to grow the polymer on the surface, functionalising the polyester or coating the surface with a different polymer or other substrate first, to increase adhesion of the polyester. This would be similar to the method that Woods used to coat the surface with cellulose, by first applying trimethylsilyl cellulose to hydrophobised silica, although the primary purpose of this functionalisation of the cellulose was to allow dissolution in organic solvents to spread on a Langmuir trough.[1]

6.6 Haematite

6.6.1 Introduction

Haematite is of interest as it is a model soil for fabrics since it is often found in highly weathered soils. It is also of interest in ore refining, for example, the substrate has been studied previously using various "collectors" (flocculation agents (surfactants)) such as poly(ethylene glycol) monooleate (PEGMO) and commercial Atrac 1563.[206] Atrac 1563 is used to extract phosphorus impurities from iron ore by reverse flotation and is combined with another surfactant, methyl isobutyl carbinol (MIBC), to enhance foaming.[206]

6.6.2 Experimental

Coating of mineral surfaces was initially attempted using a method described by Potapova *et al.* in their work on ATR-FTIR spectroscopy studying the adsorption of nonionic and anionic surfactants to magnetite.[206] They synthesised haematite in a method described by Matijevic to produce particles of about 100 nm in size.[207] These particles were then suspended in acetic acid before dipping a test substrate (a glass slide) into the suspension using a Nima trough. We purchased similarly sized particles of haematite, however this process did not work, as the particles formed aggregates which were too large to remain in suspension, so sedimented quickly and we were unable to deposit a layer. Instead, we moved on to a different method; evaporating iron onto the substrate and then oxidising it in a furnace. This method, developed by Jubb and Allen for coating a substrate (KBr) with haematite, used physical vapour deposition (PVD).[147] They evaporated iron slugs

with an electron beam to form films 20 nm to 100 nm thick. They then annealed the iron films to form haematite in a furnace for 4 h in air at 575 °C.

Our haematite layer (figure 1.19) was prepared by evaporating 99.95 % pure iron pellets purchased from Kurt J. Lesker, UK in an Edwards Auto 306 evaporator (Edwards, UK). The iron film was then oxidised in air in an furnace (Carbolite, UK) for 4 h at 575 °C to form iron (III) oxide.

6.6.3   Surface Characterisation

As a trial, we deposited, via PVD, a 21.5 nm thick iron film (according to the quartz crystal modulator (QCM) thickness gauge) onto a glass slide and hemisphere simultaneously which, after oxidation in a furnace, yielded a haematite layer of thickness 39.1 nm (measured on the slide by Rutherford backscattering spectrometry (RBS)). The haematite layer was gold-coloured and of good uniformity. Figure 6.36 shows the slide coated with the above 39.1 nm layer of haematite.

The film adhered well and is not removable by adhesive tape. Figure 6.37 shows the Raman spectra of a coated glass slide. We can see that haematite is present on the surface, by comparing with data for magnetite (another iron oxide) and haematite from literature data.[208] We observe peaks at 411 cm^{-1}, 529 cm^{-1}, and 614 cm^{-1} which are consistent with literature results. The peak overlap means that it is hard to determine if any magnetite is present.

We have been unable to obtain any Raman signal of water or other adsorbed material though the haematite films. The haematite is visible but no water is visible through the layer (figure 6.38). Adding surfactant to improve wetting of the surface has no effect. There is minimal fluorescence and the background is lower than the expected water signal.

Sample damage by the laser (observed after irradiating the surface for ≈5 min) on ≈40 nm haematite films (on the hemisphere with the cell filled with water) is undetectable at ≈700 mW. Under TIR, the damage threshold will be lower due to higher electric field strength in the evanescent field. Thicker (≈53 nm) haematite films suffer permanent damage when exposed to powers around 100 mW where permanent holes appear in the layer. This damage could be due to the water normally providing a cooling effect and this is lost on creation of air bubbles.

We also observed a patch remaining visible after the laser has been switched off on a 9.5 nm layer of haematite. This dark patch appears to return to normal after
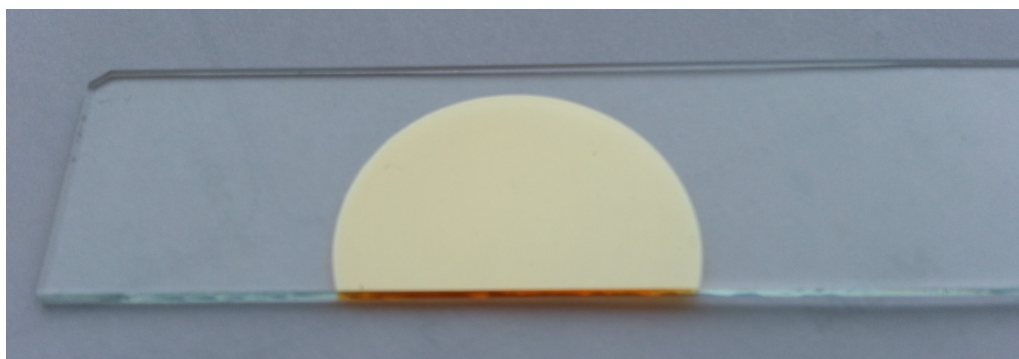
Figure 6.36: Photo of deposited, oxidised haematite layer on glass slide
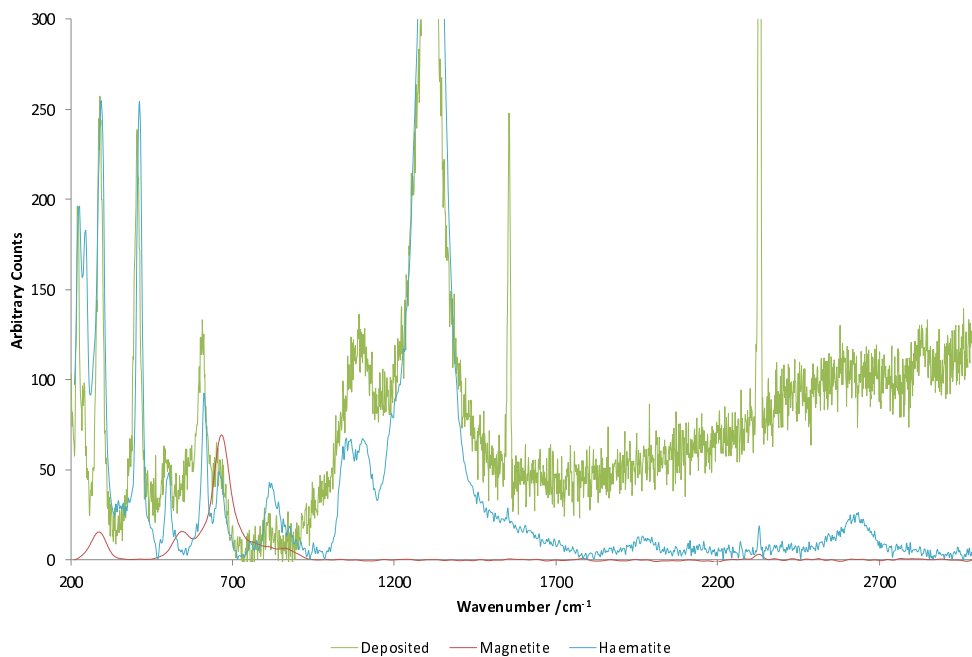
Figure 6.37: 20 nm Deposited haematite layer on glass slide 532 nm Raman spectrum after annealing (700 mW) compared with reference spectra of haematite and magnetite from the Romanian Database of Raman Spectroscopy, reference 208

approximately 60 s. The patch changing over time is visible in figure 6.39. The patch would appear to be the formation of an air bubble, since using degassed water stops this effect. The formation of Newton's rings indicates the presence of a ($\approx$1 µm) layer of something. The time scale would suggest that it is unlikely to be steam and the melting point of haematite is 1475 °C to 1565 °C.

The formation of a layer of air would be consistent with the lack of water signal in the Raman spectrum of the layer; however, this problem of no signal remains even after the water has been degassed. Therefore, further understanding of this problem is required. Even the 9.5 nm layer of haematite (formed from depositing $\approx$2 nm of iron) yielded no water signal. Surfactants did not improve the wettability of the layer, still no water was visible.

Addition of hydrochloric acid (HCl) to the cell removed the haematite layer, and the water signal returned to normal.

We did attempt to use our 660 nm laser to look at haematite to reduce florescence, but we saw no improvement.

We also decreased the angle of incidence to 45°, to below the critical angle. We were able to detect some water signal, but no surfactant (C_{14}TAB), which is expected as the bulk solution is now being probed, where there is a low surfactant concentration.

6.6.4 Discussion

We developed a good, reproducible method for coating the hemisphere with haematite, however, when the hemisphere was coated with haematite no water or surfactant signal was ever detected under TIR-Raman so these experiments were not continued. No explanation
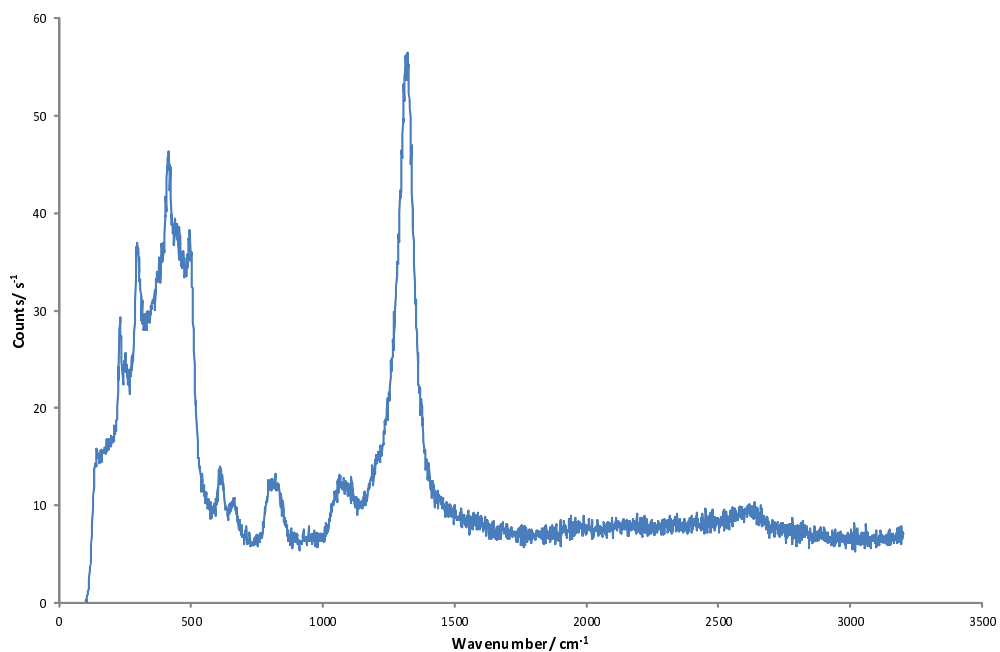
Figure 6.38: TIR-Raman spectra of haematite coated hemisphere, in water. 53.1 nm layer thickness, 20 mW, 10 s exposure. Renishaw spectrometer, 532 nm

could be provided as to why all water signal was blocked, other than suggesting that air bubbles were nucleated at the laser spot, even after degassing the water.
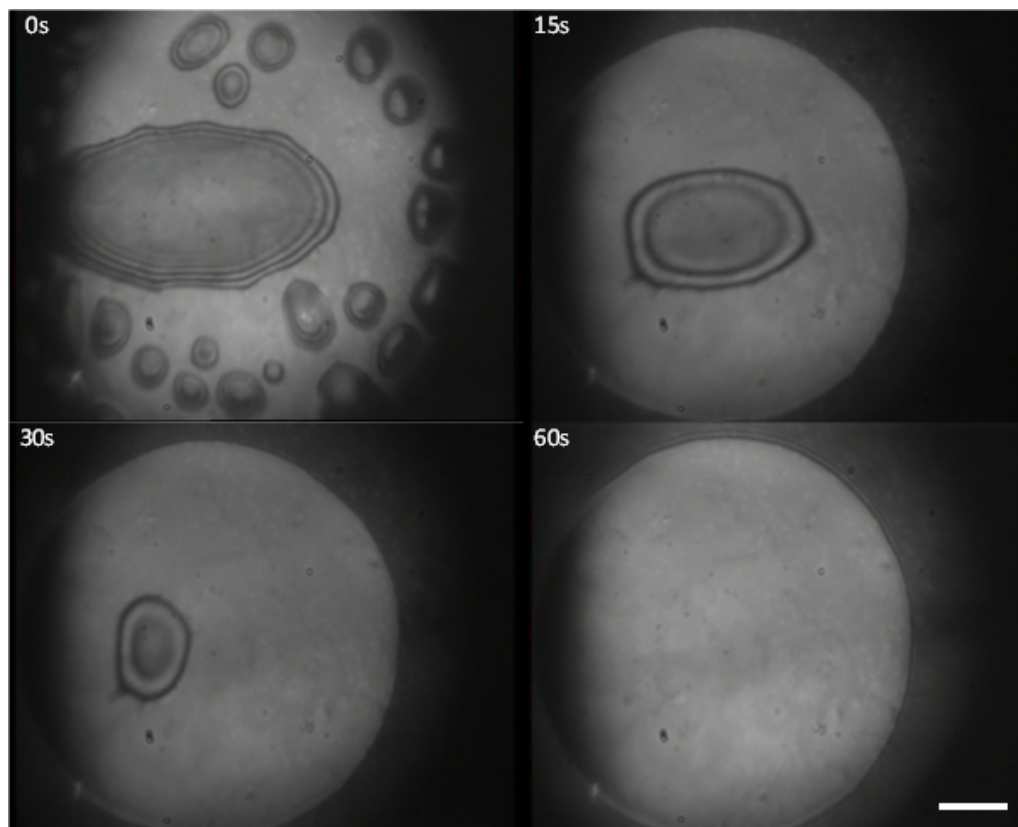
Figure 6.39: Optical micrograph of rings appearing on 9.5 nm haematite coated hemisphere after 200 mW laser exposure (2 s) in contact with water. Scale bar = 10 μm

6.7 Conclusions

We have managed to obtain insight into the kinetics of adsorption of nonionics onto zeolite and kaolinite, with our data matching expected trends in head- and tail-group size. Our isotherm data for $C_{14}TAB$ and $C_{16}TAB$ on zeolite did not compare well with literature, but we know that others have found surfactant adsorption to these substrates highly dependant on surface composition.

Overall, only zeolite and kaolinite were successful surfaces to study. Polyester, while initially looking promising, had reproducibility problems combined with removal of the coating by the surfactant, and our haematite surface yielded no workable results. Further investigation to characterise the thin films, including thickness measurements, is required to demonstrate that the silica does not influence the adsorption, however the results have demonstrated behaviours which differ to those on pure silica. XPS and x-ray diffraction studies of our adsorbed layers may reveal more information as to their structure.

Further work is also required to investigate a polyester layer, perhaps also incorporating different types of polyesters (different monomer constituents) in order to determine adsorption characteristics of surfactants to the surface.

In conclusion, TIR-Raman is a valid way to study silicate minerals, although variations in background do complicate analysis. Before additional study, we need to establish what scientific questions we want to investigate on our zeolite and haematite substrates.

Additional studies on mixed surfactant adsorption to silicate minerals and/or adsorption to them at varying pH could be a useful use of this technique.

Chapter 7

Conclusions

7.1 Spectrometer

The results obtained on the new system were more reliable and repeatable and the simple change in rotation the cell has virtually eliminated the problem of bubbles rising and sticking to the surface. The ability to electronically control and monitor all aspects of the spectrometer have greatly improved efficiency and simplicity of operation.

The greater flexibility of the new spectrometer has already been utilised for initial scoping measurements to monitor gasses adsorbing on catalytic surfaces by another research group. They have been able to monitor the adsorption and reactions of gasses (nitrogen, hydrogen, helium and ethylene) on a hemisphere coated with an undisclosed catalyst, in real time. Scoping measurements to follow the UV polymerisation of styrene were also performed on the system by another group member.

7.2 In-line Mixer

Our in-line mixer has allowed us to study, in greater concentration detail, the isotherms of some of these surfactants on our substrates in a time-efficient and effective way. Although, we did see some unexplained results when working with sucrose, and with surfactants at initial concentrations. In order to follow the increase in concentration and more accurately determine t_0 in our surfactant experiments, we could have used a small amount of acetonitrile in the surfactant solution as an internal standard for all measurements. The addition of a small quantity of acetonitrile should not affect the adsorption or diffusion of the surfactant and it should give a strong Raman signal, which we have shown to be proportional to concentration. Three component TFA analysis may be more difficult though, as it may be harder to separate this internal standard from surfactant component weight, *i.e.* we may end up with some acetonitrile in our surfactant component if the rate of surfactant adsorption is fast.

Overall the use of the mixer seems to produce good data provided we work at modest concentrations (<100 mM) and external factors to the technique, such as variable backgrounds and focus, do not prevent component separation. We have, in this thesis, demonstrated many successful experiments using this technique, but further work using

different non-adsorbing solutes to model surfactant diffusion is required in order to fully understand our results.

7.3 Surfactant Behaviour

When component separation and signal levels have been good, we have seen that we are able to obtain good isotherms, monitor phase transitions and are able to monitor ion interactions with DHDAB bilayers. Our results for the C_nTAB isotherms on silica match literature values for surface excess where available, and trends for the remaining series match trends observed by others.

On both silica and our other substrates, C_{16}TAB produced the most reproducible data, with the smallest overshoot at the CMC. Impurities in the samples of C_{12}TAB and C_{14}TAB remained an issue despite repeated recrystallisation steps. Additionally, the higher signal levels of C_{16}TAB from increased adsorption and the longer chain contributing more $C-H$ groups to the spectra helped improve data by increasing the signal to noise ratio.

Our collaborative studies on DHDAB using TIR-Raman have provided some useful insight into how bilayers of this surfactant behave at different temperatures. However, our original aim to study the Hofmeister series was unable to draw any firm conclusions.

Our study of mixed surfactant system of C_{12}LAS and $C_{12}E_6$ on hydrophobic silica was largely unsuccessful due to the inability to separate the two surfactants and problems encountered with using the Renishaw spectrometer system. A different combination of surfactants or the use of deuterated surfactants may allow for use of this TIR-Raman technique.

7.4 Study on Thin Films

We were able to form well-adhered layers of the silicates zeolite and kaolinite on silica and were able to study surfactant adsorption to these substrates using TIR-Raman. However, the variation in background limits the use of this technique for accurate determination of adsorbed amounts. In the literature there is also variation due the known heterogeneous surface charge (due to the isomorphous substitution of Si^{4+} by Al^{3+}) and variation between the different structure types of zeolite.

We have studied the adsorption of surfactants to a range of surfaces. Haematite was unsuccessful, but zeolite, kaolinite and polyester did show some promising results. Studying the two silicates at varying pH may be one area which could be investigated further (haematite is removed at low pH).

We have been able to follow the kinetics, and monitor isotherms for a wide range of surfactants on these substrates and determine approximate adsorbed amounts. The new spectrometer's increased time resolution has provided more data for kinetic studies of nonionics on mineral surfaces, when compared to the Renishaw spectrometer. Adsorbed amounts of nonionics match known trends in head- and tail-group size. We have estimated nonionic adsorption to kaolinite to be higher and proposed that this difference is due to the increase in number of cations on zeolite repelling the slightly positive nonionic

surfactant EO groups. The reduction in cationic surfactant adsorption compared to silica was explained by the reduction in ζ potential.

Our polyester layer was removed by surfactants and we were unable to draw any conclusions from this study.

We are still puzzled as to why haematite was not transparent to the evanescent wave, the possibility of studying surfactant adsorption to this model soil would have been a novel use of this TIR-Raman technique. Further work on other metal oxide mineral soils could help develop better detergents and/or ore flotation surfactants.

7.5 Further Work

If I had had more time on the project, there are a number of areas I would like to investigate further. Continuing the study on bilayers by undertaking further study in the Hofmeister Effect of ions in bilayers, including using additional Raman active ions may be of interest. Investigations using an anionic surfactant and a cationic counterion may show if the Hofmeister Effect is observable in the cation series. If possible, the use of deuterated dichain surfactants would reduce variance due to the water background, although at substantial cost. One could also try using D_2O as the solvent to reduce background variance with the standard surfactant, but again this would increase costs.

The use of our new spectrometer (due to the 90° cell rotation) to study these bilayer systems would also aid study, as bubbles were a cause of many experimental failure as they destroyed the bilayer. We could also use the new spectrometer on our hydrophobic surface as this system was also plagued by bubbles.

I would also like to investigate diffusion with the mixer in more detail, using sucrose of higher purity or a long-chained alcohol to match the diffusion coefficient of surfactant molecules more closely. This may allow for a better understanding of how the surfactant molecules are behaving. We could also investigate further the oscillations occasionally observed when using high concentrations of solute with the in-line mixer. Overall the behaviour of the in-line mixer is still not fully understood, but it can produce good results, for example when used with deuterated methanol.

The use of silica coated calcium fluoride (CaF_2) hemispheres to sharpen peaks in the background produced by the substrate would allow for clearer observation of the peaks of any adsorbed species. I also looked at making some silica coated CaF_2 hemispheres, using chemical vapour deposition (CVD) in the thermal evaporator to evaporate silica monoxide in an atmosphere of oxygen. The process was shown to work on a BK7 glass hemisphere, but resulted in some fluorescence.

Adapting the spectrometer system for Raman imaging of the interface would provide greater information on the formation and structure of the monolayer or bilayer formed. However, Raman imaging is typically slow and would therefore most probably be restricted to interfaces at equilibrium. Using Raman imaging it may be possible to establish if the layers formed were uniform and discover if the removed (rinsed) surfactant layers are fully detached from the surface. Later work in our group simplified the acquisition of images by utilising bandpass filters to target selected wavenumber bands.

The study of mixed surfactant adsorption to zeolites may be of interest as they are commonly used for wastewater treatment.

I would have liked to have looked more at developing a reproducible polyester layer and investigated the kinetics of adsorption of different surfactants. This is because of the numerous real-world applications of providing a suitable model layer, and method, to study surfactant adsorption to polyester for the detergent and fabric industry to investigate cleaning and dying processes. As we have discussed, finding a way of functionalising the substrate and/or polyester may increase the adhesion to the surface. Alternatively, placing a thin polyester film on the hemisphere, with a thin layer of index matching fluid to minimise unwanted reflections or refraction between the interfaces may allow this substrate to be studied by TIR-Raman. Although, Woods was unsuccessful with this method when looking at mica.

Bibliography

[1] D. A. Woods, *PhD Thesis*, University of Durham, 2011.

[2] U. The NIST Reference on Constants and Uncertanty, *CODATA Values*, Online, 2015, `http://physics.nist.gov/cuu/Constants/`.

[3] *Surfactants*, ed. T. Tadros, Academic Press Inc., London, 1984.

[4] C. Tanford, *The hydrophobic effect: formation of micelles and biological membranes*, Wiley, 1980.

[5] M. Miwa, A. Nakajima, A. Fujishima, K. Hashimoto and T. Watanabe, Effects of the Surface Roughness on Sliding Angles of Water Droplets on Superhydrophobic Surfaces, *Langmuir*, 2000, **16**, 5754–5760, DOI: 10.1021/la991660o.

[6] L. Feng, S. Li, Y. Li, H. Li, L. Zhang, J. Zhai, Y. Song, B. Liu, L. Jiang and D. Zhu, Super-Hydrophobic Surfaces: From Natural to Artificial, *Advanced Materials*, 2002, **14**, 1857–1860, DOI: 10.1002/adma.200290020.

[7] D. J. Shaw, *Introduction to Colloid and Surface Chemistry*, Butterworths, 3rd edn., 1980.

[8] J. N. Phillips, The energetics of micelle formation, *Trans. Faraday Soc.*, 1955, **51**, 561–569, DOI: 10.1039/TF9555100561.

[9] E. Tyrode, M. W. Rutland and C. D. Bain, Adsorption of CTAB on Hydrophilic Silica Studied by Linear and Nonlinear Optical Spectroscopy, *Journal of the American Chemical Society*, 2008, **130**, 17434–17445, DOI: 10.1021/ja805169z.

[10] C. D. Bain, P. B. Davies and R. N. Ward, In-Situ Sum-Frequency Spectroscopy of Sodium Dodecyl Sulfate and Dodecanol Coadsorbed at a Hydrophobic Surface, *Langmuir*, 1994, **10**, 2060–2063, DOI: 10.1021/la00019a006.

[11] P. Somasundaran and D. W. Fuerstenau, Mechanisms of Alkyl Sulfonate Adsorption at the Alumina-Water Interface1, *The Journal of Physical Chemistry*, 1966, **70**, 90–96, DOI: 10.1021/j100873a014.

[12] Y. Gao, J. Du and T. Gu, Hemimicelle formation of cationic surfactants at the silica gel-water interface, *J. Chem. Soc., Faraday Trans. 1*, 1987, **83**, 2671–2679, DOI: 10.1039/F19878302671.

[13] A. W. Adamson, *Physical Chemistry of Surfaces*, Wiley-Interscience, 3rd edn., 1976.

[14] M. J. Rosen, *Surfactants and Interfacial Phenomena*, Wiley-Interscience, 2nd edn., 1989.

[15] *Adsorption from Solution at the Solid/Liquid Interface*, ed. G. D. Parfitt and C. H. Rochester, Academic Press Inc., London, 1983.

[16] C. H. Giles, T. H. MacEwan, S. N. Nakhwa and D. Smith, Studies in adsorption. Part XI. A system of classification of solution adsorption isotherms, and its use in diagnosis of adsorption mechanisms and in measurement of specific surface areas of solids, *J. Chem. Soc.*, 1960, 3973–3993, DOI: 10.1039/JR9600003973.

[17] C. H. Giles, D. Smith and A. Huitson, A general treatment and classification of the solute adsorption isotherm. I. Theoretical, *Journal of Colloid and Interface Science*, 1974, **47**, 755–765, DOI: 10.1016/0021-9797(74)90252-5.

[18] W. A. Ducker and E. J. Wanless, Adsorption of Hexadecyltrimethylammonium Bromide to Mica: Nanometer-Scale Study of Binding-Site Competition Effects, *Langmuir*, 1999, **15**, 160–168, DOI: 10.1021/la9710942.

[19] S. C. Howard and V. S. J. Craig, Adsorption of the Cationic Surfactant Cetyltrimethylammonium Bromide to Silica in the Presence of Sodium Salicylate: Surface Excess and Kinetics, *Langmuir*, 2009, **25**, 13015–13024, DOI: 10.1021/la901889m.

[20] H. Hanna and P. Somasundaran, Equilibration of kaolinite in aqueous inorganic and surfactant solutions, *Journal of Colloid and Interface Science*, 1979, **70**, 181–191, DOI: 10.1016/0021-9797(79)90022-5.

[21] R. Atkin, V. Craig, E. Wanless and S. Biggs, Mechanism of cationic surfactant adsorption at the solid-aqueous interface, *Advances in Colloid and Interface Science*, 2003, **103**, 219–304, DOI: 10.1016/S0001-8686(03)00002-2.

[22] S. Paria, C. Manohar and K. C. Khilar, Adsorption of anionic and non-ionic surfactants on a cellulosic surface, *Colloids and Surfaces A: Physicochemical and Engineering Aspects*, 2005, **252**, 221–229, DOI: 10.1016/j.colsurfa.2004.09.022.

[23] M. Jaycock and R. Ottewill, in *Proc. 4th Intern. Congr. Surface Active Substances, Brussels, 7–12 September, 1964*, Gordon and Breach Science Publishers New York, 1967, vol. 2, pp. 545–553.

[24] T. Okubo, H. Kitano, T. Ishiwatari and N. Ise, Conductance Stopped-Flow Study on the Micellar Equilibria of Ionic Surfactants, *Proceedings of the Royal Society of London A: Mathematical, Physical and Engineering Sciences*, 1979, **366**, 81–90, DOI: 10.1098/rspa.1979.0040.

[25] J. Rassing, P. J. Sams and E. Wyn-Jones, Kinetics of micellization from ultrasonic relaxation studies, *J. Chem. Soc., Faraday Trans. 2*, 1974, **70**, 1247–1258, DOI: 10.1039/F29747001247.

[26] E. A. G. Aniansson and S. N. Wall, Kinetics of step-wise micelle association, *The Journal of Physical Chemistry*, 1974, **78**, 1024–1030, DOI: 10.1021/j100603a016.

[27] E. A. G. Aniansson and S. N. Wall, Kinetics of step-wise micelle association. Correction and improvement, *The Journal of Physical Chemistry*, 1975, **79**, 857–858, DOI: 10.1021/j100575a019.

[28] E. A. G. Aniansson, S. N. Wall, M. Almgren, H. Hoffmann, I. Kielmann, W. Ulbricht, R. Zana, J. Lang and C. Tondre, Theory of the kinetics of micellar equilibria and quantitative interpretation of chemical relaxation studies of micellar solutions of ionic surfactants, *The Journal of Physical Chemistry*, 1976, **80**, 905–922, DOI: 10.1021/j100550a001.

[29] J. F. Scamehorn, in *Phenomena in Mixed Surfactant Systems*, ed. J. F. Scamehorn, American Chemical Society, 1986, ch. 1, pp. 1–27, DOI: 10.1021/bk-1986-0311.ch001.

[30] D. M. Colegate and C. D. Bain, Adsorption Kinetics in Micellar Solutions of Nonionic Surfactants, *Phys. Rev. Lett.*, 2005, **95**, 198302, DOI: 10.1103/PhysRevLett.95.198302.

[31] S. Paria and K. C. Khilar, A review on experimental studies of surfactant adsorption at the hydrophilic solid-water interface, *Advances in Colloid and Interface Science*, 2004, **110**, 75–95, DOI: 10.1016/j.cis.2004.03.001.

[32] P. C. Pavan, E. L. Crepaldi, G. de A. Gomes and J. ao B Valim, Adsorption of sodium dodecylsulfate on a hydrotalcite-like compound. Effect of temperature, pH and ionic strength, *Colloids and Surfaces A: Physicochemical and Engineering Aspects*, 1999, **154**, 399–410, DOI: 10.1016/S0927-7757(98)00847-4.

[33] J. Penfold, E. Staples, L. Thompson, I. Tucker, R. K. Thomas and J. R. Lu, The Effect of Temperature on the Adsorption of Non-Ionic Surfactants and Non-Ionic Surfactant Mixtures at the Air-Water Interface, *Berichte der Bunsengesellschaft fr physikalische Chemie*, 1996, **100**, 218–223, DOI: 10.1002/bbpc.19961000306.

[34] G. Quincke, Ueber eine neue Art elektrischer Ströme, *Annalen der Physik*, 1859, **183**, 1–47, DOI: 10.1002/andp.18591830502.

[35] M. U. Ahmad, A laboratory study of streaming potentials, *Geophysical Prospecting*, 1964, **12**, 49–64, DOI: 10.1111/j.1365-2478.1964.tb01889.x.

[36] A. W. Adamson and A. P. Gast, *Physical Chemistry of Surfaces*, Wiley-Interscience, New York, 6th edn., 1997.

[37] E. Marques, O. Regev, A. Khan and B. Lindman, Self-organization of double-chained and pseudodouble-chained surfactants: counterion and geometry effects, *Advances in Colloid and Interface Science*, 2003, **100–102**, 83–104, DOI: 10.1016/S0001-8686(02)00068-4.

[38] J. Harris, *MChem project*, University of Durham, 2012.

[39] I. Tucker, J. Penfold, R. K. Thomas, I. Grillo, J. G. Barker and D. F. R. Mildner, The Surface and Solution Properties of Dihexadecyl Dimethylammonium Bromide, *Langmuir*, 2008, **24**, 6509–6520, DOI: 10.1021/la703415m.

[40] L. Lunar, S. Rubio and D. Perez-Bendito, Analysis of linear alkylbenzene sulfonate homologues in environmental water samples by mixed admicelle-based extraction and liquid chromatography/mass spectrometry, *Analyst*, 2006, **131**, 835–841, DOI: 10.1039/B604298H.

[41] P. M. Holland and D. N. Rubingh, in *Mixed Surfactant Systems*, ed. P. M. Holland and D. N. Rubingh, American Chemical Society, 1992, vol. 501, ch. 1: An Overview, pp. 2–30.

[42] S. Yokoyama, in *Mixed surfactant systems*, ed. M. Abe and J. F. Scamehorn, Marcel Dekker, 2nd edn., 2005, vol. 124, ch. Delayed Degradation of Drugs by Mixed Micellization with Biosurfactants, p. 831.

[43] F. Portet-Koltalo, P. L. Desbne and C. Treiner, Self-Desorption of Mixtures of Anionic and Nonionic Surfactants from a Silica/Water Interface, *Langmuir*, 2001, **17**, 3858–3862, DOI: 10.1021/la001785p.

[44] L. Huang, C. Maltesh and P. Somasundaran, Adsorption Behavior of Cationic and Nonionic Surfactant Mixtures at the Alumina–Water Interface, *Journal of Colloid and Interface Science*, 1995, **117**, 222–228, DOI: 10.1006/jcis.1996.0024.

[45] R. Zhang, C. Liu and P. Somasundaran, A model for the cooperative adsorption of surfactant mixtures on solid surfaces, *Journal of Colloid and Interface Science*, 2007, **310**, 377–384, DOI: 10.1016/j.jcis.2007.01.099.

[46] D. A. Woods, J. Petkov and C. D. Bain, Surfactant Adsorption Kinetics by Total Internal Reflection Raman Spectroscopy. 2. CTAB and Triton X-100 Mixtures on Silica, *The Journal of Physical Chemistry B*, 2011, **115**, 7353–7363, DOI: 10.1021/jp201340j.

[47] P. Kurzendörfer, in *Physical Chemistry. A Series of Monographs*, ed. H. v. E. Hutchinson and P. van Rysselberghe, WILEY-VCH Verlag GmbH, 1965, vol. 77, ch. Colloidal Surfactants. Some Physicochemical Properties, pp. 599–599, DOI: 10.1002/ange.19650771324.

[48] N. Funasaki and S. Hada, Surface tension of aqueous solutions of surfactant mixtures. The composition of mixed micelles, *The Journal of Physical Chemistry*, 1979, **83**, 2471–2475, DOI: 10.1021/j100482a010.

[49] S. Patil, T. Mukaiyama and A. Rakshit, α-Sulfonato palmitic acid methyl ester-hexaoxyethylene monododecyl ether mixed surfactant system: Interfacial, thermodynamic, and performance property study, *Journal of Surfactants and Detergents*, 2004, **7**, 87–96, DOI: 10.1007/s11743-004-0293-y.

[50] C. M. Nguyen, J. F. Rathman and J. F. Scamehorn, Thermodynamics of mixed micelle formation, *Journal of Colloid and Interface Science*, 1986, **112**, 438–446, DOI: 10.1016/0021-9797(86)90112-8.

[51] P. A. Rock, *Chemical Thermodynamics*, University Science Books, 1983.

[52] J. F. Scamehorn, R. S. Schechter and W. H. Wade, Adsorption of surfactants on mineral oxide surfaces from aqueous solutions : II: Binary mixtures of anionic surfactants, *Journal of Colloid and Interface Science*, 1982, **85**, 479–493, DOI: 10.1016/0021-9797(82)90014-5.

[53] J. F. Scamehorn, R. S. Schechter and W. H. Wade, Adsorption of surfactants on mineral oxide surfaces from aqueous solutions : III. Binary mixtures of anionic and nonionic surfactants, *Journal of Colloid and Interface Science*, 1982, **85**, 494–501, DOI: 10.1016/0021-9797(82)90015-7.

[54] P. Stepnowski, W. Mrozik and J. Nichthauser, Adsorption of Alkylimidazolium and Alkylpyridinium Ionic Liquids onto Natural Soils, *Environmental Science & Technology*, 2007, **41**, 511–516, DOI: 10.1021/es062014w.

[55] F. Hofmeister, Zur Lehre von der Wirkung der Salze, *Archive experimentelle Pathologie und Pharmakologie*, 1888, **24**, 247–260, DOI: 10.1007/BF01918191.

[56] W. Kunz, J. Henle and B. Ninham, 'Zur Lehre von der Wirkung der Salze' (about the science of the effect of salts): Franz Hofmeister's historical papers, *Current Opinion in Colloid & Interface Science*, 2004, **9**, 19–37, DOI: 10.1016/j.cocis.2004.05.005.

[57] E. Brame and J. Graselli, *Infrared and Raman Spectroscopy (Practical Spectroscopy series)*, Marcel Dekker, 1976.

[58] P. R. Greene and C. D. Bain, Total Internal Reflection Raman Spectroscopy, *Spectroscopy Europe*, 2004, **16**, 8–15.

[59] LCT for the European data relay system: in orbit commissioning of the Alphasat and Sentinel 1A LCTs, San Francisco, California, USA, 2015, DOI: 10.1117/12.2083117.

[60] P. Atkins and J. de Paula, *Physical Chemistry*, Oxford University Press, 7th edn., 2002.

[61] C. Palmer, *Diffraction Grating Handbook*, Newport Corporation, 6th edn., 2005.

[62] Richardson Gratings, *Diffraction Grating Specification*, 2015, `http://www.gratinglab.com/Products/Product_Tables/Efficiency/Efficiency.aspx?efficiency=813`.

[63] D. A. Woods and C. D. Bain, Total internal reflection spectroscopy for studying soft matter, *Soft Matter*, 2014, **10**, 1071–1096, DOI: 10.1039/C3SM52817K.

[64] A. G. Tweet, G. L. Gaines and W. D. Bellamy, Fluorescence of Chlorophyll a in Monolayers, *The Journal of Chemical Physics*, 1964, **40**, 2596–2600, DOI: 10.1063/1.1725569.

[65] T. Ikeshoji, Y. Ono and T. Mizuno, Total Reflection Raman Spectra; Raman Scattering due to the Evanescent Wave in Total Reflection, *Appl. Opt.*, 1973, **12**, 2236–2237, DOI: 10.1364/AO.12.002236.

[66] M. Fujihira and T. Osa, Internal reflection resonance Raman spectroscopy for studies of adsorbed dye layers at electrode-solution interface, *Journal of the American Chemical Society*, 1976, **98**, 7850–7851, DOI: 10.1021/ja00440a079.

[67] T. Takenaka and H. Fukuzaki, Resonance Raman spectra of insoluble monolayers spread on a water surface, *Journal of Raman Spectroscopy*, 1979, **8**, 151–154, DOI: 10.1002/jrs.1250080307.

[68] R. Iwamoto, M. Miya, K. Ohta and S. Mima, Total internal reflection Raman spectroscopy as a new tool for surface analysis, *Journal of the American Chemical Society*, 1980, **102**, 1212–1213, DOI: 10.1021/ja00523a074.

[69] R. Iwamoto, K. Ohta, M. Miya and S. Mima, Total Internal Reflection Raman Spectroscopy at the Critical Angle for Raman Measurements of Thin Films, *Applied Spectroscopy*, 1981, **35**, 584–587, DOI: 10.1366/0003702814732102.

[70] R. Iwamoto, M. Miya, K. Ohta and S. Mima, Total internal reflection Raman spectroscopy, *The Journal of Chemical Physics*, 1981, **74**, 4780–4790, DOI: 10.1063/1.441757.

[71] A. Richter, W. Carius, W. Hölzer, O. Schröter, H. Brandt and K. Hemmelmann, Ramanspektroskopische Charakterisierung der üermolekularen Struktur von Polyethylenen, *Acta Polymerica*, 1987, **38**, 220–223, DOI: 10.1002/actp.1987.010380403.

[72] W. Hözer, O. Schröter and A. Richter, Raman study on surface layers and thin films by using total reflection experiments, *Journal of Molecular Structure*, 1990, **217**, 253–264, DOI: 10.1016/0022-2860(90)80366-R.

[73] Z. S. Nickolov, J. C. Earnshaw and J. J. McGarvey, Total internal reflection Raman spectroscopy as a method to study water structure near Langmuir-Blodgett films, *Journal of Raman Spectroscopy*, 1993, **24**, 411–416, DOI: 10.1002/jrs.1250240705.

[74] Z. S. Nickolov, J. C. Earnshaw and J. J. McGarvey, Water structure at interfaces studied by total internal reflection Raman spectroscopy, *Colloids and Surfaces A: Physicochemical and Engineering Aspects*, 1993, **76**, 41–49, DOI: 10.1016/0927-7757(93)80059-N.

[75] T. Morikawa, E. Shirai, J. Tanno, H. Takanashi, A. Yasuda and K. Itoh, Time-resolved Total Internal Reflection Raman Scattering Study on Electric-Field-Induced Reorientation Dynamics of Nematic Liquid Crystal of 4-Hexyl-4′-Cyanobiphenyl, *Molecular Crystals and Liquid Crystals Science and Technology. Section A. Molecular Crystals and Liquid Crystals*, 1998, **312**, 69–94, DOI: 10.1080/10587259808042432.

[76] H. Yui, H. Fujiwara and T. Sawada, Spectroscopic analysis of total-internal-reflection stimulated Raman scattering from the air/water interface under the strong focusing condition, *Chemical Physics Letters*, 2002, **360**, 53–58, DOI: 10.1016/S0009-2614(02)00803-5.

[77] H. Watarai and F. Funaki, Total Internal Reflection Fluorescence Measurements of Protonation Equilibria of Rhodamine B and Octadecylrhodamine B at a Toluene/Water Interface, *Langmuir*, 1996, **12**, 6717–6720, DOI: 10.1021/la960654e.

[78] N. Fujiwara, S. Tsukahara and H. Watarai, In Situ Fluorescence Imaging and Time-Resolved Total Internal Reflection Fluorometry of Palladium(II)-Tetrapyridylporphine Complex Assembled at the Toluene-Water Interface, *Langmuir*, 2001, **17**, 5337–5342, DOI: 10.1021/la010259a.

[79] K. Fujiwara and H. Watarai, Total Internal Reflection Resonance Raman Microspectroscopy for the Liquid/Liquid Interface. Ion-Association Adsorption of Cationic Mn(III) Porphine, *Langmuir*, 2003, **19**, 2658–2664, DOI: 10.1021/la026119y.

[80] S. Yamamoto and H. Watarai, Counterion-Dependent Morphology of Porphyrin Aggregates Formed at the Liquid/Liquid Interface Studied by Total Internal Reflection Resonant Rayleigh and Raman Scattering Microscopy, *The Journal of Physical Chemistry C*, 2008, **112**, 12417–12424, DOI: 10.1021/jp803328f.

[81] C. Bousquet, M. Masson and M. Harrand, Analysis of polarized Raman spectra of liquids at liquid-solid interfaces, *Journal of Raman Spectroscopy*, 1995, **26**, 273–282, DOI: 10.1002/jrs.1250260404.

[82] D. Beattie, M. L. Larsson and A. R. Holmgren, In situ total internal reflection Raman spectroscopy of surfactant adsorption at a mineral surface, *Vibrational Spectroscopy*, 2006, **41**, 198–204, DOI: 10.1016/j.vibspec.2006.02.003.

[83] C. A. Michaels, Surface-sensitive Raman microscopy with total internal reflection illumination, *Journal of Raman Spectroscopy*, 2010, **41**, 1670–1677, DOI: 10.1002/jrs.2610.

[84] C. A. Michaels, Surface Selective Raman Microscopy With Total Internal Reflection Illumination, *AIP Conference Proceedings*, 2010, **1267**, 762–763, DOI: 10.1063/1.3482796.

[85] W. Tran, L. G. Tisinger, L. E. Lavalle and A. J. Sommer, Analysis of Thin-Film Polymers Using Attenuated Total Internal Reflection-Raman Microspectroscopy, *Applied Spectroscopy*, 2015, **69**, 230–238, DOI: 10.1366/13-07024.

[86] K. J. McKee and E. A. Smith, Development of a scanning angle total internal reflection Raman spectrometer, *Review of Scientific Instruments*, 2010, **81**, 043106, DOI: 10.1063/1.3378682.

[87] K. J. McKee, M. W. Meyer and E. A. Smith, Plasmon Waveguide Resonance Raman Spectroscopy, *Analytical Chemistry*, 2012, **84**, 9049–9055, DOI: 10.1021/ac3013972.

[88] M. D. Lesoine, J. M. Bobbitt, S. Zhu, N. Fang and E. A. Smith, High angular-resolution automated visible-wavelength scanning angle Raman microscopy, *Analytica Chimica Acta*, 2014, **848**, 61–66, DOI: 10.1016/j.aca.2014.07.040.

[89] C. A. Damin, V. H. T. Nguyen, A. S. Niyibizi and E. A. Smith, Application of scanning angle Raman spectroscopy for determining the location of buried polymer interfaces with tens of nanometer precision, *Analyst*, 2015, **140**, 1955–1964, DOI: 10.1039/C4AN02240H.

[90] A. O. Kivioja, A.-S. Jääskeläinen, V. Ahtee and T. Vuorinen, Thickness measurement of thin polymer films by total internal reflection Raman and attenuated total reflection infrared spectroscopy, *Vibrational Spectroscopy*, 2012, **61**, 1–9, DOI: 10.1016/j.vibspec.2012.02.014.

[91] A. Kivioja, T. Hartus, T. Vuorinen, P. Gane and A.-S. Jääskeläinen, Use of Total Internal Reflection Raman (TIR) and Attenuated Total Reflection Infrared (ATR-IR) Spectroscopy to Analyze Component Separation in Thin Offset Ink Films After Setting on Coated Paper Surfaces, *Applied Spectroscopy*, 2013, **67**, 661–671, DOI: 10.1366/12-06961.

[92] Z. Grenoble and S. Baldelli, Adsorption of Benzyldimethylhexadecylammonium Chloride at the Hydrophobic Silica-Water Interface Studied by Total Internal Reflection Raman Spectroscopy: Effects of Silica Surface Properties and Metal Salt Addition, *The Journal of Physical Chemistry B*, 2013, **117**, 9882–9894, DOI: 10.1021/jp4015096.

[93] A. M. Jubb, D. Verreault, R. Posner, L. J. Criscenti, L. E. Katz and H. C. Allen, Sulfate adsorption at the buried hematite/solution interface investigated using total internal reflection (TIR)-Raman spectroscopy, *Journal of Colloid and Interface Science*, 2013, **400**, 140–146, DOI: 10.1016/j.jcis.2013.02.031.

[94] D. A. Woods, J. Petkov and C. D. Bain, Surfactant Adsorption Kinetics by Total Internal Reflection Raman Spectroscopy. 1. Pure Surfactants on Silica, *The Journal of Physical Chemistry B*, 2011, **115**, 7341–7352, DOI: 10.1021/jp201338s.

[95] C. Lee and C. D. Bain, Raman spectra of planar supported lipid bilayers, *Biochimica et Biophysica Acta (BBA) - Biomembranes*, 2005, **1711**, 59–71, DOI: 10.1016/j.bbamem.2005.02.006.

[96] J. Churchwell and C. Bain, 245th National Spring Meeting of the American-Chemical-Society, 2013.

[97] D. A. Beattie, S. A. Winget and C. D. Bain, Raman Scattering from Confined Liquid Films in the Sub-Nanometre Regime, *Tribology Letters*, 2007, **27**, 159–167, DOI: 10.1007/s11249-007-9214-0.

[98] M. Praveena, C. D. Bain, V. Jayaram and S. K. Biswas, Total internal reflection (TIR) Raman tribometer: a new tool for in situ study of friction-induced material transfer, *RSC Adv.*, 2013, **3**, 5401–5411, DOI: 10.1039/C3RA00131H.

[99] M. Praveena, K. Guha, A. Ravishankar, S. K. Biswas, C. D. Bain and V. Jayaram, Total internal reflection Raman spectroscopy of poly(alpha-olefin) oils in a lubricated contact, *RSC Adv.*, 2014, **4**, 22205–22213, DOI: 10.1039/C4RA02261K.

[100] D. A. Woods, J. Petkov and C. D. Bain, Surfactant adsorption by total internal reflection Raman spectroscopy. Part III: Adsorption onto cellulose, *Colloids and Surfaces A: Physicochemical and Engineering Aspects*, 2011, **391**, 10–18, DOI: 10.1016/j.colsurfa.2011.07.027.

[101] P. R. Greene and C. D. Bain, Total internal reflection Raman spectroscopy of barley leaf epicuticular waxes in vivo, *Colloids and Surfaces B: Biointerfaces*, 2005, **45**, 174–180, DOI: 10.1016/j.colsurfb.2005.08.010.

[102] L. Qi, W. Liao and Z. Bi, Adsorption investigation of two surfactants at solid/aqueous interface by a cyclic voltammetry method, *Colloids and Surfaces A: Physicochemical and Engineering Aspects*, 2005, **257258**, 429–432, DOI: 10.1016/j.colsurfa.2004.10.089.

[103] A. Angus-Smyth, C. D. Bain, I. Varga and R. A. Campbell, Effects of bulk aggregation on PEI-SDS monolayers at the dynamic air-liquid interface: depletion due to precipitation versus enrichment by a convection/spreading mechanism, *Soft Matter*, 2013, **9**, 6103–6117, DOI: 10.1039/C3SM50636C.

[104] A. Angus-Smyth, R. A. Campbell and C. D. Bain, Dynamic Adsorption of Weakly Interacting Polymer/Surfactant Mixtures at the Air/Water Interface, *Langmuir*, 2012, **28**, 12479–12492, DOI: 10.1021/la301297s.

[105] S. Manning-Benson, S. R. W. Parker, C. D. Bain and J. Penfold, Measurement of the Dynamic Surface Excess in an Overflowing Cylinder by Neutron Reflection, *Langmuir*, 1998, **14**, 990–996, DOI: 10.1021/la9710785.

[106] D. Valkovska, K. M. Wilkinson, R. A. Campbell, C. D. Bain, R. Wat and J. Eastoe, Measurement of the Dynamic Surface Excess of the Nonionic Surfactant C8E4OMe by Neutron Reflection and Ellipsometry, *Langmuir*, 2003, **19**, 5960–5962, DOI: 10.1021/la034053g.

[107] G. Fragneto, Z. X. Li, R. K. Thomas, A. R. Rennie and J. Penfold, A Neutron Reflectivity Study of the Adsorption of Aerosol-OT on Self-Assembled Monolayers on Silicon, *Journal of Colloid and Interface Science*, 1996, **178**, 531–537, DOI: 10.1006/jcis.1996.0148.

[108] M. Sekine, R. A. Campbell, D. S. Valkovska, J. P. R. Day, T. D. Curwen, L. J. Martin, S. A. Holt, J. Eastoe and C. D. Bain, Adsorption kinetics of ammonium perfluorononanoate at the air-water interface, *Phys. Chem. Chem. Phys.*, 2004, **6**, 5061–5065, DOI: 10.1039/B411044G.

[109] J. P. R. Day, P. D. A. Pudney and C. D. Bain, Ellipsometric study of the displacement of milk proteins from the oil-water interface by the non-ionic surfactant C10E8, *Phys. Chem. Chem. Phys.*, 2010, **12**, 4590–4599, DOI: 10.1039/B921887D.

[110] T. Battal, G. C. Shearman, D. Valkovska, C. D. Bain, R. C. Darton and J. Eastoe, Determination of the Dynamic Surface Excess of a Homologous Series of Cationic Surfactants by Ellipsometry, *Langmuir*, 2003, **19**, 1244–1248, DOI: 10.1021/la026566d.

[111] R. A. Campbell, P. A. Ash and C. D. Bain, Dynamics of Adsorption of an Oppositely Charged Polymer-Surfactant Mixture at the Air-Water Interface: Poly(dimethyldiallylammonium chloride) and Sodium Dodecyl Sulfate, *Langmuir*, 2007, **23**, 3242–3253, DOI: 10.1021/la0632171.

[112] J. Eastoe, A. Rankin, R. Wat and C. D. Bain, Surfactant adsorption dynamics, *International Reviews in Physical Chemistry*, 2001, **20**, 357–386, DOI: 10.1080/01442350110046766.

[113] S. Biswas and D. Chattoraj, Kinetics of Adsorption of Cationic Surfactants at Silica-Water Interface, *Journal of Colloid and Interface Science*, 1998, **205**, 12–20, DOI: 10.1006/jcis.1998.5574.

[114] T. D. Curwen, J. A. Warner, C. D. Bain, R. G. Compton and J. K. Eve, Adsorption Kinetics in a Dual-Inlet Channel Flow Cell: I. Cetyl Pyridinium Chloride on Hydrophilic Silica, *The Journal of Physical Chemistry C*, 2007, **111**, 12289–12304, DOI: 10.1021/jp0729213.

[115] T. D. Curwen, C. D. Bain and J. K. Eve, Adsorption Kinetics in a Dual-Inlet Channel Flow Cell: II. Cetyl Pyridinium Chloride on Methyl and Methyl Ether Surfaces, *The Journal of Physical Chemistry C*, 2007, **111**, 12305–12314, DOI: 10.1021/jp072922v.

[116] J. Lopata, K. Werts, J. Scamehorn, J. Harwell and B. Grady, Thermodynamics of mixed anionic/nonionic surfactant adsorption on alumina, *Journal of Colloid and Interface Science*, 2010, **342**, 415–426, DOI: 10.1016/j.jcis.2009.10.072.

[117] J. H. Harwell, B. L. Roberts and J. F. Scamehorn, Thermodynamics of adsorption of surfactant mixtures on minerals, *Colloids and Surfaces*, 1988, **32**, 1–17, DOI: 10.1016/0166-6622(88)80001-5.

[118] M. Chorro, C. Chorro, O. Dolladille, S. Partyka and R. Zana, Adsorption Mechanism of Conventional and Dimeric Cationic Surfactants on Silica Surface: Effect of the State of the Surface, *Journal of Colloid and Interface Science*, 1999, **210**, 134–143, DOI: 10.1006/jcis.1998.5936.

[119] W. Deer, R. Howie and J. Zussman, *An introduction to the rock-forming minerals*, Longman Scientific & Technical, 2nd edn., 1992.

[120] B. Jha and D. N. Singh, in *Basics of Zeolites*, Springer Singapore, Singapore, 2016, pp. 5–31, DOI: 10.1007/978-981-10-1404-8_2.

[121] E. Frida, N. Bukit and B. F. Bukit, Natural Zeolite Modification With A Surfactant Cetyl Trimethyl Ammonium Bromide (Ctab) As Material To Filler In Polypropylene, *Chemistry and Materials Research*, 2014, **6**, 34–41.

[122] L. Xu, X. Ji, S. Li, Z. Zhou, X. Du, J. Sun, F. Deng, S. Che and P. Wu, Self-Assembly of Cetyltrimethylammonium Bromide and Lamellar Zeolite Precursor for the Preparation of Hierarchical MWW Zeolite, *Chemistry of Materials*, 2016, **28**, 4512–4521, DOI: 10.1021/acs.chemmater.6b02155.

[123] J. S. Lee, J. H. Kim, Y. J. Lee, N. C. Jeong and K. B. Yoon, Manual Assembly of Microcrystal Monolayers on Substrates, *Angewandte Chemie International Edition*, 2007, **46**, 3087–3090, DOI: 10.1002/anie.200604367.

[124] J. A. Lee, L. Meng, D. J. Norris, L. E. Scriven and M. Tsapatsis, Colloidal Crystal Layers of Hexagonal Nanoplates by Convective Assembly, *Langmuir*, 2006, **22**, 5217–5219, DOI: 10.1021/la0601206.

[125] S. Li, Z. Li, K. N. Bozhilov, Z. Chen and Yan, TEM Investigation of Formation Mechanism of Monocrystal-Thick b-Oriented Pure Silica Zeolite MFI Film, *Journal of the American Chemical Society*, 2004, **126**, 10732–10737, DOI: 10.1021/ja0478429.

[126] H. S. Kim, S. M. Lee, K. Ha, C. Jung, Y.-J. Lee, Y. S. Chun, D. Kim, B. K. Rhee and K. B. Yoon, Aligned Inclusion of Hemicyanine Dyes into Silica Zeolite Films for Second Harmonic Generation, *Journal of the American Chemical Society*, 2004, **126**, 673–682, DOI: 10.1021/ja037772q.

[127] M. Viertelhaus, A. E. Taylor, L. Kloo, I. Gameson and P. A. Anderson, Silver nitrate in silver zeolite A: three-dimensional incommensurate guest ordering in a zeolite framework, *Dalton Trans.*, 2006, 2368–2373, DOI: 10.1039/B517094J.

[128] M. Battey, *Mineralogy for Students*, Longman Group, London, 2nd edn., 1981.

[129] K. Mondale, R. Carland and F. Aplan, The comparative ion exchange capacities of natural sedimentary and synthetic zeolites, *Minerals Engineering*, 1995, **8**, 535–548, DOI: 10.1016/0892-6875(95)00015-I.

[130] C. Klein and C. S. Hurlbut, *Manual of Mineralogy: (After James D. Dana).*, Wiley, New York, 20th edn., 1985.

[131] S. R. Taffarel and J. Rubio, Adsorption of sodium dodecyl benzene sulfonate from aqueous solution using a modified natural zeolite with CTAB, *Minerals Engineering*, 2010, **23**, 771–779, DOI: 10.1016/j.mineng.2010.05.018.

[132] A. C. Savitsky, B. H. Wiers and R. H. Wendt, Adsorption of organic compounds from dilute aqueous solutions onto the external surface of type A zeolite, *Environmental Science & Technology*, 1981, **15**, 1191–1196, DOI: 10.1021/es00092a006.

[133] *Mesoporous Zeolites*, ed. J. García-Martíez and K. Li, Wiley-VCH, 2015.

[134] M. M. Salim, N. A. N. N. Malek, N. I. Ramli, S. A. M. Hanim and S. Hamdan, Antibacterial activity of CTAB-modified zeolite NaY with different CTAB loading, *Malaysian Journal of Fundamental and Applied Sciences*, 2014, **10**, 129–133, DOI: 10.11113/mjfas.v10n3.267.

[135] S. Xu and S. A. Boyd, Alternative Model for Cationic Surfactant Adsorption by Layer Silicates, *Environmental Science & Technology*, 1995, **29**, 3022–3028, DOI: 10.1021/es00012a020.

[136] G. M. Haggerty and R. S. Bowman, Sorption of chromate and other inorganic anions by organo-zeolite, *Environmental Science & Technology*, 1994, **28**, 452–458, DOI: 10.1021/es00052a017.

[137] C. Chassagne, F. Mietta and J. Winterwerp, Electrokinetic study of kaolinite suspensions, *Journal of Colloid and Interface Science*, 2009, **336**, 352–359, DOI: 10.1016/j.jcis.2009.02.052.

[138] T. Leivisk, S. Gehr, E. Eijrvi, A. Sarpola and J. Tanskanen, Characteristics and potential applications of coarse clay fractions from Puolanka, Finland, *Open Engineering*, 2012, **2**, 239–247, DOI: 10.2478/s13531-011-0067-9.

[139] Z. Zhou and W. D. Gunter, The Nature of the Surface Charge of Kaolinite, *Clays and Clay Minerals*, 1992, **40**, 365–368, DOI: 10.1346/CCMN.1992.0400320.

[140] P. F. Weck, E. Kim and C. F. Jove-Colon, Relationship between crystal structure and thermo-mechanical properties of kaolinite clay: beyond standard density functional theory, *Dalton Trans.*, 2015, **44**, 12550–12560, DOI: 10.1039/C5DT00590F.

[141] J. M. G. Cowie and V. Arrighi, *Polymers : chemistry and physics of modern materials*, Taylor & Francis, 3rd edn., 2008.

[142] A. W. Birley and M. J. Scott, *Plastics materials : properties and applications*, Leonard Hill, Glasgow, 1982.

[143] T.-S. Choi, Y. Shimizu, H. Shirai and K. Hamada, Disperse dyeing of polyester fiber using gemini surfactants containing ammonium cations as auxiliaries, *Dyes and Pigments*, 2001, **50**, 55–65, DOI: 10.1016/S0143-7208(01)00033-X.

[144] J. O'Lenick, AnthonyJ., Soil release polymers, *Journal of Surfactants and Detergents*, 1999, **2**, 553–557, DOI: 10.1007/s11743-999-0105-4.

[145] K. Dillan, E. Goddard and D. McKenzie, Oily soil removal from a polyester substrate by aqueous nonionic surfactant systems, *Journal of the American Oil Chemists' Society*, 1979, **56**, 59–70, DOI: 10.1007/BF02671763.

[146] H. S. Oliveira, L. C. A. Oliveira, M. C. Pereira, J. D. Ardisson, P. P. Souza, P. O. Patricio and F. C. C. Moura, Nanostructured vanadium-doped iron oxide: catalytic oxidation of methylene blue dye, *New J. Chem.*, 2015, **39**, 3051–3058, DOI: 10.1039/C4NJ02063D.

[147] A. M. Jubb and H. C. Allen, Vibrational Spectroscopic Characterization of Hematite, Maghemite, and Magnetite Thin Films Produced by Vapor Deposition, *ACS Applied Materials & Interfaces*, 2010, **2**, 2804–2812, DOI: 10.1021/am1004943.

[148] E. Malinowski, *Factor Analysis in Chemistry*, John Wiley & Sons, Ltd., 2nd edn., 1991, DOI: 10.1002/cem.1180050607.

[149] P. K. Swain and D. Cheskis, *Back-Illuminated Image Sensors Come to the Forefront*, 2008, http://www.photonics.com/Article.aspx?PID=5&VID=22&IID=156&Tag=Features&AID=34685.

[150] T. W. Edwards and R. S. Pennypacker, *Manufacture of thinned substrate imagers*, Patent US4266334, 1981, `http://worldwide.espacenet.com/publicationDetails/biblio?CC=US&NR=4266334A&KC=A&FT=D&ND=&date=19810512&DB=&locale=en_EP`.

[151] Princeton Instruments Inc., *Spectroscopic Etaloning in Back Illuminated CCDs*, Internet Resource, 2011, `http://www.princetoninstruments.com/cms/index.php/ccd-primer/149-spectroscopic-etaloning-in-back-illuminated-ccds`.

[152] Princeton Instruments Inc., *St-130 and ST-135 Controller Operation Manual*, Princeton Instruments Inc., Version 1, Revision A edn., 1993.

[153] Princeton Instruments Inc., *LN/CCD-512TKB Specifications*, Princeton Instruments Inc., 1993.

[154] Acton Research Corporation, *Operating Instructions SpectraPro-500i*, Acton Research Corporation, 530 Main Street, Acton, MA 01720, V1097.1 edn., 1996.

[155] Ocean Optics Inc., *Calibration Light Source CAL-2000 Installation and Operation Manual*, Ocean Optics Inc., 830 Douglas Ave., Dunedin, FL, USA 34698, 2009.

[156] P. Bentley and P. Hendra, Polarised FT Raman studies of an ultra-high modulus polyethylene rod, *Spectrochimica Acta Part A: Molecular and Biomolecular Spectroscopy*, 1995, **51**, 2125–2131, DOI: 10.1016/0584-8539(95)01513-3.

[157] S. S. Shah and A. M. Khan, Determination of Critical Micelle Concentration (Cmc) of Sodium Dodecyl Sulfate (SDS) and the Effect of Low Concentration of Pyrene on its Cmc Using ORIGIN Software, *J. Chem. Soc. Pak*, 2008, **30**, 186–191.

[158] E. Weiss, K. Groenen-Serrano and A. Savall, Electrochemical mineralization of sodium dodecylbenzenesulfonate at boron doped diamond anodes, *Journal of Applied Electrochemistry*, 2007, **37**, 1337–1344, DOI: 10.1007/s10800-007-9367-4.

[159] J. Eastoe, J. S. Dalton, P. G. Rogueda, E. R. Crooks, A. R. Pitt and E. A. Simister, Dynamic Surface Tensions of Nonionic Surfactant Solutions, *Journal of Colloid and Interface Science*, 1997, **188**, 423–430, DOI: 10.1006/jcis.1997.4778.

[160] W. H. Richtering, W. Burchard, E. Jahns and H. Finkelmann, Light scattering from aqueous solutions of a nonionic surfactant (C14E8) in a wide concentration range, *The Journal of Physical Chemistry*, 1988, **92**, 6032–6040, DOI: 10.1021/j100332a039.

[161] F. Tiberg, B. Joensson, J.-a. Tang and B. Lindman, Ellipsometry Studies of the Self-Assembly of Nonionic Surfactants at the Silica-Water Interface: Equilibrium Aspects, *Langmuir*, 1994, **10**, 2294–2300, DOI: 10.1021/la00019a045.

[162] H. Akisada, J. Kuwahara, A. Koga, H. Motoyama and H. Kaneda, Unusual behavior of CMC for binary mixtures of alkyltrimethylammonium bromides: Dependence on chain length difference, *Journal of Colloid and Interface Science*, 2007, **315**, 678–684, DOI: 10.1016/j.jcis.2007.07.003.

[163] M. Swanson-Vethamuthu, E. Feitosa and W. Brown, Salt-Induced Sphere-to-Disk Transition of Octadecyltrimethylammonium Bromide Micelles, *Langmuir*, 1998, **14**, 1590–1596, DOI: 10.1021/la9608167.

[164] A. G. Diress, M. M. Yassine and C. A. Lucy, Semipermanent capillary coatings in mixed organic-water solvents for CE, *Electrophoresis*, 2007, **28**, 1189–1196, DOI: 10.1002/elps.200600440.

[165] M. L. Lambert, *MChem project*, University of Durham, 2013.

[166] E. Feitosa, P. Barreleiro and G. Olofsson, Phase transition in dioctadecyldimethyl-ammonium bromide and chloride vesicles prepared by different methods, *Chemistry and Physics of Lipids*, 2000, **105**, 201–213, DOI: 10.1016/S0009-3084(00)00127-4.

[167] *CRC Handbook of Chemistry and Physics*, ed. D. R. Lide, CRC Press, 74th edn., 1993.

[168] J. E. Bertie and Z. Lan, Liquid Water-Acetonitrile Mixtures at 25 °C: The Hydrogen-Bonded Structure Studied through Infrared Absolute Integrated Absorption Intensities, *The Journal of Physical Chemistry B*, 1997, **101**, 4111–4119, DOI: 10.1021/jp9639511.

[169] Y. Yu, Y. Wang, K. Lin, N. Hu, X. Zhou and S. Liu, Complete Raman Spectral Assignment of Methanol in the C-H Stretching Region, *The Journal of Physical Chemistry A*, 2013, **117**, 4377–4384, DOI: 10.1021/jp400886y.

[170] C. Wohlfarth, in *Refractive Indices of Pure Liquids and Binary Liquid Mixtures (Supplement to III/38)*, ed. M. Lechner, Springer Berlin Heidelberg, 2008, vol. 47 of Landolt-Börnstein - Group III Condensed Matter, pp. 564–566, DOI: 10.1007/978-3-540-75291-2_358.

[171] Z. Bi, W. Liao and L. Qi, Wettability alteration by CTAB adsorption at surfaces of SiO2 film or silica gel powder and mimic oil recovery, *Applied Surface Science*, 2004, **221**, 25–31, DOI: 10.1016/S0169-4332(03)00948-6.

[172] A. Fan, P. Somasundaran and N. J. Turro, Adsorption of Alkyltrimethylammonium Bromides on Negatively Charged Alumina, *Langmuir*, 1997, **13**, 506–510, DOI: 10.1021/la9607215.

[173] E. S. Pagac, D. C. Prieve and R. D. Tilton, Kinetics and Mechanism of Cationic Surfactant Adsorption and Coadsorption with Cationic Polyelectrolytes at the Silica-Water Interface, *Langmuir*, 1998, **14**, 2333–2342, DOI: 10.1021/la971308f.

[174] E. M. Furst, E. S. Pagac and R. D. Tilton, Coadsorption of Polylysine and the Cationic Surfactant Cetyltrimethylammonium Bromide on Silica, *Industrial & Engineering Chemistry Research*, 1996, **35**, 1566–1574, DOI: 10.1021/ie9506577.

[175] G. B. Ray, I. Chakraborty, S. Ghosh, S. P. Moulik and R. Palepu, Self-Aggregation of Alkyltrimethylammonium Bromides (C10-, C12-, C14-, and C16TAB) and Their Binary Mixtures in Aqueous Medium: A Critical and Comprehensive Assessment of Interfacial Behavior and Bulk Properties with Reference to Two Types of Micelle Formation, *Langmuir*, 2005, **21**, 10958–10967, DOI: 10.1021/la051509g.

[176] A. K. Vanjara and S. G. Dixit, Adsorption of Alkyltrimethylammonium Bromide and Alkylpyridinium Chloride Surfactant Series on Polytetrafluoroethylene Powder, *Journal of Colloid and Interface Science*, 1996, **177**, 359–363, DOI: 10.1006/jcis.1996.0044.

[177] J. Beckwith, Summer Project, 2011.

[178] X.-M. Bai and M. Li, Differences between solid superheating and liquid supercooling, *The Journal of Chemical Physics*, 2005, **123**, 151102, DOI: 10.1063/1.2085147.

[179] E. Feitosa, J. Jansson and B. Lindman, The effect of chain length on the melting temperature and size of dialkyldimethylammonium bromide vesicles, *Chemistry and Physics of Lipids*, 2006, **142**, 128–132, DOI: 10.1016/j.chemphyslip.2006.02.001.

[180] M. Goto, Y. Ito, S. Ishida, N. Tamai, H. Matsuki and S. Kaneshina, Hydrostatic Pressure Reveals Bilayer Phase Behavior of Dioctadecyldimethylammonium Bromide and Chloride, *Langmuir*, 2011, **27**, 1592–1598, DOI: 10.1021/la104552z.

[181] P. C. F. Pau, J. O. Berg and W. G. McMillan, Application of Stokes' law to ions in aqueous solution, *The Journal of Physical Chemistry*, 1990, **94**, 2671–2679, DOI: 10.1021/j100369a080.

[182] C. Guha, J. M. Chakraborty, S. Karanjai and B. Das, The Structure and Thermodynamics of Ion Association and Solvation of Some Thiocyanates and Nitrates in 2-Methoxyethanol Studied by Conductometry and FTIR Spectroscopy, *The Journal of Physical Chemistry B*, 2003, **107**, 12814–12819, DOI: 10.1021/jp030731w.

[183] T. Sata, K. Kawamura, M. Higa and K. Matsusaki, Electrodialytic transport properties of anion-exchange membranes in the presence of α-cyclodextrin, *Colloid and Polymer Science*, 2001, **279**, 413–419, DOI: 10.1007/s003960000459.

[184] C. Yan, A. Angus-Smyth and C. D. Bain, Adsorption kinetics of non-ionic surfactants in micellar solutions: effects of added charge, *Faraday Discuss.*, 2013, **160**, 45–61, DOI: 10.1039/C2FD20118F.

[185] S. Wang and Y. Peng, Natural zeolites as effective adsorbents in water and wastewater treatment, *Chemical Engineering Journal*, 2010, **156**, 11–24, DOI: http://dx.doi.org/10.1016/j.cej.2009.10.029.

[186] H. Faghihian, A. Malekpour and M. Maragheh, Removal of Radioactive Iodide by Surfactant-modified Zeolites, *Adsorption Science & Technology*, 2003, **21**, 373–381, DOI: 10.1260/026361703322405088.

[187] C.-F. Chang, C.-Y. Chang, K.-H. Chen, W.-T. Tsai, J.-L. Shie and Y.-H. Chen, Adsorption of naphthalene on zeolite from aqueous solution, *Journal of Colloid and Interface Science*, 2004, **277**, 29–34, DOI: 10.1016/j.jcis.2004.04.022.

[188] L. Seifi, A. Torabian, H. Kazemian, G. N. Bidhendi, A. A. Azimi, S. Nazmara and M. AliMohammadi, Adsorption of BTEX on Surfactant Modified Granulated Natural Zeolite Nanoparticles: Parameters Optimizing by Applying Taguchi Experimental Design Method, *CLEAN - Soil, Air, Water*, 2011, **39**, 939–948, DOI: 10.1002/clen.201000390.

[189] J. Rocha, J. Klinowski and J. M. Adams, Synthesis of zeolite Na-A from metakaolinite revisited, *J. Chem. Soc., Faraday Trans.*, 1991, **87**, 3091–3097, DOI: 10.1039/FT9918703091.

[190] E. Lippmaa, M. Maegi, A. Samoson, M. Tarmak and G. Engelhardt, Investigation of the structure of zeolites by solid-state high-resolution silicon-29 NMR spectroscopy, *Journal of the American Chemical Society*, 1981, **103**, 4992–4996, DOI: 10.1021/ja00407a002.

[191] P. K. Dutta and B. Del Barco, Raman spectroscopy of zeolite A: influence of silicon/aluminum ratio, *The Journal of Physical Chemistry*, 1988, **92**, 354–357, DOI: 10.1021/j100313a022.

[192] H. K. Hunt, *PhD Thesis*, California Institute of Technology, 2009.

[193] L. Tosheva and V. P. Valtchev, Nanozeolites: Synthesis, Crystallization Mechanism, and Applications, *Chemistry of Materials*, 2005, **17**, 2494–2513, DOI: 10.1021/cm047908z.

[194] Y.-Y. Luo, Z.-P. Du, Y.-H. Lu and B.-X. Liu, Adsorption of CTAB on Zeolite A Detected by Surfactant Ion-selective Electrode, *Tenside Surfactants Detergents*, 2009, **46**, 175–178, DOI: 10.3139/113.110022.

[195] H. Hosokawa and K. Oki, Synthesis of Nanosized A-type Zeolites from Sodium Silicates and Sodium Aluminates in the Presence of a Crystallization Inhibitor, *Chemistry Letters*, 2003, **32**, 586–587, DOI: 10.1246/cl.2003.586.

[196] P. Levitz, Aggregative adsorption of nonionic surfactants onto hydrophilic solid/water interface. Relation with bulk micellization, *Langmuir*, 1991, **7**, 1595–1608, DOI: 10.1021/la00056a010.

[197] S. K. Singh and S. M. Notley, Adsorption of Nonionic Surfactants (CnEm) at the Silica-Water and Cellulose-Water Interface, *The Journal of Physical Chemistry B*, 2010, **114**, 14977–14982, DOI: 10.1021/jp107224r.

[198] J. F. Lambert, W. S. Millman and J. J. Fripiat, Revisiting kaolinite dehydroxylation: a silicon-29 and aluminum-27 MAS NMR study, *Journal of the American Chemical Society*, 1989, **111**, 3517–3522, DOI: 10.1021/ja00192a005.

[199] A. Tahani, H. Damme, C. Noik and P. Levitz, Adsorption of Nonionic Surfactants on Kaolins, *Journal of Colloid and Interface Science*, 1996, **184**, 469–476, DOI: 10.1006/jcis.1996.0642.

[200] D. Nevskaia, A. Guerrero-Ruíz and J. D. López-González, Adsorption of Polyoxyethylenic Surfactants on Quartz, Kaolin, and Dolomite: A Correlation between Surfactant Structure and Solid Surface Nature, *Journal of Colloid and Interface Science*, 1996, **181**, 571–580, DOI: 10.1006/jcis.1996.0414.

[201] Q. Xu and P. Somasundaran, Adsorption of nonionic surfactants, anionic/nonionic surfactant mixtures, and hydrophobically modified polymers on minerals and its effect on their flotation and dispersion, *Proc. XV111 Int. Miner. Process. Congr., Sydney*, 1993, 601–606.

[202] R. L. Frost, T. H. Tran and T. Le, in *Progress in Fourier Transform Spectroscopy*, ed. J. Mink, G. Keresztury and R. Kellner, Springer Vienna, 1997, vol. 14 of Mikrochimica Acta Supplement, pp. 747–749, DOI: 10.1007/978-3-7091-6840-0_197.

[203] A. J. Melveger, Laser-raman study of crystallinity changes in poly(ethylene terephthalate), *Journal of Polymer Science Part A-2: Polymer Physics*, 1972, **10**, 317–322, DOI: 10.1002/pol.1972.160100211.

[204] Filmetrics, Inc, *Refractive Index of PET, Estar, Melinex, Mylar*, 2013, `http://www.filmetrics.com/refractive-index-database/PET/Estar-Melinex-Mylar`.

[205] J. Elman, J. Greener, C. Herzinger and B. Johs, Characterization of biaxially-stretched plastic films by generalized ellipsometry, *Thin Solid Films*, 1998, **313314**, 814–818, DOI: 10.1016/S0040-6090(97)01001-8.

[206] E. Potapova, I. Carabante, M. Grahn, A. Holmgren and J. Hedlund, Studies of Collector Adsorption on Iron Oxides by in Situ ATR-FTIR Spectroscopy, *American Chemical Society*, 2010, **49**, 1493–1502, DOI: 10.1021/ie901343f.

[207] E. Matijevic, Production of Monodispersed Colloidal Particles, *Annual Review of Materials Science*, 1985, **15**, 483–516, DOI: 10.1146/annurev.ms.15.080185.002411.

[208] N. Buzgar, A. I. Apopei and A. Buzatu, *Hematite Raman spectra*, 2013, `http://rdrs.uaic.ro/minerals/hematite.html`.

Appendix A

Circuit Diagrams

The following circuit diagrams were used. They were manufactured in-house by our departmental electronics workshop.

A.1 Stepper Motor Driver

Stepper motor driver control shown in figure A.1. The board was controlled by 5 V TTL logic via inputs for step, enable motor, reverse direction, half speed, and quarter speed.
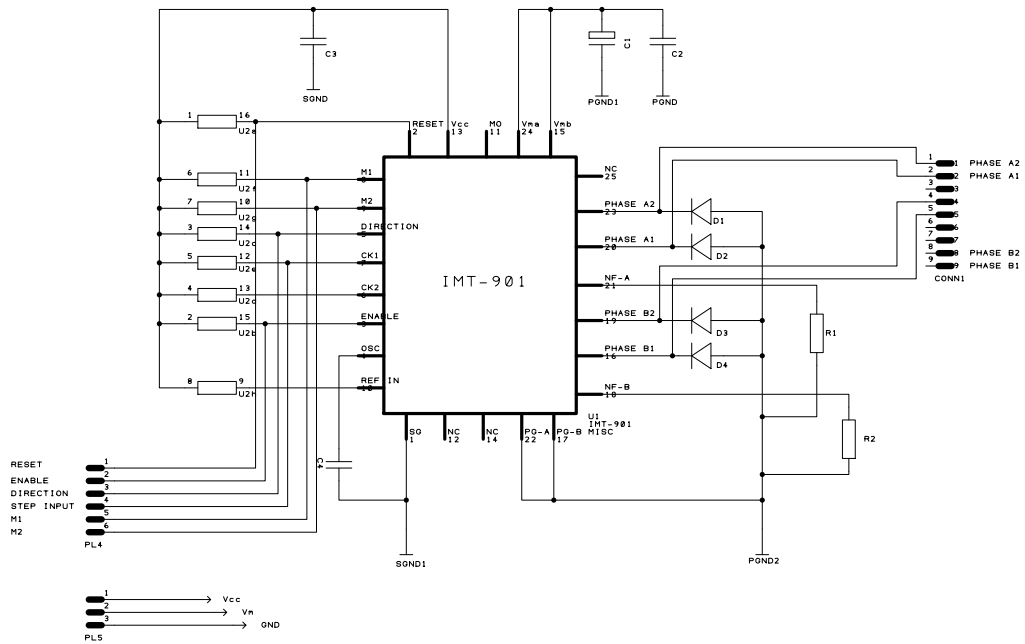
Figure A.1: Stepper motor driver circuit diagram

A.2 Thermocouple

Thermocouple board signal conditioner shown in figure A.2. This generated an output of $5\,\mathrm{mV/°C}$. N.B. The $-5\,\mathrm{V}$ rail was not powered as temperatures below $0\,°\mathrm{C}$ were not measured.
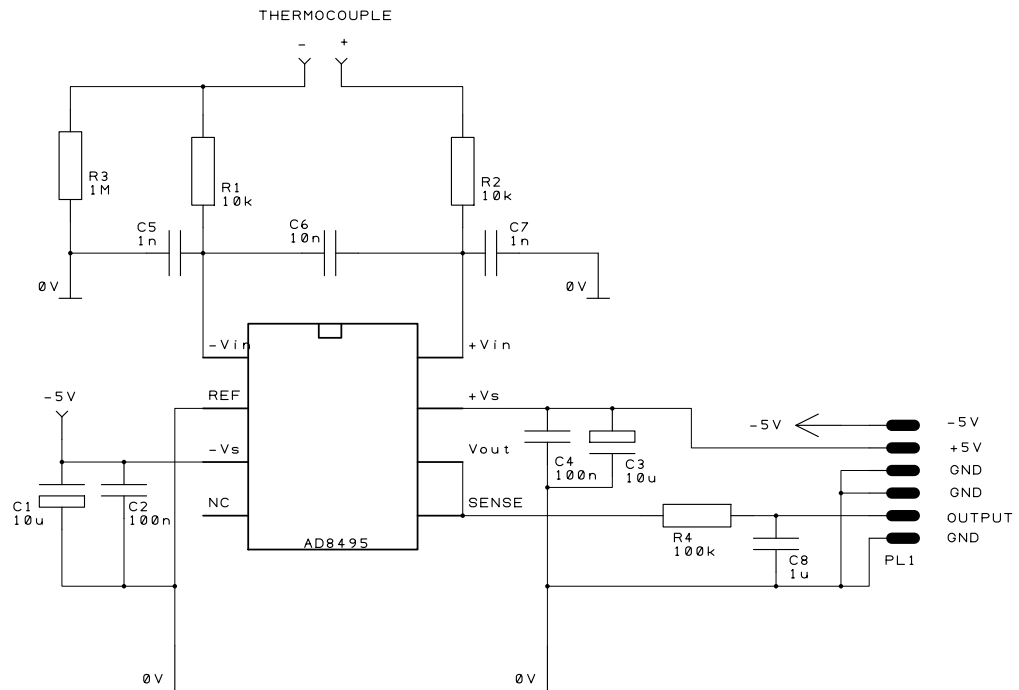
Figure A.2: Thermocouple board circuit diagram

Appendix B

MATLAB Code

The code on the following pages is the MATLAB code which was used during this project.

List of Code

B.1 Data Import

readSPE.m

Reads simple SPE files into MATLAB. Adapted from sample on MATLAB code repository.

```matlab
function rawdata= readSPE(filename)

%reads *.SPE files into Matlab
%Run as either: readSPE('{filename}') or
    without variable to be prompted for file

if ~exist('filename','var') || isempty(
    filename)

    fid = -1;
    msg = 'Please select file';
    while fid < 0
        disp(msg);
        filename = input('Open file: ', 's');
        [fid,msg] = fopen(filename);
    end

else

    fid=fopen(filename,'r');

end


header=fread(fid,2050,'uint16'); %4100 bytes/2

points=header(1); %number of points/pixels
noofspectra=header(18); %number of spectra (
    frames) from file
ImMat=fread(fid,points*noofspectra,'uint16');
    %read file data
rawdata=reshape(ImMat,points,noofspectra); %
    convert into matrix
fclose(fid); %release lock
rawdata=double(rawdata).'; %convert to double
    precision
```

Listing B.1 : readSPE.m

mySPEreader.m

Reads SPE files into MATLAB and adds wavelength.

```matlab
function [mydata,badpoints]= mySPEreader(
    filename,timesfile,centre,excitation,
    M0peak,badpoints)
%% Generate wavenubers

limit=15; % change detection limit for bad
    pixels
m=1;

x=1;

mydata(1,2:513)=wavenumbergenerator(centre,
    excitation,M0peak);

figure(1)
subplot(1,1,1);

%% Read SPE File

if ~exist('filename','var') || isempty(
    filename);
% disp('file');
fid = -1;
msg = 'Please select file';
while fid < 0
    disp(msg);
    filename = input('Open file: ', 's');
    [fid,msg] = fopen(filename);

end
else

        fid=fopen(filename,'r');


end

%reads *.SPE files into Matlab
```

```matlab
%% Check files exist
if ~exist('filename','file')==2 || ~exist('
    filename','var')==1
    error('SPEReader:File_missing','SPE file
    does not exist');
end

if exist(timesfile,'file')~=2
    error('SPEReader:File_missing','Time (CSV
    ) file does not exist');
end
%% read the SPE file

if ~exist(filename,'var')==1

    header=fread(fid,2050,'uint16'); %4100
    bytes/2
    noofspectra=header(18);
    ImMat=fread(fid,512*noofspectra,'uint16')
    ;
    rawdata=reshape(ImMat,512,noofspectra);
    fclose(fid);
    rawdata=double(rawdata).';
else

    rawdata=double(filename);
    noofspectra=size(rawdata,1);
end

rawdata(:,end)=rawdata(:,end-1); % Remove
    last pixel as reads high
rawdata(:,1)=rawdata(:,2); % Remove first
    pixel as reads high


%% Import times

%%% Import the data
% msg = 'Please select CSV file containing
    times';

[~, ~, raw] = xlsread(timesfile);
raw = raw(2:end,:);

%%% Replace non-numeric cells with 0.0
R = cellfun(@(x) ~isnumeric(x) || isnan(x),
    raw); % Find non-numeric cells
raw(R) = {0.0}; % Replace non-numeric cells

%%% Create output variable
mytimes = cell2mat(raw);


%% Extract times

while x<=noofspectra

    mydata(x+1,1)=mytimes(x+2,2);



    mydata(x+1,2:513)=rawdata(x,:);



    x=x+1;

end

plot(mydata(1,2:end),mydata(2:end,2:end).');


%% detect bad pixels

        myavg=(mydata(1,2:end));
        myavg(2,:)=mean(mydata(2:end,2:end));
if ~exist('badpoints','var') || isempty(
    badpoints)

        m=1;
        p=1;
        while p<size(myavg,2)

            if myavg(2,p+1)-myavg(2,p)>limit

                badpoints(m)=p;
                m=m+1;
            end
            p=p+1;
        end

end

        plot(myavg(2,:))
        hold on
```

```matlab
            plot(badpoints,myavg(2,badpoints)
        ,'or');

            hold off

            disp('Bad points found at:');
disp(badpoints);


%% remove these points
while true
    key=input('Do you want to delete these
        bad pixels? ','s');
    switch key
        case 'y'
            rawspectra=mydata(2:end,2:end).';

                f=1;
            while f<=size(badpoints,2)

                if badpoints(f)~=1

                    rawspectra(badpoints(f)
        ,:)=rawspectra(badpoints(f)-1,:);

                        plot(rawspectra(f,:));
                else
                    rawspectra(badpoints(f)
        ,:)=rawspectra(badpoints(f)+1,:);
                end

                f=f+1;


            end

            plot(rawspectra);

            mydata(2:end,2:end)=rawspectra.';

                break
        case 'n'
            %nothing!
            break
    end
    disp('You must enter "y" or "n"');
end

while true

    if key~='y'
        cont=input('Do you want to continue?
        ','s');
    else
        cont='y';    %we want to continue
    end

    switch cont
        case 'y'

            break;
        case 'n'
            disp('Manually edit badpoints
        variable');
            break;
    end
end


%% Remove cosmic rays

while true
    key=input('Does this contain cosmic rays?
        ','s');
    switch key
        case 'y'
            mydata=
        removeCosmicRaysFromTimeSeries(mydata);
            break
        case 'n'
            %nothing!
            break
    end
    disp('You must enter "y" or "n"');
end

plot(mydata(1,2:end),mydata(2:end,2:end).');

r=1;
            while r<noofspectra

            plot(mydata(1,2:end),mydata(2:r
        +1,2:end).');
            title(r-1);
            pause(0.002);
            r=r+20;
            end
            plot(mydata(1,2:end),mydata(2:end
        ,2:end).');
            title(r-1);

            str = sprintf('File ''%s''
        imported succefuly', filename);

            disp(str)
```

PRNreader.m

Reads PRN (CSMA extracted SPE files)
files into MATLAB.

```matlab
function [data]=PRNreader(prefix,files)

pixels=512;

reverseStr = '';

DELIMITER = ' '; %space? delimeted
HEADERLINES = 0; %are there column names?
i=1;
pixel=1;

data=zeros(512*files,5);

n=1;

    while i<files+1

    filename=[prefix,num2str(i),'.PRN'];

    %     file=fopen(filename);
    %     data=fread(file);


    % Import the file
    output = importdata(filename, DELIMITER,
     HEADERLINES);

    data(i,1:pixels)=output(:,2).'; %+1 to
     allow for times later

  %    data(i:1)=i;

    %pixel=pixel+pixels;
    i=i+1;

    percentDone = 100 * i / files;
    msg = sprintf('Percent done: %3.1f',
     percentDone); %Don't forget this
      semicolon
    fprintf([reverseStr, msg]);
    reverseStr = repmat(sprintf('\b'), 1,
      length(msg));

    end


    n=n+1;

%end
plot(data);
```

wavenumbergenerator.m

Generates wavenumbers from calibration.

```matlab
function [wavenumbers]= wavenumbergenerator(
    centre,excitation,M0peak)


c1=0.970427676;
c2=0.045837295;
c3=-2.37966E-07;
c4=-1.82373E-12;


pixel=1;
pixels=512;

wavenumbers=zeros(1,512).';


pulses=round(0.0000205507845526479*centre
    ^2+0.188319698570221*centre
    +3793.41687363496);


exp_equiv=pulses/115;


while pixel<=pixels
```

```
act_px=((exp_equiv)*115)
    ^2*0.000043823+3.0989*(115*(exp_equiv))+
    pixel-M0peak;


wavelength=c1+c2*act_px+c3*act_px^2+c4*act_px
    ^3;

wavenumbers(pixel)=(1/excitation-1/wavelength
    )*10000000;


pixel=pixel+1;

end
```

X0generator.m

This code generates the target spectra (X0).

```
function target=X0generator(data)
figure(1);
subplot(1,1,1);
while true
    disp('Press 1 for ''in'' and 2 for ''out''
        ');
    type=input('Measurment type: ','s');

    switch type
        case '1' % in measurment take start
        away from end
            water=mean(data(2:2+17,2:end),1)
        .';
            disp('Water spectrum:');
            plot(water);
            pause(1);
            disp('Surf spectrum:');
            while true
                disp('Enter start of surf or
        press y when done');
                surfstart=input('surf start:
        ','s');
                switch surfstart
                    case 'y'
                        break;

                end
                surfstart=str2double(
        surfstart);
                surf=mean(data(surfstart:
        surfstart+17,2:end),1).';
                plot([surf,water]);
            end

            break;
        case '2' % out measurment take end
        away from start
            water=mean(data(end-17:end,2:end)
        ,1).';
            disp('Water spectrum:');
            plot(water);
            pause(1);
            disp('Surf spectrum:');
                surf=mean(data(1:10,2:end),1)
        .';

                plot([surf,water]);

            break;
    end
    disp('You must choose a type!');
end


scale=1;
while true
    target=[water,surf-scale*water];
    plot(target)
    disp('Enter scale factor or press y when
        done, n to quit');
    scale=input('Scale factor: ','s');

    switch scale
        case 'y'
            break;
        case 'n'
            error('X0generator:scale_facor','
        Program aborted by user');
    end

scale=str2double(scale);
target=[water,surf-scale*water];
plot(target)
end
```

removeCosmicRaysFromTime Series.m

This code identifies and removes cosmic rays in a time series. Used with permission from reference 1.

```
function cleanedSpectra =
    removeCosmicRaysFromTimeSeries(spectra,
    varargin)
% (spectra, bounds, droppedPoints)
% takes a time series of spectra, and removes
    the cosmic rays from them
% (hopefully). Ignores the first row and
    column on the assumption that they
% are axis labels. Spectra should be in the
    rows
% bounds says how many standard deviations to
    permit
% droppedPoints says how many of the highest
    points to ignore when
% calculating the standard deviation

if length(varargin) > 0
    bounds = varargin{1};
else
    bounds = [];
end
if length(varargin) > 1
    droppedPoints = varargin{2};
else
    droppedPoints = [];
end

cleanedSpectra = spectra;
repeat = 'y'; % default value

while repeat(1) == 'y'
    cleanedSpectra = removeFromTimeSeriesImpl
        (cleanedSpectra, bounds, droppedPoints);
    plot(cleanedSpectra(2:end,2:end).');
    transpose='y';

    transpose = input('Do you wish to also
        scan columns for spurious points? (y,n)
        [y] ', 's');
    if isempty(transpose)
        transpose = 'y';
    end
    if transpose(1) == 'y'
        cleanedSpectra =
        removeFromTimeSeriesImpl(cleanedSpectra
        .', bounds, droppedPoints); % do
        transpose too
        cleanedSpectra = cleanedSpectra.'; %
        reverse transpose
        plot(cleanedSpectra(2:end,2:end).');
    end
    repeat = input('Repeat? (y,n) [y] ', 's')
        ;
    if isempty(repeat)
        repeat = 'y';
    end
end


function cleanedSpectra =
    removeFromTimeSeriesImpl(spectra, bounds
    , droppedPoints)

cleanedSpectra = spectra(1,:); % copy the
    first row

firstTime = true;

rotatedSpectra = spectra.';

for k=rotatedSpectra(:,2:end) % go across
    columns of rotatedSpectra (.: rows of
    spectra)
    replacement = removeCosmicRays([
    rotatedSpectra(2:end,1)  ,k(2:end)]); %
    do a spectrum at a time
                                        %
    always passing wavenumbers too

    % trim wavenumbers off replacement
    replacement = replacement(:,2);
    replacement = [k(1), replacement.']; %
    add back in the first column (and rotate
    replacement)
    cleanedSpectra = [ cleanedSpectra;
    replacement]; % append the next row to
    the result
end
```

removeCosmicRays.m

This code identifies and removes cosmic rays.
Used with permission from reference 1.

```matlab
function cleanedSpectrum = removeCosmicRays(
    spectrum, varargin)
% (spectra, bounds, droppedPoints)
% removes any peaks which are obviously
    cosmic rays
% should be passed an 'x by 2' or '2 by x'
    array
% containing the peak heights
% bounds says how many standard deviations to
    permit (default is 10)
% droppedPoints says how many of the highest
    points to ignore when
% calculating the standard deviation (default
    is 3)

if ~isempty(varargin)
    bounds = varargin{1};
else
    bounds = [];
end
if length(varargin) > 1
    droppedPoints = varargin{2};
else
    droppedPoints = [];
end

if isempty(bounds)
    bounds = 10;
end
if isempty(droppedPoints)
    droppedPoints = 3;
end

[n,m] = size(spectrum);

if m>n
    spectrum = spectrum.'; % transpose the
        spectrum
    flipped = 1;
    temp = n; n = m; m = temp; % swap n and m
else
    flipped = 0;
end

if m ~= 2
    error('spectrum should consist of
        wavenumbers and intensities. Too few
        columns');
end


cleanedSpectrum = linearRegScan(spectrum, 50,
    bounds, droppedPoints);

if flipped
    cleanedSpectrum = cleanedSpectrum.';
end % else no rotation needed


function cleanedSpectrum = linearRegScan(
    spectrum, points, bounds, droppedPoints)
% points defines how big a region to look at
    once

[rows,columns] = size(spectrum);

if points > rows % process entire spectrum at
    once
    cleanedSpectrum = linearRegImpl(spectrum,
        spectrum);
    return;
end

% for the first part, process a chunk between
    the start of the spectrum
% and the 0.75 of points (for testrange), and
    the start of the spectrum and
% points, for regressionRange
spectrum(1:points,:) = linearRegImpl(spectrum
    (1:points, :), spectrum, bounds,
    droppedPoints);

testRangeStartPoint = points + 1;


validRange = true; % this is true until set
    false

% now do a loop to cover the rest of the
    spectrum
while validRange
    %testRangeEndPoint = testRangeStartPoint
        + int32(0.5*points);
    testRangeEndPoint = testRangeStartPoint+
        points;
    % create a range for which the testRange
        is in the middle of the
    % regression range, which is twice its
        size
%   regRangeStartPoint = testRangeStartPoint
        - 0.25*points;
%   regRangeEndPoint = testRangeEndPoint +
        0.25*points;
```

```matlab
    regRangeStartPoint = testRangeStartPoint;
    regRangeEndPoint = testRangeEndPoint;


    if regRangeEndPoint > rows % we have gone
        out of range
        validRange = false; % stop next go
        regRangeEndPoint = rows;
        testRangeEndPoint = rows; % terminate
        them both at the same point

        if testRangeStartPoint > rows % check
        the start is still valid
            break;
        end;
    end

    % if the start is still valid then do the
        proceedure
    % and append the result to
        cleanedSpectrum

    spectrum(testRangeStartPoint:
        testRangeEndPoint,:) = linearRegImpl(
        spectrum(testRangeStartPoint:
        testRangeEndPoint, :), spectrum, bounds,
        droppedPoints);


    % increment the start point
    %testRangeStartPoint =
        testRangeStartPoint + int32(0.5*points)
        + 1;
    testRangeStartPoint = testRangeStartPoint
        +points+1;
end

cleanedSpectrum = spectrum;

%disp('do we ever get out of this');

% cleanedSpectrum should now contain the
    answer




function cleanedRange = linearRegImpl(
    spectrumRange, wholeSpectrum, bounds,
    droppedPoints)
% spectrumRange should be a x*2 array
% wavenumbers and intensities
% in principle a large portion of the data
    should overlap
% wholeSpectrum is so we can plot it if needs
    be

% find the largest three point in spectra and
    remove it since it will be this
% point (if any) that is the cosmic ray, so
    it's best if it doesn't scew
% the deviation
trimmedSpectrum = spectrumRange;
if numel(trimmedSpectrum(:,2)) >
    droppedPoints
    for k = 1:droppedPoints
        [value, index] = max(trimmedSpectrum
    (:,2));
        trimmedSpectrum(index,:) = []; %
    delete
    end
end

% do a linear regression on the regression
    range
p = polyfit(trimmedSpectrum(:,1),
    trimmedSpectrum(:,2),1);
m = p(1); c = p(2);
%[m,c] = linearRegression(trimmedSpectrum);

% calculate expected values for each point in
    the range test range
% based on the results of the linear
    regression
expected = [ spectrumRange(:,1), m *
    spectrumRange(:,1) + c ];

trimmedExpected = [ trimmedSpectrum(:,1), m *
    trimmedSpectrum(:,1) + c];

% variation from predicted line
% use the trimmed versions, so as to ignore
    the largest points
differences = trimmedSpectrum(:,2) -
    trimmedExpected(:,2);

% work out stddeviation for this region
% (based on the deviation from the line)
deviation = std(differences);

% find points that are higher than the
    expected value plus the deviation
% these are marked as true
comparison = (expected(:,2)+(deviation*bounds
    )) < spectrumRange(:,2);

%close; figure; plot(wholeSpectrum(:,1),
    wholeSpectrum(:,2), expected(:,1),
    expected(:,2), expected(:,1), expected
```

```matlab
        (:,2)+(deviation*bounds));
%pause;

% turn comparison into something with 2
        columns (both of which are
% indentical
comparison = [ comparison , comparison ];

% copy across points where the thing is
        within range
cleanedRange = spectrumRange;

% check everything else with the user
cleanedRange(comparison) = checkValues(
        spectrumRange(comparison), expected(
        comparison), wholeSpectrum);


function newValues = checkValues(values,
        replacements, spectrum)
% values is a x*2 array, containing either
        zeros, or values which need to
% be changed
% replacements is the same
% spectrum is just so we can plot it

newValues = [];

[n,m] = size(values);

values = reshape(values, n/2, 2);
replacements = reshape(replacements, n/2, 2);

%re-get
[n,m] = size(values);

for k = 1:n
    plot(spectrum(:,1),spectrum(:,2),
     replacements(:,1), replacements(:,2),'ro
     '); % so they can see the point
     hopefully
    disp('Dubious point found at:');
    disp(values(k,:)); % display the point
%    delete=input('Do you want to delete
    this point? (y,n) [y] ', 's');
        delete = 'y';
        pause(0.01);
    if (isempty(delete))
        delete = 'y';
    end



    if delete(1) == 'y'
        newValues = [newValues; replacements(
    k,:)];
    else
        newValues = [newValues; values(k,:)];
    end
end
```

```matlab
counts=cell2mat(rawdata(1+n:512+n,5)).';

plot(counts);
% pause(0.1);


    mydata(x+1,2:513)=counts;


    x=x+1;
end

plot(mydata(1,2:end),mydata(2:end,2:end).');
```

ProcessKinetics.m

importkinetics.m

This code imports the kinetic data.

```matlab
function [mydata]=importkinetics(mytimes,
        rawdata,centre,exitation,M0peak)


%
% %%% Import the data

%



m=1;

x=1;


mydata(1,2:513)=wavenumbergenerator(centre,
        exitation,M0peak);



frames=size(rawdata,1)/512;

while x<=frames

    mydata(x+1,1)=mytimes(x+2,2);


    n=(x-1)*512+1;
```

B.2 Data Analysis

Data was analysed using the following code:

ADProcessKinetics.m

This code processes kinetic data.

```matlab
function [kinetics,improvedspectra,rawdata,
    CompWeights,c] = ADProcessKinetics(
    no_of_components,target_spectra_guess,
    data)

delaytime=5; %time between queued expeiments


%% Data import

if ~exist('data','var') || isempty(data)

    rawdata=uiimport('-file');
    fnames = fieldnames(rawdata);

    rawdata = getfield(rawdata,fnames{1});
    figure(1);
    rawdata=OrderSpectra(rawdata);
else
    %We have been given the data, therefore
      do not need to import it


rawdata = data;
end

%% The data processing part
wavenumbers = rawdata(1,2:end).';
subplot(1,1,1);
plot(wavenumbers,rawdata(2:end,2:end).');
xlabel('Wavenumber/ cm^{-1}');
ylabel('Counts');


while true
    key=input('Does this contain cosmic rays?
      ','s');
    switch key
        case 'y'
            rawdata=
    removeCosmicRaysFromTimeSeries(rawdata);
            break
        case 'n'
            %nothing!
            break
    end
    disp('You must enter "y" or "n"');
end

 while true
     key=input('Do you need to do Subtract
     the baseline? ','s');
     switch key
         case 'y'
             rawdata(2:end,2:end)=
     averageOfRangeToZero(rawdata(2:end,2:end
     ).',3,20).';
             break
         case 'n'
             %nothing!
             break
     end
     disp('You must enter "y" or "n"');
 end

times = rawdata(2:end,1);
rawdata=rawdata(2:end,2:end).';

figure(1); plot(rawdata,wavenumbers);

xlabel('Wavenumber/ cm^{-1}');
ylabel('Counts');

improvedspectra=tfa(rawdata,no_of_components,
    target_spectra_guess);     %make
      no_of_components automatic
subplot(2,2,3)
plot(wavenumbers,improvedspectra);
xlabel('Wavenumber/ cm^{-1}');
ylabel('Counts');
title('Components');


% Simulated spectra with noise removed
subplot(2,2,4)
[r,c] = afa(rawdata);

plot(wavenumbers,r(:,1:4)*c(1:4,:))
title('Regenerated comps 1-4');
ylabel('Counts');
xlabel('Wavenumber/ cm^{-1}');

figure(2)
```

```matlab
plot(wavenumbers,r(:,3:5));

figure(1)

CompWeights=lfa(rawdata,improvedspectra).';
subplot(2,2,1);
plot(times, CompWeights);
xlabel('Row 1 Unit');
ylabel('Component Weight');
title('Raw');


subplot(2,2,2)
% figure(2)
normalised=(CompWeights(:,1).\CompWeights
    (:,2));

plot(times,normalised);
xlabel('Row 1 Unit');
ylabel('Component Weight');
title('Normalised');

improvedspectra = [wavenumbers,
    improvedspectra];

kinetics = [times,CompWeights,normalised];

drawnow();
```

Listing B.9 : ADProcessKinetics

afa.m

This is the abstract factor analysis code. Used with permission from reference 1.

```matlab
% ****************************************
% ** afa.m
%                                     **
% ****************************************
%
% returns the abstract factors, or optionally
      the n most important abstract
% factors. Also returns reproduced data based
      on those n factors
%
% function [r, c, cleanedData] = afa(d, n)
%
% IN:
%  d = data matrix
%  n = number of significant factors which
      are important (optional)
% OUT:
%  r = rows
%  c = columns
% cleanedData = data reproduced with only n
      factors (r*c)
function [r, c, cleanedData] = afa(d, n)

[rows, columns] = size(d);

smallest = min([rows,columns]);

switch (nargin)
    case (1)
        sigNo = smallest;
    case (2)
        sigNo = n;
    otherwise
        error('afa.m takes one or two
    arguments.');
end

if (rows<columns)
    [v, s, u] = svd(d', 0);
else
    [u, s, v] = svd(d, 0);
end


c = v(:,1:sigNo)';
r = u(:,1:sigNo)*s(1:sigNo,1:sigNo);
cleanedData = r*c;
```

Listing B.10 : afa.m

tfa.m

This is the target factor analysis code. Used with permission from reference 1.

```matlab
% ****************************************
% ** tfa.m
%                                     **
```

```matlab
% *******************************************
%
% tfa.m  target factor analysis - a program
%        designed to target test
%        suspected factors
%
% function [xp] = tfa(d,n,x)
%
% d = an (r x c) data matrix
% n = number of factors used in target test
% x = an (r x n) matrix composed of n test
%     vectors, each vector with r
%     elements
% xp = improved x matrix
% xExtra = additional factors needed to
%     makeup n factors
%
% no provision is made for handling missing
%     points (blanks) in the targets.
function [xp] = tfa(d,n,x)
format short e

[rx,nx] = size(x);
[r,c] = size(d);
 if (rx ~= r)
     error('Target vectors must emulate
     columns of the data matrix! PROGRAM
     ABORTED')
 end

ldngs = r;
s = c;
if (r<c)
    ldngs = c;
    s = r;
    [v ,sv, u] = svd(d.',0); % I'm pretty
    sure we want .' as transpose, not '
else
    [u, sv, v] = svd(d,0);
end

% original code - vectorised code is below
%for j = 1:s
%    ev(j) = sv(j,j) * sv(j,j); % ev=lamda^0
%    _j (eqn. 4.17)
%                              % (with eqn
%    3.84)
%    rev(j) = ev1(j) / ((r-j+1)*(c-j+1)); %
%    reduced eigenvector (eqn. 4.82)
%    u(:,j) = u(:,j) * sv(j,j); % R = US
%end
ev = (diag(sv).^2).';
rev = ev ./ ( ((r+1)-(1:s)).*((c+1)-(1:s)) );
u = u*sv; % could this be done quicker with
    knowledge that sv is diagonal?!

ubar = u(:,1:n); % only the important factors
% again, original code - equivalent
    vectorised code below
%sev = 0;
%sdf = 0;
%for k = n+1:s
%    sev = sev+ev(k); % sum of eigen vectors
%    (of all unimportant factors)
%    sdf = sdf + (r-k+1) * (c-k+1);
%end
sev = sum(ev(n+1:s));
sdf = sum( ((r+1)-(n+1:s)) .* ((c+1)-(n+1:s))
    );

re = sqrt(sev / (ldngs*(s-n))); % re = real
    error (eqn 4.44)
% tested the vectorisation of this and it's
    fine!
%for j=1:nx
%    t(:,j) = pinv(ubar) * x(:,j); %(eqn
%    3.121)
%    xp(:,j) = ubar * t(:,j); % calculate
%    predicted target vector (eqn. 3.108)
%    dx(:,j) = xp(:,j) - x(:,j);
%end

%%
t = pinv(ubar) * x;% x2;
xp = ubar * t;
dx = xp(:,1:nx) - x;


for j=1:nx
    % aet - apparent error in test vector (
    eqn 4.97)
%    aet(j) = sqrt((dx' * dx) / (rx-n));
    aet(j) = sqrt((dx(:,j)' * dx(:,j)) / (rx-
    n));
    % rep -  real error predicted vector (eqn
    4.112)
    rep(j) = re * norm(t(:,j));
end

    % ret - real error in target vector
%    if rep(j) > aet(j)
%       ret(j) = 0;
%    else
%          ret(j) = sqrt(aet(j)^2 - rep(j)^2);
%    % eqn 4.108
%    end
repgaet = rep > aet;
    ret(repgaet) = 0;
    ret(~repgaet) = sqrt(aet(~repgaet).^2 -
```

```matlab
    rep(~repgaet).^2);
%end
    % p. 129
    % if spoil < 1.0, reproduced data is
    improved by target vector (and
    % target vector is worsened by data)
    % otherwise spoiled by target vector (but
    target vector is improved by data)
%    spoil(j) = ret(j) / rep(j);
%    f(j) = (sdf * r * aet(j)^2) / ((r-n+1) *
    (c-n+1) * sev * t(:,j)' * t(:,j));
%end
spoil = ret ./ rep;
f = (sdf * r * aet.^2) ./ ( (r-n+1) * (c-n+1)
    * sev * diag(t(:,j)' * t(:,j)) );
%clc

df1 = rx - n;
df2 = s - n;
disp('RESULTS OF TARGET TESTING (see Section
    4.6)')
disp(['F(df1,df2) = F(', int2str(df1), ','
    int2str(df2), '), see eq. 4.118'])

%for j = 1:nx
%    tx(j,1) = j;
%    tx(j,2) = aet(j);
%    tx(j,3) = rep(j);
%    tx(j,4) = ret(j);
%    tx(j,5) = spoil(j);
%    tx(j,6) = f(j);
%end
tx = [ (1:nx); aet(1:nx); rep(1:nx); ret(1:nx
    ); spoil(1:nx); f(1:nx) ].';

disp('    target #        AET           REP
              RET         SPOIL          F')
disp(tx)

end
```

Listing B.11 : tfa.m

lfa.m

This is the loading factor analysis code.
Used with permission from reference 1.

```matlab
% *******************************************
% ** lfa.m
% *******************************************
%
% function [loadings, loaderr] = lfa(d,x)
%
% d = an(r x c) data matrix
% x = an(r x n) matrix composed of n test
%     vectors
% The factor space is assumed to be n
%     dimensional
% No provision is made for handling missed
%     points (blanks) in the targets.
function [loadings, loaderr] = lfa(d,x)

format short e

[rx, n] = size(x);
[r,c] = size(d);
if rx ~= r
    error('Target vectors must emulate
    columns of the data matrix!')
end

l = r;
s = c;
if r<c
    l = c;
    s = r;
    [v, sv, u] = svd(d', 0);
else
    [u, sv, v] = svd(d, 0);
end

%original code below - vectorised version
    follows
%for j=1:n % based on r=us (from svd), so u
    is transformed to r (eqn 3.82)
%          % isn't worth proceeding beyond
    the n factors for time
%          % constraints
%    u(:,j) = u(:,j) * sv(j,j);
%end
ubar(:,1:n) = u(:,1:n)*sv(1:n,1:n);

%ubar=u(:,1:n); % select important u's and v'
    s
vbar=v(:,1:n); % v' = C

% vectorised version follows
%for j=1:n
%    t(:,j)=pinv(ubar)*x(:,j); % solving
    x_load = RT^-1 (eqn 3.136)
```

```matlab
%      xp(:,j)=ubar*t(:,j); % test  equation  the
          other  way  round
%      dx=xp(:,j)-x(:,j);
%end
t  =  pinv(ubar)*x;
xp  =  ubar*t;
dx  =  xp  -  x;


loadings=inv(t)*vbar'; % predict  y  in  eqn
      3.132  from  transformation

e  =  d  -  x*loadings; % x  =  satisfactor  test
      vector
xx  =  inv(x'*x); % part  of  eqn  1.35  (without  W
      )

for  j=1:c
      v=xx*(e(:,j)'*e(:,j))/(r-n); % eqns.
      4.135  &  4.136
      %for  k=1:n
      %       loaderr(k,j)=sqrt(v(k,k));
      %end
      loaderr(:,j)  =  sqrt(diag(v));
end
```

Listing B.12 :   lfa.m